

Nanofabrication for On-Chip Optical Levitation, Atom-Trapping, and Superconducting Quantum Circuits

Thesis by
Richard Alexander Norte

In Partial Fulfillment of the Requirements
for the Degree of
Doctor of Philosophy



California Institute of Technology
Pasadena, California

2015
(Defended August 13, 2014)

© 2015

Richard Alexander Norte

All Rights Reserved

Looking back, it's hard to recognize the unbelievably small odds of ending up with the wonderful life I have. This is to my friends and family. You are the winning numbers who made this lottery-ticket of a life possible.

Acknowledgments

To Oskar Painter, thank you for courageously advocating for me when it mattered and making sure that your students' well-being and excitement for science came first.*

I'd like to thank my lab mates who have been a significant driving force during my graduate endeavors. Surrounding myself with a group of such highly motivated, focused, and enthusiastic colleagues has been essential to my growth during my Ph.D. experience. To Kang-Kuen, thanks for your patience and guidance into the field of optics... and experiments in general! To Dal, thanks for being great to work with and also introducing me to this field! Thanks to Simon, whose encouragement, enthusiasm for science, and friendship has transformed my Caltech experience. To Alex and Tim, your mere presence brought sunshine into the yellow-room and then ruined my devices; thank you! Thanks Michelle, you have been incredible in making my time here so much easier... and thanks for the much needed candy-breakfasts. Thanks to Barry, who kept our cleanroom running smoothly and the only person who knows the staff at BWW as well as I do. Thanks to Melissa who was always willing to help me out in the KNI with anything at anytime with little to no advanced warning. HI JEFF. To Amir, for his no-nonsense advice and encouragement. To Ari, thanks for always being great to talk to, both professionally and personally! It was always great to have someone else freak out about random cleanroom nuances. To Justin, for advice on anything cleanroom. To Sean, for his to-the-point suggestions on most anything not-cleanroom. Thanks to Tao for his unstoppable optimism. To Johannes, thanks for always keeping me on task.. It's not easy, I know. To Ale, thanks for getting me addicted to coffee. The coffee breaks really made the difference. To Lukas, thanks for putting up with us while you were in the fridge hot-seat. To Su-Peng, thanks for being great to work with and for being the best trainee I've ever had. Thanks to Jon for being so awesome to work with during hours of high-power laser alignment and etchings. I'd like to also thank the students in the Kimble group whose dedication to their work was always an amazing motivator. Thanks to Jeff Kimble, for your support while I worked in your lab. You always asked the important questions and it was great learning experience.

Thanks to my mom who always supported my academic endeavors and worked hard so I could spend time to think about the weirder, more abstract things in life. Thanks to my aunt Marilyn, who helped raise me and always provided me with the support I needed. Your cool nature has helped me ride through the more crazy times. To Frank, thank you for bringing me up with your enthusiasm and wonder about science and nature. Your need to learn about the world around you has very much rubbed off on me. I'm very lucky for this. To Tina, thank you for your love, support and friendship which have been crucial towards this endeavor. Thanks to Zac, who has done everything with me, from elementary school to middle school to high school to our doctorates. Thanks for always being up for a 2am bike ride or a 2 hour long debate. Thanks to Art for his amazing friendship throughout grad school. You were essential in keeping me grounded. Kari, thank you for all the adventures.... grad school would have been a sadder, quieter, and more normal place without you. Thanks to Jeff Kaplan for being a great friend, roommate and gravity buddy. Thanks to Drew, my physics buddy, for always being a positive and helpful force in my life. Thanks to Aysen, whose support, patience, altruism and friendship always made the downturns in life so much easier to navigate! Five years ago we randomly began living together and I had no comprehension of the luck I'd stumbled upon.

Abstract

Researchers have spent decades refining and improving their methods for fabricating smaller, finer-tuned, higher-quality nanoscale optical elements with the goal of making more sensitive and accurate measurements of the world around them using optics. Quantum optics has been a well-established tool of choice in making these increasingly sensitive measurements which have repeatedly pushed the limits on the accuracy of measurement set forth by quantum mechanics. A recent development in quantum optics has been a creative integration of robust, high-quality, and well-established macroscopic experimental systems with highly-engineerable *on-chip* nanoscale oscillators fabricated in cleanrooms. However, merging large systems with nanoscale oscillators often require them to have extremely high aspect-ratios, which make them extremely delicate and difficult to fabricate with an “experimentally reasonable” repeatability, yield and high quality. In this work we give an overview of our research, which focused on microscopic oscillators which are coupled with macroscopic optical cavities towards the goal of cooling them to their motional ground state in room temperature environments. The quality factor of a mechanical resonator is an important figure of merit for various sensing applications and observing quantum behavior. We demonstrated a technique for pushing the quality factor of a micromechanical resonator beyond conventional material and fabrication limits by using an optical field to stiffen and trap a particular motional mode of a nanoscale oscillator. Optical forces increase the oscillation frequency by storing most of the mechanical energy in a nearly loss-less optical potential, thereby strongly diluting the effects of material dissipation. By placing a 130 nm thick SiO₂ pendulum in an optical standing wave, we achieve an increase in the pendulum center-of-mass frequency from 6.2 to 145 kHz. The corresponding quality factor increases 50-fold from its intrinsic value to a final value of $Q_m = 5.8(1.1) \times 10^5$, representing more than an order of magnitude improvement over the conventional limits of SiO₂ for a pendulum geometry. Our technique may enable new opportunities for mechanical sensing and facilitate observations of quantum behavior in this class of mechanical systems. We then give a detailed overview of the techniques used to produce high-aspect-ratio nanostructures with applications in a wide range of quantum optics experiments. The ability to fabricate such nanodevices with high precision opens the door to a vast array of experiments which integrate macroscopic optical setups with lithographically engineered nanodevices. Coupled with atom-trapping experiments in the Kimble Lab, we use these techniques

to realize a new waveguide chip designed to address ultra-cold atoms along lithographically patterned nanobeams which have large atom-photon coupling and near 4π Steradian optical access for cooling and trapping atoms. We describe a fully integrated and scalable design where cold atoms are spatially overlapped with the nanostring cavities in order to observe a resonant optical depth of $d_0 \approx 0.15$. The nanodevice illuminates new possibilities for integrating atoms into photonic circuits and engineering quantum states of atoms and light on a microscopic scale. We then describe our work with superconducting microwave resonators coupled to a phononic cavity towards the goal of building an integrated device for quantum-limited microwave-to-optical wavelength conversion. We give an overview of our characterizations of several types of substrates for fabricating a low-loss high-frequency electromechanical system. We describe our electromechanical system fabricated on a Si_3N_4 membrane which consists of a 12 GHz superconducting LC resonator coupled capacitively to the high frequency localized modes of a phononic nanobeam. Using our suspended membrane geometry we isolate our system from substrates with significant loss tangents, drastically reducing the parasitic capacitance of our superconducting circuit to ≈ 2.5 fF. This opens up a number of possibilities in making a new class of low-loss high-frequency electromechanics with relatively large electromechanical coupling. We present our substrate studies, fabrication methods, and device characterization.

Preface

In 2009 I started working as part of a newly formed experimental collaboration between Oskar Painter and Jeff Kimble. The Kimble lab had previously worked on characterizing and cooling commercially purchased 50 nm thick Si_3N_4 square membranes which had excellent optical and mechanical properties for coupling with macroscopic optical cavities. The idea of the collaboration was to use nano-fabrication developed in the Painter Lab to realize custom, engineerable membranes which could be optically trapped in order to achieve high frequency modes with high mechanical quality factors, both important for observing quantum behavior. We soon began to understand the immense challenge of fabricating a membrane whose mechanical properties could be significantly dominated by a relatively weak optical trap. This required making membranes attached to the substrate with a single nanometer-scale tether which were so fragile they could be completely destroyed by a subtle handling movement during fabrication or even just the ventilation in our labs! I spent a year developing nano-fabrication techniques which allowed us to achieve these weakly clamped and extremely fragile membranes with high yield and extreme precision (discussed in Chapter 2). These state-of-the-art techniques were able to achieve extremely delicate nano-devices suspended over large openings through the chip which allowed optical access to the devices. In collaboration with Kang-Kuen Ni, Dalziel Wilson, Jon Hood, and Darrick Chang, we optically characterized, tested, and trapped these membranes which are the results discussed in Chapter 1. During this time, another team in Kimble group (Goban et al. [1]) had just succeeded in trapping atoms near the surface of a tapered optical fiber in order to observe strong atom-light interactions. It was quickly realized that using fiber-coupling techniques recently developed in the Painter group (J. Cohen et al. [2]) along with methods I developed to make delicate nanostructures over large optical windows, it would be feasible to fabricate nanofibers which would be lithographically patterned and engineered to enhance their interaction with cold atoms beyond the conventional limits of other groups using tapered optical fibers (e.g., Rauschenbeutel, Hakuta, Kimble, Balykin). In 2012 I began a year-long collaboration with the Kimble lab which combined their expertise on ultra-cold atom experiments, atom-trapping simulation and design with the Painter lab's expertise in simulating, designing, and nanofabricating fiber-coupled photonic crystal structures, with the goal of realizing the first on-chip trapping of cold-atoms near a photonic crystal structure. During this time I worked on simulating

the optical and mechanical structure of the nanostring devices, developed the groundwork fabrication based on my previously experience, and performed the initial optical characterizations in the Painter labs. The fabrication techniques gave us the ability to produce atom-trapping devices that were too fragile to feasibly fabricate using conventional fabrication methods and additionally gave us the accuracy, precision and robustness needed to achieve nanostrings that were optically compatible with the stringent requirements of Kimble lab's ultra-high-vacuum atomic setups. With a collaboration of this magnitude it was important to have a transfer of knowledge and experience between groups – working with Justin Cohen and Sean Meenehan, we trained Kimble group members in the fundamentals of nanofabrication, fabrication of the fiber-coupled nanostring cavities and simulations of the device's optical properties. Using these initial nanostring devices, we developed methods that allowed us to cleanly transport the devices from our characterization lab to the Kimble labs where the first atomic signals were measured (Discussed in Chapter 3). Chapter 4 is an overview of my first non-collaborative work within the Painter group towards building an integrated opto-electro-mechanical device for quantum-limited microwave-to-optical wavelength conversion – crucial in the optical interconnection of spatially-separated microwave quantum nodes. During this project I worked with Johannes Fink, Ale Pitante, and Lukas Heinzle in order to design, fabricate, and characterize our electromechanical system in our dilution refrigerator at cryogenic temperatures.

Contents

Acknowledgments	iv
Abstract	vi
Preface	viii
List of Figures	xiii
1 Optomechanics with Optically Trapped Membranes	1
1.1 Motivations for Optically Trapped Membranes	1
1.2 $Q_m f_m$ Enhancement Through Optical Trapping	3
1.3 Fabrication of Membranes for Optical Trapping	8
1.3.1 General Fabrication Process for Si_3N_4 Membranes	9
1.3.1.1 Initial Fabrication of Suspended Membranes	9
1.3.1.2 Geometric Design of Membranes	12
1.3.1.3 Electron-Beam Lithography of Thin Tethers	14
1.3.1.4 Characterization of Mechanical Quality Factor	17
1.3.1.5 Si_3N_4 Membrane Optical Absorption	19
1.3.2 General Fabrication Process for SiO_2 Membranes	21
1.3.2.1 Advantages of Silicon Dioxide Membranes	21
1.3.2.2 SiO_2 Membrane Fabrication	23
1.3.2.3 Deflection for Membranes and FEM Simulations	25
1.4 Experiments and Results	31
2 Turbulence-Shielding Fabrication Methods	40
2.1 Introduction	40
2.1.1 Micro-Pendulums for Cavity QED Optomechanics	44
2.1.2 “Floating” Substrate for High Q_m Optomechanics	47
2.1.3 Atom-Trap Nanostring Fabrication	50
2.1.4 Discussion	51

3	Nanowire Photonic Crystal Waveguide for Atom-Photon Interactions	52
3.1	Motivation for On-Chip Nanowire Trapping	52
3.2	Design of Nanowire Structures	53
3.2.1	Fiber Coupling and Overlap Integrals	54
3.2.2	Simulations of Adiabatic Condition in Waveguides	55
3.2.3	Single-Waveguide Atom-Coupling Region	58
3.2.3.1	Tapering Effect on Cavity Properties	59
3.2.3.2	Single-Mirror Nanostring with Fiber Coupling	61
3.2.3.3	Overview of Initial Characterization	62
3.2.3.4	Measurements of Reflectivity from Single Mirror Devices	64
3.2.4	Nanostring Chip Inserted into Ultra-High Vacuum Chamber	65
3.2.4.1	Studies on Signal and Cleaning Techniques	66
3.2.4.2	Experimental Procedure for Cs Loading on Nanostring Devices	68
3.2.4.3	Measurements of Cs Absorption with TE-Polarized Probe	70
3.2.5	Photonic Crystal Overview	72
3.2.5.1	Nanobeam Waveguide Photonic Crystal Design	72
3.2.5.2	Design Evolution of Photonic Crystal Mirrors	74
3.3	Fabrication of Nanowire Photonic Crystal Waveguides	76
3.3.1	General Fabrication Process for Nanostrings	77
3.3.1.1	Electron-Beam Lithography Techniques for Nanostrings	81
3.3.1.2	V-grooves Coupled with MOT Beam Window	84
3.3.1.3	Finite Element Simulations: Structural Failure Due to Stress	85
3.3.1.4	Safety Rails Required for High Nanostring Fabrication Yield	88
3.4	Measurement and Characterization	91
3.4.1	APCW Design for Trapping Cs Atoms	91
3.4.2	Nanostring Photonic Crystal Waveguide Components	93
3.4.3	Measurements and Characterization of APCW Devices	94
4	Integrated Phononic Cavity with Superconducting Circuits on Si_3N_4 Membranes	97
4.1	Optical to Microwave Conversion	97
4.1.1	Motivations for Optical to Microwave Wavelength Conversion	97
4.1.2	Theoretical Background for Wavelength Conversion	99
4.2	Microwave Resonator Coupling to Phononic Cavity	104
4.2.1	Overview of Electromechanical Coupling	105
4.3	Substrate Materials for Microwave and Mechanics	106
4.3.1	Experiments: Substrate Effects on Microwave Resonator Quality Factors	108

4.3.2	Single Material Substrate Mechanical Structures	114
4.4	High Stress LPCVD Silicon Nitride Membranes	116
4.4.1	Material Properties of Silicon Nitride Membranes	116
4.4.2	Electromechanical Device on Membranes	117
4.4.3	Phononic Cavity Design	118
4.4.4	Gap Engineering Using Internal Membrane Stress	120
4.5	Microwave Resonator Designs	127
4.6	Fabrication of Electromechanical Device	129
4.6.1	(A): Fabrication of Mechanics	130
4.6.1.1	Window Alignment Methods and Dry Etch	130
4.6.1.2	Nanobeam Alignment and Short Undercut for Shadowing	132
4.6.2	(B): Fabrication of Superconducting LC Resonator	136
4.6.2.1	Electron Beam Lithography and Shadow Evaporation	136
4.6.2.2	Sacrificial LOR Layer and Reflow	137
4.6.2.3	Spiral Inductors Fabrication	139
4.6.3	(C): Membrane Undercut using TMAH	140
4.6.4	Final Devices	145
4.6.5	Post-Fabrication Examination of Gaps	146
4.7	Nanobeam Fundamental Mode Measurements	148
4.7.1	Dilution Refrigerator Overview	148
4.7.2	Experimental Setup	149
4.7.3	Microwave Cavity Characterization	151
4.7.4	Nanobeam Mechanical Frequency Characterization	152
4.7.5	Introduction to Electromagnetically Induced Transparency: Atomic Ensembles	152
4.7.6	EIT Analog in Electromechanical System	156
4.7.7	EIT measurements	157
5	Publications	161
	Bibliography	162

List of Figures

1.1	Realistic vs. Ideal Scheme	3
1.2	COMSOL Simulations of U_o/U_m	7
1.3	Crack Fronts in High Stress Si_3N_4	10
1.4	Processing Steps for Tethered Membranes	11
1.5	Evolution of Tethered Membrane Design	13
1.6	Electron-Beam Lithography Back-Scattering	15
1.7	Gridding for High-Aspect-Ratio Electron-Beam Lithography	16
1.8	Characterization of Mechanical Quality Factor	17
1.9	Optical Absorption at High Powers	20
1.10	Comparison of Si_3N_4 and SiO_2	22
1.11	XeF_2 Release of SiO_2 Pendulums	24
1.12	Origins of Tensile and Compressive Stress	26
1.13	Deflections in Cantilevers	27
1.14	Stress Gradient in Free Standing Cantilever	28
1.15	Pendulum Deflections	30
1.16	Final SiO_2 Devices	32
1.17	Optical Trapping Experimental Setup	33
1.18	Retro-reflecting Trap Misalignment	34
1.19	Optical Trapping of a Membrane Disk	36
1.20	Mechanical Q Enhancement Through Optical Trapping	38
2.1	Conventional Handling and Challenges	41
2.2	Turbulence Shielding Holder	43
2.3	Fabrication Process for Pendulums	45
2.4	Si_3N_4 Pendulum Fabrication Challenges	46
2.5	Low-Frequency Disk with Ultra-Small Tethers	47
2.6	Suspended Substrates	48
2.7	Suspended Substrates Measurements	49

3.1	General Nanostring Trap Structure	53
3.2	Fiber Coupling to Waveguide	55
3.3	Waveguide Mode Profiles	56
3.4	Waveguide Tapering Design	57
3.5	Optimizing Cooperativity	59
3.6	Tapering Effects on Photonic Crystal Cavity	60
3.7	Free Spectral Range and Quality Factors	61
3.8	Single-Mirror Nanostrings	63
3.9	Schematic of Characterization Setup	64
3.10	Scan of Nanobeam Length	65
3.11	Scan of Nanobeam Length	65
3.12	Reflection Signal from PC Nanostrings	66
3.13	Reflection Signal	67
3.14	Artifacts of Particulate Contamination	68
3.15	Cs Atom Transport near Nanostring using MOTs	69
3.16	Transmission Spectra for Thermal Atoms Detuned from $F = 4 \rightarrow F' = 5$ Cs Transition	71
3.17	Photonic Crystal Matching Conditions	73
3.18	PC Mirror Design Evolution	75
3.19	Nanostring Chip Fabrication for Atom-Light Coupling	79
3.20	Gridding Technique for Nanostring Lithography	82
3.21	Stitching Errors Between Main-Fields	83
3.22	V-groove Alignment	84
3.23	KOH Etching Techniques	86
3.24	FEM Simulations of Internal Stress	87
3.25	Effects of Stress on “Double-Beam” Mirrors	88
3.26	Undercut Corners	89
3.27	Safety Rails	90
3.28	Band Structure and Atomic Transitions	91
3.29	Design of APCW	92
3.30	Schematic of Final APCW Structure	93
3.31	Reflection and Transmission Spectra	95
4.1	Envisioned Wavelength Conversion Scheme	98
4.2	General Model for Optical to Microwave Conversion	99
4.3	Coherent pump tones for wavelength conversion	100
4.4	One-sided Circuit Coupling to Nanobeam	105

4.5	Resonator and Transmission Line Layout	107
4.6	Microwave Resonator Plots	109
4.7	Intrinsic Quality Factors for Different Substrates	111
4.8	Aggressively Undercut Silicon-on-Insulator	113
4.9	General Device Geometry	115
4.10	General Device Geometry	117
4.11	Phononic Crystal Design	119
4.12	Different Circuit Geometries for Different Couplings	120
4.13	FDTD Simulations of Membrane and Nanobeam	121
4.14	FDTD Simulations of Membrane and Nanobeam	123
4.15	Achieving Small Gaps	125
4.16	Tensile Stress Simulations	127
4.17	Different Circuit Designs for Superconducting LC Resonator	128
4.18	General Overview of Fabrication Process	130
4.19	Fabrication of Back Windows	131
4.20	Etching of Nanobeams	132
4.21	Etching Straight Capacitive Gap Sidewalls	134
4.22	Evaporation of First Aluminum Layer	136
4.23	LOR Bridge Fabrication for Circuit Cross-Overs	138
4.24	Fabrication of Spiral Inductor (Second Aluminum Layer)	141
4.25	Undercut of the Membrane Electromechanics	145
4.26	Final Device Images	146
4.27	Imaging of Gaps	147
4.28	Dilution Refrigerator Operation	148
4.29	RF Measurement Setup	150
4.30	Microwave Cavity Characterization	151
4.31	Self Sustained Mechanical Oscillations	153
4.32	Basic Configurations for EIT	154
4.33	EIT Transparency Windows	155
4.34	Theoretical EIT Probe Reflection	157
4.35	EIT for Different Drive Detuning	158
4.36	EIT for Different Photon Number	159
4.37	EIT Parameter Fits	160

Chapter 1

Optomechanics with Optically Trapped Membranes

The quality factor of a mechanical resonator is an important figure of merit for various sensing application and for observing quantum behavior. Here, we demonstrate a technique for pushing the quality factor of a micromechanical resonator beyond conventional material and fabrication limits by using an optical field to stiffen and trap a particular motional mode of a nanoscale oscillator. Optical forces increase the oscillation frequency by storing most of the mechanical energy in a nearly lossless optical potential, thereby strongly diluting the effect of material dissipation. By placing a 130 nm thick SiO₂ pendulum in an optical standing wave, we achieve an increase in the pendulum center-of-mass frequency from 6.2 to 145 kHz. The corresponding quality factor increases 50-fold from its intrinsic value to a final value of $Q_m = 5.8(1.1) \times 10^5$, representing more than an order of magnitude improvement over the conventional limits of SiO₂ for a pendulum geometry. Our technique may enable new opportunities for mechanical sensing and facilitate observations of quantum behavior in this class of mechanical systems.

1.1 Motivations for Optically Trapped Membranes

There has been a significant amount of research focused on coupling high- Q_m modes of a mechanical system to high-finesse optical cavities in order to observe quantum behavior at mesoscopic scales. A larger goal of this scheme has been to prepare high- Q_m modes of a nanomechanical system in a quantum state by cooling these systems to their motional quantum ground state [3] as a method of observing quantum behavior at the macroscopic level. Ground-state cooling of a mechanical oscillator requires that the product of the oscillator's mechanical quality factor and the frequency of the mechanical mode, $Q_m \cdot f_m > k_B T_{\text{bath}}/h$ where k_B is Boltzmann's constant, T_{bath} is the temperature of the surrounding bath environment and h is Planck's constant. These parameters are also important in calculating the number of coherent oscillations the mechanical oscillator can make

before one thermal phonon enters the system which is determined by the ratio $Q_m f_m h / k_B T_{\text{bath}}$. Preparing mechanical devices in a quantum regime is interesting in their own right, but they could have numerous applications in ultra-sensitive detection [4] and quantum information science [5]. In order to reach this regime one must be able to minimize the thermalization and decoherence rates of the mechanical system by reducing their coupling to thermal environments. As of yet experiments that have cooled nanomechanical devices down to their motional ground states ([6] [7] [8]) have utilized dilution refrigeration to reach cryogenic temperatures and reduce decoherence of their systems. An interesting extension of this would be ground-state cooling in room temperature environments where there would be much more stringent requirements on the condition $Q_m \cdot f_m > k_B T_{\text{bath}} / h$. For room-temperature, this condition has been lightly satisfied by experiments in which extremely thin (50 nm thick) Si_3N_4 membranes are dispersively coupled to macroscopic high-finesse optical cavities ([9]) nominally referred to as “membrane-in-the-middle” geometries. Because of their ultra-thin geometry (≈ 50 nm thick) under high-tensile stress, their physical clamping to the substrate is small allowing it to have low mechanical dissipation and thus high- Q_m modes with high frequency modes. The low absorption of the silicon nitride membranes makes them compatible with low-loss optical system where radiation pressure dominates over photothermal effects. One would also like to reduce these decoherence rates by reducing dissipation and thermalization rates of these systems through their clamping and material supports [10].

A novel approach was proposed to completely eliminate material supports by optically levitating a nano-mechanical system inside a Fabry-Perot optical cavity [11] which under good vacuum conditions can lead to extremely low mechanical damping rates [12]. It had been shown that one could perform quantum-limited position measurements using optically levitated microspheres [13] and it was later shown that using such an approach one could realize quantum behavior in room-temperature environments when the levitated oscillators are sub-wavelength scale such that optical scattering becomes negligible [14]. Specifically Chang et al. [14] showed analytically that the center-of-mass (CM) motion of the levitated nanosphere can be optically self-cooled ([15] [16]) to its motional ground state starting from room temperature, thus completely negating the use cryogenic refrigeration. From a practical standpoint, the ability to prepare nanomechanical oscillators in a quantum state without the need for dilution refrigeration would be a significant step forward in reducing the infrastructure and complicated refrigeration needed to achieve devices with quantum properties. The CM motion of an optically levitated nanospheres is completely isolated from the surrounding environment and inherently decoupled from any internal modes of the nanosphere. The long coherence times resulting from this isolation would allow for the preparation of coherent quantum evolution. Our approach involves optically trapping a cleanroom fabricated membrane-disk with minimal clamping to the substrate in the anti-node of a high-power optical standing wave (Figure 1.1). In order to minimize the mechanical contribution of tethers which anchor the membrane

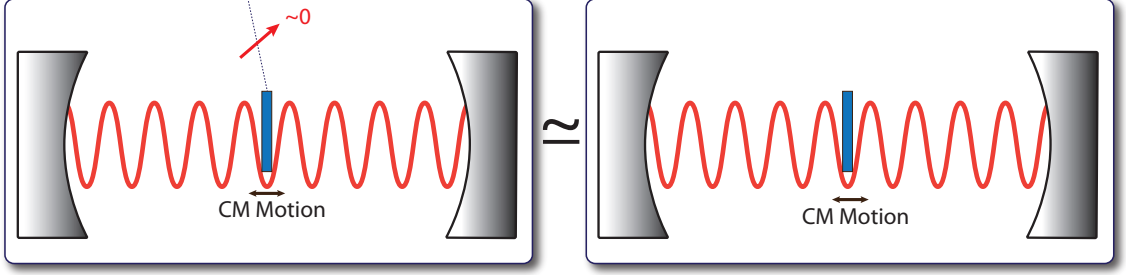


Figure 1.1: **Realistic vs. Ideal Scheme.** By minimizing the clamping of the disk to the outside thermal environment (left) allows the optical field to be the dominant source of internal energy. The smaller this clamping is, the closer we come to an ideal situation (right) in which a freely levitated disk is trapped at the anti-node of the trapping beam allowing us to greatly enhance its center-of-mass (CM) frequency and mechanical quality factor.

to the substrate and to allow the lossless optical potential to dominate, we engineered a pendulum geometry which consists of a disk that is weakly attached to the substrate by a single thin tether. Similar to the nanosphere scheme, we concentrate on the CM mode of a sub-wavelength disk oscillating in an optical potential where the ratio of potential energy stored in the optical field, U_o , dominates over the strain energy in the mechanical support (tether), U_m , characterized by the ratio U_o/U_m . Using this method we could achieve nano-mechanical system with extremely high $Q_m \cdot f_m$ as the dissipation through internal friction is minimized. There are certain advantages of utilizing a disk over a sphere as the nanoscale oscillator in these “membrane-in-the-middle” schemes. A significant limiting factor in cooling a nanosphere to its ground-state is motion heating through photon-recoil heating (photons scattered out of the cavity by the nanosphere leads to heating via moment recoil kicks), since a nanosphere by its nature scatters light omni-directionally [14]. This could be minimized by using a disk geometry which scatters in the direction of the cavity, significantly reducing recoil heating. Another attractive feature of disk pendulums is the ability to fabricate several arrays of these disks on a chip, allowing one to simply move the chip within the cavity to trap different devices as shown in Figure 1.16(a). Using our newly developed nanofabrication techniques we can make disks which have excellent mechanical and optical properties (low mechanical dissipation and absorption). Our investigation focused on the enhancement of the mechanical quality factor with optical trapping as a first step towards ground-state cooling in room temperature environments.

1.2 $Q_m f_m$ Enhancement Through Optical Trapping

In this section we will give an overview of the Q-enhancing mechanisms introduced by optically trapping a mechanical oscillator. One simplified way to look at how optical trapping enhances mechanical quality factors is by calculating the final enhanced quality factor as a ratio of the total

stored energy in the system (including both optical and mechanical components) and dissipation through each of these components such that

$$Q_{m,f} \propto \frac{U_m + U_o}{\delta E_m + \delta E_o} = \frac{1 + \frac{U_o}{U_m}}{\frac{\delta E_m}{U_m} + \frac{\delta E_o}{U_m}} \approx \frac{\frac{U_o}{U_m}}{\frac{\delta E_m}{U_m} + \frac{\delta E_o}{U_m}} \approx Q_{m,i} \frac{U_o}{U_m} \quad (1.1)$$

where $Q_{m,f}$ is the final mechanical quality factor with optical trapping of the mechanical oscillator, δE_m is energy dissipation through the mechanical clamping, δE_o is the energy dissipation through optical field, and $Q_{m,i}$ is the initial mechanical quality factor of the mechanical resonator mode (without trapping). In the approximation we assume that the optical field is nearly lossless such that $\delta E_o/U_m \approx 0$ and that $U_o/U_m \gg 1$. In order to get a realistic limit to the enhancement factor U_o/U_m we need to consider our specific disk geometry with tether included.

The following calculations of the realistic optical enhancement we can achieve are based on the detailed analysis in [17]. First we consider the mechanical modes of a free disk with thickness d and radius a . In the presence of a optical standing wave $E(z) = E_0 \cos(kz)$, where the thin disk sits at an anti-node and experiences a gradient dipole force at $z = 0$. The optical field traps the sub-wavelength thickness disk with a restoring frequency,

$$\omega_o(r) = \sqrt{\frac{2k^2 I(r)(\epsilon - 1)}{\rho c}} \quad (1.2)$$

where r is the radial coordinate about the center of the disk, $I(r)$ is the rotationally symmetric beam intensity profile on the disk, $k = 2\pi/\lambda$ is the wavevector, ρ is the mass density, and ϵ is the dielectric constant. Now considering the internal stresses, we can write equation for mechanical displacement from equilibrium $\xi(x, y)$ as

$$\frac{\partial^2 \xi}{\partial t^2} = -\omega_o^2(r)\xi - \frac{Ed^2 \nabla^4 \xi}{12\rho(1 - \sigma^2)} \quad (1.3)$$

where E is the Young's modulus of the disk and σ is Poisson's ratio. The field intensity is rotationally symmetric and we expect solutions which are also rotationally symmetric in the form $\xi(x, y) = f(r) \cos(m\theta) e^{-i\omega_m t}$, where m and n are the usual indexing of modes. In our experiments we use silicon dioxide (SiO_2) as the material of choice for our pendulums for its low absorption and ease in fabrication. Using material parameters for SiO_2 which has $E = 72$ GPa, $\sigma = 0.17$, and $\rho = 2.2$ g/cm³ we can calculate the frequency of the (2,0) internal mode of the free disk *without* an optical trap at $\omega_m^{(2,0)}/2\pi \approx 1.8$ MHz for a disk of thickness 130nm and diameter of 10 μm . In order to calculate a limit on the Q_m enhancement we can achieve, we look specifically at the thermoelastic damping because it has been analytically studied in detail [18] and because it serves as a fundamental limit for ideal devices with internal dissipative processes. Thermoelastic damping comes from the flexural motion of an oscillator which creates volume changes in the material which then create temperature

gradients and irreversible heat flow. This heat flow puts a limit on mechanical Q of an oscillator. It can be shown [17] that the work done in driving the heat flow over one cycle is

$$\Delta W \approx -\frac{\kappa_{\text{th}}}{T_{\text{bath}}} \int_0^{2\pi/\omega_m} dt \int d^3\mathbf{r} \Delta T(\mathbf{r}) (\partial^2 \Delta T / \partial z^2) \quad (1.4)$$

which can be used to express the thermoelastically limited quality factor,

$$Q_{\text{m}}^{\text{TE}} = 2\pi(U_o + U_m)/\Delta W \quad (1.5)$$

where the temperature field on the disk is given by $T(x, y, z, t) = T_{\text{bath}} + \Delta T(x, y, z, t)$ and ΔT satisfies the driven heat equation,

$$\left(c_v \frac{\partial}{\partial t} - \kappa_{\text{th}} \frac{\partial^2}{\partial z^2} \right) \Delta T = \frac{E\alpha T_{\text{bath}} z}{3(1-2\sigma)} \frac{\partial}{\partial t} \nabla^2 \xi \quad (1.6)$$

with boundary condition $\partial \Delta T / \partial z = 0$ at the surface of the disk ($z = \pm d/2$), c_v is the heat capacity per unit volume, κ_{th} is the thermal conductivity, and α is the volumetric thermal expansion coefficient. The thermoelastic limited $Q_m \times f_m$ can be written as

$$Q_{\text{m}}^{\text{TE}} f_m = \frac{45\kappa_{\text{th}}}{\pi E d^2 T_{\text{bath}} \alpha^2} \frac{1-\sigma}{1+\sigma} \left(1 + \frac{U_o}{U_m} \right) \quad (1.7)$$

The derivation of this limit is shown in detail in [17]. If we consider a free disk with a spatial uniform beam of intensity $I(r) = I_0$ then we know the trapping potential, $\omega_o(r)$, is uniform across the disk. The CM mode then has no internal strain and does not exhibit thermoelastic dissipation but realistically our optical beam has a Gaussian profile with waist w so that $I(r) = I_0 e^{-2r^2/w^2}$ which will introduce internal strain within the disk as different parts are trapped with different intensities. This effect becomes smaller as the beam becomes larger than the disk and intensity on the disk does not experience the large difference between the center intensity and the weaker tail ends of the outer Gaussian profile. Practically a disk has two disadvantages: (i) scattering from the edges of the disk which will contribute to photon recoil heating, and (ii) our disk is attached to a tether which will also be driven as the beam becomes larger than the disk. We now derive the effects of the tether.

We consider a simplified model with a tether attached to a perfectly rigid point particle of mass M in an optical potential with frequency ω_o so that internal stresses only act on the tether. The tether has length L defined along x such that $0 \leq x \leq L$ and displacement field of the tether $\phi(x, t)$ is a solution to the beam equation

$$\frac{\partial^2 \phi}{\partial t^2} = -\frac{Eb^2}{12\rho} \frac{\partial^4 \phi}{\partial x^4} \quad (1.8)$$

where b is the width of the tether with a square cross section. We express a tether clamped to

the substrate with boundary conditions at $x = 0$, $\phi(0, t) = \partial_x \phi(0, t) = 0$ and $x = L$ has boundary conditions such that $\partial_x^2 \phi(L, t) = 0$ and $M \partial_t^2 \phi(L, t) = -M \omega_o^2 \phi(L, t) + Eb^4 \partial_x^3 \phi(L, t)/12$. The latter boundary condition represents the acceleration of the disk due to optical restoring force and shear force imparted by the tether. We can then use standard methods to get an equation for the eigenfrequencies of this system,

$$M(\omega^2 - \omega_o^2)(\cos \gamma \sinh \gamma - \sin \gamma \cosh \gamma) + \frac{Eb^4 \beta^3 \omega^{3/2}}{12}(1 + \cos \gamma \cosh \gamma) = 0 \quad (1.9)$$

where $\gamma = \beta L \sqrt{\omega}$. When we consider large disk to tether mass ratios such that $M/m_t \gg 1$ and large optical forces such that $\omega_o \gg \omega_p$ then Equation 1.9 can be satisfied when

$$M(\omega^2 - \omega_o^2)(\cos \gamma \sinh \gamma - \sin \gamma \cosh \gamma) \approx 0 \quad (1.10)$$

This yields two solutions which consist of CM mode at frequency $\omega_m \approx \omega_o$ or tether modes which are described by $(\cos \gamma \sinh \gamma - \sin \gamma \cosh \gamma) \approx 0$. When both of these conditions are true at degeneracy points, the second term in Equation 1.9 becomes dominant and results in avoided crossings where the CM mode and tether modes mix. Now we calculate the enhancement factor U_o/U_m using

$$U_o = \frac{1}{2} M \omega_o^2 \phi^2(L) \quad \text{and} \quad U_m = \frac{Eb^4}{24} \int_0^L dx (\phi_{xx})^2 \quad (1.11)$$

By positioning the CM mode far away from any avoided crossing (between two tether modes) where we expect to have maximum U_o/U_m we find that this max is $(U_o/U_m)_{\max} \approx 8M/m_t$. Our simulations using finite element simulations show similar behavior at avoided crossing. In order to confirm this analysis we used finite-element method solver, COMSOL, to simulate all of our nanofabricated structures. Using CAD files used to input our membrane designs into the electron beam lithography tool, we load the exact membrane designs into COMSOL and first solve for mechanical displacements caused by stress (compressive or tensile) in the film. Using the numerical static solution as the initial conditions on our system, we run a series of simulations in which the pendulum (as shown in Figure 1.2(a)) is centered on a Gaussian trapping beam with restoring frequency $w_o(I(r))$. Our pendulum in this example is 50 nm thick, with a disk radius of 12 μm , tether length of 50 μm , and tether width of 500 nm with 800 MPa of tensile stress. For each value of restoring frequency with increasing trapping beam intensity, $I(r)$, we simulate the entire spectrum of modes of the pendulum as seen in the Figure 1.2(c). Here we see (circled in green) the crossing of the CM mode (in red) with the violin tether modes. We can also see that violin modes are also stiffened and form anti-crossings because the Gaussian trap beam overlap with the tether which it stiffens. In Figure 1.2(b) each of these anti-crossing has a corresponding dip in the U_o/U_m (circled in green) as predicted by theory. These simulations help us in our design of tethered membranes. One can see

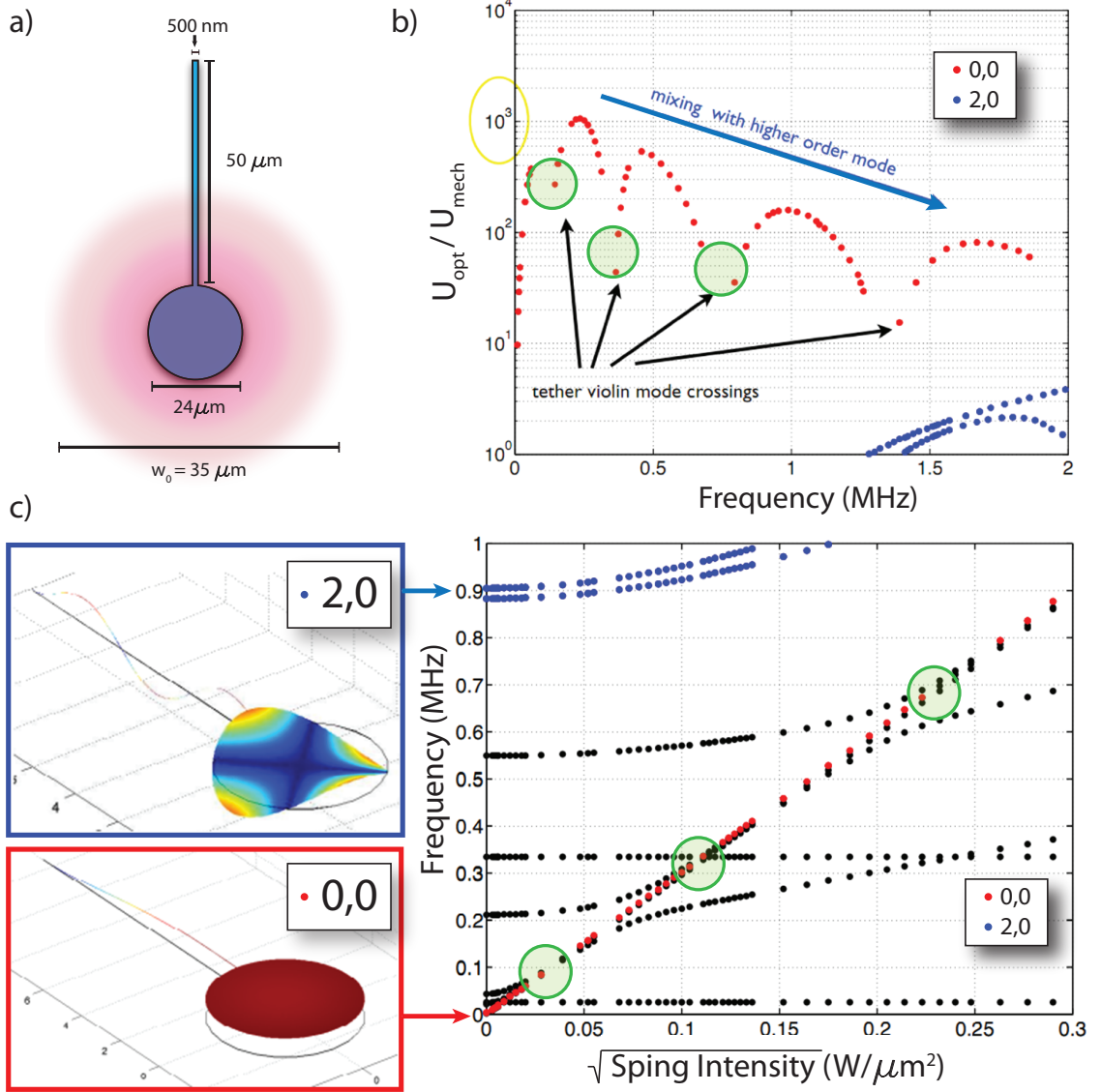


Figure 1.2: **COMSOL Simulations of U_o/U_m .** (a): Schematic of the COMSOL simulation. Shows a hanging 50 nm-thick pendulum with 50 μm long, 500 nm thin tether attached to a 24 μm disk with a Gaussian beam having a 35 μm waist. (b): Shows the FEM simulated U_o/U_m vs frequency of the mechanical modes. We see that as the CM mode (in red) is stiffened to higher frequency there are dips in U_o/U_m as the CM mode interacts with tether violin mode-crossing (discussed in Figure 1.19). The gradual decrease in U_o/U_m after these crosses is attributed to the CM mode mixing with the internal modes of the disk (2,0) shown in blue. (c): (left) Shows COMSOL simulations of the CM (0,0) mode and (2,0) disk modes and (right) shows simulation of frequency stiffening of each mode with increasing intensity of the trapping beam. Here we can clearly see the violin tether mode crossing which corresponds to dips seen in the plot (b). Plots courtesy of Kang-Kuen Ni.

that making the disk too large (to improve M/m_t) or too thin can introduce a number of internal disk modes which decay our U_o/U_m at higher intensities. Making the tethers too long (to reduce U_m) introduces more low-frequency violin modes which deteriorate U_o/U_m by introducing more anti-crossing points. In order confirm this analysis we used finite-element method solver, COMSOL, to simulate all of our nanofabricated structures. Using CAD files used to input our membrane designs into the electron beam lithography tool, we load the exact membrane designs into COMSOL and first solve for mechanical displacements caused by stress (compressive or tensile) in the film. Using the numerical static solution as initial conditions on our system, we run a series of simulations in which the pendulum as shown in Figure 1.2(a) is centered on an Gaussian trapping beam with restoring frequency $w_o(I(r))$. Our pendulum in this example is 50 nm thick, disk radius of 12 μm , tether length of 50 μm , and tether width of 500 nm with 800 MPa of tensile stress. For each value of restoring frequency with increasing trapping beam intensity, $I(r)$, we simulate the entire spectrum of modes of the pendulum as seen in the Figure 1.2(c). Here we see (circled in green) the crossing of the CM mode (in red) with the violin tether modes. We can also see that violin modes are also stiffened and form anti-crossings because the Gaussian trap beam overlaps with the tether that it stiffens. In Figure 1.2(b) each of these anti-crossings has a corresponding dip in the U_o/U_m (circled in green) as predicted by theory. These simulations help us in our design of tethered membranes. One can see that making the disk too large (to improve M/m_t) or too thin can introduce a number of internal disk modes which decay our U_o/U_m at higher intensities. Making the tethers too long (to reduce U_m) introduces more low-frequency violin modes which deteriorate U_o/U_m by introducing more anti-crossing points.

1.3 Fabrication of Membranes for Optical Trapping

Idealistically one would like to have a completely free optically levitated disk in the same way one would levitate a silica nanosphere as was done in several experiments[[19] [20]]. Nanospheres are trapped by utilizing piezo-shaker tables in high vacuum which can release several nanospheres sitting on its surface. Such an approach would not be possible with fabricated free micro-disks sitting on similar piezo-shaker stage as Van der Waal forces make it extremely difficult to release from the surface (due to the micro-disks' large contact surface area) . Initial fabrication efforts centered on fabrication of high-stress Si_3N_4 membranes with reduced clamping to the substrate (via tethers). Because of the high-stresses still present in the tethered membranes, we concentrated on making tether designs that would significantly reduce the stress in the membrane allowing the optical potential to dominate over the mechanical energy stored in the tethers. Using calculations outlined in [17], we found the maximal enhancement in the mechanical quality factor, Q_m , to be limited by the ratio of the membrane and tether masses, M/m_t . During this project we developed our fabrication

techniques in order to achieve increasingly thinner tethers with less of them (eventually converging on a single thin tether attached to the membrane). We will describe how efforts converged to the final geometry and material substrates.

1.3.1 General Fabrication Process for Si_3N_4 Membranes

1.3.1.1 Initial Fabrication of Suspended Membranes

One of the first attempts at making suspended tethered membranes was by trying to etch them directly from commercially available 50nm thick high-stress (800 MPa) Si_3N_4 membranes ($500\mu\text{m} \times 500\mu\text{m}$) from Norcada (Figure 1.3(a)). We spun electron-beam resist (ZEP520A) onto the membrane at ≈ 4000 rpm and performed an electron beam lithography which defines a tethered membrane. Using the ICP-RIE plasma etch using a $\text{SF}_6/\text{C}_4\text{F}_8$ mixture, we etched through the silicon nitride membrane not covered by ZEP520A. This resulted in membranes that would fracture explosively. It was initially believed that the Si_3N_4 membrane's thin dimension limited its ability to conduct heat (produced during the plasma etch) to the substrate causing thermally induced fracturing. To test this we etched the membrane with a series of short etches (≈ 20 seconds) and long intermediate cooling times ($\approx 5 - 10$ minutes). Despite increasingly shorter etches and longer cooling times, the ICP-RIE plasma etch would result in the same explosive behavior as soon as we etched completely through the membrane (since we could optically check the progress of our etch during each cooling period). In order to confirm that neither thermal fracturing nor design were the reason for the explosive behavior we used a focused-ion-beam (FIB) which milled a 5 nm diameter hole in the $500\mu\text{m} \times 500\mu\text{m}$ membrane taking < 1 second to mill through membrane. The short FIB milling also resulted in explosive structural failure of the membrane as seen in Figure 1.3(b) which allowed us to neglect thermal fracturing as a reason for this behavior since FIB milling does not significantly heat the sample.

Instead of trying to etch the tethered membranes from a pre-undercut membrane (under high tensile stress), we plasma etched the same patterns into thin Si_3N_4 layers deposited on a thick Si substrate and undercut the sample using potassium hydroxide (KOH) wet etch to etch away the silicon underneath the suspended membrane as shown in Figure 1.4. Using this process we were able to fabricate tethered membranes that did not fracture explosively because the structure was slowly released during the KOH undercut. This would lead us to believe the explosive nature associated with etching through the membrane is an artifact of the internal residual stresses in the silicon nitride film. An analogue of this can be seen in Prince Rupert Droplets as seen in Figure 1.3(c) which shows formations created by dripping hot molten glass into a cold water bath where it cools into a tadpole-shaped droplet. The water rapidly cools the molten glass on the outside of the droplet while the inner parts of the drop remain significantly hotter. When the glass on the inside cools,

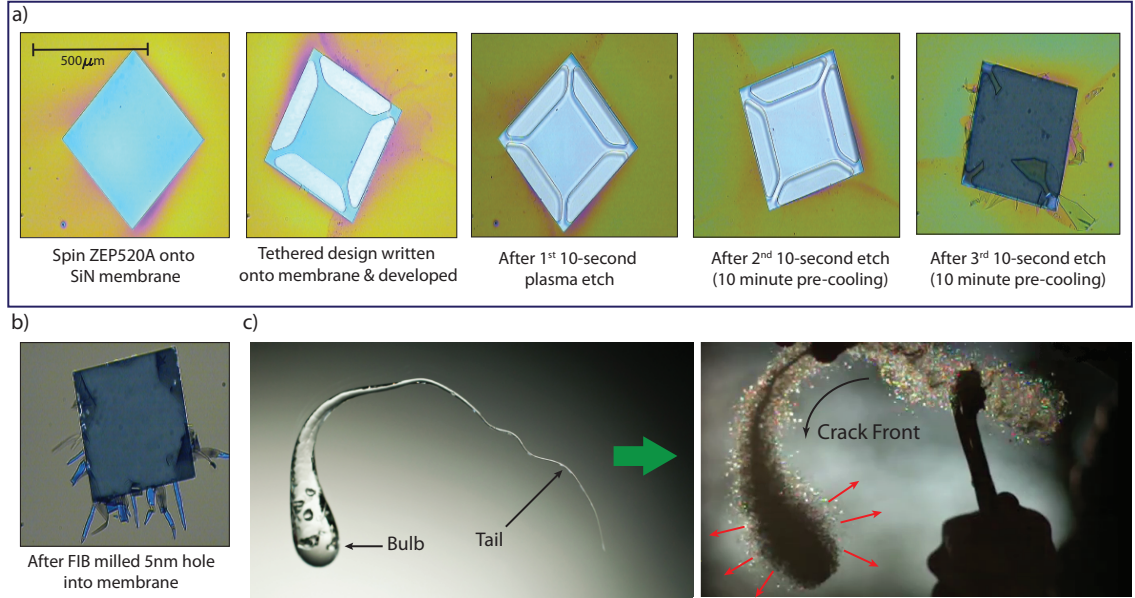


Figure 1.3: **Crack Fronts in High Stress Si_3N_4 .** (a): Microscope images showing a series of short $\text{SF}_6/\text{C}_4\text{F}_8$ etches on a 50nm thick, $500\mu\text{m} \times 500\mu\text{m}$ Norcada membrane. (b): Shows the explosive results from milling a 5nm diameter hole into the $500\mu\text{m} \times 500\mu\text{m}$ membrane using a focused-ion-beam (c): Similar dynamics can be seen in Prince Rupert Droplets where tensile stress stored in the droplet of molten glass (quickly cooled with ice water) allow the bulb to be resistant to hammer impacts. However, a small crack in the tail can send a “crack front” through the entire droplet resulting in an explosive disintegration.

it contracts inside the colder, quickly-solidified outer parts. This contraction between inner and outer parts of the bulb result in a very large compressive stress on the surface while the bulb of the drop is in a state of tensile stress similar to toughened glass. The high residual stress inside the bulb of the Prince Rupert droplet gives rise to unusually high structural integrity which allows it to withstand a blow from a hammer on the *bulb* without breaking, while explosively disintegrating if the tail end is slightly damaged (Figure 1.3(c)). When a portion of the tail is damaged, the large amount of potential energy stored in the internal structure is released, causing fractures to propagate through the glass toward the bulb at very high speeds which break the entire structure into flakes. Examination of Prince Rupert Droplets by the use of high speed video has revealed “crack fronts” which start at the tail end and eventually disintegrate the bulb. In the case of high-stress Si_3N_4 , we found that a similar process occurs when one breaks through the high stress membrane. Even a hole as small as 5 nm in the membrane causes catastrophic structural failure (Figure 1.3(b)). Using COMSOL, a finite element solver, we can see that a $500\mu\text{m} \times 500\mu\text{m}$ membrane with a 5 nm hole has a significant amount of stress surrounding the area immediately around the hole. By milling a hole into the membrane we suddenly introduce a large stress gradient near the hole which propagates throughout the membrane. By undercutting a membrane using KOH etch, as shown in Figure 1.4,

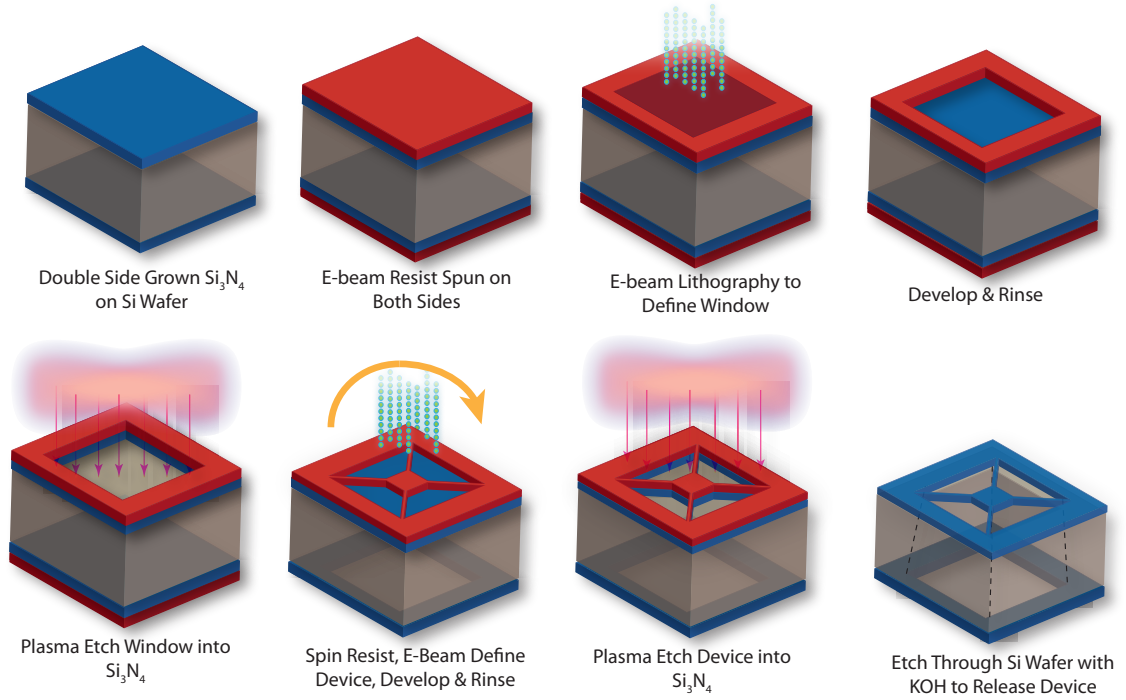


Figure 1.4: **Processing Steps for Tethered Membranes.**

we adiabatically undercut the membrane, with the tethers undercut first, followed by the membrane in the center, which allows us to slowly introduce the stress gradient into the undercut structure.

Once the tethered structures were undercut they were cleaned thoroughly using piranha solution in order to remove residual salt left from the KOH undercut. As shown in Figure 1.4, we start with a substrate that consists of 50 nm of 800 MPa Si_3N_4 deposited on both sides of a double-side polished $200\mu\text{m}$ thick Si wafer. We cover both sides of the chip with electron-beam lithography resist (ZEP520A) in order to write windows in the back of the chip and to protect the front side of the chip where our tethered structure will be written. We etch the windows into the back layer of silicon nitride (in order to allow uninterrupted optical access to the membrane after the undercut). The chip is then cleaned and ZEP520A is respun on the front in order to lithographically define the tethered membrane structure which is ICP-RIE plasma etched into the Si_3N_4 layer with ZEP520A as a selective mask. We carefully align the front tethered membrane to the window in the back so when the sample is undercut with KOH we have a clear opening through the chip for optical access. These membrane consist of tethers which are “doubly-clamped” which retain relatively high stresses and are robust. The sample is then immersed in KOH at 75°C for ≈ 2 hours (since we wet etch from both sides simultaneously). The sample is rinsed thoroughly in deionized water to remove the KOH, cleaned in hot piranha solution for 10 minutes to remove KOH residues and clean the device, and rinsed again with deionized water, IPA, and dried.

1.3.1.2 Geometric Design of Membranes

In order to increase the U_o/U_m , our initial goal was to reduce the mechanical energy stored in internal stresses of the structure, U_m , by reducing the intrinsic stress through the tethers. One of our initial figures of merit was CM frequency of the structure, where one would consider the mass of the membrane, M , along with the effective spring constant of the tethers, k_{eff} , such that our CM frequency is $f_{\text{CM}} = \sqrt{k_{\text{eff}}/M}$. By reducing k_{eff} we could allow the mechanical energy stored in the optical fields, U_o to dominate over U_m . Figure 1.5 demonstrates the evolution of our designs with the goal of reducing the effective spring constant of the structure by making tethers with less internal tensile stress. Prior experiments ([21], [9]) utilized commercially purchased 50nm thick Si_3N_4 membranes from Norcada which were square membranes clamped to the substrate on all sides and had CM mode frequencies ≈ 800 kHz with $Q_m \approx 10^6$. We chose to fabricate all of the devices shown in Figure 1.5 from a 50nm silicon nitride film since it has been shown [22] that thinner films produce devices with larger mechanical quality factors due to reduced clamping losses. Figure 1.5(a) shows an SEM image of our first structure which consisted of a $75\mu\text{m} \times 75\mu\text{m}$ square membrane suspended by four $5\mu\text{m}$ wide tethers in a $500\mu\text{m} \times 500\mu\text{m}$ window. The smaller membrane (suspended from tethers) allows for a lower mass oscillator and the reduced clamping to the substrate. This device had a reduced frequency of 172 kHz with a mechanical quality factor $Q_m = 1.31 \times 10^7$. One of the simplest ways to reduce the mechanical energy stored in the tethers was to make increasingly thinner tethers as shown in Figure 1.5(b) where we fabricated a similar structure as Figure 1.5(a) with tethers reduced in width ($5\mu\text{m} \rightarrow 1\mu\text{m}$). This further reduced the CM frequency to 106 kHz and also reduced mechanical quality factor to $Q_m \approx 10^6$. Although one does reduce clamping losses by fabricating thinner tethers, we also significantly reduce the tensile stress in the structure. There have been several groups investigating the beneficial effects of tensile stress on achieving high Q_m silicon nitride oscillators ([23], [24]). It was found that effects from intrinsic material damping become smaller as the tensile stress is increased. This allows Si_3N_4 structures with high tensile stress to exhibit extraordinarily high quality factors. As the structures are “destressed”, it is known that intrinsic material friction starts to limit Q_m . For this reason in Figure 1.5, we see a slow decrease in Q_m as the frequency of the oscillator decreases (due to reduced tensile stress in the tethers). Figure 1.5(c) shows a similar suspended membrane which has incorporated “kinks” into the tether geometry in order to dramatically relieve stress in the structure which produced a structure with 60 kHz CM mode with a $Q_m \approx 10^4$. These kind of delicate structures were achieved using our turbulence-shielded fabrication techniques reviewed in Chapter 2. These fabrication techniques became essential as the device geometries became “floppier” (lower frequency CM frequencies) since such structures became fragile and susceptible to small perturbations in the fabrication process (air flow through the chip, liquid flow during fabrication, etc.). Figure 1.5(d) shows the FEM structure and CM mode displacement of a fabricated tri-spoke geometry which reduces total number of tethers

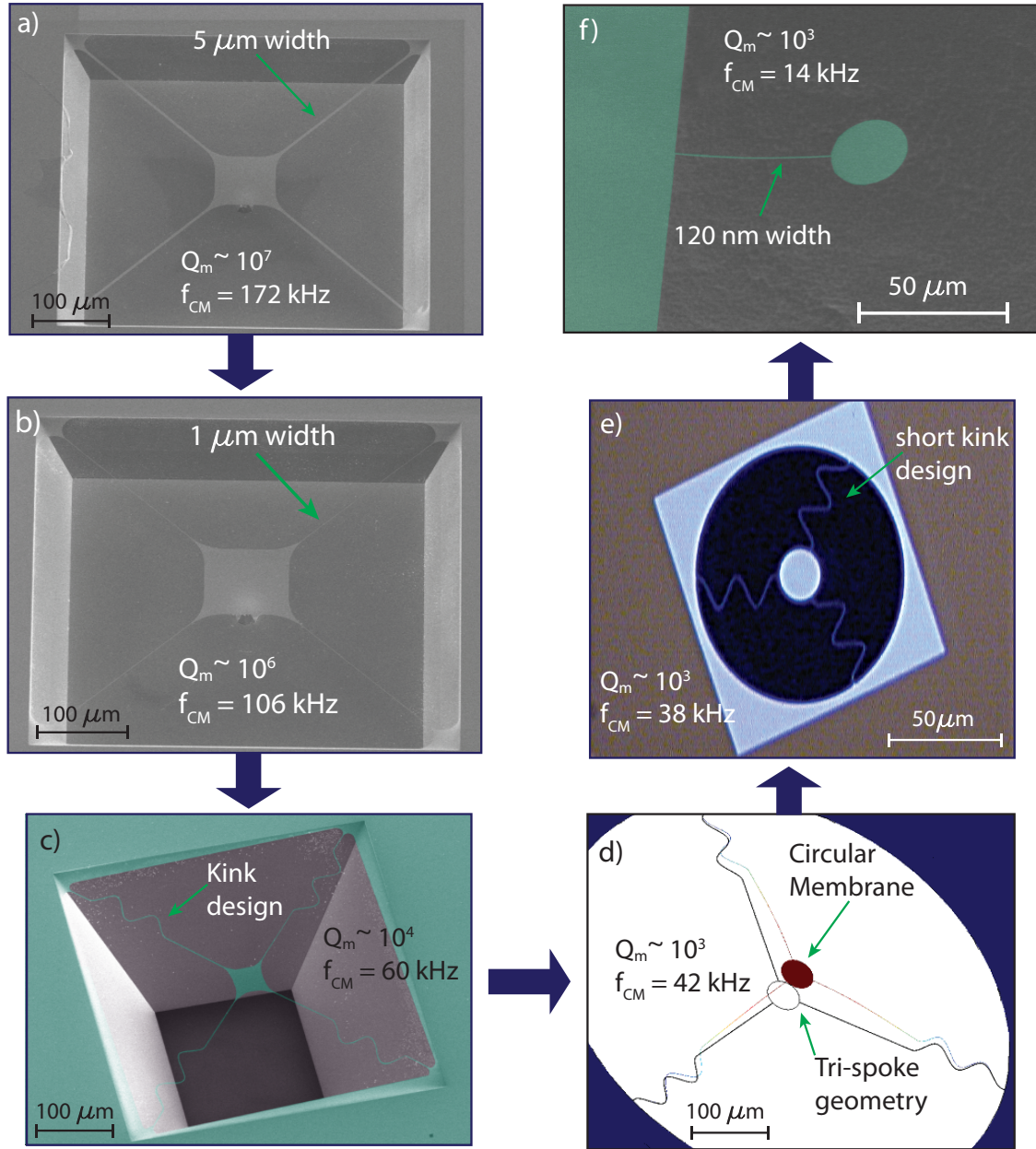


Figure 1.5: **Evolution of Tethered Membrane Design.** All the devices were fabricated from 50 nm thick Si_3N_4 on Si substrate (Figure 1.4). (a): SEM of initial tethered membranes with 5 μm wide tethers. (b): SEM of membrane where tethers have a reduced width (1 μm). (c): Colorized SEM of membrane with “kinked” tethers which significantly reduce the tensile stress. (d): Simulation image of center-of-mass mode of fabricated tri-spoke structure. This reduces the number of tethers and the intrinsic stress in the structure by not allowing opposing tethers to form doubly-clamped beams. (e): Optical microscope image of membrane with improved M/m_t by removing a significant length of the tethers. Kinked tethers keep the structure low frequency despite the shorter tethers. (f): Colorized SEM of pendulums which maximize U_o/U_m .

attached to a circular membrane disk. We moved to a circular disk geometry to allow mode matching of our trapping beam (assumed to be Gaussian) to the disk and to minimize the number of the disk's internal modes induced by the trapping beam's Gaussian profile. Because the 500 nm tethers in the tri-spoke geometry are not opposite one another (as one would find in the four tether structures) they are not allowed to form in-line doubly-clamped beams across the membrane, which would maintain the tensile stress across the structure. In order to reduce the ratio of membrane mass to total tether mass, M/m_t , we reduced the length of the tethers, as seen in Figure 1.5(e). In this optical microscope image, it can be seen that the most of tether length has been removed with the exception of the kinks in the tethers in order to preserve the structure's low frequency CM mode. In Figure 1.5(f) we show our final geometric design for our nanomechanical oscillators, which consists of a circular disk attached to a single 50 μm long tether with widths between 50-200nm.

The pendulum geometry minimizes the ratio M/m_t by reducing the number of tethers attached to the disk. M/m_t could be minimized by making the tethers increasingly shorter, but this would also increase the stiffness of the pendulum, making it increasingly difficult to optically trap. Shortening the tether would also bring the disk closer to the edge of the window and allow the Gaussian beam to be clipped by the substrate window edge. Reducing the thickness of the pendulum would reduce the reflectivity of the membrane and thereby reduce the optomechanical coupling. The challenge is then to fabricate pendulums with tethers having the smallest widths possible. Methods to achieve these are discussed in the next section.

1.3.1.3 Electron-Beam Lithography of Thin Tethers

One of the largest challenges was reducing the size of the tethers in our devices. Large windows through the chip are required to gain optical access of our trapping beam to the suspended disk. In the middle of these large areas we use electron beam lithography to define a disk with small tethers ($\approx 50 - 200$ nm) which span across large windows (diameter = 350 μm) as seen in Figure 1.6(a). Because electrons have a much smaller wavelength than the light used in photo-lithography, we use e-beam lithography in order to achieve a higher intrinsic resolution. Our electron-beam lithography tool (EBPG) has a maximum resolution which is limited by scattering of the electrons. There are two types of scattering which are forward and back scattering. In forward scattering, the paths of the incoming electrons are deflected by the atoms' Coulomb potential into a cone-like trajectory. Back-scattering involves the electron beam path which is deflected by an angle greater than 90° where electrons are scattered back to expose a much larger area of the resist than intended (Figure 1.6(d)). Exposing large areas creates a significant amount of overexposure to the thin tethers from electron back-scattering as shown in Figure 1.6(bc). We see that the tethers and disk are overexposed as a result of back-scattering exposure from large surrounding areas. One method of reducing this overexposure is to use proximity effect corrections based on Monte-Carlo simulations to properly dose

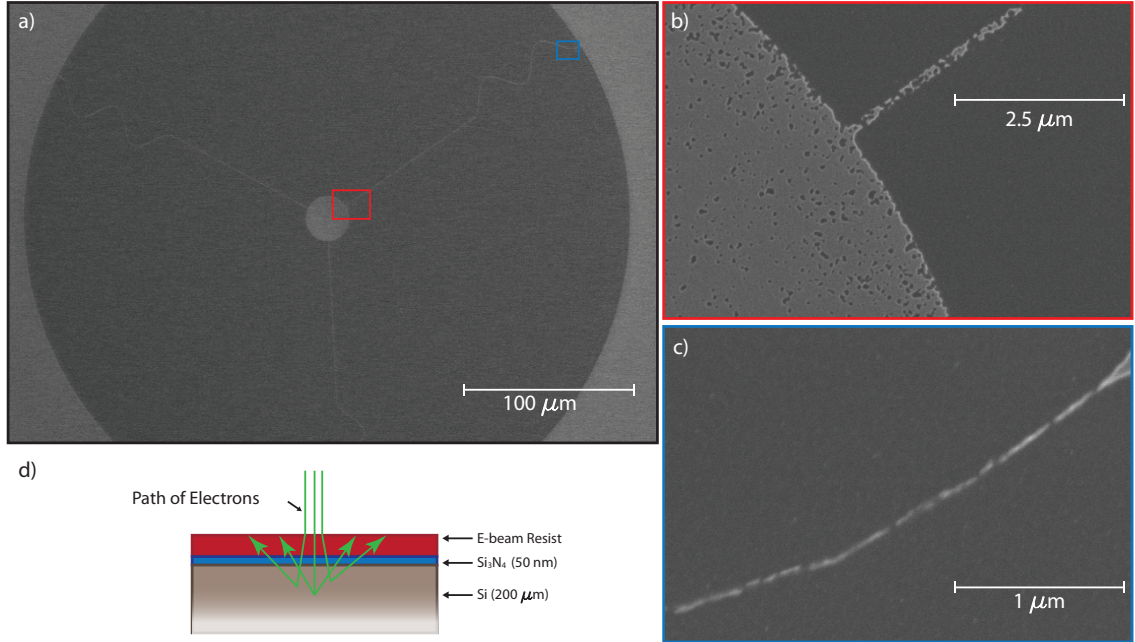


Figure 1.6: **Electron-Beam Lithography Back-Scattering.** (a): SEM image of tri-spoke design before a KOH undercut. Disk and long, thin tethers are surrounded by areas which are exposed through e-beam lithography. (b): Close-up SEM of tether intersecting the disk. Electron back-scattering from exposure of the surrounding areas causes additional exposure of the disk and tethers which leave a rough surface. (c): Close-up SEM of tethers near the clamping point. These are also overexposed because of electron back-scattering. (d): Illustration of electron back-scattering from substrate giving an extra exposure to surrounding areas.

the large areas. Despite these well established methods to correct for dose, defining tethers about a hundred nm wide which run through large areas hundreds of microns wide is prohibitively difficult to expose repeatably. In order to produce reliably defined small features in large exposed windows using electron beam lithography, we developed a “gridding” technique. Instead of attempting to expose the large areas that define the window through the chip, we fill that area with a grid of unexposed squares. The large window area is now left mostly unexposed, which significantly reduces the electron back-scattering as seen in Figure 1.7. We can see that our final structure is defined within a grid of thin lines so that small tethers are defined using a small area immediately surrounding the tether (Figure 1.7(bc)). Here we see close-up SEM images demonstrating how the tethers are defined in this large window. Because we use the window to define a large hole through the chip (used for optical access) with a long undercut, the unexposed grid of Si_3N_4 squares will be completely undercut and forced away from the device by the production of H_2 gas bubbles that are a byproduct of the KOH etching process. Because the devices are “floppy” and able to move several microns when undercut, we make sure the size of squares in the grid is smaller than that central disk. This ensures that our device is undercut last and remains static throughout the undercut of the smaller grid square. In

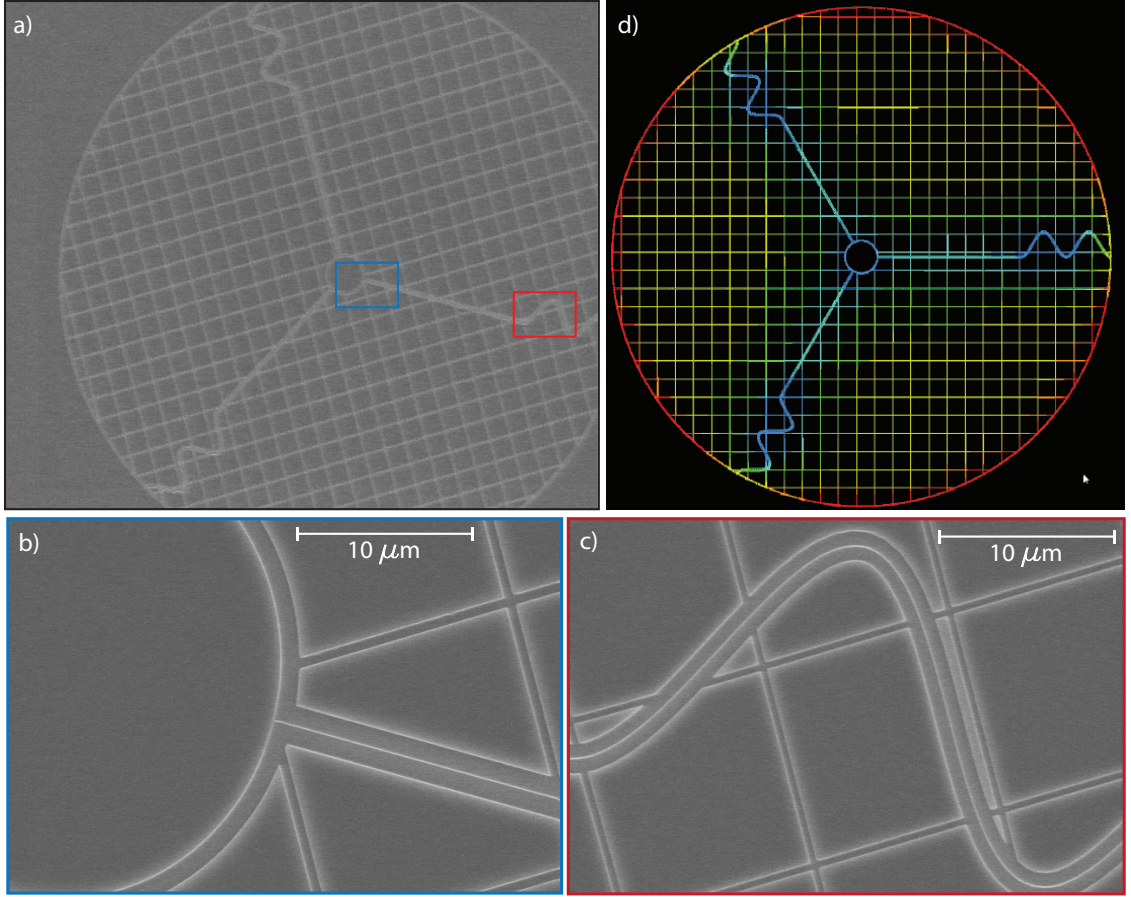


Figure 1.7: **Gridding for High-Aspect-Ratio Electron-Beam Lithography.** (a): SEM image of the chip after electron beam lithography and ICP-RIE plasma etch. The large areas which are normally exposed (to define a window) are now filled with a grid of unexposed squares. When the structure is undercut with KOH, the squares will be lifted off of the sample (by the ejection of H_2 gas) leaving a large window which continues to etch through the chip. (b): Close-up SEM of the tether connecting with the disk. The gridding squares fill in the areas surrounding the tethers. This allows us to reliably use e-beam lithography to write smooth, well-defined tethers as small as 50 nm in the middle of a large window 350 μm in diameter. (c): Close-up SEM of the “kinked” portion of the tether. The gridding squares are made smaller than the membrane disk so they are undercut before the structure is free to move. (d): Shows a mapping of the electron-beam dosing with proximity effect correction. Red areas are dosed more while blue areas are dosed less.

Figure 1.7 we used 15 μm squares to grid the large areas, defining a “tri-spoke” disk with a diameter of 25 μm . If we make the squares too large, they would undercut after our suspended membrane structure, allowing it to move and stick to the large static squares which surround it. If the square grids are designed too small, the density of exposed lines increases, thereby increasing the amount of backscattering. Although this method works well to reduce the back-scattering exposure, we improve it even further by applying a dose correction throughout the grid using proximity effect correction based on Monte-Carlo simulations that model the behavior of electrons impinging a layer of resist

on a silicon wafer for electron energies of 100 KeV. The effects of the 50 nm Si_3N_4 film are negligible and can be ignored. In Figure 1.7(d) we show a mapping of the dosing of the grid using proximity effect corrections. The surrounding areas near the edge (mostly in red) are dosed more with the EBPG than the areas near the middle of the window which are significantly exposed by electron back-scattering from the surrounding areas. Because the edges are adjacent to large unexposed areas outside the window, they do not receive the same amount of additional back-scattering exposure and thus requires a larger dosing. This type of gridding allows us to fabricate the small tethers required to achieve large U_o/U_m . Another practical benefit of this technique is that we wish to expose large areas with small features which usually requires writing the large window area with a small current electron beam (used for defining small features like tethers) or outline-exposing the small features with a small beam and filling in large areas with a large current beam which coarsely exposes left over areas. By gridding the large window area, not only can we improve the resolution of small features, but more practically we can immensely reduce the amounts of electron-beam lithography writing time we require to define a window by leaving most of the large area filled with a grid of unexposed squares. This reduction in area needing exposure reduces a 2 hour long e-beam lithography to a 6 minute write!

1.3.1.4 Characterization of Mechanical Quality Factor

We can characterize the dissipation of an oscillating mechanical system by the mechanical quality factor, $Q_m = 2\pi \cdot (E_m / \delta E_m)$, which we define as the cycle-averaged energy E_m of the oscillator divided by the energy dissipated over one mechanical cycle δE_m . When the system is modeled as an under-damped harmonic oscillator, it can be shown [22] that quality factor Q_m can be written as the ratio of the mechanical frequency over the rate of mechanical energy dissipation in angular units, $Q_m = \Omega_m / \Gamma_m$. Characterizing the intrinsic mechanical quality factor of this structure is

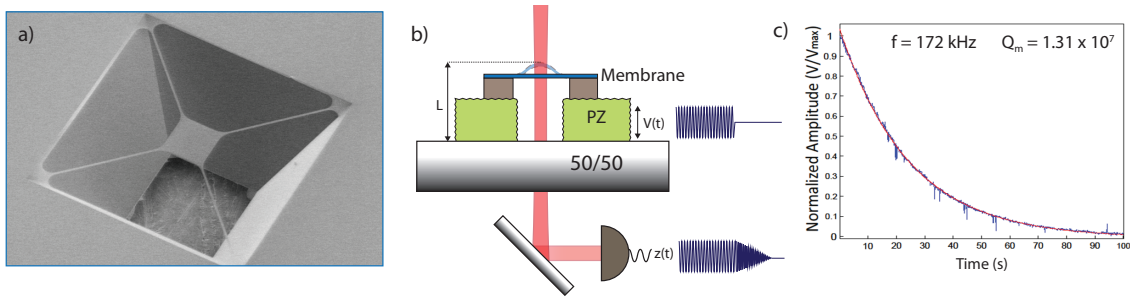


Figure 1.8: **Characterization of Mechanical Quality Factor.** (a): SEM image of an undercut tethered membrane with “through-chip” window for optical access. (b): Illustration of the testing setup under vacuum. The membrane’s center of mass mode is modulated using a piezoelectric ring-stage in order to allow optical access. The piezo stage is driven with an oscillating voltage which is then turned off, allowing measurement of the ring down which gives us CM mechanical quality factors of $Q_m = 1.31 \times 10^7$ and a frequency of 172 kHz.

important, since the final enhanced mechanical quality factor relies on the initial Q_m such that $Q_f \propto Q_m \cdot (U_o/U_m)$. In order to learn about the effects of membrane geometry (membrane size, tether width, tether length, etc.) on Q_m , we use ringdown measurements to characterize the center-of-mass mode of our suspended membrane. Using a ringdown measurement, we perturb the system and watch it evolve towards equilibrium in order monitor the energy dissipation. We can use the evolution of a weakly damped harmonic oscillator, which is characterized by a cycle-averaged energy that decays exponentially, to directly measure Q_m . Let us consider a damped harmonic oscillator's equation of motion for amplitude a ,

$$\ddot{a}(t) + \Gamma_m \dot{a}(t) + \Gamma_m^2 a(t) = F_{\text{ext}}(t)/m \quad (1.12)$$

where Γ_m is the damping rate, Ω_m is the mechanical frequency, F_{ext} , is the driving force, and m is the effective mass of the oscillator. We also consider the case in which we have a sinusoidal drive force $F_{\text{ext}}(t) = F_0 \sin(\Omega_0 t)$, which can be applied to the suspended membranes using a piezo-ring shaker as shown in Figure 1.8. For a harmonic oscillator driven near resonance, we find that the steady state solution to equation of motion is sinusoidal amplitude $a(t) = a_0 \sin(\Omega_0 t + \phi_0)$, where the amplitude can be approximated by a Lorentzian function:

$$a_0^2 \approx \left(\frac{F_0^2 Q_m^2}{m \Omega_m^4} \right) \frac{(\Omega_m/2Q_m)^2}{(\Omega_m - \Omega_0)^2 + (\Omega_m/2Q_m)^2} \quad (1.13)$$

We drive the oscillator until a steady state energy is reached defined as $W_0 = (1/2)ma_0^2$. The external force is immediately shut off at time t_0 . The cycle averaged energy's evolution can be related to the work done on the environment over a period $\tau_m = 2\pi/\Omega_m$, such that

$$E_m = E_0 e^{-\Gamma_m(t-t_0)} = E_0 e^{-\Omega_m(t-t_0)/Q} \quad (1.14)$$

In order to measure the mechanical quality factors of these membranes we use an interferometry measurement as shown in Figure 1.8(b). We placed our membrane chip with optical access (hole through the substrate) onto a piezoelectric ring-shaker which sits on a partially reflecting 50/50 mirror. This configuration forms an low-finesse etalon between the membrane and partially reflecting mirror which is probed with a focused 1064nm laser beam. This measurement setup sits inside a vacuum chamber at $< 10^{-6}$ Torr in order to eliminate mechanical damping of the suspended membrane's oscillations due to air. We can read out the amplitude and phase of the transmitted signal and their dependence on etalon spacing between the membranes and partially reflecting mirror, L , which depends on the amplitude of the suspended membrane oscillating surface. The transmitted steady-state power is detected with a photodetector whose transimpedance amplifier is connected to a network analyzer (HP 4395A). For an asymmetric loss-less etalon it is known that the steady-state

transmitted power can be written as

$$P_T = \left(\frac{T_{\max}}{1 + (2F/\pi)^2 \sin^2(2\pi L/\lambda)} \right) P_{in} \quad (1.15)$$

where $T_{\max} = \left(\frac{t_m t_0}{1 - r_m r_0} \right)^2$, $F = \frac{\pi \sqrt{r_m r_0}}{1 - r_m r_0}$ is the etalon finesse, L is the etalon spacing between the membrane and mirror, P_{in} is the input power, r_m is the membrane reflectivity, and r_0 is the partial mirror's reflectivity. We can measure the center-of-mass mode displacements with the transmitted signal while positioned on a fringe slope. The change in power due to change in etalon length can be expressed as

$$\frac{dP_T}{dL} = -P_T \left(\frac{4F}{\lambda} \right) \sqrt{\frac{F^2}{\pi^2/4 + F^2}} \quad (1.16)$$

As shown in Figure 1.8(b), we perform the ringdown measurement by modulating the piezoelectric ring shaker (made from Ferroperm Inc. Pz27). The network analyzer source is connected to the piezoelectric shaker with a source frequency centered at the mechanical frequency such that $\Omega_{NA} \approx \Omega_m$. The piezoelectric ring excites the CM mode of the suspended membrane until the steady-state amplitude is achieved, at which time the network analyzer is disconnected from the shaker. We can then monitor $V(t)$, the decaying envelope of the oscillation at carrier frequency Ω_m in zero-span mode as shown in Figure 1.8(c). We fit the decaying magnitude $V(t)$ to an exponential to infer the mechanical quality factor Q_m . From the decay signal shown in Figure 1.8(c) we find that the mechanical quality factor of our suspended membrane with 5 μm wide tethers is $Q_m = 1.31 \times 10^7$. This type of characterization allowed us to see effects of various geometries on Q_m .

1.3.1.5 Si₃N₄ Membrane Optical Absorption

In this section we review several of the properties of silicon nitride and some of the complications we encountered when we optically trapped these devices with high powers from 2-20 W. Besides excellent mechanical quality factors achieved by using high-stress LPCVD silicon nitride, it is known that the LPCVD process produces films with few impurities and very low optical absorption characterized by the imaginary component of the refractive index, $\text{Im}[n]$ ([25], [21], [9]). Extremely low absorptions on the order of $\text{Im}[n] \approx 10^{-6}$ have been measured in Si₃N₄ for wavelengths between 800 nm and 1064 nm. This low absorption was critical in minimizing optical losses when integrating the suspended membranes into high finesse cavities. Even with the very good optical absorption in LPCVD Si₃N₄, the extremely high trap powers used in our experiments meant that even small amounts of absorption in our film could cause significant heating in our films. We can calculate the power absorbed by

$$P_{\text{abs}} = 4\pi P_{\text{in}} \frac{t}{\lambda} \text{Im}[n] \quad (1.17)$$

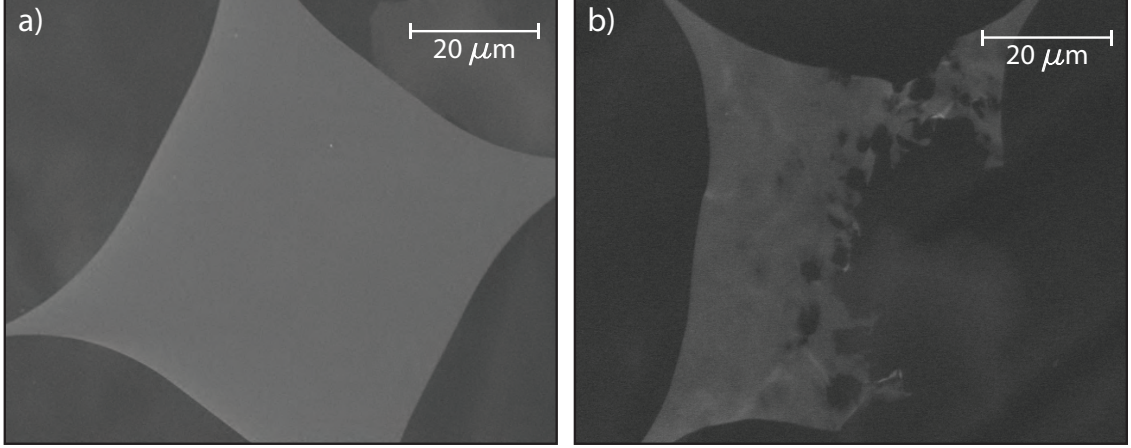


Figure 1.9: **Optical Absorption at High Powers.** SEM image of a Si_3N_4 suspended membrane (a): before optical trapping. (b): after optically trapping using $15\ \mu\text{m}$ spot size beam at 1064 nm with 7 W of power. Small contaminations on the surface absorb optical power and heat the membrane to its thermal fracture limit.

where P_{in} is the incoming beam power, t is the thickness of the membrane (50 nm), and λ is the wavelength of the light. However this does not take into account any contamination left on the suspended membranes after fabrication. To minimize any contamination on our devices we cleaned all the structures with hot Nanostrip and only exposed the devices to fumehood environments with extremely low particle counts when packaging and unpackaging. Previous experiments that used conventional square membranes which are well clamped on all sides (commercially available through Norcada) had varying mechanical quality factors depending on how the chip substrate was secured to the experimental setup [22]. Because our suspended membranes were clamped to the substrate though thin tethers, we did not observe a dependence of Q_m on the method of securing the chip. The weak clamping of our structures to the substrate also resulted in minimized ability to dissipate heat from the suspended membrane through thermal conduction. We can quantify the temperature rise in the membrane clamped to the substrate with thermally conducting tethers as

$$T_{\text{cond}} = \frac{P_{\text{abs}}}{Ak/L_t j} \quad (1.18)$$

where A is the tether cross section (thickness \times width), k is the thermal conductivity of Si_3N_4 ($\approx 20\text{W}/\text{m}\cdot\text{K}$), L_t is the length of the tethers, and j is the number of tethers attached to the suspended membrane. The high optical powers used for trapping the suspended membrane coupled with their limited ability to thermally conduct heat away resulted in sudden thermal fractures in the membranes, as seen in Figure 1.9. Here we see an SEM image of the 50 nm thick silicon nitride membrane attached to the substrate with $200\ \mu\text{m}$ long, 500nm wide tethers before and after being optically trapped with 7 W of power. This thermal fracturing was a practical limit of Si_3N_4

since integrating these membranes with a high finesse optical cavity would involve even larger intra-cavity powers. Adding more tethers to the membrane to increase the thermal conductivity would significantly reduce our U_o/U_m and our ability to enhance the mechanical quality factor. In Chapter 2, we discuss the challenges in achieving thorough cleaning of delicate devices.

1.3.2 General Fabrication Process for SiO_2 Membranes

1.3.2.1 Advantages of Silicon Dioxide Membranes

As discussed in the previous section, Si_3N_4 membranes had several absorption issues when coupled with a high power (≤ 20 W) trapping beam (Figure 1.9). These absorption issues are a combination of the intrinsic absorption ($\text{Im}[n] \approx 10^{-6}$), thermal conduction, and contamination left from the fabrication and transfer process. The highest power trapping beam we could use on a silicon nitride membrane was ≈ 12 W before the structure would thermally fracture (Figure 1.9). A significant issue was the fabrication process, which utilized potassium hydroxide wet-etch to release the pendulums (Figure 1.4) which inherently leaves salt residues throughout the devices (as can be seen on the Si walls in Figure 1.10(a)). This typically requires a Nanostrip clean after the pendulums are released to ensure their cleanliness, however, because of their devices' fragility the gentle acid clean is limited in its ability to clean thoroughly. As described in Chapter 2, the wet-etch release is extremely long and tedious with a yield that did not make it practical for quick replacement of devices inside the vacuum chamber. KOH etches produce hydrogen gas as a by-product which results in a barrage of bubbles that emanate from the silicon substrate during the wet etch and can destroy the pendulums. At conventional etch temperatures ($\approx 75^\circ\text{C}$) these hydrogen bubbles violently rise from the window where silicon is being etched away at a fast rate, which can easily pull the delicate pendulums far enough that they stick (through Van de Waal forces) to the substrate, as seen in Figure 1.10. The KOH reaction rate with silicon is exponentially dependent on temperature, so by performing the undercut at room temperatures we significantly decrease the rate at which the hydrogen bubbles are produced and improve yield. At conventional temperatures the small hydrogen bubbles are produced quickly in succession and can combine into larger bubbles which rise with increased velocity through the pendulum micro-disks. At room temperature, the hydrogen bubbles are produced at a slower rate which allows small bubbles to form and slowly lift off individually without combining with one another to form larger, more destructive H_2 bubbles. Using low temperature KOH improved the yield of our pendulums from 0% to $\approx 60\%$ with thinner tethers having a lower yield. However using low temperature KOH solutions reduced the etch rate of Si from $1\text{ }\mu\text{m}/\text{min}$ at 75°C to $1\text{ }\mu\text{m}/\text{hr}$ at 30°C which required ≈ 4 days to completely etch through the chip from both sides. With delicate pendulums which can easily succumb to a number of catastrophic failures including overheating from the high power trapping beam, small air movements through the chip during its transfer into the

vacuum chamber, and air movements during the evacuation of the chamber, these long time-scales for the wet-release made this an impractical recipe for producing test devices. In light of these

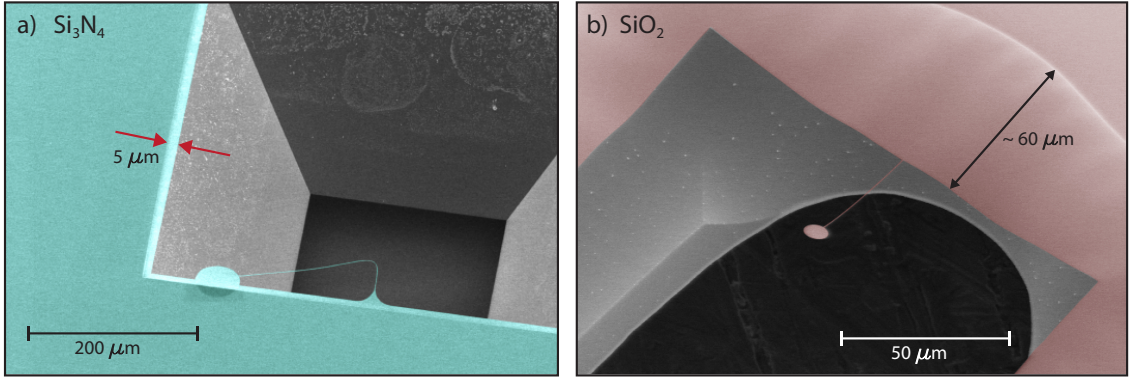


Figure 1.10: **Comparison of Si₃N₄ and SiO₂.** (a): Colorized SEM image of Si₃N₄ pendulum undercut with KOH wet etch. KOH isotropic etching is minimal resulting in a 5 μm undercut around the border. (b): Colorized SEM image of SiO₂ pendulum dry-released with XeF₂ which etches Si isotropically resulting in large surrounding “annulus” which is ≈ 50 μm wide.

material and fabrication problems, we switched to suspended membranes fabricated from thin layers of silicon dioxide (SiO₂) on 200 μm silicon substrate. One important advantage of SiO₂ over Si₃N₄ is its extremely low optical absorption which is ≈ 3 orders of magnitude smaller ($\text{Im}[n] \approx 10^{-9}$). Eventually this allowed us to put up to 17 W of optical trapping power onto the SiO₂. Gas releases like XeF₂ are preferable for these types of delicate devices because the dry-release process does not submit the pendulums to surface tension in liquids and can have extremely high selectivity between SiO₂ and Si. This resulted in almost ≈ 100% yield for tethers 50 μm in length and tethers (> 150 nm). Because the Si etching could be done quickly without affecting the yield of the devices, we could etch through chip in about 30-45 minutes to produce devices with much smaller tethers, as shown in Figure 1.10(b). Another advantage of using XeF₂ was the ability to thoroughly clean the chip with a hot piranha solution before the gas-release which left no residue on the sample, allowing us to immediately package the devices (after the release) without the need for an additional cleaning step. The improved optical absorption, improved yield, and ease of fabrication made the switch to SiO₂ a considerable improvement to Si₃N₄ membranes.

One of the drawbacks of the SiO₂ fabrication process was isotropic etching of Si by the XeF₂ gas. This resulted in outward etching of the Si which left a large (≈ 50 μm wide) “annulus” surrounding the chip window. This was a problem because the wide annulus harbored several low-frequency modes which would impede our ability to enhance Q_m since the center-of-mass mode would couple with each annulus mode as we optically stiffened to higher frequencies. KOH release on the other hand etches Si anisotropically in the [1-0-0] plane, and very slowly etches the [1-1-1] plane, leaving behind a small overhang that surrounds the window (≈ 5 μm wide) as seen in Figure 1.10.

1.3.2.2 SiO₂ Membrane Fabrication

Here we will give a comprehensive overview of the fabrication process of the SiO₂ membranes. In order to grow the highest quality silicon dioxide with the lowest optical absorption we utilized many of the SiO₂ growth techniques used to make ultra-low-loss SiO₂ optical delay lines on Si chips [26]. We used Bromine-doped 200 μm thick silicon wafers with high resistivity ($\rho > 10,000 \Omega \cdot \text{m}$) which had a lower doping rate resulting in ultra-high-quality SiO₂ films. Before we thermally oxide the silicon wafers in a high temperature furnace, we clean the Si substrate of any contaminants by performing a piranha solution clean at 150°C for 10 minutes. We dip the wafer in 48% hydrofluoric acid (HF) for 5 minutes in order to remove any low-quality native oxides on the silicon wafer from the piranha clean which oxides the silicon surface. We use a Tystar Furnace to simultaneously grow silicon dioxide on both sides of a double-side polished silicon wafers using a dry thermal oxidation process at 1000°C and steady flow of high-purity oxygen (O₂) gas for 4 hours to produce a 120 nm thick SiO₂ film. Wet oxidations have a significantly faster growth rate but result in an SiO₂ which is more porous than the dense high-quality films one can achieve with a dry thermal oxidation. The oxidation step is ended by stopping the flow of O₂ to the furnace and flowing nitrogen gas (an inert gas). The sample is then annealed at 1000°C for 3 hours in order to improve the density and quality of the silicon dioxide film and to decrease the intrinsic compressive stresses in the film due to mismatch of thermal expansion coefficients in Si and SiO₂. As discussed in the next subsection, this compressive stress results in doubly-clamped beams and membranes which buckle. Once the SiO₂ was grown onto the silicon wafers, we followed the same fabrication steps as shown in Figure 1.4 to define a window and pendulums into the back and front layers of SiO₂, respectively. We spun photo-resist on both sides of the chip in order to protect the front of the chip while we exposed the back window. We UV exposed a large window in the layer of photo-resist (AZ5214) on the back of the chip. We develop and rinse the exposed areas away and etch a window into the back using a C₄F₈/SF₆ plasma etch using an Oxford RIE-ICP system. The photo-resist is cleaned off using a series of solvents (IPA, Acetone, TCE) and cleaned with a hot piranha solution to ensure that the surface is clean before the electron-beam lithography. We spin e-beam resist ZEP520A onto the front side of the chip and bake for 2 minutes at 180°C on a hotplate. We use the gridding technique as shown in Figure 1.11 to define a pendulum with small tethers inside a larger window. Once the patterns are exposed in the layer of ZEP520A, we develop for 2.5 minutes in ZND-N50 developer and 30 seconds in MIBK rinse. The pattern is etched and transferred into the SiO₂ layer using a C₄F₈/SF₆ plasma etch with ZEP520A as a mask. ZEP520A is cleaned away using hot piranha solution. At this point (Figure 1.11(a)) is where our fabrication process changes significantly from the Si₃N₄ devices which are released using KOH – instead we use a XeF₂ gas etch to etch away the silicon and release the device as shown in Figure 1.11(b). Before the sample is released with a XeF₂ dry etch we thoroughly clean the chip using a hot piranha solution at 150°C. This is followed by a quick 10 second dip in buffered

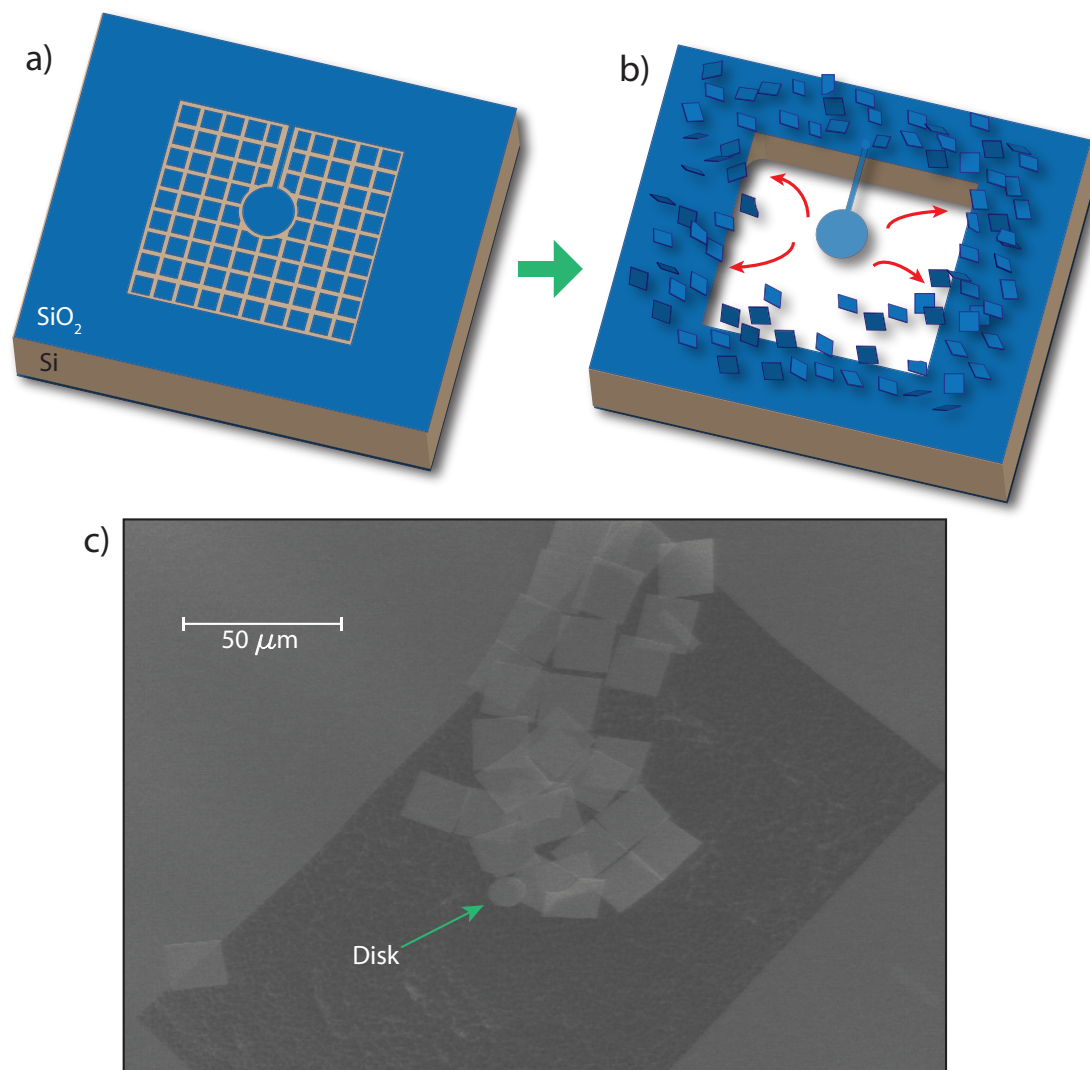


Figure 1.11: **XeF_2 Release of SiO_2 Pendulums.** (a): Illustration showing the SiO_2 film (on Si substrate) which has been patterned with a window containing a pendulum. The window has been filled with a grid of square, which are smaller than the disk, ensuring that they are released before the pendulum is released. (b): Illustration showing how the XeF_2 gas etch would release the pendulum and square grids. (c): SEM showing the case when the squares in the grid are made larger than the disk. The pendulum is released before the grid, allowing it to attach to them before they are also released.

HF to remove surface oxidation on the silicon surface by the piranha solution, which could produce an etch stop for the XeF_2 and make it take much longer to etch through the Si substrate. One very important step is dehydrating the chip in a cleanroom oven at 150°C for 10 minutes immediately before the sample is etched in the XeF_2 chamber. This baking step evaporates any H_2O that collects on the sample from moisture in the air which combined with the XeF_2 gas produces hydrofluoric acid (HF) which etches SiO_2 very quickly. This is extremely important for ensuring that the selec-

tivity to SiO_2 remains high, since we need the silicon dioxide layer to remain absolutely unetched while the XeF_2 gas aggressively etches through the silicon substrate. Once the sample is baked it is immediately moved to the XeF_2 chamber before the chip cools and re-condenses water on its surface. It's also important to note that a XeF_2 etch is not selective enough to release Si_3N_4 devices because it would make the disks rough (unsuitable for optics) or completely etch away the very thin Si_3N_4 layer before it etches through the silicon substrate. As shown in Figure 1.11(b), the grid squares are undercut before the disk is completely undercut, allowing the squares to fall off the sample (by placing the sample upside down during the XeF_2 etch). If the squares in the grid are made larger than the disk such that pendulum is free to move and attach to adjacent square grids before they are too undercut, this can result in a pendulum covered in pieces of this grid, as shown in Figure 1.11(c).

1.3.2.3 Deflection for Membranes and FEM Simulations

We have discussed several of the properties that can result from the intrinsic stresses in the film. While intrinsic tensile stresses found in LPCVD Si_3N_4 (on Si) can produce clamped membranes which are flat, the compressive stress found in SiO_2 (on Si) result in clamped membrane which are wrinkled and buckled. We will review in this section how the stresses arise from a mismatch in thermal expansion coefficients between the substrate and the film being grown. We also review the consequences of this stress on cantilever structures similar to our pendulums. In this case, the sign of the stress in the film (i.e., compressive or tensile) results in a deflection of the pendulum. We can understand how these different stresses can arise by considering the sequence of events shown in Figure 1.12. The thermal expansion coefficient is defined as the change in strain in a material with change in temperature written as

$$\alpha = \frac{d\epsilon}{dT} \quad (1.19)$$

We can simplify the strain caused by thermal expansion by assuming the thermal expansion coefficients are temperature independent so that

$$\epsilon(T) = \epsilon(T_0) + \alpha \cdot \Delta T \quad (1.20)$$

in which the first term is negligible and the second term is the strain caused by the thermal expansion. When the film is grown onto the substrate at high temperatures and allowed to cool to room temperature, the difference in thermal expansion coefficients causes stress in the films. The higher a temperature is, the larger the difference there is between growth temperature and the temperature the wafer is eventually cooled to (room temperature), resulting in a larger magnitude of either compressive or tensile stress. In both in silicon nitride and silicon dioxide films, the optical properties are improved by growing films at very high temperatures, which created large stresses in the devices

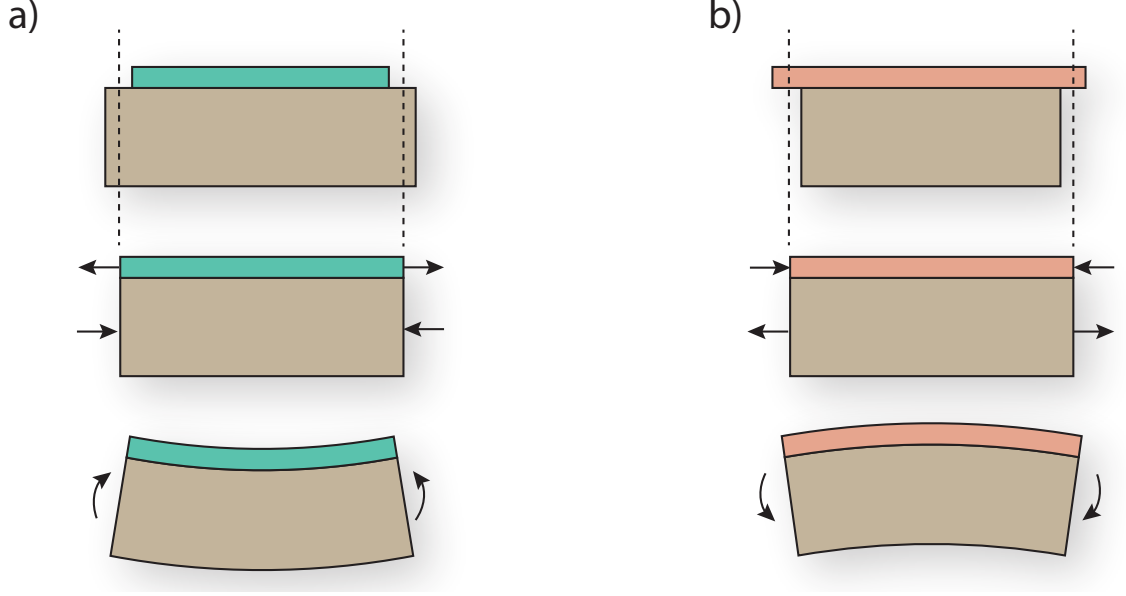


Figure 1.12: **Origins of Tensile and Compressive Stress.** (a): Order of events resulting in a tensile stress typically seen in LPCVD Si_3N_4 films on Si. (b): Order of events resulting in a compressive stress typically seen in SiO_2 films on Si. (Adapted from [27])

we fabricated. In Figure 1.12(a) we consider the situation where the film shrinks relative to the substrate since $\alpha_f > \alpha_s$. We know that once the film has been deposited on the substrate and allowed to cool, they must have the same dimensions. Accordingly the film is constrained to this dimension and stretched while the substrate contracts. The tensile forces in the film are negated by the compressive forces in the substrate. In equilibrium this produces moments at the ends of the substrate which allow it to elastically bend to counteract unbalanced moments. Because the substrate is much thicker than the deposited film, we can assume that the film's effects on the final state of the substrate are negligible such that we can write the strain in the substrate as

$$\epsilon_s = -\alpha_s \cdot \Delta T \quad (1.21)$$

where α_s is the thermal expansion coefficient of the substrate and the minus sign representing the compression in the film. Because the film is attached to the substrate we can assume the film experiences the same strain such that

$$\epsilon_{f,\text{deposited}} = -\alpha_s \cdot \Delta T \quad (1.22)$$

If the film were to exist without being attached to a substrate the strain could be written as

$$\epsilon_{f,\text{free}} = -\alpha_f \cdot \Delta T \quad (1.23)$$

We can then calculate the thermal mismatch in the film by looking at the difference in strain with and without attachment to the substrate so the thermal mismatch strain can be written as

$$\epsilon_{f,\text{mismatch}} = \epsilon_{f,\text{deposited}} - \epsilon_{f,\text{free}} = (\alpha_f - \alpha_s) \cdot \Delta T \quad (1.24)$$

which leads to a stress in the film ($\sigma = E/(1 - \nu)\epsilon$) such that,

$$\alpha_{f,\text{mismatch}} = \frac{E}{1 - \nu} (\alpha_f - \alpha_s) \cdot \Delta T \quad (1.25)$$

Tensile stresses are expressed as a positive value stress while compressive stresses are negative. We can then see that a compressive stress will result whenever $\alpha_f < \alpha_s$ and tensile stress produced when $\alpha_f > \alpha_s$. Now we can look more closely at the specific case of a cantilever which closely resembles our

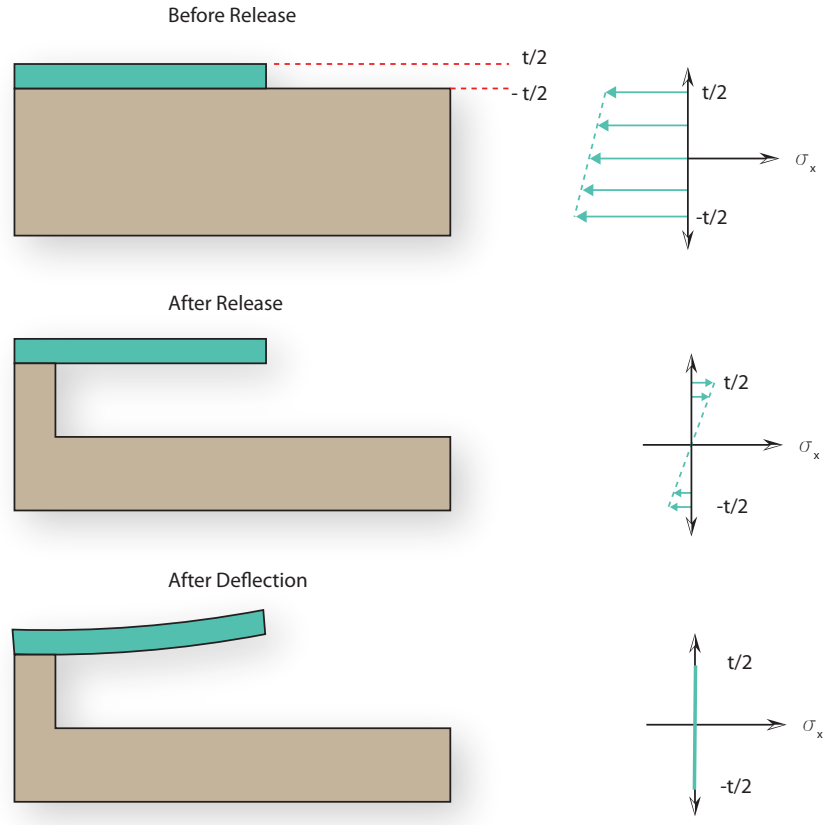


Figure 1.13: **Deflections in Cantilevers.** Illustration showing how the curvature is caused by stress gradients in the freestanding films of thickness, t . (Adapted from [27])

pendulum structures. Let us consider an unreleased cantilever fabricated on a silicon substrate as shown Figure 1.13. By the nature of the film whose bottom is attached to the contracting substrate and whose top surface is free we have a stress gradient in the film which is on average compressive.

When the film is released, but before it relaxes into its equilibrium state, we see that the average stress is zero since the free standing film is free to expand or contract. We see in this state that the top of the film would be under tensile stress while the bottom of the film would be compressive. Naturally the film reacts to these stresses and relaxes by curving towards the side of the film which is tensile until the stress across the thickness of the film is zero. We can calculate the shape of this bending and its dependence on strain. Let us consider a thin film of thickness, t_f , and Young's modulus, E_f , deposited onto a substrate of thickness, t_s , and Young's modulus, E_s (Figure 1.14). We know when the film is deposited onto this substrate at an elevated temperature that forces and stresses are induced in the structure. We can represent these stresses by considering the static forces and moments onto the film where F_f and M_f are those in the film, and F_s and M_s are those in the substrate, respectively. And we know in equilibrium that $F_f = F_s$ since the film and substrate are attached. F_f acts uniformly over the cross-sectional area defined by $t_f \cdot w$ or at the middle of the section at $z = t_f/2$. In order to have equilibrium in the film we know $F_f(t_f/2) = M_f$ and for the complete structure shown in Figure 1.14(a) the equilibrium equation can be written as,

$$F_f \left(\frac{t_f + t_s}{2} \right) = M_f + M_s \quad (1.26)$$

We consider an isolated cantilever section as shown Figure 1.14(c) where we assume the longitudinal

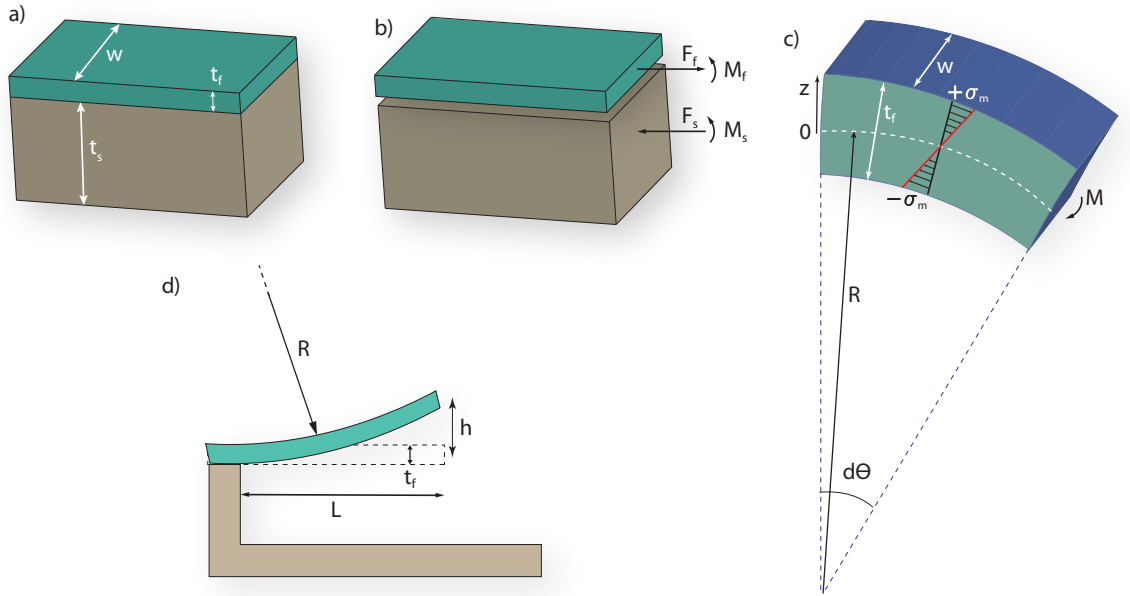


Figure 1.14: **Stress Gradient in Free Standing Cantilever.** (a): Illustration showing the structure of the substrate with thin layer on substrate. (b): Free-body diagrams of thin film and substrate with forces and end moments. (c): Illustrating elastic bending of a cantilever segment under a moment, M . (d): Shows relaxed cantilever under the influence of an internal stress gradient. (Adapted from [27])

contraction or dilation which changes depending on their distance away from the central axis (dashed white line). The stress gradient varies linearly across the center axis of the beam from maximum tension, $+\sigma_m$, at the top of the beam to the maximum compression, $-\sigma_m$, on the bottom. We know that the length of the neutral axis where stress in the beam is zero can be written as $L_{z=0} = R \cdot d\theta$, where R is the radius of curvature of the beam segment and $d\theta$, the angle of angle defining the beam segment. We can then easily see how any length an arbitrary distance z away from the neutral axis can be written as $L_z = (R + z)d\theta$. We know that any strain along the z axis is the difference in length between the neutral axis and a position at z which can be written as

$$\epsilon_z = \frac{L_y - L_{z=0}}{L_{z=0}} = \frac{(R + z) \cdot d\theta - R \cdot d\theta}{R \cdot d\theta} = \frac{z}{R} \quad (1.27)$$

If the film is restricted to move in one direction we can relate the stress and strain by $\sigma = E\epsilon$ such that the stress at position z can be given by

$$\sigma_z = E \frac{z}{R} \quad (1.28)$$

and the maximum stress at the top and bottom of the beam is

$$\sigma_m = \pm E \frac{z}{2R} \quad (1.29)$$

such that compressive stress is at the top and negative in accordance with convention and the tensile stress on the bottom is positive. We would now like to use our expression for the linear stress gradient in the film to write an equation for the radius of curvature of the cantilever at its relaxed state. We can write the stress gradient $\Delta\sigma$ as the difference in stress between the top and bottom of the film as

$$\Delta\sigma = E \frac{t_s}{R} \quad (1.30)$$

We can write the radius of curvature as the

$$R = \frac{L^2}{2h} \quad (1.31)$$

We can use this in our equation of the stress gradient $\Delta\sigma$ to get the deflection of the beam h as

$$h = \frac{\Delta\sigma L^2}{2t_s E} \quad (1.32)$$

This confirms that for a tensile film like Si_3N_4 on silicon, we will have pendulums that deflect away from the substrate, while a compressive SiO_2 film will produce cantilevers which deflect towards the substrate. This derivation for the shape of a free-standing cantilever is a good estimate for the

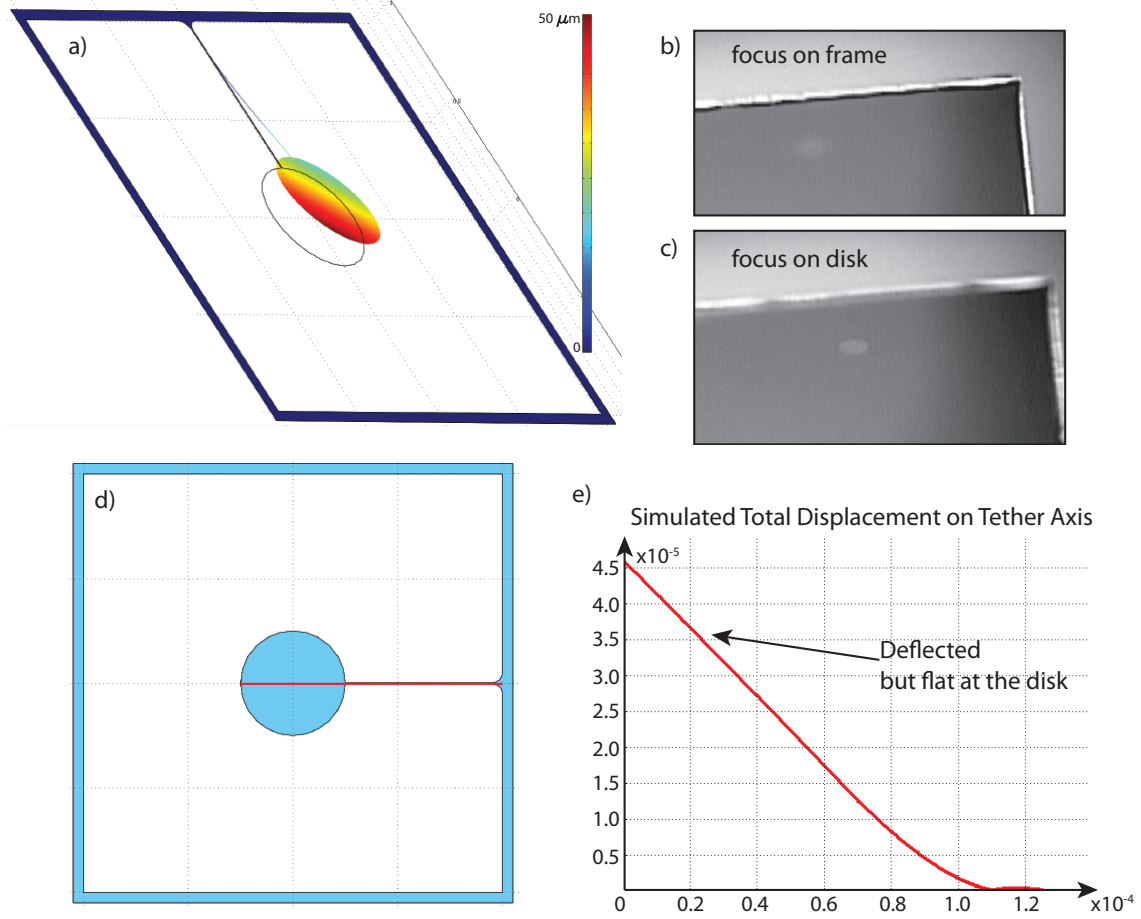


Figure 1.15: **Pendulum Deflections.** (a): COMSOL simulation 3D plot showing total displacement of a tested pendulum with stress gradient included. (b): Microscope image of simulated pendulum (focused on the frame of the window) (c): Microscope image of simulated pendulum (focused on the disk) (d): Shows x-y view of the pendulum simulation. We simulate the total displacement of the pendulum along the axis of the tether (red line). (e): Plot of simulated total displacement along the red line in (d). Shows that despite the deflection resulting from stress gradients within the dielectric film, the membrane is flat and could be tilted in order to align with an incoming beam without the membrane crossing several fringes of the trap beam.

deflections observed in our fabricated pendulums where $L = L_t + d_{disk}$ where L_t is the length of the tether attached to the disk and d_{disk} is the diameter of the disk. We also use COMSOL simulations in order to simulate the deflections that are more specific to our structures by inserting the linear stress gradient into finite-element model of our tested pendulums as shown in Figure 1.15(a). One of the simplest ways to measure the deflection on the disk was by using an optical microscope to view the devices. Using a micrometer screw to position the imaging system, one can focus on the frame of window (same focal plane as the substrate) where the pendulum is clamped, as seen in Figure 1.15(b). Then one can use the micrometer screw to accurately position the microscope until the tip of the disk is in focus (Figure 1.15(c)) and determine from the micrometer screw how far

the pendulum has deflected by taking the difference of the two positions. Measuring the deflection using an SEM was very difficult, as the charge built up from the electron beam caused the devices to displace large amounts which risked destroying the pendulums due to their “floppiness”. In the case of the pendulum in Figure 1.15, the FEM simulation gave us a deflection at the tip of the pendulum of $48.9\ \mu\text{m}$ and a measured deflection of $45\ \mu\text{m}$. This becomes an important issue when looking at the alignment of optics to the disk in order to either optically trap it with a beam or incorporate it into a macroscopic optical cavity. It would be difficult to losslessly integrate these membranes into the optical beam setups if the membrane has a radius of curvature. We used COMSOL to simulate the total displacement of the pendulum along the length of the tether (red line in Figure 1.15(d)). For our structures we see that the disk is deflected but flat along the disk, which would allow us to simply tilt the device with respect to the incoming beam in order to achieve normal incidence onto the disk.

1.4 Experiments and Results

We experimentally demonstrate a technique that enables the quality factor of a mechanical system to be enhanced beyond the conventional material limits of SiO_2 . Our technique involves optically trapping a thin, dielectric membrane whose geometry is designed so that the natural material forces are extremely weak [17]. In this limit, almost all mechanical energy is stored in an ultralow-loss potential provided by strong optical restoring forces, which dilute the effects of internal material dissipation ([17] [28]). The trapped oscillator is analogous to a mechanical oscillator with a spring that is stiffened by increased mechanical tensile stress ([29] [30] [31]) in that both the oscillator frequency and the Q_m increase. Our general scheme is implemented for a particular example of an SiO_2 dielectric disk supported by a single thin tether, trapped in an optical standing wave. We observe an increase in the “pendulum” mode frequency from 6.2 to 145 kHz as the optical power is increased, leading to a final quality factor $Q_f = 5.8(1.1) \times 10^5$. Q_f represents greater than 50-fold increase over the intrinsic Q_i of our device in the absence of optical trapping forces and more than an order of magnitude improvement over the estimates of conventional dissipation rate of our SiO_2 disk ([32]). These results substantiate the potential of our technique to facilitate mechanical sensors with enhanced sensitivity and quantum devices based upon mechanical systems. Optical forces are generally feeble compared to mechanical forces, which makes optical manipulation of mechanical oscillators challenging. To implement optical trapping of membranes, we begin by fabricating a nearly freestanding dielectric film in a pendulum geometry. We chose SiO_2 as the membrane material mainly for its low optical absorption [33]. The final device used in our experiments (Figure 1.16) consisted of a $10\ \mu\text{m}$ diameter disk held up a $50\ \mu \times 430\text{nm}$ tether, which is attached to a large square annulus of SiO_2 that has a width of $\approx 60\ \mu\text{m}$. The thickness of all the suspended parts (i.e.

the disk, the tether, and the annulus) is 130nm. To investigate properties related to the trapped

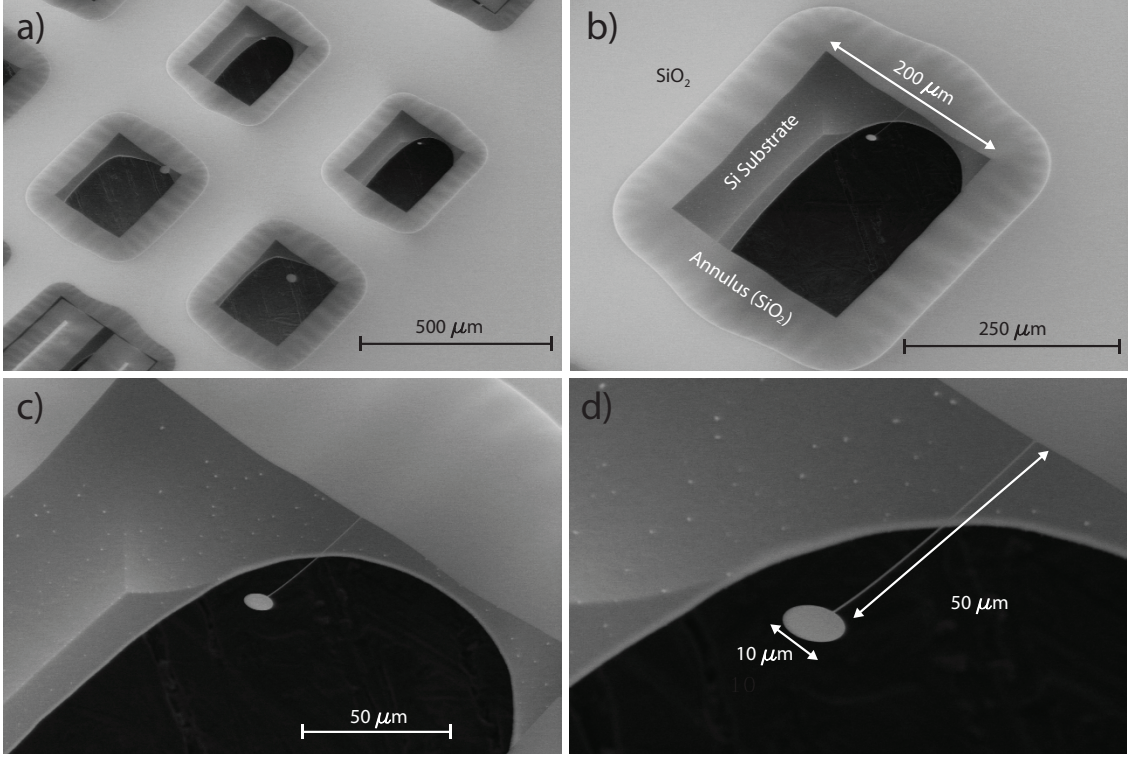


Figure 1.16: **Final SiO₂ Devices.** Scanning electron micrographs of the device: a 130nm thick SiO₂ membrane forms the pendulum which consists of a 10 μm diameter disk and a 50 $\mu\text{m} \times 430$ nm tether. (a): SEM image of the chip layout. Several windows, each with its own pendulum, can be fabricated onto a single 1 \times 1 cm chip. (b): Overview: The pendulum is suspended from a 60 μm wide SiO₂ annulus. The annulus (wrinkled area) and the pendulum are etched into a SiO₂ film for which the Si substrate directly underneath has been removed. The dark background in the center is a clear opening of the substrate. (c): Close-up SEM of the pendulum. (d): Closer view of the pendulum which is deflected 10-15° out of the plane of the substrate due to residual stress of the film.

pendulum, we load the 1 \times 1 cm sample chip, which typically contains dozens of devices, into a vacuum chamber traversed by an optical standing wave. A schematic of the experimental setup is shown in Figure 1.17(a). The pendulums hang vertically inside the chamber which is evacuated to a pressure below 10^{-7} mbar to make gas damping negligible. The optical standing wave is formed by a retro-reflected Gaussian beam, which has been focused to a $1/e^2$ waist $\omega_0 \approx 17 \mu\text{m}$ at the position of the disk. The trap beam is derived from a high power Nd:YAG laser operating at a wavelength of $\lambda = 1064 \text{ nm}$. We vary the incident laser power between 3 mW to 17 W using a wave plate and polarizing cube. The centering of the trap beam on the pendulum disk is critical for achieving large trapping potentials without mixing “center-of-mass” (CM) motion of the pendulum with vibrational modes of the tethers. This degree of freedom is carefully aligned by monitoring transmission of the forward and retro-reflected beams through the disk. To ensure that the disk

is perpendicular to the optical standing wave, we implement a pair of actuators to tip and tilt the sample chip to prevent the pendulum from settling into a configuration in which the disk extends over multiple periods of the standing wave due to deflections caused by stress (Figure 1.15). In order to align the retro-reflecting beam onto the disk we move the chip using the tip/tilt actuators and a positioning stage (using micrometers) to measure the transmission of the low-power incoming beam into PD₂ as we move the chip (and the pendulums) in the x-y plane normal to the incoming beam. As the disk moves across the incoming beam we measure an symmetric dip in the transmission about the center of the disk. We then align M₂ by measuring the reflected signal back through the pendulum in a similar fashion (also at low power around 3 mW). Alignment of the incoming and retro-reflecting beam are incredibly important at high powers where a misalignment of the retroreflecting trap can easily displace the disk unevenly, causing the pendulums to be irreversibly bent out of plane or even twisted (Figure 1.18). For the optical standing wave configuration shown

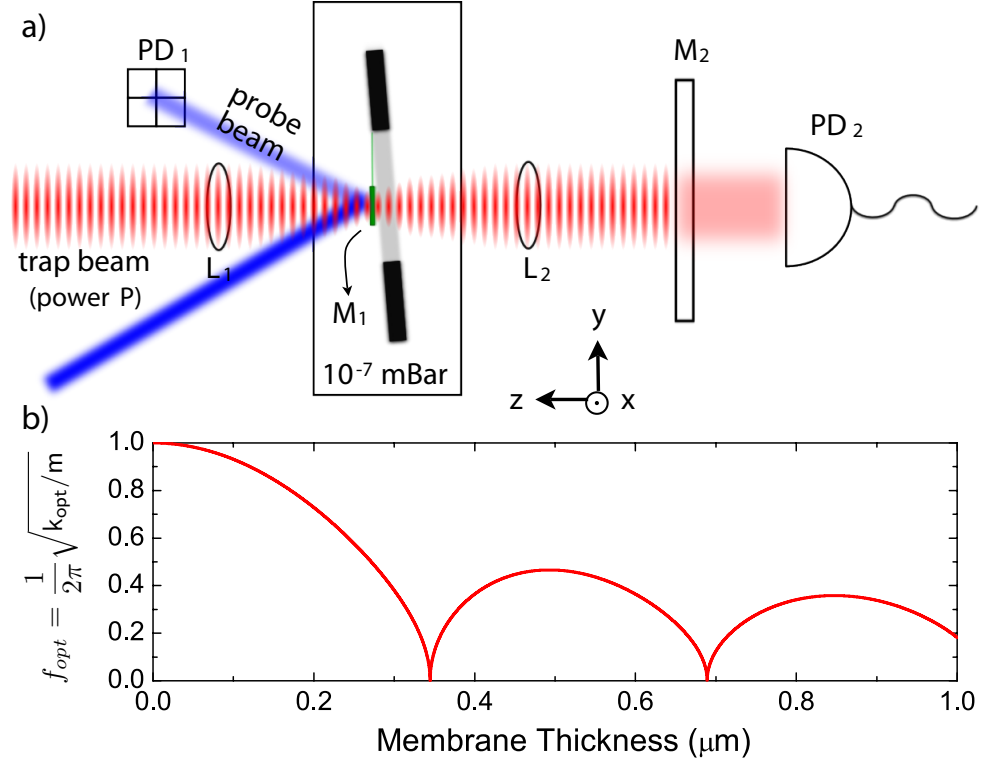


Figure 1.17: Optical Trapping Experimental Setup. (a): Schematic of the experimental setup. The sample chip is enclosed inside a vacuum chamber. We trap the disk in an optical standing wave formed by a single laser beam at 1064 nm wavelength and its reflection from the disk (M₁) and a mirror (M₂, reflectivity = 0.98). We monitor the thermal motion of the pendulum by the deflection of an off-axis probe beam (blue) reflected from the disk on to a quadrant photodiode (PD₁) and transmitted intensity onto PD₂. (b): Calculated trap frequency f_{opt} vs membrane thickness d_m normalized to f_{opt} at $d_m/\lambda \rightarrow 0$ for a fixed optical power. For $d_m \approx \lambda$, we solve for the steady electric field amplitude on the left and right of the membrane.

schematically in Figure 1.17(a), we estimate the trapping potential by balancing expressions for the radiation pressure force on either side of the membrane. To simplify the problem, we assume that the disk is infinitely stiff, that it is free to move along the axis of the trap and that the incident optical beam is smaller than the disk so that diffraction from the edges may be ignored. We solve for the electric field of a single beam in the presence of two reflectors, M_1 (the disk) and M_2 , as a function of the membrane thickness, d_m . Stable equilibria occur at the positions, where the force between the incoming beam and the finite electric field built up between M_1 and M_2 are balanced, which are neither at node or antinodes of the standing wave. At each equilibrium position, the optical spring constant of the trap is $k_{\text{opt}} = \frac{16\pi}{\lambda} \frac{r_m}{t_m} \frac{P}{c}$, where P is the incoming power, r_m and t_m are reflectance and transmittance of the membrane determined by d_m and the index of refraction of the film [34] and c is the speed of light. In Figure 1.17(b), we plot the calculated optical trapping frequency, $f_{\text{opt}} = \frac{\sqrt{k_{\text{opt}}/m}}{2\pi}$, normalized to the prediction for a membrane with $d_m/\lambda \rightarrow 0$. It is interesting to note that the optical spring constant for a membrane in the middle of a high-finesse Fabry-Perot cavity is also $k_{\text{opt}} = \frac{16\pi}{\lambda} \frac{r_m}{t_m} \frac{P}{c}$, where P is now the circulating power. In this case the membrane center would be trapped specifically at either an antinode or a node of the standing wave depending on the membrane thickness. Intrinsic vibrational modes and frequencies of the pendulum structure

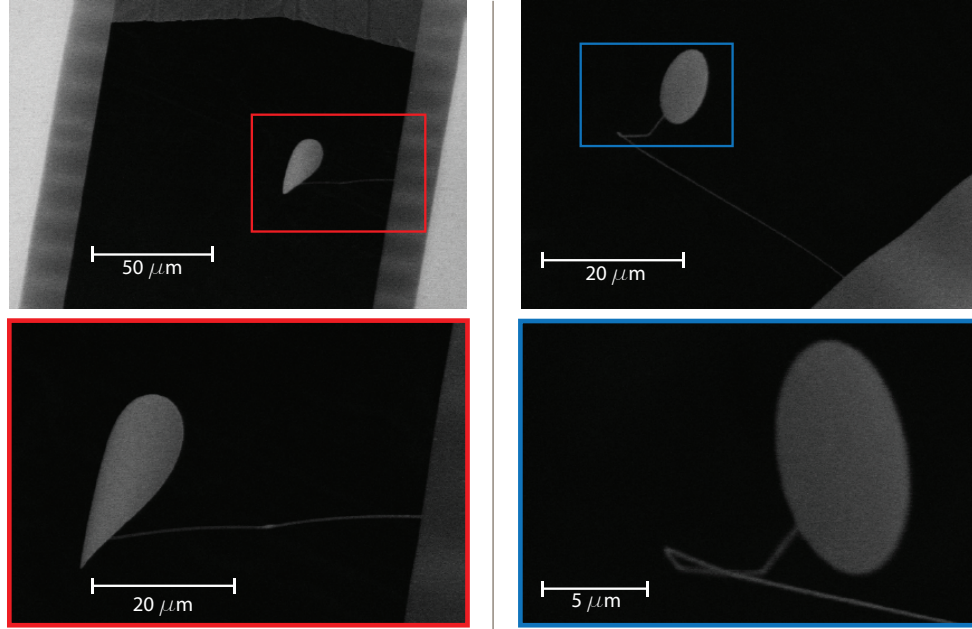


Figure 1.18: **Retro-reflecting Trap Misalignment** . Scanning electron micrographs showing the 2 pendulums which were bent due to uneven trapping at high powers ($\approx 3 - 7$ W) caused by an misalignment of incoming beam and retro-reflected beam.

are probed by reflecting an independent “probe” beam ($\lambda = 852$ nm) from the disk at an oblique angle (50°) with respect to the trap. The reflected beam is directed to a quadrant photodiode

(PD₁) [35] which is calibrated using a sample tip and tilt actuators. The quadrant photodiode can be split into two horizontal pairs of sensors (“top” and “bottom”) and two vertical pairs of sensors (“left” and “right”). Analysis is performed on the difference between the top and bottom combined photosignals (expressed as a transimpedance-amplified photocurrent, $V_{TB(t)}$) and the difference between the left and right combined signals ($V_{LR(t)}$). Fourier transforms of $V_{TB(t)}$ and $V_{LR(t)}$ reveal the frequencies and tip/tilt orientation of the vibrational modes (Figure 1.19(a)). We identify low-order vibrational modes by comparison of the observed frequency spectrum and their characteristic mode shapes to a COMSOL finite-element simulation based on membrane material properties and its geometry measured using a scanning electron microscope. We see approximately a factor of 2 discrepancy in the simulated frequencies versus measurements in the absence of optical forces. This is most likely due to an overestimate of the Young’s modulus for the very thin SiO₂ film where the surface effects can be important. The mode shapes in the absence of the optical forces calculated from simulation are illustrated in Figure 1.19(c) as (a_1) the pendulum mode, also called the CM mode where the pendulum disk swings along the axis of the trapping beam ($f_{0a} = 6.2$ kHz), (b_1) the “violin” mode ($f_{0b} = 93$ kHz), and (c_1) the “torsional” mode ($f_{0c} = 109$ kHz). One additional mode that is not shown in the figure is (d_1) the transverse pendulum mode swinging orthogonal to the axis of the trapping beam (25 kHz). We are the most interested in the CM mode because it exhibits the least mechanical deformation which leads to energy dissipation. In the presence of an optical trap, vibration frequencies of the membrane are determined by the sum of the optical restoring force and the intrinsic mechanical restoring force. The contribution from gravity is small (< 100 Hz) and is neglected. The trap is first aligned at low trapping power (3 mW). To ensure that the tether does not provide a significant initial restoring force, we also fine tune the trapping laser wavelength so that the equilibrium position of the trap coincides with the natural axial position of the membrane. We diagnose their coincidence by minimizing the vertical deflection of the probe beam (evident in the mean value of V_{TB} when the trap is turned on). Figure 1.19(a) shows the power spectrum of V_{TB} , which reflects the vertical angular displacement of the pendulum, as a function of trap power, P . For comparison we show a spectrum generated by a finite-element model (Figure 1.19(b)) that treats the optical trap as a restoring force with a Gaussian transverse profile. Close comparison of the observed and model spectra adds to our understanding of several distinct features. As the optical trap power is increased, the frequencies of the three lowest visible modes increase as $\sqrt{f_{0i}^2 + \alpha_i P}$, where f_{0i} represents their natural frequency and α_i is the trapping slope coefficient for each mode. As the CM mode frequency increases, the mode shape also changes via the bending of the tether. This change is first evident in the reduction of the CM mode signal near 50 – 75 kHz. The reduction occurs as the mode shape changes from Figure 1.19 (C, a_1) to (C, a_2), which to first order does not deflect vertically. In addition, as expected, we do not see such a reduction for corresponding trapping beam transmission on PD₂ (not displayed) that probes pure axial disk displacement. The

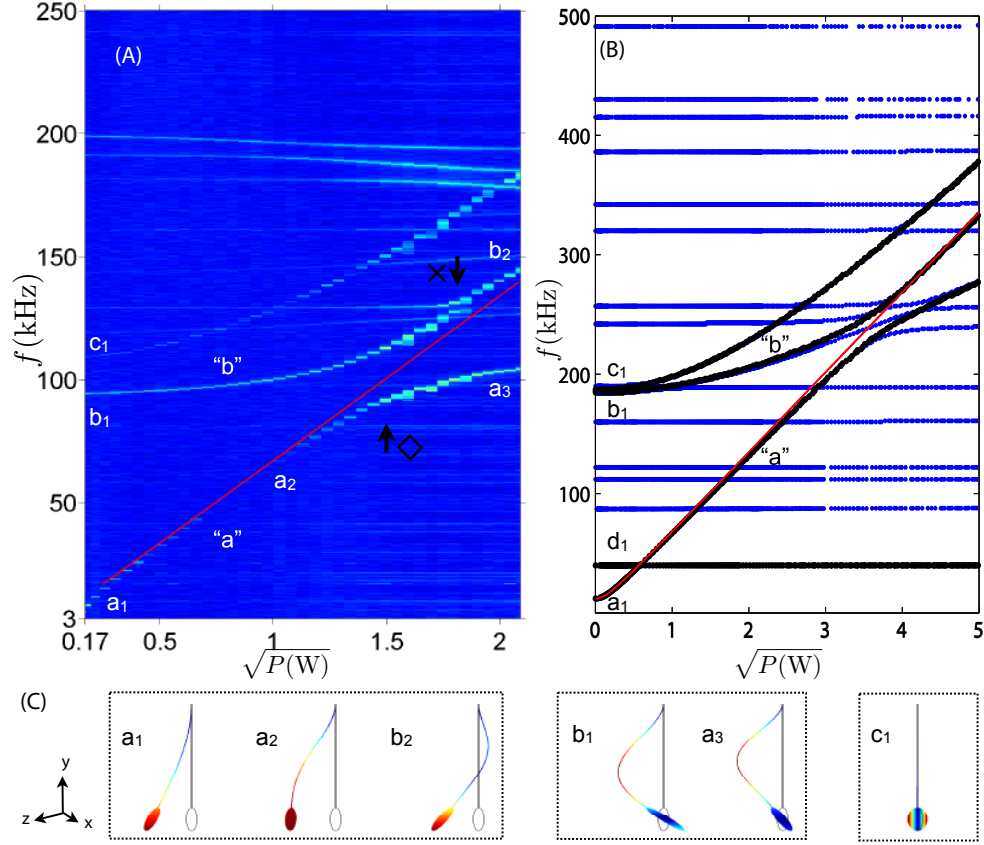


Figure 1.19: **Optical Trapping of a Membrane Disk.** Displacement power spectrum of vibrational modes. (a): Spectrogram of vertical angular displacement (inferred from deflection measurement, Fig. 1.17a) versus trapping power, P . Several vibrational mode branches are evident, e.g., “a” and “b”. As the optical trap power is increased (in discrete steps), the frequencies of the three lowest modes (a_1 , b_1 , c_1) increase as $\sqrt{f_{0i}^2 + \alpha_i P}$ (see text). Two avoided crossings are visible here: (\diamond) formed by the CM mode and the violin mode: (\times) formed by the CM and the annulus mode. At higher powers, the CM mode is a hybrid of pendulum and violin motion (b_2). Other visible modes in the spectrum are associated with vibrations of the annulus. Overall the CM frequency shifts from 6.2 to 145 kHz when 4.3 W of optical power is applied. (b) Finite-element simulated spectrum of an optically trapped pendulum (black) suspended from an annulus (blue) that is in turn anchored to a substrate for qualitative comparison to (a). The red lines in both (a) and (b) are drawn for a trapping slope $\alpha = 4500 \text{ kHz}^2/W$. (c): Simulated mode shapes for different optical trapping forces in (a). (a_1) the pendulum mode, also called the CM mode, (b_1) the violin mode, and (c_1) the torsional mode.

mode shape again changes as the CM mode and the violin mode [Figure 1.19 (C, b_1)] form an avoided crossing near 93 kHz. At higher power, the CM mode crosses an annulus mode. Overall the CM mode frequency shifts from 6.2 to 145 kHz when 4.3 W of optical power is applied, corresponding to a trapping slope coefficient of $\alpha_{\text{CM}} = 4880 \text{ kHz}^2/W$, in good agreement with the simulated value of $\alpha_{\text{CM}^{\text{FEM}}} = 4500 \text{ kHz}^2/W$ (the inferred value from the measurement being overestimated due to the avoided crossing). At trapping power greater than 4.3 W, we find that the CM frequency ($f = 145$

kHz) is near yet another vibrational mode of the annulus. With further increases in power, the large thermal displacements of the annulus mode greatly dominate the motion of the CM pendulum mode, making it difficult to identify. One of the most important consequences of the optical trapping is an increase of the mechanical Q [17]. The large increase in frequency of the CM mode through optical trapping implies that the amount of mechanical energy stored in the optical fields U_o dominates over that stored in internal stresses, U_m . Because the optical potential is nearly loss-less due to the low optical absorption of SiO_2 [33], the effects of material dissipation are diluted by a factor $U_m/(U_o + U_m)$. Therefore we would expect the mechanical Q of the system to increase as the inverse of the dilution factor $\approx U_o/U_m$ for a frequency-independent damping mechanism. For an ideal system, one would expect an indefinite increase in the ratio $U_o/U_m = (f/f_0)^2$ with increasing trap power. In practice, this ratio saturates due to factors such as the mass ratio between the trapped disk and the untrapped tether, the mode mixing with the modes of the support structure (tether and annulus in our case), and induced mechanical strain due to the inhomogeneous trapping beam profile. Accounting for these effects, our finite-element simulation predicts a maximum of $U_o/U_m \approx 100$ in our experimentally achievable frequency range. Further improvement on reduction of the tether width will increase the U_o/U_m ratio. To infer the Q of the trapped pendulum, we record the thermal motion $X(t) \propto V_{TB}(t)$ at each laser power for a few minutes and numerically compute the energy autocorrelation, $R_E(\tau) \equiv \langle X^2(t)X(t+\tau)^2 \rangle$, over a Fourier frequency range encompassing the mechanical frequency. For a high Q oscillator driven by a Gaussian thermal noise, $R_E(\tau)$ is characterized by an exponential decay with time constant τ_E , in correspondence to our measurements and relates to the mechanical quality factor by $Q = 2\tau_E$. We verify our oscillator is driven by thermal energy by comparing the pendulum disk angular displacement energy in the absence of the optical trap to the expected thermal energy at 300 K and find the agreement to be within 20%. This agreement rules other technical noise drive such as seismic noise or beam pointing noise as insignificant. The pendulum in the absence of trapping forces has an initial value $Q_i = 1.1(2) \times 10^4$ and a 20% deviation from shot to shot.

A summary of our Q -measurement results is presented in Figure 1.20(b). We compare the result of monitoring vertical angular displacement of the pendulum on PD₁ (data in circles) with the result of monitoring axial displacement of the pendulum via the trap beam transmission through M₂ on PD₂ (triangles). The results are consistent in both cases. We observe that the initial Q increase to a maximum value $Q_a = 6.9 \times 10^5$ is consistent with the $(f/f_0)^2$ scaling and in contrast with the stress induced Q -increase studied in Si_3N_4 nanostrings ([29] [30] [31]). After the initial increase, Q then drops as the CM mode crosses the violin mode, which is a consequence of an increase of the strain energy due to the bending of the tether. Beyond the avoided crossing with the violin mode and a subsequent annulus mode (arrow \times), the Q of CM mode increases again by a factor > 50 relative to the Q_i to a final value of $Q_f = 5.8(1.1) \times 10^5$. The dependence of Q on frequency

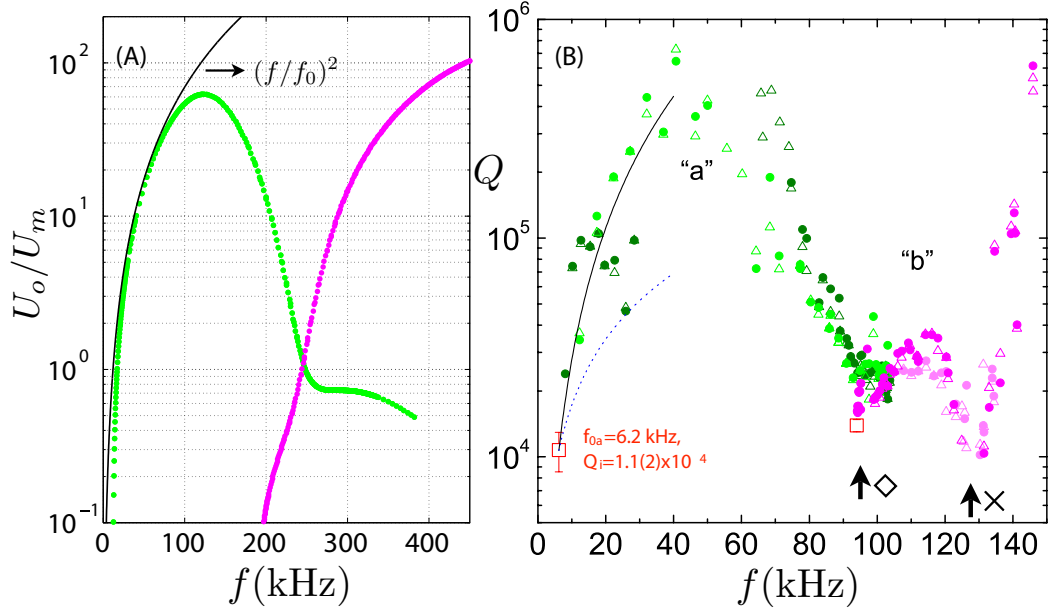


Figure 1.20: **Mechanical Q Enhancement Through Optical Trapping.** (a): Finite-element calculation of the ratio between the energy stored in the optical potential (U_o) and the mechanical potential (U_m) vs trap frequency. The two branches correspond to “a” and “b” vibrational modes, respectively, in Figure 1.19(b). Q vs trapping frequency for two vibrational modes in the trap, independent recorded on PD₁ (circles) and PD₂ (triangles). In addition, two data sets with slightly different optical trapping alignments are shown for “a” (light and dark green) and “b” (light and dark magenta). The Q of the CM mode increases 60-fold from its natural value, $Q_i = 1.1(2) \times 10^4$ ($P=0$, data in red square) with a slope that is consistent with $(f/f_0)^2$ scaling (solid line) before turning over near the avoided crossing (◇) with a violin mode. Beyond this avoided-crossing, Q increases again followed by a minimum near the annulus avoided-crossing (×) and then a steep increase. We also show the expectation of a Q-increase that scales as f/f_0 (dashed line) for comparison. We find the measured Q increase to be in qualitative agreement with the calculated $1 + \frac{U_o}{U_m}$ in (a).

is in qualitative agreement with the calculated U_o/U_m in Figure 1.20(a). Overall, we demonstrate that by adding optical energy without additional dissipation into the system, we can increase the mechanical Q by more than an order of magnitude.

We expect that further significant advances can be made with refined fabrication techniques and a shift to materials with better mechanical characteristics. For instance, the mechanical frequency and the corresponding Q-factor of our trapped pendulum is limited in part by the large suspended annulus to which the tether is attached. Using wet chemical anisotropic etching of Si to release the pendulum, it should be possible to fabricate a device with an annulus less than 10 μm wide. Furthermore, while SiO₂ proved to be convenient to work with initially, it suffers a relatively low intrinsic quality factor of $Q_i \approx 10^4$ that could be limited by surface-related damping mechanism ([32] [36]). Although the nature of the surface-related damping is still an open question and not necessarily a fundamental limitation, we can still compare our observed Q_i to other SiO₂ devices.

From the extensive phenomenological study of SiO_2 loss angle [36] and the surface-to-volume ratio of the our pendulum, we would expect $Q_i \approx 9200$, which is consistent with our observation of $Q_i \approx 1.1 \times 10^4$. Switching platforms to stressed silicon nitride or crystalline silicon should enable material quality factors of $Q_i \approx 10^5 - 10^7$ ([9] [37] [38]). In initial experiments with Si_3N_4 , for example, we have fabricated stressed, tethered structures (similar to [13]) with bare frequencies of 172 kHz and $Q_i \approx 1. \times 10^7$. We know from Figure 1.5 that reducing the stress in the structure while good for improving the U_o/U_m also degrade the intrinsic Q_i . Using a Si_3N_4 four-tether structure as seen in Figure 1.5(a) with 5 nm tethers could reach $f \times Q \approx 10^{15}$ Hz using 20 W of power. Such values would be unprecedented for any fabricated nano- or micromechanical system and remarkably would be competitive with the prediction for untethered levitated nanoparticles ([14] [39] [40]).

Our technique holds promise as a tool to reduce the role of mechanical dissipation in a wide variety of sensing application as well as in the emerging field of quantum optomechanics [41]. Our device can be integrated into a high-finesse cavity employing the “membrane-in-the-middle” geometry, for example, and could provide the long coherence times necessary to observe quantum behaviors (i.e. macroscopic entanglement) in a room temperature environment ([42] [43]). This work reveals a fascinating new aspect of the interplay between motion and light and should stimulate further exploration.

Chapter 2

Turbulence-Shielding Fabrication Methods

2.1 Introduction

While most fabrication often focuses on making small devices with small dimensions where the amplitude of thermal motion is small, in this chapter we describe our turbulence-shielding fabrication techniques in order to realize delicate nanodevices with extremely small dimensions and high aspect ratios. Using conventional handling, fabricating such devices would produce prohibitively low yield rates due to their susceptibility to breaking when met with small forces. This is especially relevant in the large subset of nanofabrication involving wet processes (wet etching and cleaning, etc). Delicate devices can become extremely sensitive to mechanical failure or move with large displacements which cause failure of the nanodevice. When using fabrication methods which rely on conventional handling, devices are subjected to a number of forces: viscous forces induced by small handling movement, turbulence near the interface liquid/air interface, and surface tension present at air-liquid and liquid/liquid interfaces. When delicate nanostructures become easily fractured or displaced by small forces, repeatability in every aspect of the fabrication process becomes a significant challenge. Small and stochastic deviations in the way delicate devices are handled during fabrication result in wide variations of success once devices become extremely fragile. In this chapter, we'll focus on the fabrication of devices from thin layers of stoichiometric LPCVD silicon nitride (Si_3N_4) on [1-0-0] Si wafer. The general principles involved in our methods are easily applicable to almost any material and fabrication process involving wet processing.

Our method addresses several inherent challenges in releasing delicate structures with wet etching. During these steps the nanostructures on the chip are free to move in the liquids and susceptible to small forces. A typical wet-chemistry process involves several liquid solutions – when a wet-etchant is used, it is usually followed by several rinses to remove the etchant, and possibly followed by a cleaning solution which also requires subsequent rinsing solutions. A fundamental

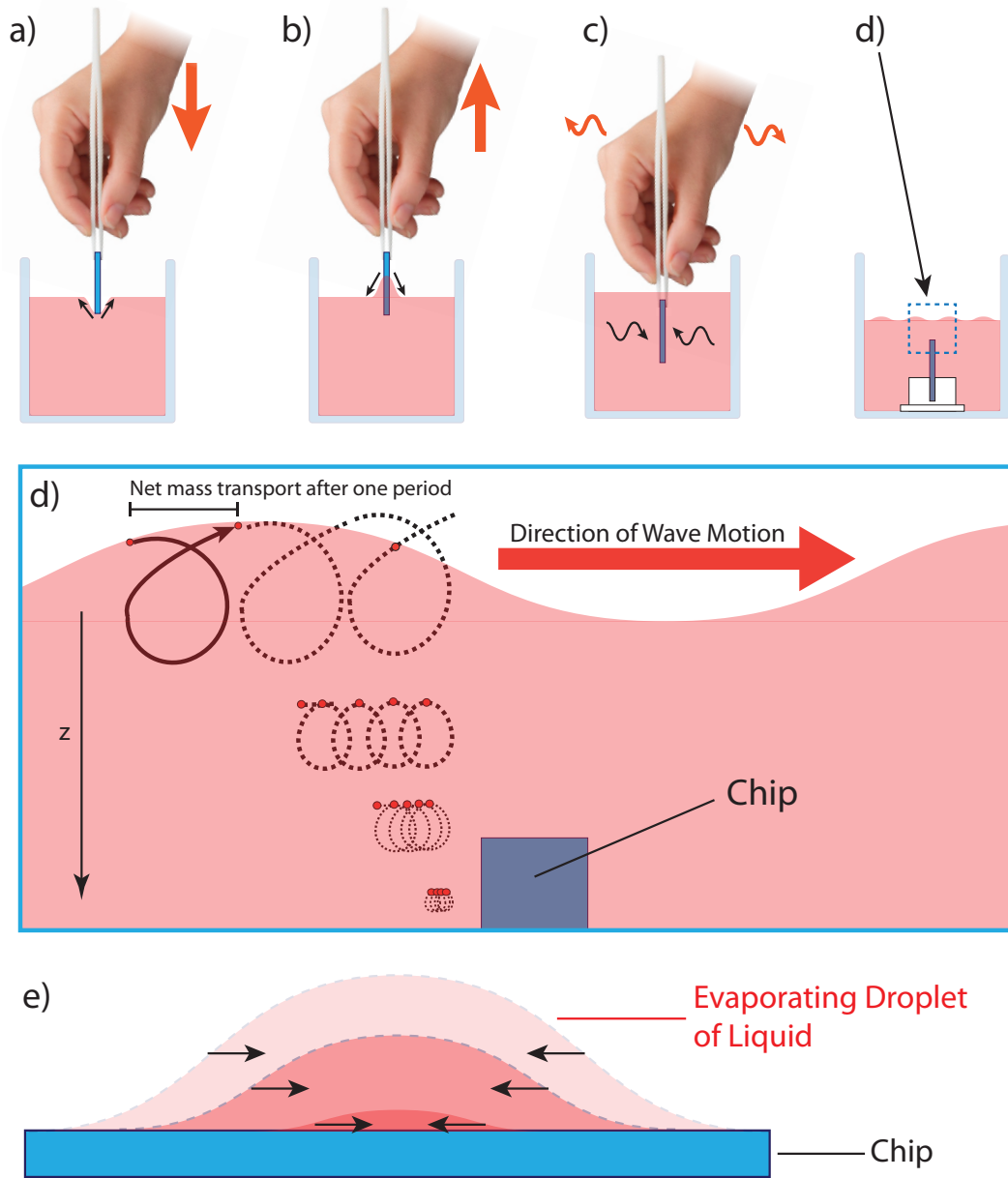


Figure 2.1: Conventional Handling and Challenges. High-aspect ratio nanodevices are delicate and can be destroyed with even small forces during wet-fabrication. (a): As samples are introduced into a liquid, the fragile devices on the chip (in blue) will likely be destroyed by the air-liquid interface surface tension as they pass through the interface. (b): The sample experiences equivalent surface tension forces as the sample is removed from the liquid. (c): Small stochastic handling movements at any point in the process introduce small stochastic flow across the chip which can destroy a frail device. (d): Shows a zoom of the surface of any body of liquid. Every air-surface interface has small waves that propagate across the surface. This produces a turbulent net force near the surface (Stokes drift) which is damped as one moves away from the surface. Even small flows created by Stokes drift can destroy fragile devices. The red dots represent particles in the liquid which are moved due to Stokes drift. (e): Illustration of a droplet of liquid evaporating on a chip. During this evaporation of the liquid the surface tension at the droplet/air interface pulls nano-devices inward with it as it volatilizes and its volume becomes smaller.

challenge is transferring delicate devices through a series of liquid solutions (wet etching, cleaning, rinsing) without exposing the fragile devices to a number of forces inherent in this transferring process. In Figure 2.1(a), we illustrate the transfer of a chip substrate (in blue) into a liquid. As the chip passes through the air-liquid interface the surface tension destructively pulls on the devices on the chip. The same is true when a chip is pulled out from a liquid where it's exposed to surface tension – extremely delicate devices on the chip can easily be destroyed by these small forces. As one handles the sample inside liquids, forces induced from small unavoidable movements in handling are large enough to break fragile nano-structures. While one can put a sample into a holder (as seen in Fig. 2.1(d)) and allow it to rest inside a liquid without moving, small handling movements are unavoidable, as handling is still required to introduce and remove the chip and holder from different solutions. The small turbulence introduced during transfers of the chip from one liquid to another are enough to destroy these sensitive devices. Another important source of destructive turbulence can be associated with Stokes drift. Naturally any body of liquid will have small waves which propagate across the surface which induces circulating flow near the surface as illustrated in Fig. 2.1(d). The magnitude of these displacements of liquid become smaller with increasing distance, z , from the liquid surface. While the chip can be submerged far from surface so that it experiences negligible Stokes drift, at some point during the transferring of the chip in and out of a liquid solution, the devices on the chip will pass through the region (near the surface) where Stokes drift is significant. After the wet-etching process the devices must be dried of all liquids. Fig. 2.1(e) shows an evaporating droplet of liquid on a chip as it loses mass and volatilizes on its surface. As the droplet shrinks due to evaporation, the surface tension at its interface also pulls nanostructures on the chip along with it, destroying delicate nanodevices. This is a common problem which has been solved with the use of critical point dryers (CPD), which is a process where the liquid surrounding the sample is placed in a high temperature-pressure environment such that it is induced into a supercritical fluid phase where distinction between liquid and gas ceases to be valid. The supercritical fluid which now surrounds the sample is evacuated without the chip experiencing surface-tension forces associated with evaporation from crossing from phase transition from liquid to gas. Any wet fabrication process we develop must be compatible with critical point drying as a last step. In order to achieve turbulence-shielding (TS) for our nano-fabrication process, we designed a holder to facilitate in the handling of samples such that one can fully release delicate nano-structures from their substrates, take them through the entire wet processing and drying them while shielding them from turbulence, handling movements and surface tension. As shown in Figure 2.2(a), the TS holder carries the 1×1 cm chips vertically in a cylindrical vessel. The base of the holder is made from polytetrafluoroethylene (PTFE) since it is a chemically inert material compatible with a large array of acids, bases and solvents. In order to maneuver the TS holder and securely hold the liquid in the container, as seen in figure Figure 2.2(c), a threaded Teflon rod fastens into a threaded hole in the

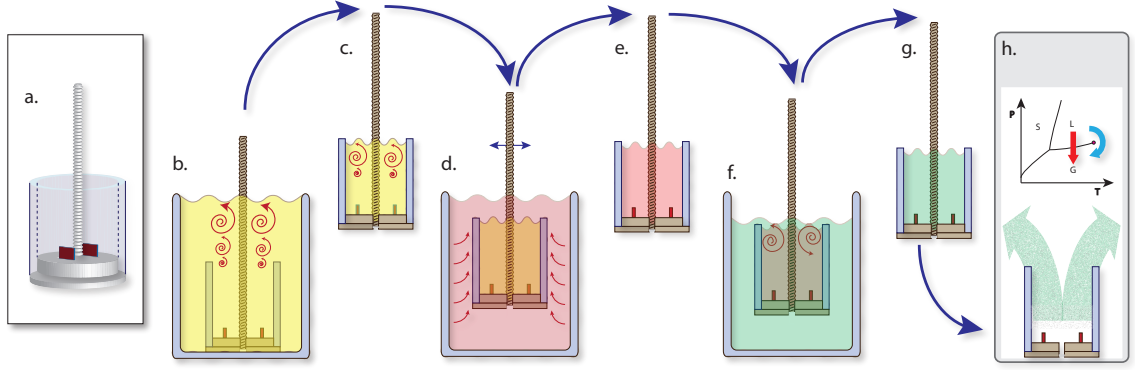


Figure 2.2: **Turbulence Shielding Holder.** (a): Configuration of the holder with two chips (in red) sitting vertically inside the container with a threaded rod to securely move the samples and the surrounding volume of liquid. (b): Two chips sit vertically in the turbulence-shielding (TS) holder inside a larger container of solution. The holder with chips sits far from the moving air-liquid interface and minimizes exposure to Stokes drift turbulence. (c): Using the threaded rod as a handle and secure plug for the liquid inside the TS holder, the chips are transferred from one solution to another. The chips sit deep inside the holder vessel, shielding the devices from Stokes drift turbulence at the air-liquid surface of the holder. (d): The TS holder shields the devices from viscous forces caused by handling movements. (e): Devices are slowly diluted from one solution to the next – minimizing effects from liquid-liquid surface tension. (f): Mixing two liquids at different temperatures or two solutions that react violently can cause turbulence. The chips sit far from these interfaces. (g): The chips are transferred to their final solvent solution. (h): The chips are transferred into a critical point dryer (CPD) which uses high pressure (P) and temperature (T) to move around critical point (blue arrow) and avoid the evaporative phase transition from liquid (L) to gas (G). It is essential to use CPD as the final step in drying the samples since evaporation (red arrow) exposes the samples to surface tension [Fig 2.1(e)]. This technique allows us to completely wet-process the sample and significantly reduce turbulence and surface tension on the sample.

base of the holder. At an air-liquid interface, a particle in liquid will experience a net Stokes drift in the direction of wave propagation at the surface. In the deep-liquid limit when one considers linear propagation of a sinusoidal wave on the surface, the average horizontal speed of the Stokes drift decays exponentially away from the free surface as $v_s = A^2 e^{2kz}$, where ω is angular frequency of the wave, k is the wave number, A is the amplitude of the wave, and z is the distance of the particles from the free surface. Our samples remain sufficiently far away from Stokes drift turbulence regardless of whether they sit in a large liquid container (Figure 2.2(b)) or are being transferred between processes (Figure 2.2(c)). As shown in Figure 2.2(d), The TS holder also protects against viscous forces created from small handling movements inside liquids. The enclosure around the chips allows one to move chips without dragging them through liquids by simultaneously moving the liquid volume surrounding the chips. The turbulence-free holder allows chips to be slowly and controllably diluted from one liquid to another, which significantly reduces the liquid-liquid interfacial surface tension when transferring from one liquid to the next. Using the threaded rod one can control how slowly two liquids mix. Additionally one can allow for the thermalization of two liquids at different

temperatures, which can cause temperature induced turbulence and increased liquid-liquid surface tension. The holder submerges the chips far away enough from surfaces that the initial turbulence caused by two liquids mixing does not affect the devices, as seen in Figure 2.2(f). One can finish the complete wet chemistry process and finish with a critical point drying so that the chips are not exposed to surface tension (i.e., from handling, transferring between liquids, and drying) and forces induced by handling. The holder allows one to not only produce delicate devices but also allows for repeatability and control that would not be possible with standard handling.

2.1.1 Micro-Pendulums for Cavity QED Optomechanics

Several groups are interested in studying cavity QED coupled with optomechanics by optically trapping SiO_2 nanospheres inside of high finesse cavities. Optically trapping the nanosphere allows one to increase the frequency of the nanosphere's center-of-mass mode with increasing intensity and eliminates clamping losses. Such a system would allow one to probe quantum interactions of light and matter and provide a way to couple a high mechanical Q resonator with an optical cavity. One analogous method described in Chapter 1 is to have on-chip devices such as thin micro-disks with minimal clamping to the substrate through one thin tether. This allows the optical trapping to dominate over the stored mechanical energy of the tether. This requires making the tether's width as thin as possible and the structure as "floppy" as possible. Taking such devices through a series of liquid solutions without destroying them becomes an immense challenge. An added complication to fabricating these delicate structures was the need for large openings through the silicon substrates in order to get optical access for the trapping beam to our disk pendulums. Wet-etching was preferred over dry releasing using XeF_2 because gas releases etch isotropically the silicon substrate underneath, creating a large overhang around device which introduced unwanted modes associated with the annulus as seen in Figure 1.10(b). KOH etches anisotropically through the chip, which minimizes this surrounding undercut to a width of $5\text{ }\mu\text{m}$. The micropendulums were extremely sensitive to fluid flow through the substrate if the chips were moved through liquid. In our process (Figure 2.3) we began with $200\text{ }\mu\text{m}$ [1-0-0] silicon wafers deposited with 50 nm of thick high-stress LPCVD Si_3N_4 on both sides. Electron beam lithography is used to pattern pendulums in the front of the chip and large windows in the back of the substrate. Using electron beam resist as a mask, a $\text{C}_4\text{F}_8/\text{SF}_6$ plasma was used to etch the devices into the Si_3N_4 layer. Our pendulum patterns were etched into the top layer of silicon nitride while large rectangular windows (aligned with our pendulums) were etched onto the back layer of silicon nitride. The windows with pendulums and the window in the back of the chip are etched with potassium hydroxide (KOH) to etch through the silicon substrate from both sides until etching from both sides meets in the middle of the substrate creating a large hole for optical access. The device is then rinsed in several cycles of deionized water to remove the KOH, cleaned with a hot sulphuric acid solution, rinsed in several cycles of deionized

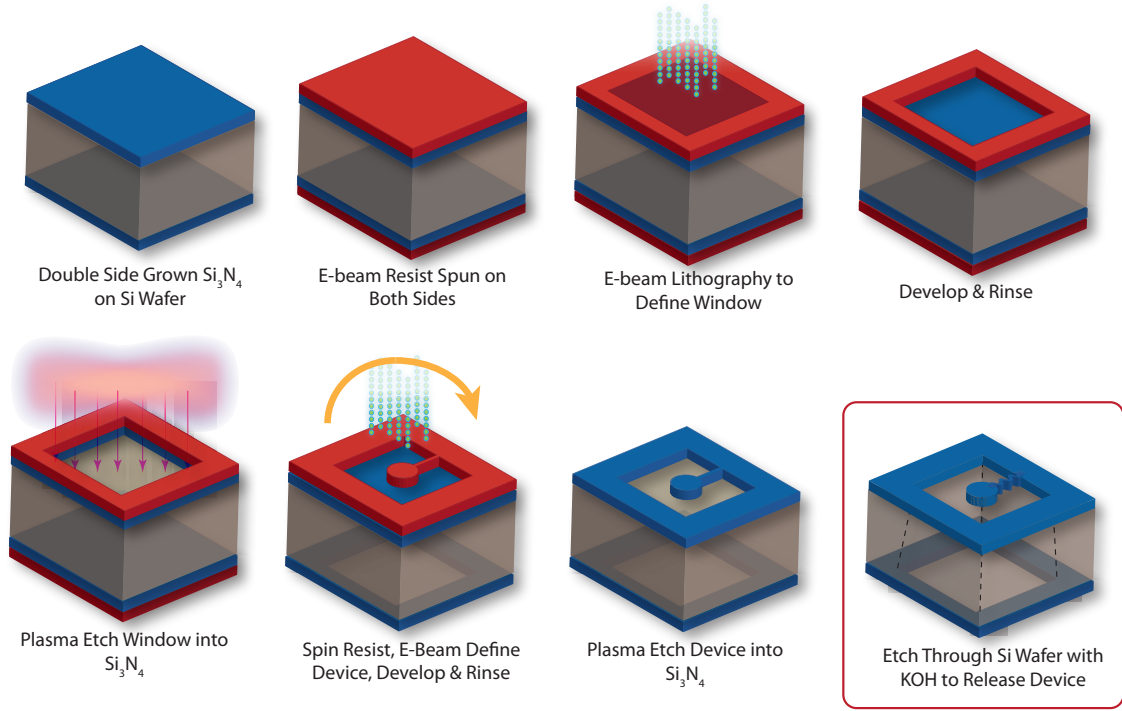


Figure 2.3: **Fabrication Process for Pendulums.**

water to remove the acid, and finally rinsed in isopropyl alcohol (IPA) before critical point drying the sample. We fabricate 50nm thick Si_3N_4 pendulums consisting of 25 μm diameter discs attached to the substrate by a 50 μm long tether (tether width of 150nm). The fabrication steps for the Si_3N_4 pendulums are outlined in Figure 2.3. We focus on the last step of the processing involving the release of the device using KOH wet etching at room temperature. For low frequency “floppy” devices, the H_2 gas bubbles produced in the KOH-Si reaction have surface tension which can be violent for the pendulums at high temperatures as the hydrogen bubbles rise through the liquid. At a low temperature, the rate of bubble production reduces exponentially also decreasing the radius of of the average bubble the microdisks comes in contact with. At high KOH temperatures ($\approx 75^\circ\text{C}$), we would commonly see failures like Figure 2.3(a), in which the bubbles would rise and lift the pendulums with them, allowing the pendulums to stick to the surface of the chip via Van der Waals forces. These are also the type of failures one would see when the chips were moved through wet processing without shielding due to strong viscous flows through the chip. Transferring from one liquid to another was also a significant impediment to good yield since the surface tension would pull the pendulums up as the chip was dipped into the next solution. Because of the low KOH etch rates required to safely release the pendulums (silicon etch rate: 1 $\mu\text{m/hr}$) this meant that pendulums would release in KOH solution for almost 4 days in order to completely etch a hole through the substrate. This required shielding our samples from Stokes drift throughout the entire fabrication

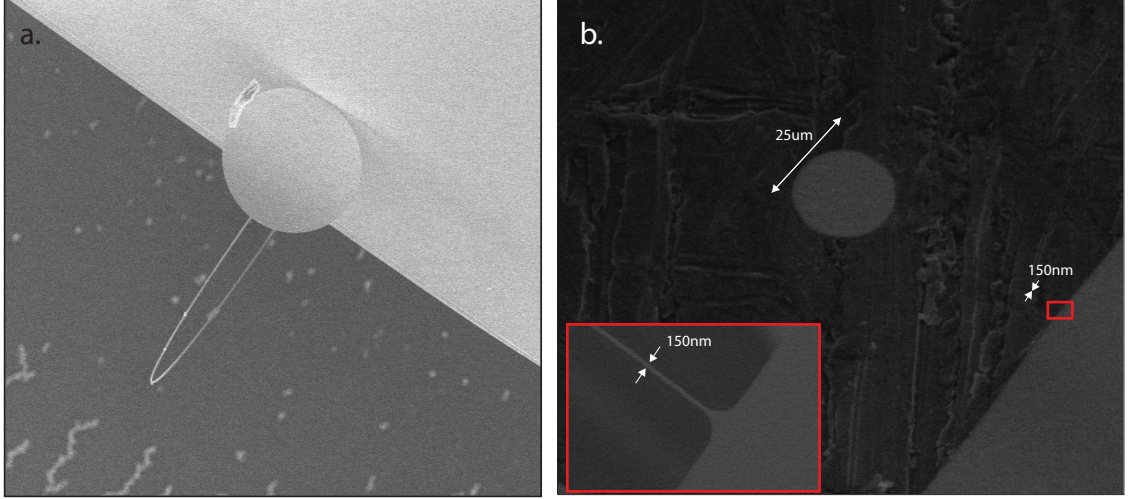


Figure 2.4: **Si_3N_4 Pendulum Fabrication Challenges.** (a): Common failure when the microdisk pendulum is released without turbulence shielding. Small flow across or through the chip at any point in the processing allow the extremely floppy pendulum to move with large enough displacements to stick on the surface of the chip with Van der Waals forces. (b): Using turbulence shielding, one can fabricate 50 nm thick Si_3N_4 pendulum microdisks with $25\mu\text{m}$ diameter disk with 150nm tether width.

process. Our shielding did this by keeping the chips far away from any air-liquid interfaces where Stokes drift is strongest. Figure 2.4(b) shows the type of pendulums that can be fabricated using turbulence shielding with a $25\mu\text{m}$ diameter disk and a tether (Length = $50\mu\text{m}$, Width = 150 nm) connecting it to the substrate. One major challenge in fabricating these devices was cleaning them thoroughly without agitating the device during processing. The trapping beam used in these experiments was produced with a high power Nd:YAG laser at 1064 nm with incident laser powers of up to 17 W with a $1/e^2$ waist of $17\mu\text{m}$ on the disk. This required that the delicate pendulums also be extremely clean of any contaminations (dirt, salt, etc.) since it could highly absorb the power from the trapping beam, heat up, and also heat up the pendulum enough to induce explosive thermal fracturing. After the KOH release is finished, the sample is rinsed with water several times before being immersed in a Nanostrip bath (homogenized sulphuric acid solution), and then rinsed thoroughly before it is critical point dried. Nanostrip is chosen over piranha solution since the latter bubbles violently, which can easily destroy the devices. The turbulence shielding holder was designed to completely drain all previous liquids in order to avoid introducing acids into the CPD system or unwanted liquids in later solutions.

Because of the pendulum geometry’s “floppy” geometry, the smallest width tether we could feasibly fabricate was $\approx 150\text{ nm}$, as seen in Figure 2.4(b). Figure 2.5 shows an example of 50 nm thick “tri-spoke” suspended membrane which consists of a $20\mu\text{m}$ -diameter disk attached to the substrate by three 50 nm wide tethers with “kinked” geometries. Because of the additional tethers

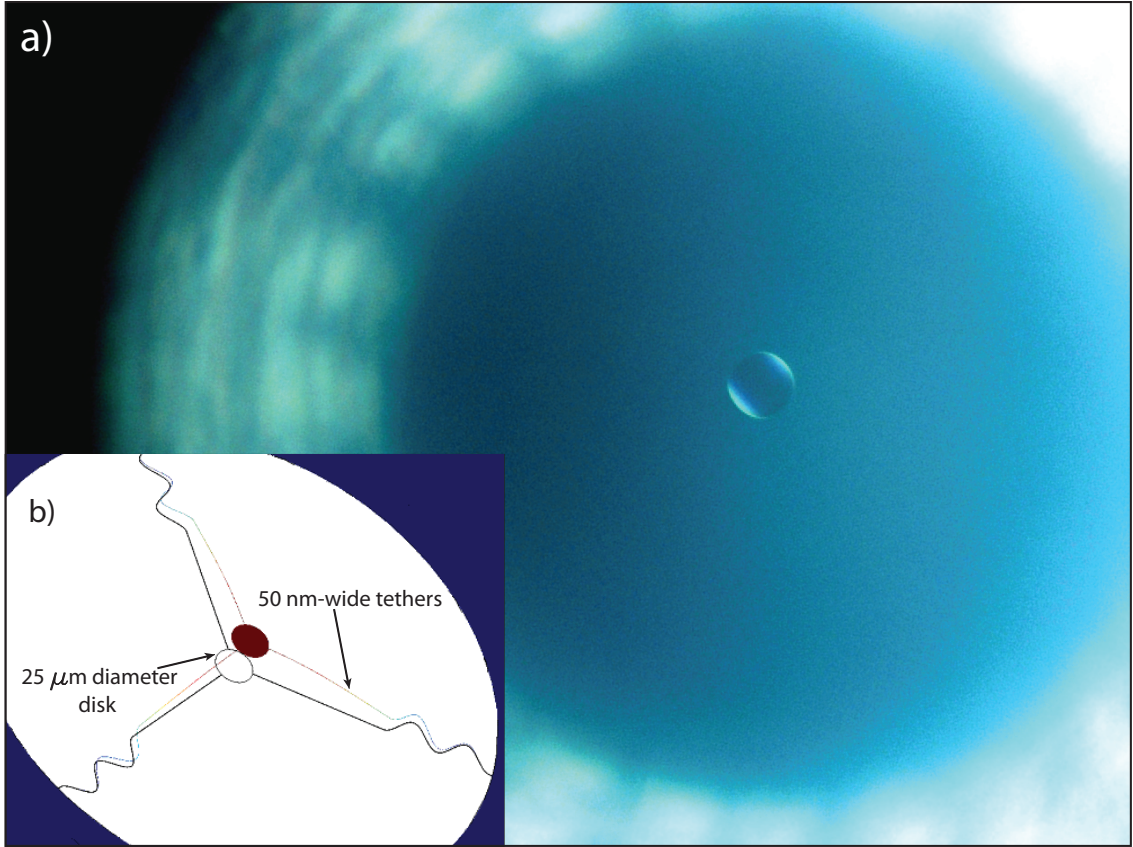


Figure 2.5: **Low-Frequency Disk with Ultra-Small Tethers.** (a): Microscope image of the suspended disk which has been undercut and released using a KOH wet-etch. The 50 nm wide tethers are so thin they become difficult to image. (b): Shows a COMSOL image of the suspended tethered structure’s CM mode motion. The “tri-spoke” structure is fabricated from 50 nm thick Si_3N_4 and extremely small tethers ≈ 50 nm wide, attached to a 20 μm diameter disk.

this structure was more robust and allowed us to push the limits of tether widths down to 50 nm (Figure 2.5(b)). The structure shown in Figure 2.5(c) is so weakly clamped to the substrate that we needed a plastic wind-shield around the microscope stage in order to reduce its movements due to small air currents in the room. The turbulence-shielding gives us the ability to undercut and suspend such fragile structures in bubbling KOH for ≈ 2 hours, rinse the sample thoroughly of KOH, clean the sample in a hot acid, and thoroughly rinse again followed by a CPD dry.

2.1.2 “Floating” Substrate for High Q_m Optomechanics

Generally the nanomechanics community has recognized the role of resonator size, substrate size, and design of mechanical attachments in mechanical dissipation. In the case of square silicon nitride membranes, it was found that the way a chip is mounted in an experimental setup, like a monolithic optical cavity or mirror, can have a detrimental effect on the membrane mechanics [22]. When

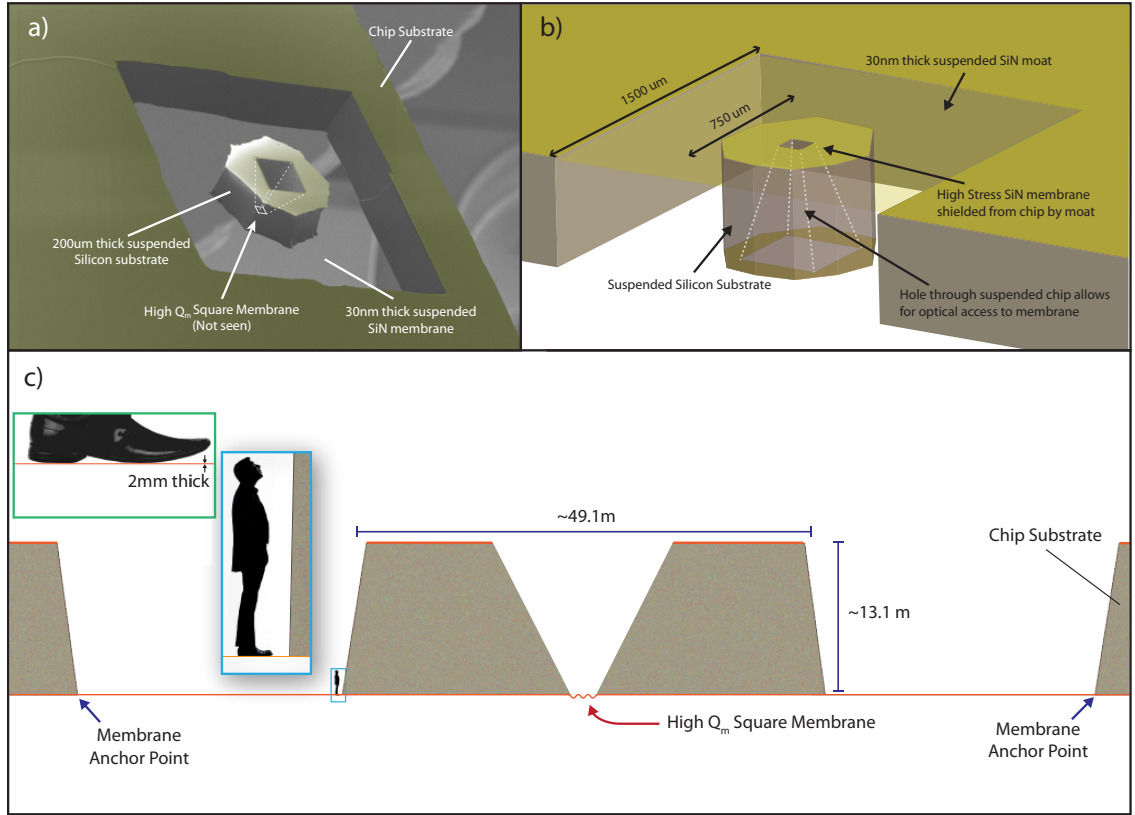


Figure 2.6: **Suspended Substrates.** (a): Colorized SEM image of chip substrate with 30 nm thick membrane holding up ($800\mu\text{m} \times 800\mu\text{m}$, $200\mu\text{m}$ thick) which itself has a small square membrane. The surrounding membrane can experience large torque and viscous forces during fabrication. (b): Illustration showing the general geometry of the suspended substrate and small high stress square membrane. (c): Cross-section view of the device shows that the surrounding support membrane and small high Q_m membrane are fabricated from the same layer. In order to demonstrate the aspect ratios involved, we scale up the device to compare to an average sized human. 30 nm thick membrane holding up a $200\mu\text{m}$ thick substrate is equivalent in size to having a 13.3m tall, 3-4 story mansion held up by a film only 2mm thick).

characterizing different membranes' mechanical quality factors, it was found that depending on the method used to secure the substrate to the setup (clamp, variations of gluing), one would see significantly decreased mechanical quality factors for lower order modes compared to higher order modes. This effect was carefully investigated in [22]. One way to mitigate the effects of substrate mounting on our resonators was to fabricate the membrane resonators on its own small "floating" substrate of silicon that was itself minimally suspended from rest of the silicon chip (Figure 2.6). We wet-etched a $20\mu\text{m} \times 20\mu\text{m} \times 30\text{nm}$ thick silicon nitride membrane into small suspended silicon substrate ($800\mu\text{m} \times 800\mu\text{m} \times 200\mu\text{m}$ thick). This suspended silicon substrate hangs from a $1.5\text{mm} \times 1.5\text{mm}$ sheet of 30nm thick silicon nitride attached to the main chip. The supporting and the membrane resonator are made from the same layer 30nm thick layer of silicon nitride. It is known

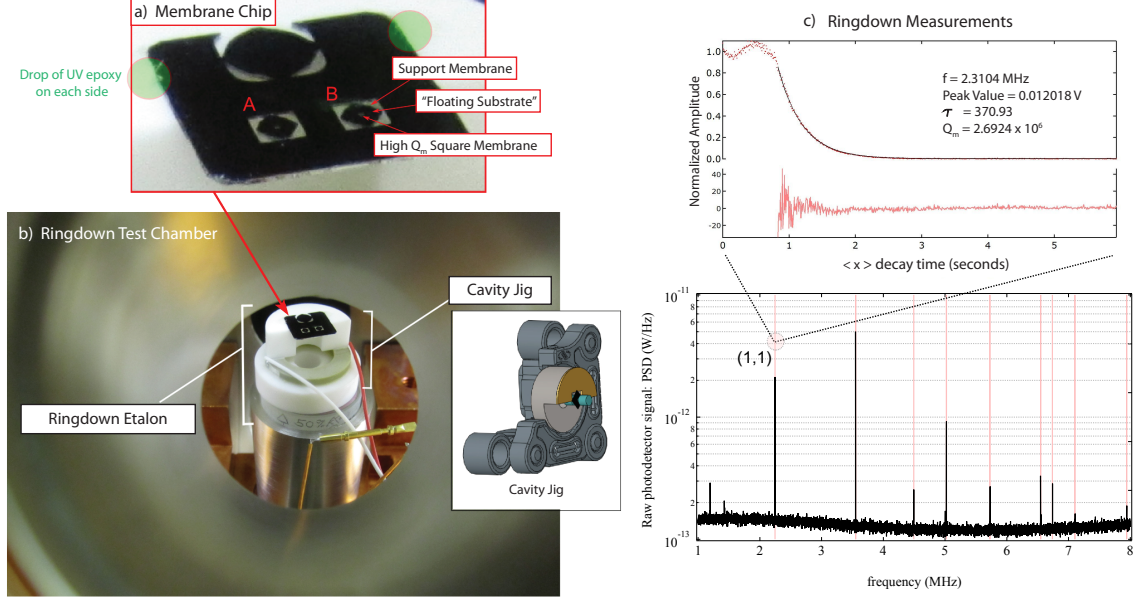


Figure 2.7: **Suspended Substrates Measurements.** (a): Photograph shows a close-up image of the 1×1 cm chip with 2 “floating substrates” suspended by a 50 nm thick Si_3N_4 membrane. Each of these floating substrates ($200 \mu\text{m}$ thick) has a $180 \times 180 \mu\text{m}$ high Q_m membrane. (b): Shows the chip attached to a cavity jig for characterization. (c): Shows the thermal noise spectrum of membrane “A” with ringdown measurements for the (1,1) mode $Q_m \approx 2 \times 10^6$. (Figure courtesy of Dalziel Wilson)

that high mechanical quality factors in membrane resonators come from high tensile stresses in the film that arise from the mismatch in thermal expansion coefficients of Si and Si_3N_4 when deposited at high temperatures and then cooled to room temperature. This chip architecture allows one to isolate the resonator from the rest of the chip without sacrificing the high tensile stresses formed by directly clamping to a silicon substrate. Characterization of Q_m on several membranes with GHz center-of-mass modes showed that without the isolation sheet of Si_3N_4 , the membrane resonators have quality factors that deteriorate when the chips were glued or clamped down to a mirror, resulting in $Q_m \approx 10^5$. When the same resonators were fabricated on a suspended substrate and similarly mounted, we measured $Q_m \approx 10^6$. Figure 2.7 shows measurements results of a “floating substrate” geometry. Figure 2.7(a) shows an image of the 1×1 cm chip with two structures similar to the ones in Figure 2.6(a). In this figure we also show the thermal noise spectrum of membrane A on the chip and ringdown measurements of the small membranes (1,1) mode with a frequency of 2.31 MHz and a $Q_m \approx 2 \times 10^6$. We use the turbulence-shielding techniques to fabricate this type of high-aspect ratio device. In order to demonstrate the extreme scales involved in having a 30nm thick Si_3N_4 membrane suspend a $200 \mu\text{m}$ thick Si substrate, Figure 2.6(c) shows the side profile of the Si_3N_4 sheet holding up a large silicon substrate. Figure 2.6(c) shows that if the silicon substrate were scaled up to the size of an average 13.3 m tall mansion, the membrane holding up the mansion

would be 2mm thick. In Figure 2.6(c) we show a human for scale next to such a block of silicon. At these scales, releasing such a structure using traditional handling techniques would not be possible. With the conventional handling shown in Figure 2.1, the large displacements caused by having such a large mass attached to a thin membrane coupled with their large surface area put an intolerable amount of strain on the supporting Si_3N_4 membrane sheet. If the chip was moved slightly through the liquids the flow across this fragile structure would easily rip the floating substrates from the rest of the chip. The turbulence-shielding techniques reduce the structure’s exposure to liquid flows when the chip is being handled during processing.

2.1.3 Atom-Trap Nanostring Fabrication

The Si_3N_4 nanostring cavity structures for atom-light coupling (discussed in Chapter 3) are 2mm-long optical waveguides with an average width of $\approx 500\text{nm}$. This extreme aspect-ratio nanostring was attached to the substrate with extremely thin tethers (62 microns long with a cross-section of $100 \times 200\text{ nm}$). In Figure 3.19 we show an overview of the nanostring fabrication process. In this chapter we focus on the last step of Figure 3.19 in which the nanostrings are undercut with KOH and wet-released. The structure was made even more difficult to fabricate by the need to have a large $1.5 \times 3\text{ mm}$ optical access window through the chip for shuttling cold atoms to the waveguides. This large opening caused increased flow through the chip making the delicate nanostrings very susceptible to small viscous perturbations. KOH (or TMAH) wet-etch was *required* to fabricate this type of waveguide because it was coupled with an 780-HP optical-fiber which sat firmly inside KOH-defined V-grooves. The turbulence-shielding made it possible to fabricate such delicate weakly-clamped high-aspect-ratio structures by eliminating the nanostring’s exposure to turbulence throughout the entire wet-release process. Using these techniques we were not only able to reliably fabricate the free-standing nanostrings, but even incorporate “double-beam” designs as seen in Figure 3.18(b-d). Structures such as these had to be wet-processed while keeping the closely spaced parallel beams from touching and sticking to one another with only hundreds of nanometers of separation over hundreds of microns. We found this type of structure to be impossible to fabricate using hand-held conventional methods which would typically result in broken devices or double-beam structures stuck to one another via van der Waal Forces.

This structure was also challenging because of the level of precision and accuracy required in etching through the entire silicon substrate. The KOH etch needed to be highly calibrated such that flow and temperature gradient variations were minimized, allowing us to etch through the entire chip in the same amount of time. This timing was important because the V-grooves needed to be wet etched for a certain amount of time, which gave the correct sized V-groove for optimal fiber alignment to the device as shown in Figure 3.8. Over-etching for minutes too long would cause the V-groove to be over-etched and result in major misalignment of the optical fiber to the waveguide

coupler as seen in Figure 3.22. The turbulence-shieldings ability to reduce flows through the chip not only helped fabricate fragile structures, but also kept the flows from giving us inconsistent KOH silicon etch rates throughout the ≈ 2 hour wet-etch. These fiber-coupled nanostrings are a perfect example of the type of devices, which the turbulence-shielding is designed for. These are large-aspect ratio devices require TS fabrication in order to maintain incredibly small optical gaps between two very large and flimsy components. This also holds true for devices such as accelerometers of the type seen in [44] which incorporate large, weakly-clamped masses which modulate extremely small optical gaps.

2.1.4 Discussion

We demonstrated the extreme high-aspect-ratio devices possible with our turbulence-shielding techniques to realize state-of-the-art nanostructures which push the limits of feasible nanofabrication. By removing the element of human error in handling, we have been able to create structures which would previously be near-impossible due to their high susceptibility to incredibly small forces inherent to conventional fabrication handling. Instead of a sample being dipped and transferred from solution to solution, the chip essentially remains unperturbed as it is slowly diluted from one solution to the next. This allows us to fabricate delicate devices through several liquid solutions to end with a critical point dry and produce a final nanostructure without ever exposing it to surface tensions anywhere in the process. By enclosing the samples in our holder we also eliminate several sources of turbulence which are certainly destructive to our devices. Turbulence-shielding joins the benefits of extremely delicate etching normally reserved for dry-released structures with the benefits of wet-etchants.

Chapter 3

Nanowire Photonic Crystal Waveguide for Atom-Photon Interactions

3.1 Motivation for On-Chip Nanowire Trapping

There has been a considerable amount of scientific effort towards achieving strong interaction between light and single atoms in an integrated system. A well known avenue for such interactions has been the utilization of cavity quantum electrodynamics in which the atom-photon interactions are enhanced in micro- and nanoscale optical cavities ([45] [46] [47] [25] [48]). Recently groups have worked towards this enhanced atom-light interactions using nanoscale dielectric waveguides where the effective area of the guided mode can be comparable to atomic radiative cross sections leading to complex photon transport in 1-D ([49] [50] [51] [52] [1] [53]). 1-D and 2-D photonic crystals fabricated from planar dielectrics offer a configurable platform for engineering strong atom-light interactions for single atoms and photons with a extensive ability to lithographically engineer structures which progressively enhance this coupling. While several groups have been able to integrate fiber-Bragg-gratings (FBG) into tapered nanofibers ([50] [51]) to form nanostring cavities for trapping and probing atoms, the integrated mirrors (typically FBGs) are typically produced using focused-ion-beams to mill corrugated structures into the fiber. The FBGs are typically milled into the optical fiber using a focused-ion-beam (FIB), which produces rough edges, and deposits by-products from the milling process onto the fiber producing mirrors which can suffer from many losses. Tapered fibers are formed using “taper-pulling techniques” in which optical fibers are heated and pulled into a thin tapered nanofiber. Fiber-pulling techniques, while well-established, are also limited to producing single thin tapered-nanofibers. Producing an atom-light coupling structure on-chip using lithographic methods offers the ability to produce a vast array of geometric designs (in our case we are able to engineer a double-beam system to enhance atom-light coupling). Photonic crystal

mirrors produced using well-known clean-room techniques result in mirrors which are high quality, and easily tunable to match with atomic transitions. The ability to engineer every aspect of these nanostrings with high quality and accuracy makes them a promising tool for dispersion-engineered photonic crystal waveguides which permit the trapping and probing of ultracold neutral atoms with equivalent spatial periodicity for both trap and probe optical fields that have disperse free-space wavelengths. Such a system can lead to atom-atom interactions efficiently mediated by photons within the waveguide ([54] [55] [56]). In photonic crystal waveguide, atom-photon coupling can be enhanced near the band-edge via slow-light effects ([57] [58]) and can be tailored to explore quantum many-body physics with atom-atom interactions that can be readily engineered. In this chapter we give a detailed overview of the significant technical challenges that exist for developing hybrid atom-photonic systems arising from the following requirements: (1) the fabrication is sufficiently precise *and* robust to match waveguide photonics properties to atomic spectral lines, (2) atoms are stably trapped in the presence of substantial Casimir-Polder forces yet achieve strong atom-light interactions, (3) coupling to and from guided modes of the nano-photonic elements is efficient, (4) sufficient optical access exits for external laser cooling and trapping, and (5) optical absorption is low and the net device thermal conductivity is high, permitting optical power handling to support ≈ 1 mK trap depths.

3.2 Design of Nanowire Structures

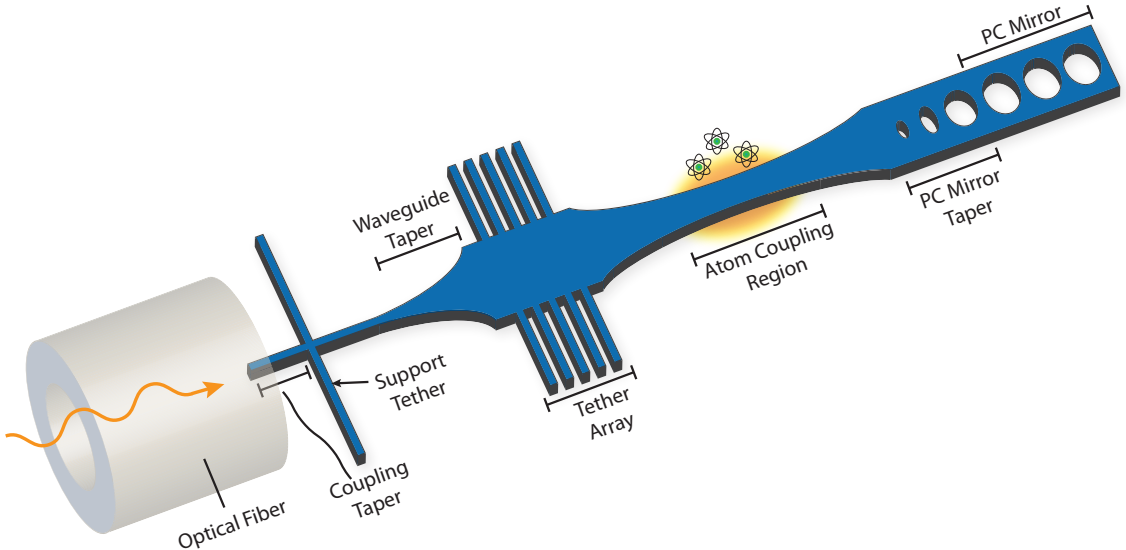


Figure 3.1: **General Nanostring Trap Structure.**

In this section we will give a comprehensive overview of the general suspended nanostring system

for atom-light coupling as shown in Figure 3.1. First we will cover the mode-matching required to achieve efficient coupling from the optical fiber into the nanostring waveguide. We then consider the design of the support tether which keeps the waveguide aligned with the center of the optical fiber. We will then review the adiabatic transitions from a small waveguide to a large width such that losses are minimized. This is followed by an overview of our tether array design which is used for structural support and thermal conduction to the substrate. We will then discuss the design of the adiabatic transition to a thin atom-coupling region of the waveguide where the evanescent field of the trap beam interacts with the Cs atoms. After this we will discuss the design of the photonic mirrors in our structure and then their design evolution.

3.2.1 Fiber Coupling and Overlap Integrals

One of the goals of this project was to engineer an integrated atom-light interaction system wherein one could efficiently couple light into the device using standard optical fibers placed onto a chip. This type of fiber coupling would allow for easy integration of the atom-light photonic crystal systems to larger optical networks [59]. One method for doing this was developed for optical coupling to optomechanical cavities in efforts to achieve quantum-limited motion transduction [2] where efficient coupling and collection of light was crucial. In order to design the waveguide with the dimensions required to optimize the coupling efficiency we simulated the guided transverse modes of the waveguide and the optical fiber (780-HP) at 852 nm wavelength with an FEM solver. Using these mode profiles from the simulation we can calculate the coupling efficiency from the optical fiber into the waveguide using the mode overlap integral,

$$\eta_{\text{overlap}} = \text{Re} \left[\frac{\int \mathbf{E}_1 \times \mathbf{H}_2^* \cdot d\mathbf{S} \int \mathbf{E}_2 \times \mathbf{H}_1^* \cdot d\mathbf{S}}{\int \mathbf{E}_1 \times \mathbf{H}_1^* \cdot d\mathbf{S} \int \mathbf{E}_2 \times \mathbf{H}_2^* \cdot d\mathbf{S}} \right] \quad (3.1)$$

where 852 nm wavelength laser light is chosen to coincide with the Cesium atom D_2 transition at 852.34727582(27) nm. This sub-telecommunications wavelength also requires small fiber-optic cables with significantly smaller outgoing mode diameters (5 μm diameter mode for 780-HP). A priori we use 200 nm thick Si_3N_4 layer to fabricate our 852 nm devices and so our simulations assume a set thickness for the entire waveguide of 200 nm. Any optimizations to the waveguide are made by varying the width of the waveguide (in the direction of the light's E field polarization). If the cross-section of the waveguide is sufficiently large, the mode will be well confined within the dielectric with a small evanescent field while decreasing the size of the width of the waveguide will result in a mode which is not well confined and consists of a large evanescent field surrounding the thin waveguide. In order to have a high coupling efficiency, the tip of the waveguide (waveguide coupler) needs to be thin in order to have a large evanescent field mode profile that overlaps well with the 5 μm diameter mode from the 780-HP optical fiber, as shown in Figure 3.2(a). We optimize the

coupler tip by simulating the transmission efficiency vs waveguide coupler tip width, as shown in Figure 3.2(b). We find the highest transmission efficiency of $\approx 90\%$ for a waveguide-tip width of 130 nm. It is important to note the precision required in fabricating a 130 nm waveguide coupling

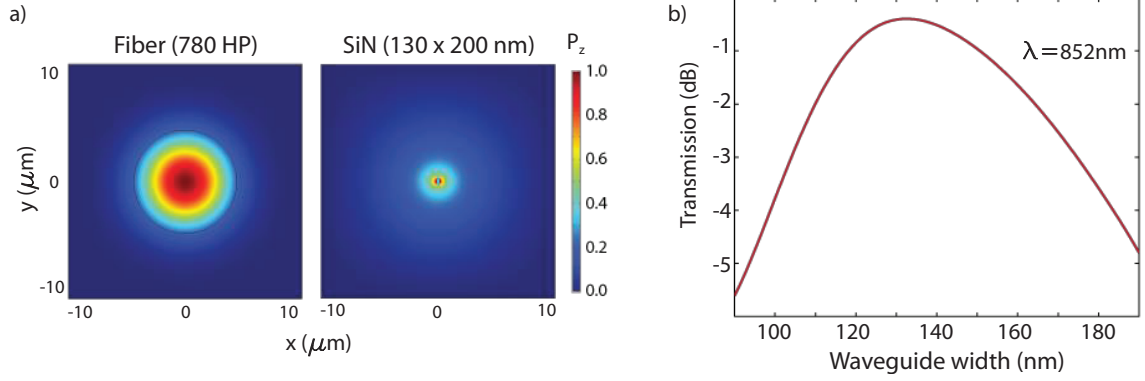


Figure 3.2: **Fiber Coupling to Waveguide.** (a): Finite-Element-Method plots of optical mode profile for mode from the fiber (left) and coupler tip of the waveguide (right). (b): Finite-difference time-domain plot of transmission of 852 nm light into the waveguide vs width of the waveguide coupler tip. (Courtesy of Seán Meenehan)

tip where a deviation of 10nm in the width can cause 0.5 dB in transmission efficiency. Because the 852 nm light used in this experiment we use 780-HP fiber which has a smaller diameter core and a smaller mode diameter than most C-band telecom wavelength fiber cables (1530-1565 nm). To achieve high coupling rates we must align the waveguide to the center of the fiber core with higher precision than that required for aligning to telecom wavelength optical fibers.

3.2.2 Simulations of Adiabatic Condition in Waveguides

In this section we describe the adiabatically transition from 130 nm-wide waveguide coupling tip to regions of the waveguide that require larger widths (i.e. tether array, photonic crystal, etc.). We use a finite-element-method solver, COMSOL, to simulate the mode profiles and effective refractive indices of different waveguide cross sections. Given a 2-D cross-section, we simulate a waveguide with infinite length. If the waveguide has a large cross section (Figure 3.3(a)) then the guided mode will be well confined within the silicon nitride with refractive index $n = 2$. Because the refractive index of air is $n_{\text{air}} = 1$ and the mode is confined mostly within the $n = 2$ dielectric, we expect the effective refractive index to be between 1 and 2. For the $500 \text{ nm} \times 200 \text{ nm}$ cross-section waveguide the effective index is simulated to be $n_{\text{eff}} = 1.43$. When the waveguide is designed with a small cross section (Figure 3.3(b)) the guided mode is composed of a large evanescent field surrounding the waveguide. Because most of the guided mode resides in the air surrounding the fiber the effective index is approximately $n_{\text{eff}} \approx 1$. As the waveguide widens from a narrow single-mode region into a larger multi-mode portion of the waveguide, there can be mixing of the fundamental guided

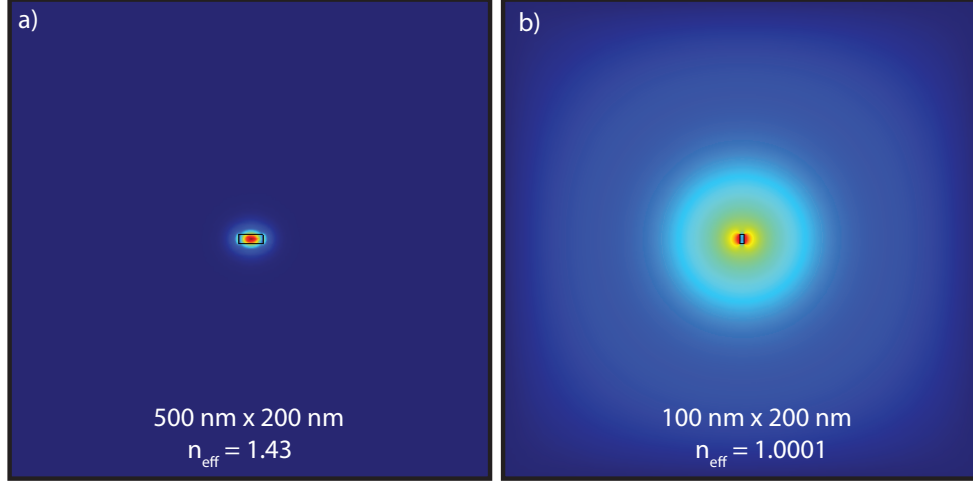


Figure 3.3: **Waveguide Mode Profiles.** Finite-element-method (COMSOL) simulated mode profile for Si_3N_4 waveguide with (a): width of 500 nm and height of 200 nm. The effective refractive index is $n_{\text{eff}} = 1.43$ since optical mode resides mostly in the dielectric with refractive index $n = 2$ (b): width of 100nm and height of 200nm. The effective refractive index is $n_{\text{eff}} \approx 1$.

mode with the higher order modes (radiation modes) in the multi-mode regions. To minimize the transmission loss due to the radiation field coupling, we use a adiabatic tapering in the waveguide width which very gradually tapers the width of the waveguide from a small to large width waveguide (and vice versa). To characterize whether our waveguide's tapering region transitions slowly enough to make radiation losses small, we use the adiabatic condition expressed as

$$\frac{dw}{dz} \ll |n_{\text{eff},1} - n_{\text{eff,rad}}| \approx |n_{\text{eff},1} - 1| \quad (3.2)$$

where w is the width of the waveguide, z is the direction which the waveguide runs along, and $n_{\text{eff},1}$ and $n_{\text{eff,rad}}$ are the effective refractive indices of the fundamental mode and the higher-order radiation modes. The condition asserts that one can minimize radiation losses to the fundamental guided mode if the change in width of the waveguide along its axis in z changes much slower than the difference in effective refractive index of the fundamental mode and higher order radiation modes. We assume that radiation modes are usually guided in air and have $n_{\text{rad}} \approx 1$. This is a condition which we try to meet along the entirety of the waveguide between adjacent infinitesimal slices (Figure 3.4(a)). If the transition is made over a short distance of waveguide, the shape of the tapering has a more dramatic effect on the radiation losses, but if the distance over which the adiabatic transition is made are long, we see that the function characterizing the shape of the waveguide transition matters less, as shown in Figure 3.4(b) where linear, quadratic, cubic and quartic functions are simulated with different waveguide lengths. We use finite-difference time-domain (FDTD) software Lumerical to accurately calculate the radiation losses as the fundamental guided mode propagates through the

Si_3N_4 waveguide. Simulations find that by using a cubic tapering over a $200\ \mu\text{m}$ waveguide, we can

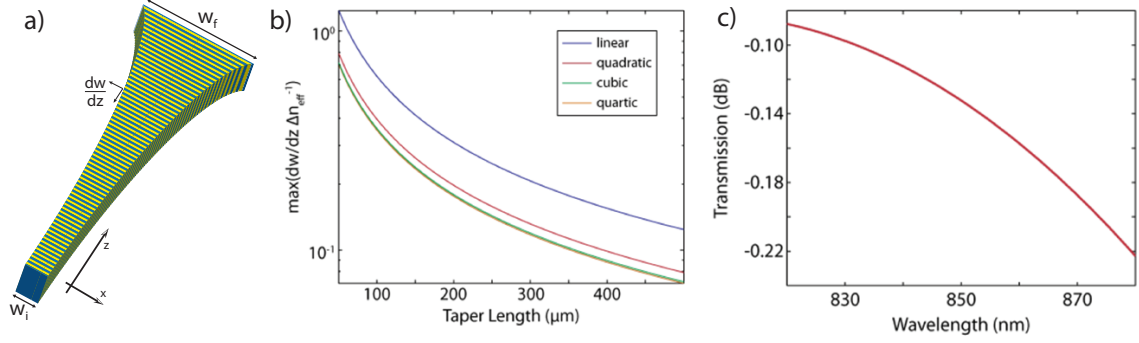


Figure 3.4: **Waveguide Tapering Design.** (a): Illustration of the section of waveguide which increases width from w_i to w_f along z . (b): Plot of simulated $w'(z)/\Delta n_{\text{eff}}$ for different taper shape functions vs waveguide taper length. (c): Plot showing sensitivity of design in the wavelength of incoming light using a quadratic function designed for 852 nm. (Plots courtesy of Seán Meenehan)

achieve transmission of 97% of 852 nm light. The shortest transition in our design happens between the waveguide coupling tip and the first support tether. One would like to design the tapering from the width at the waveguide coupling tip to the largest possible width at the tether without inducing severe radiation losses. Because the support tether fully extends in the x direction in order to clamp to the substrate, it introduces a suddenly large dw/dz . One would like to have the largest width waveguide at the support tether which well-confines the mode in the dielectric such that only a small portion (small evanescent field) experiences the sudden change from the tethers. Because waveguides with small widths have large evanescent fields and $n_{\text{eff}} \approx 1$, the tapering conditions are more stringent in thin waveguides with dw/dz needing to be extremely small to avoid large transmission losses. Because of fabrication considerations, the distance between the waveguide coupling tip and tether is $5\ \mu\text{m}$ (larger distances effectively make the waveguide coupling tip into a long cantilever with considerable deflection from stress in the Si_3N_4 which misalign it from the center of the fiber core). This limited distance also limits the width of the waveguide we can adiabatically taper up to at the tether. This makes the support tether one of the largest sources of transmission loss. This loss can be mitigated by fabricating an increasingly thinner support tether. Lumerical simulations show that with a 80nm wide tether we can achieve transmission through the support tether of $\approx 90\%$. Past the first tether the waveguide width is adiabatically increased to a region of the waveguide with an array of tethers where the width is $\approx 1\ \mu\text{m}$. The array of tethers have two functions which are (i) structural support for the nanostring and (ii) a channel for thermal conduction from nanostring to substrate. The $1\ \mu\text{m}$ wide waveguide ensures that the guided mode is well confined in the dielectric and minimally sees the changes in n_{eff} resulting from the array of tethers. Even with a $1\ \mu\text{m}$ wide waveguide there still exists a small evanescent field which overlaps the array of tethers. Losses occurring from this can be mitigated by choosing the width and spacing of the tethers in the

array. Chosen appropriately, the array of tethers can act as a photonic crystal which increases the transmission of the 852 nm evanescent field, resulting in 98% simulated transmission through this region.

3.2.3 Single-Waveguide Atom-Coupling Region

Similar to recent experiments where atoms were coupled via the evanescent fields of a thin tapered optical fiber ([49] [1]), we designed our initial experiments with a single tapered beam. While these experiments relied on efficient coupling of light to atoms using a one-way pass of the light, we intended on surrounding our atom-coupling tapered waveguide with photonic crystal (PC) mirrors to form a cavity which would enhance atom-light interactions, achieving several passes of the light through the atoms with the circulating light formed inside the cavity. A similar version of this consisted of a tapered optical fiber with integrated fiber Bragg gratings to form a cavity [50]. We designed the tapered beam with the optimal width for coupling to the atoms. The performance of the cavity with respect to atom-light coupling is governed by the parameters g/κ and g/γ , where g denotes the atom-light coupling strength, 2κ is the cavity photon decay rate, and 2γ is the free-space spontaneous emission rate of the atom. We know that to observe coherent dynamics we should meet the condition

$$g \gg \kappa \quad \text{and} \quad g \gg \gamma \quad (3.3)$$

which are conditions that can also be expressed with a weaker condition involving cooperativity,

$$C = \frac{g^2}{2\kappa\gamma} = \frac{3\epsilon_0\zeta_0^2 F}{\hbar\beta^3\Delta\nu_{\text{FSR}}} \gg 1 \quad (3.4)$$

where C is cooperativity which given a two-level atom can be described using properties of the cavity where β is the propagation constant of the mode, ζ_0 is the field per photon at the position of the atom, F is the optical cavity finesse, and $\Delta\nu_{\text{FSR}}$ is the optical cavity's free spectral range. We use an FEM solver to simulate different cross sections from 100-400 nm widths, given a thickness of 200nm and calculate cooperativities given a cavity length of $L_{\text{cav}} = 500\mu\text{m}$ and cavity finesse of $F = 100$ which are plotted in Figure 3.5. If the waveguide is too wide, the evanescent field will be small resulting in poor mode overlap with the atoms. It requires the atoms to be excessively close to the surface of the dielectric (to couple with the evanescent field) where Casimir-Polder forces become dominant. If the waveguide is small, the evanescent field will be large but the mode volume will also be large, reducing the coupling with the atoms. At the top of Figure 3.5 we see a mode profile for the TE and TM modes of the optimal cross-section with dimension 300×200 nm, which is optimal for atoms 100-200 nm from the waveguide.

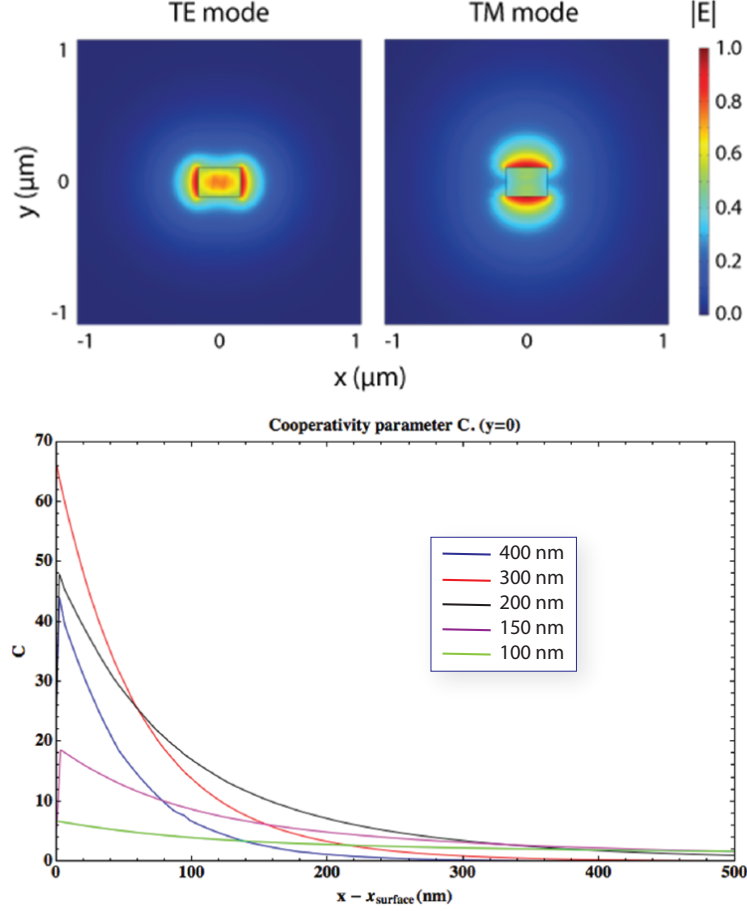


Figure 3.5: **Optimizing Cooperativity.** (Top): Shows the TE and TM modes for a 300×200 nm cross section. (Bottom): Plot of cooperativities as a function of distance from the waveguide's surface for difference waveguide widths. (Plots courtesy of Daniel Alton)

3.2.3.1 Tapering Effect on Cavity Properties

In order to test the losses incurred in a cavity due to the tapered region between the photonic crystal mirrors we fabricated a series of cavities from the 200 nm thick Si_3N_4 on Si. The nanostring cavity was patterned onto the silicon nitride substrate using electron-beam-lithography and $\text{C}_4\text{F}_8/\text{SF}_6$ plasma etch the cavities from the silicon nitride layer. A short KOH wet etch was used to undercut the samples with a $5 \mu\text{m}$ wide trench (open area) surrounding the nanostring. As a final step the sample was cleaned using an aggressive piranha solution to clean off contamination on the surface. As shown in Figure 3.6(a) the cavities consist of two photonic crystal mirrors which surround the tapered waveguide region with a cubic shape. The width of the tapered waveguide was varied from 893 nm to 193 nm in order to see the effects on cavity performance. We used 1550 nm light through a “dimpled” glass fiber to evanescently couple to the nanostring cavity (dimple set near region between mirror and tapered waveguide region where dielectric overlap is maximized).

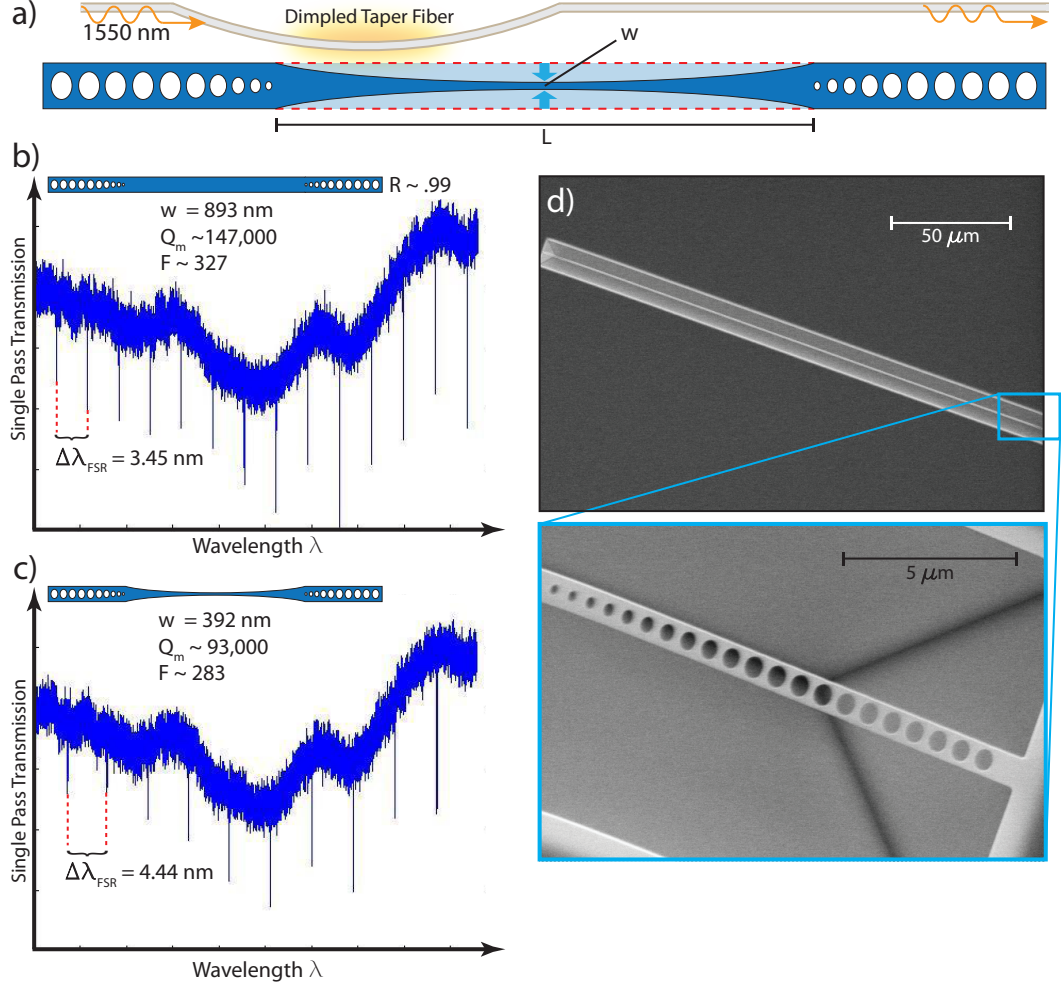


Figure 3.6: **Tapering Effects on Photonic Crystal Cavity.** (a): Schematic of the dimpled taper fiber coupling 1550 nm light to tapered nanosttring cavity. We tested a series of devices with identical mirrors while varying the tapered waveguide's center width w . (b): Transmission spectra after coupling with PC cavity with $w = 893$ nm. (c): Transmission spectra after coupling with PC cavity with $w = 392$ nm. (d): SEM image of initial doubly clamped devices. Close up shows mirrors at the end.

The transmission signal was collected through an erbium-doped fiber amplifier (EDFA) followed by a high-speed photodetector connected to a real-time spectrum analyzer (Figure 3.6(b)(c)). Here, because of the long cavity lengths, we see a series of cavity resonances. As expected we find that the untapered beam ($w = 893$ nm) has a larger free spectral range (FSR) than the tapered beam since the FSR (in wavelength) can be expressed as

$$FSR = \frac{\lambda^2}{2 \int_0^L n_{\text{eff}}(s) ds} \quad (3.5)$$

where λ is the wavelength of the light residing in the cavity and $\int_0^L n(s)ds$ is the optical path length (OPL) for varying waveguide width (i.e., varying n_{eff}) along the length of the fiber s . Because the 893 nm wide nanostring cavity has larger OPL we expect a smaller FSR (Figure 3.7). We found the optical quality factor, Q_o , while higher with a larger width ($w = 893$ nm, $Q_o \approx 147,000$) was not extremely deteriorated at smaller taper width ($w = 393$ nm, $Q_o \approx 93,000$). It is also important to note that optical resonance signals drop dramatically on devices with 300 and 200 nm taper widths. This can be attributed to the small space between the nanostring cavity and the substrate. When the width of the beam becomes small the evanescent field becomes large and overlaps with the surrounding silicon substrate, inducing large optical losses. Because of the minimal losses induced in the $w = 893$ nm nanostring cavity, we can use this device to calculate the PC mirror reflectivities with $R \approx 99\%$ at 1550 nm.

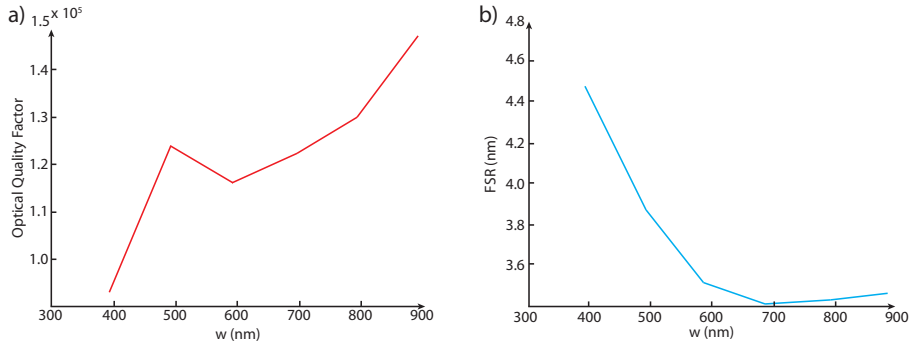


Figure 3.7: **Free Spectral Range and Quality Factors.** (a): Plot of optical quality factors vs taper width w . (b): Plot of Free Spectral Range vs taper width w . Both devices on our chip with $w < 393$ had no resolvable resonance signals due to the large evanescent field coupling to the surrounding silicon substrate and resulting in large optical losses.

3.2.3.2 Single-Mirror Nanostring with Fiber Coupling

One of the earliest fiber-coupled devices we fabricated was a Si_3N_4 nanostring with a single photonic crystal mirror (Figure 3.8). Using such a patterned waveguide we were able to trap cold atoms spatially overlapped with a nanobeam and observe a resonant optical depth of $d_0 \approx 0.15$. In order to construct an on-chip device compatible with atomic and ultra high vacuum (UHV) systems, several unconventional requirements must be met for our on-chip waveguide design. Our chip requires a robust and efficient coupling of light into and out of the waveguide (in UHV environments) from the external laser source and detectors. Another requirement is that the chip itself must be designed so that atoms can be concentrated and cooled in close vicinity of the waveguide to allow them to interact strongly with the evanescent modes. The structure itself must be mechanically robust to withstand the wet etching and aggressive cleaning processes during fabrication. In order to achieve input coupling of light into our waveguide we applied a design that allows for direct coupling of

an optical fiber mode into our waveguide [2]. The waveguide coupling tip is designed to maximize the mode overlap between the fiber mode and waveguide mode. The fiber is self-aligned to the waveguide center by lowering it into a V-shaped groove (“V-groove”) aligned to the waveguide (as both are defined with the same electron beam lithography step). As seen in Figure 3.8(b) there are five devices on a single chip with only one device being fiber coupled. The probe light is launched into the waveguide from a cleaved optical fiber (Figure 3.8(c)) sitting (and glued) in the V-groove. The core of the fiber is well-aligned to the waveguide coupling tip using the well-known etching of [1-0-0] silicon with potassium hydroxide (KOH). A single thin tether which clamps to the side of the V-groove acts as a support for the waveguide coupling tip. Such a tether is not robust enough to reliably support the entire ≈ 2 mm long nanostring structure, so the waveguide’s width is adiabatically increased to a tether array (Figure 3.8(d)) used to increase the mechanical stability of the device and as channel for thermal conductivity when the device is heated with optical power. The device then adiabatically tapers hundreds of microns over a large hole, which has been etched through the silicon substrate, meant for optical access to a magneto-optical trap (MOT) beam such that it can cool atoms near the waveguide. A large 1.5×3 mm hole is made through the chip’s silicon substrate using a KOH chemical etch. This hole allows for near 4π Steradian access but makes the chip considerably more fragile. The region of the nanostring with a width ($w = 300$ nm) optimized for coupling of atoms with the guided optical probe field (Figure 3.8(e)) sits centered over the large “through-chip” hole. The guide probe light is reflected by a photonic crystal mirror (Figure 3.8(f)) and back into the fiber mode. The PC mirror is designed to reflect in-plane polarization (TE mode) while allowing TM modes to penetrate through.

3.2.3.3 Overview of Initial Characterization

In this section we’ll give a brief overview of our characterization setup (Figure 3.9) which we used to test the coupling efficiency from the optical fiber to the photonic crystal waveguide and the effectiveness of our PC mirrors in reflecting input light. Our test setup begins with tunable cavity diode Velocity laser source operating from 836-856 nm. This signal is coupled into a 780-HP optical fiber (used to transmit light throughout the setup) sent through an optical attenuator before being sent into Port 1 of the 50:50 fiber-optic beam-splitter. The signal is then split 50:50 into Port 2 and Port 3. The signal from Port 2 is then sent through fiber polarization controllers (FPC) to align the polarization of the light with that of the in-plane linear polarization of the photonic crystal mirrors. The signal is then sent into a 780-HP optical fiber which has been glued into a V-groove of the chip and couples light into our waveguide devices. The light propagates through the waveguide and reflected by photonic crystal mirror in the waveguide and back into Port 2 of the 50:50 splitter and detected at photo-detector PD₁, sent to an optical pre-amplifier, followed by a National Instruments data acquisition system (DAQ). The signal from Port 3 is detected in the

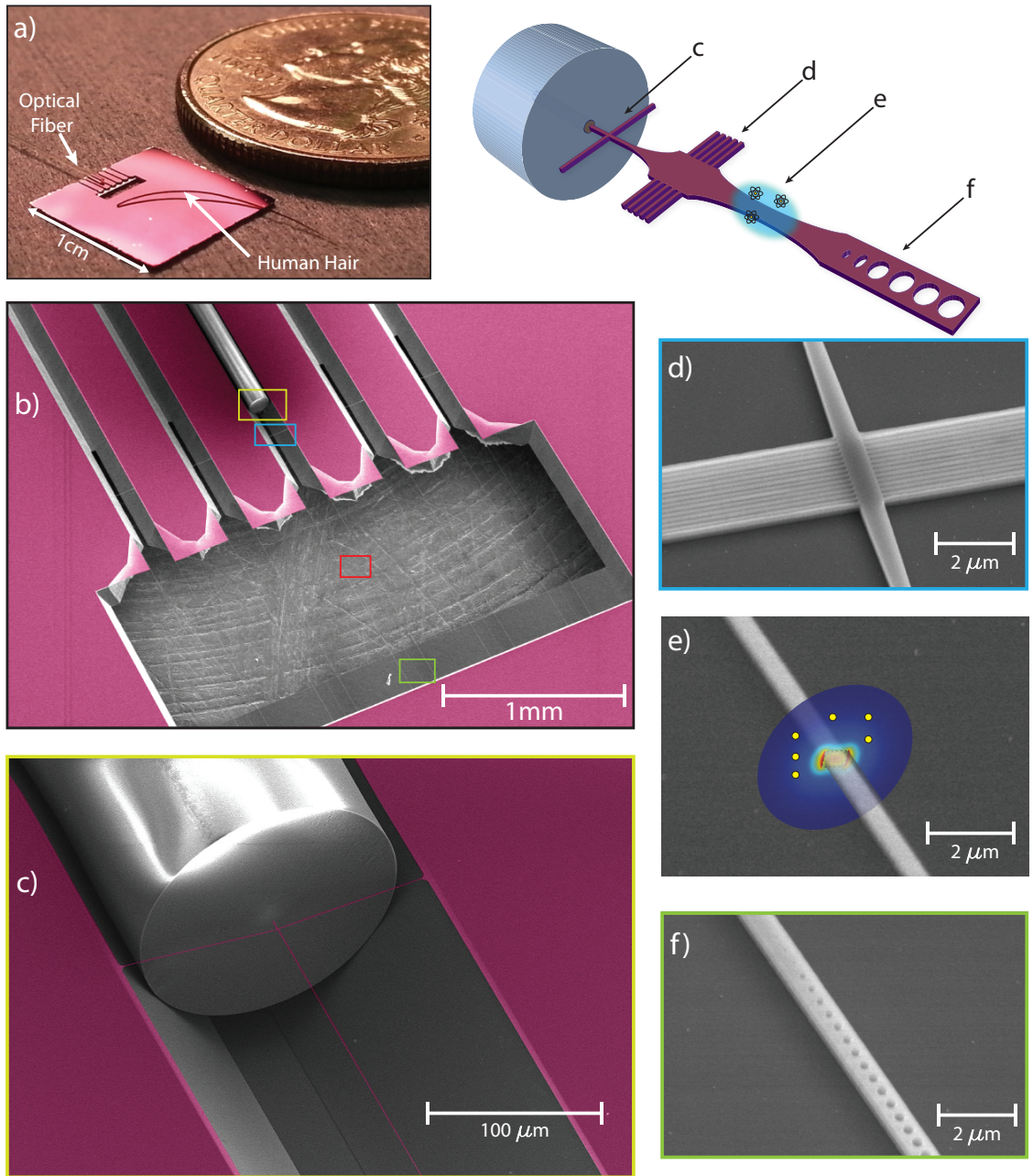


Figure 3.8: **Single-Mirror Nanostrings.** (Top Right): Schematic illustration of a device. (a): Photograph of 1×1 cm chip with large hole through the substrate for MOT access. Shows scale of the chip in comparison to a human hair and U.S. quarter. (b): Colorized SEM image of the large opening through chip and V-grooves where optical fibers are placed. (c): Colorized close-up SEM of the waveguide coupling tip held up by the support tether being aligned to the center of the optical fiber. (d): Close-up SEM of tether array used for mechanical stability and heat-sinking. (e): Close-up SEM of atom-coupling region of the waveguide. (f): Close-up SEM of the photonic crystal mirror.

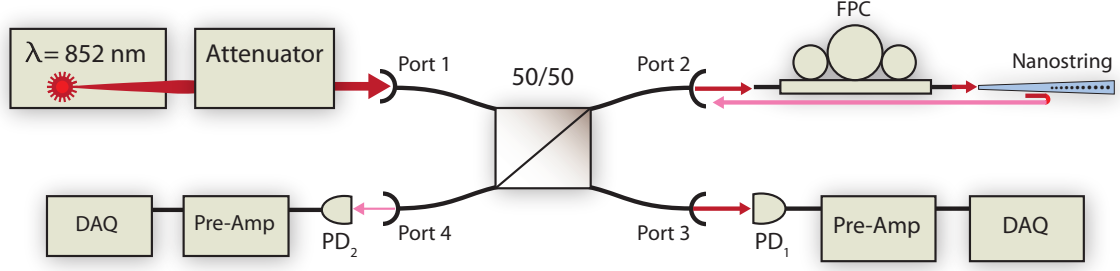


Figure 3.9: **Schematic of Characterization Setup.**

same way as Port 4 and used as a reference power to normalize the reflected signal measured at Port 4. In order to characterize the actual losses from the optical fiber connections in our setup we first replace the fiber-coupled chip with a silver mirror. Because the silver mirror reflects nearly all of the light, we can use it to characterize the losses in our fiber optic setup. The waveguide coupler tip has a weak wavelength dependence which needs to be calibrated separately. Two ways to align the polarization are to maximize the fringe visibility but there is very little sensitivity when maximizing a signal. Simulations of the intensity distribution and polarization of the scattered light from the support tether suggest that we could align to the TM polarization by minimizing the scattered light seen in our CCD camera. From this point we can rotate our half-wave-plate in the FPC by 45° to align with the TE-mode.

3.2.3.4 Measurements of Reflectivity from Single Mirror Devices

The chip we characterized in this section consisted of five “single-mirror” nanostring devices of the type in Figure 3.8 with different lengths ($1700 \mu\text{m}$, $1340 \mu\text{m}$, $980 \mu\text{m}$, $620 \mu\text{m}$, $260 \mu\text{m}$) which are designated D₁-D₅, respectively. Characterization measurements were taken in a positive-pressure environment pumped with high purity nitrogen gas. Instead of gluing five different fibers into the chip’s V-grooves, we simply lifted an optical fiber (connected to the FPC) in and out of the each V-groove using the vertical positioning stage and the x-y stage to move the chip and align different V-grooves to the single input fiber in our measurements setup. A typical reflection spectrum from these devices is shown in Figure 3.12(a). The fringes are ones one would expect to be signatures of a low-finesse cavity that has forms between the highly reflective photonic crystal mirror and the small reflections that occur from a combination of the surface of optical fiber and the single support tether as the reflected light from the photonic crystal propagates back into the fiber. Taking the Fourier transform of the fringes we can extract the total optical path length as shown in Figure 3.12(b). The absorption coefficient is 0.22 per mm (power loss per mm) which is shown in Figure 3.10(b). For D₁-D₂ we have lengths of ($1700 \mu\text{m}$, $1340 \mu\text{m}$, $980 \mu\text{m}$, $620 \mu\text{m}$, $260 \mu\text{m}$) with single pass nanobeam loss of (0.94, 0.86, 0.79, 0.72, 0.66). Since we have varying lengths, we fit the ratio $r_1/r'_1 = 0.43$. The

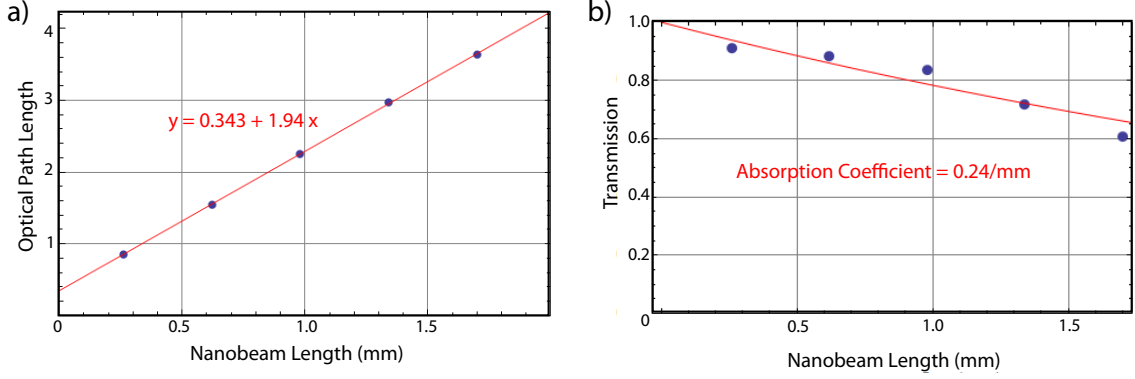


Figure 3.10: **Scan of Nanobeam Length.** (a): Optical Path Length plotted against nanobeam length. The fit gives an effective index of refraction of 1.94 for the nanobeam and total optical path length of $343 \mu\text{m}$ for the section before the nanobeam. (b): Single pass power loss as a function of nanobeam lengths. The absorption coefficient (power loss per unit length) is 0.22 per mm

fitted values for the reflection of the first reflector are $r_1^2 = (0.058, 0.051, 0.059, 0.061, 0.044)$ and the FDTD simulated value is $r_1^2 = 0.07$, as shown in Figure 3.11(a). We also fitted value for $t_1^2 \approx 0.62$ with a simulated $t_1^2 = 0.76$, which can be seen in Figure 3.11(b). But if we take into account the propagation loss along the $225 \mu\text{m}$ initial section, according to the loss coefficient the simulated value would be $t_1^2 = 0.69$.

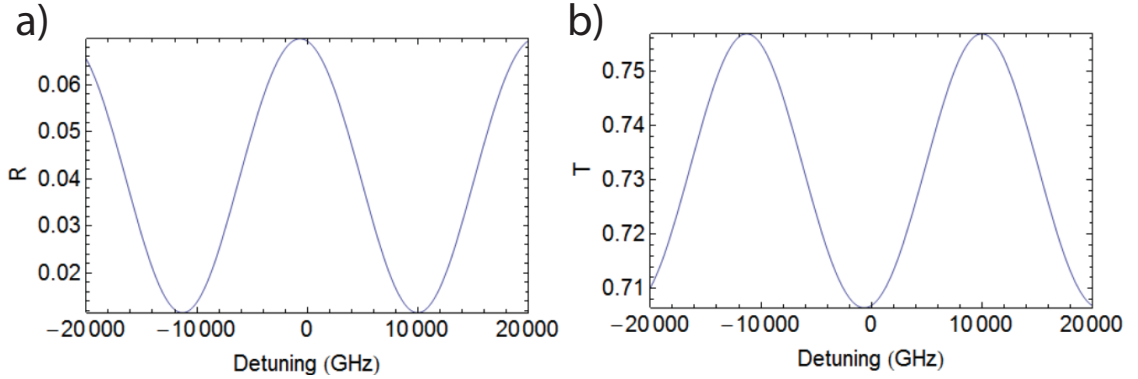


Figure 3.11: **Scan of Nanobeam Length.** (a): FDTD simulated reflection (a) and transmission (b) of the combined fiber-coupling and support tether section as a function of frequency.

3.2.4 Nanostring Chip Inserted into Ultra-High Vacuum Chamber

Here we discuss a number of characterizations of the nanostring photonic crystal waveguide in an ultra-high vacuum system. From the five devices on this chip we used D₂ to perform our measurements. Because of the low thermal dissipation of nanostrings in high vacuum environments they were very susceptible to thermal fracturing when coupled with a high optical powers. Using

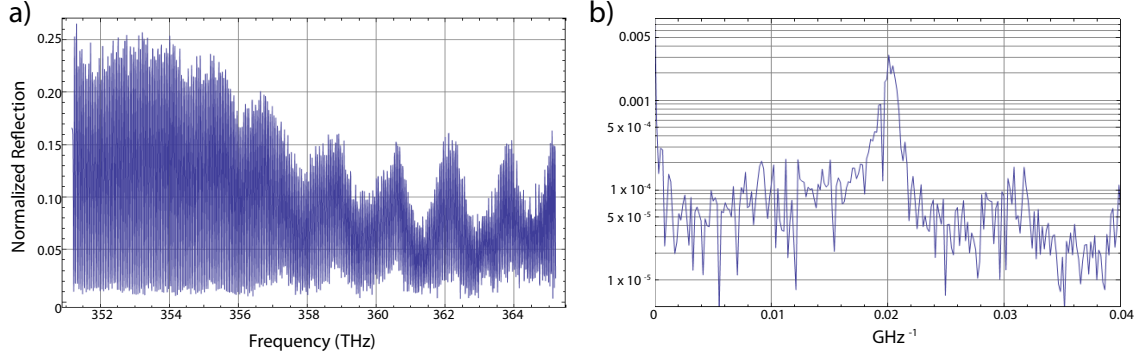


Figure 3.12: **Reflection Signal from PC Nanostings.** (a): D_2 fringe signal in vacuum. (b): Fourier-transformed spectrum of the fringe data (a) to extract the total optical path length.

a reflection setup in vacuum, we got normalized reflection spectra from D_2 , seen in Figure 3.12, which has a 50 GHz fringe, modulated by a 30 THz due to very short low-finesse cavity made between the optical fiber and the support tether on the waveguide, and by 2 THz modulation due to a random contaminant (i.e. dirt) which scatters and becomes a lossy reflector also forming a low finesse cavity. The 2 THz modulation could be included in the model by including a scatterer 85 μm from the end mirror which has $R_{\text{PC}} \approx 0.3\%$. The noise in the fringe is also due to other parasitic reflectors on the surface of the waveguide. Using all the parameter simulated using FDTD software Lumerical, and leaving only loss as a free parameter and including the parasitic reflector, we find reasonable agreement shown in Figure 3.13(a) where only the max and min peak values are plotted for the data. Comparing the Fourier transformed spectrum with the clean data, we see a lot more noise around the main peak. In the clean data we can identify individual parasitic reflectors (Appendix), but this signal is too noisy to identify single peaks which can be attributed to dust or other noise sources. We also tried fitting the local fringe, which is shown in Figure 3.13(b). Using the single cavity model (Appendix), we can fit the local fringe near the Cs transition.

3.2.4.1 Studies on Signal and Cleaning Techniques

These very long and thin nanostings were especially susceptible to small contamination such as dirt or dust on the waveguide surface. One reason for this is the small wavelength (852 nm) used in our devices which optically interact with smaller scatterers that lie on the surface. The geometry of the chip positions these waveguides over large holes through the substrate where air easily flows, bringing with it optical scatterers and contaminants which can stick to the waveguide surface (Figure 3.14(c)). In general this is a large problem, as the scatterers can absorb enough optical power to heat up the waveguide and cause thermal fracturing. For this reason we never tested devices on this chip past 150 nW over fears of overheating. Because 852 nm is in the visible range we can observe the scattering

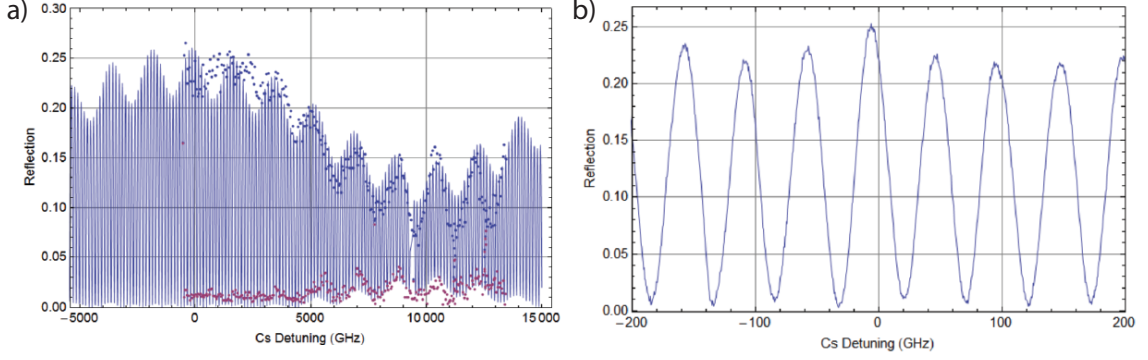


Figure 3.13: **Reflection Signal.** Maximum (blue) and minimum (purple) points of the measured fringe compared with simple cavity model using simulated parameters and leaving loss as a free parameter (also including parasitic reflector)

of the in-coupled light from the dust in our camera, as seen in Figure 3.14(c) where one can see several points of scattering (dust) along the waveguide. This ability to observe these scatterers is useful, as they are not typically visible using a scanning electron microscope. We know the hole through the chip (for MOT beam access) increases the likelihood of contamination on our waveguide, as we repeatedly saw on numerous chips that concentrated amounts of the scatterers were localized at regions of the waveguide suspended over this large opening (as opposed to regions suspended above the V-groove which showed very few scatterers.) This dust is also a problem because it acts as reflector which can add large modulations to our fast-fringe signal by forming small low-finesse cavities along the waveguide. After the structures are released in the fabrication process using KOH, they are cleaned using sulfuric acid solution (Nanostrip) for 10 minutes before being rinsed in deionized water and ultra-filtered IPA. Despite these precautions, we still get a signal which seems to have large modulations over the whole signal, low input/output efficiency, indicative of large losses throughout the waveguide as seen in Figure 3.14(i) where the max of the normalized reflectivity is $\approx 14\%$ for D_2 on our device. Because the nanostrings are very delicate and almost certainly destroyed by the surface tension of the liquids used to clean them, we clean the device of organic contaminants using an RIE plasma etching system to perform an oxygen plasma which etches carbon-based contaminants and has almost infinite selectivity with Si_3N_4 . We administered an O_2 plasma to the chip using a pressure of 20 mTorr, oxygen flow of 20 sccm, RIE power of 80 W, and a DC bias of 144 V for 10 minutes. After the chip is removed from the oxygen plasma chamber, we put the chip into a N_2 cleaned plastic chip holder which is wrapped in several layers of aluminum foil and plastic wrap and transferred to the nitrogen-pumped positive pressure enclosure for our optical characterization (the chip was packaged in a clean-room environment). After the O_2 plasma clean (using the same polarization and alignment adjustments as before) we could see a much cleaner signal with minimal modulations on the height of the fringes and much improved reflected

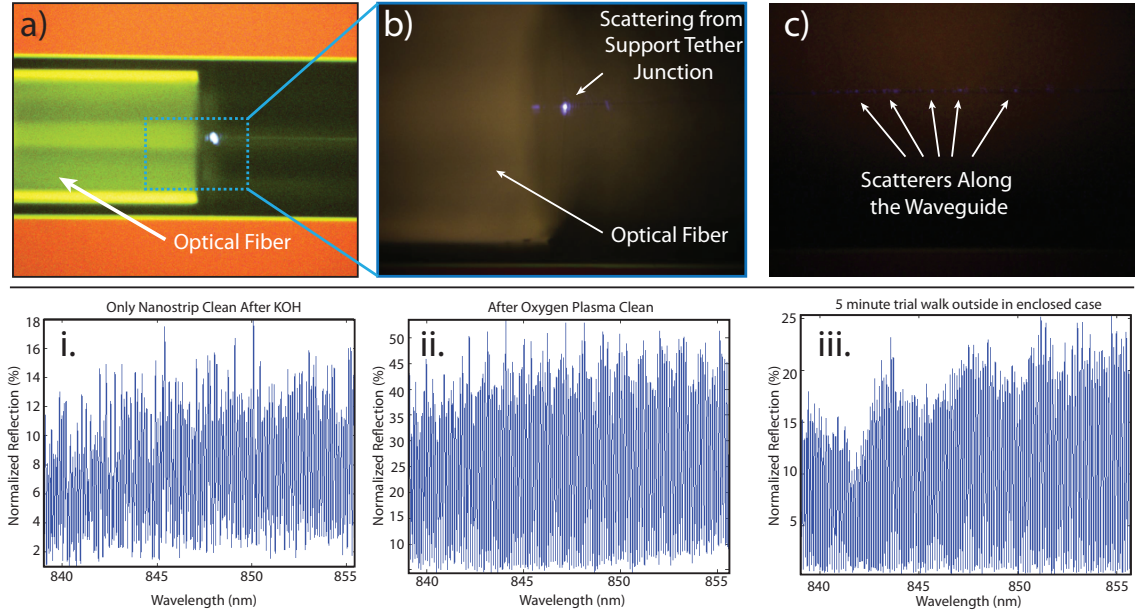


Figure 3.14: **Artifacts of Particulate Contamination.** (a): Camera still of optical fiber being inserted into a V-groove and while coupling to coupler tip of the nanostring. (b): Close-up image shows scattering of input light from the junction where the support tether and waveguide meet. (c): Shows region of waveguide where several particles of dust or dirt stuck. We also show the reflected transmission spectra from D₂ (i): after fabrication involving Nanostrip clean for 10 minutes followed by deionized water rinse, filtered-IPA, critical point dried and packaged in a clean-room environment. (ii): after O₂ plasma clean to etch away organic contaminants (iii): after device was well packaged and moved between labs 5 minutes away and brought back to characterization set-up.

powers from the nanostring device (max fringe reflectivity $\approx 45\%$), all indicating that contaminants were removed from the substrate (Figure 3.14(ii)). After this realization, ending the fabrication process with an O₂ plasma clean became standard practice. In order to show the optical sensitivity of these devices to contaminants, the device was then repackaged with several layers of aluminum and plastic wrap and inserted in a half-atmospheric pressure transport container and walked to the Kimble lab about 5 minutes away and returned back to our characterization setup. We could not reproduce the high reflectivity as seen in Figure 3.14(ii) with a max fringe reflectivity of $\approx 20\%$ as seen in Figure 3.14(iii) with a large modulation appearing in the fast-fringe signal. It was repeatedly observed that these devices were extremely sensitive to cleanliness of the packaging location and post-fabrication handling.

3.2.4.2 Experimental Procedure for Cs Loading on Nanostring Devices

The following experiments were performed in the Kimble Lab's UHV atomic setups. In order to prevent a device from being contaminated by cesium, the vacuum system consists of a source and experiment chamber separated horizontally by 70 cm. A room-temperature reservoir connected to

the source chamber supplies the Cs vapor, typically $P_{\text{Cs}} \approx 10^{-8}$ Torr. The source magneto-optical trap (MOT₁) runs in a standard MOT configuration with a loading time < 1 s. In addition, the linearly polarized pushing beam, with the detuning of +15 MHz from $F = 4 \rightarrow F' = 5$ transition and cw power of 3 mW, is aligned through the center of the MOT₁. From MOT₁, a pulsed push beam of ≈ 1 mm diameter extracts a flux of cold atoms that are slow enough to be recaptured in the experimental MOT (MOT₂) located in the UHV region. The atomic flux passes through a differential pumping tube such that the Cs vapor pressure in the experimental chamber maintains low pressure, $P_{\text{Cs}} \approx 10^{-11}$. The MOT₂ is loaded for 1 s to obtain $\approx 50 \times 10^7$ atoms and then compress the MOT₂ for a duration of 50 ms by increasing the MOT₂ laser detuning further to -30 MHz and attenuating the power. What results is a cloud of cold Cs atoms with a peak density of $\approx 5 \times 10^{11}$ atoms/cm³ and a temperature of $T = 40$ μ K about 1 cm away from the window of the device (Figure 3.15(i)). To transport the cold atoms near the nanostrings which are suspended in the window, the center of the magnetic field gradient is abruptly shifted to the center of the window at $t = 0$ ms. For a duration of 2 ms, the cloud of cold atoms are exposed to the MOT₂ laser beams and kicked toward the center of the large opening in our chip substrate by radiation pressure. After the MOT₂ laser beams are shut off, atoms freely propagate as shown in Figure 3.15(ii). When atoms arrive at the chip window ($t = 8$ ms), an additional MOT beam (mini-MOT) is turned on to cool and trap the kicked atoms in the vicinity of the suspended nanostrings photonic crystal waveguides. The procedure allows us to produce a cloud of cold Cesium atoms (diameter of ≈ 400 μ m) with a peak density of 1×10^{11} atoms/cm³ and a free space optical depth of typically ≈ 3 , spatially overlapped with suspended nanostrings. We can also determine the polarizations of the probe beam by observing

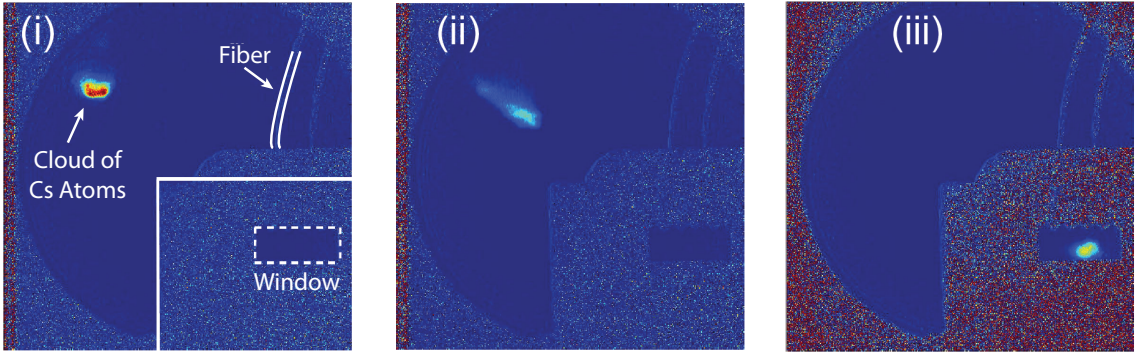


Figure 3.15: Cs Atom Transport near Nanostring using MOTs. (i): Camera images shows the 1×1 cm chip at the lower right corner with a 3×1.5 mm window where photonic crystal nanostrings are suspended and exposed to near 4π Steradian optical access for MOT beams. We also show and emphasize the outline of an optical fiber coupling into the chip. Here we also see a cloud of the Cs atoms at $t = 0$ ms. (ii) $0 \text{ ms} < t < 2 \text{ ms}$ – cloud of atoms are exposed to a MOT₂ and kicked towards the chip. At $t = 2$ ms, MOT₂ is shut off and Cs cloud moves freely towards the chip window. (iii): At $t = 8$ ms, the cloud of Cs atoms arrives at the chip window where mini-MOT beams cool and trap the atoms near the nanostrings.

the angular distribution of the Rayleigh scattering from the support tether (Figure 3.14(a) and (b)) using a CCD camera with a polarizer aligned along the waveguide axis. At a time-of-flight delay of $\tau = 1$ ms from turning off a mini-MOT, the thermal atoms are interrogated by a probe pulse (1 ms) with an optical power P_{probe} with a detuning δ_{probe} to the $F = 4 \rightarrow F' = 5$ transition. The weak probe pulse with TE polarization (typically with $P_{\text{probe}} \approx 1$ pW) is reflected by the photonic crystal mirror and detected with a single-photon avalanche photodiode. We then wait 8 ms for atoms to dissipate and probe the waveguide transmission with a reference pulse to determine the input power of the probe pulse.

3.2.4.3 Measurements of Cs Absorption with TE-Polarized Probe

In order to carry out absorption spectroscopy of the Cs atoms, the probe pulse was set at $P_{\text{probe}} \approx 1$ pW with $P_{\text{probe}} \ll P_{\text{sat}}$, where the saturation power for thermal atoms 100 nm away from the surface is $P_{\text{sat}} \approx 18$ pW. The transfer matrix of atoms based on Beer's law model is then rewritten by

$$M_{\text{atom}}(\Delta) = \begin{bmatrix} e^{-d(\Delta)/2} & 0 \\ 0 & e^{d(\Delta)/2} \end{bmatrix} \quad (3.6)$$

where an optical depth $d(\Delta)$ is given by

$$d(\Delta) = \frac{d_0}{1 - \frac{i2(\Delta - \Delta_0)}{\Gamma}} \quad (3.7)$$

with a resonant optical depth d_0 and a detuning Δ relative to the $F = 4 \rightarrow F' = 5$ transition with a transition frequency shift Δ_0 relative to the free-space line center, and total decay rate Γ . Since the reflection spectra of the nanostrings are well described using transfer matrix formalism, we can integrate the atomic response $M_{\text{atom}}(\Delta)$ into the same model and fit transmission spectra with this model to extract details about the resonant optical depth d_0 , a total decay rate Γ and a transition frequency shift Δ_0 . Figure 3.16(i) shows the fitted reflection spectra of the waveguide at different positions of the fringes (a)-(f) where the dashed vertical line is the $F = 4 \rightarrow F' = 5$ transition of Cesium. Figure 3.16(a-f) displays the transmission spectra T for the thermal atoms at the different positions of the fringe relative to the $F = 4 \rightarrow F' = 5$ transition. We found that the position of the fringe slowly drifts due to the heating effect caused by the MOT beams. We can see in Figure 3.16(i) that the Cs resonance frequency is located near the top of the fringe (a) and the middle of the fringe (a) and the middle of the fringe (f). Thus the transmission spectrum of Figure 3.16(a) is almost symmetric and transmission spectrum (f) shows asymmetric line shape due to the slope of the fringe. In Figure 3.16(a) the resonant optical depth of $d_0 = 0.14 \pm 0.005$, the linewidth of $\Gamma = 9.4 \pm 0.5$ MHz, compared to the free-space radiative linewidth $\Gamma_0 = 5.2$ MHz with a transition frequency shift of $\Delta_0 = 0.8 \pm 0.1$ MHz relative to the free-space line center, are

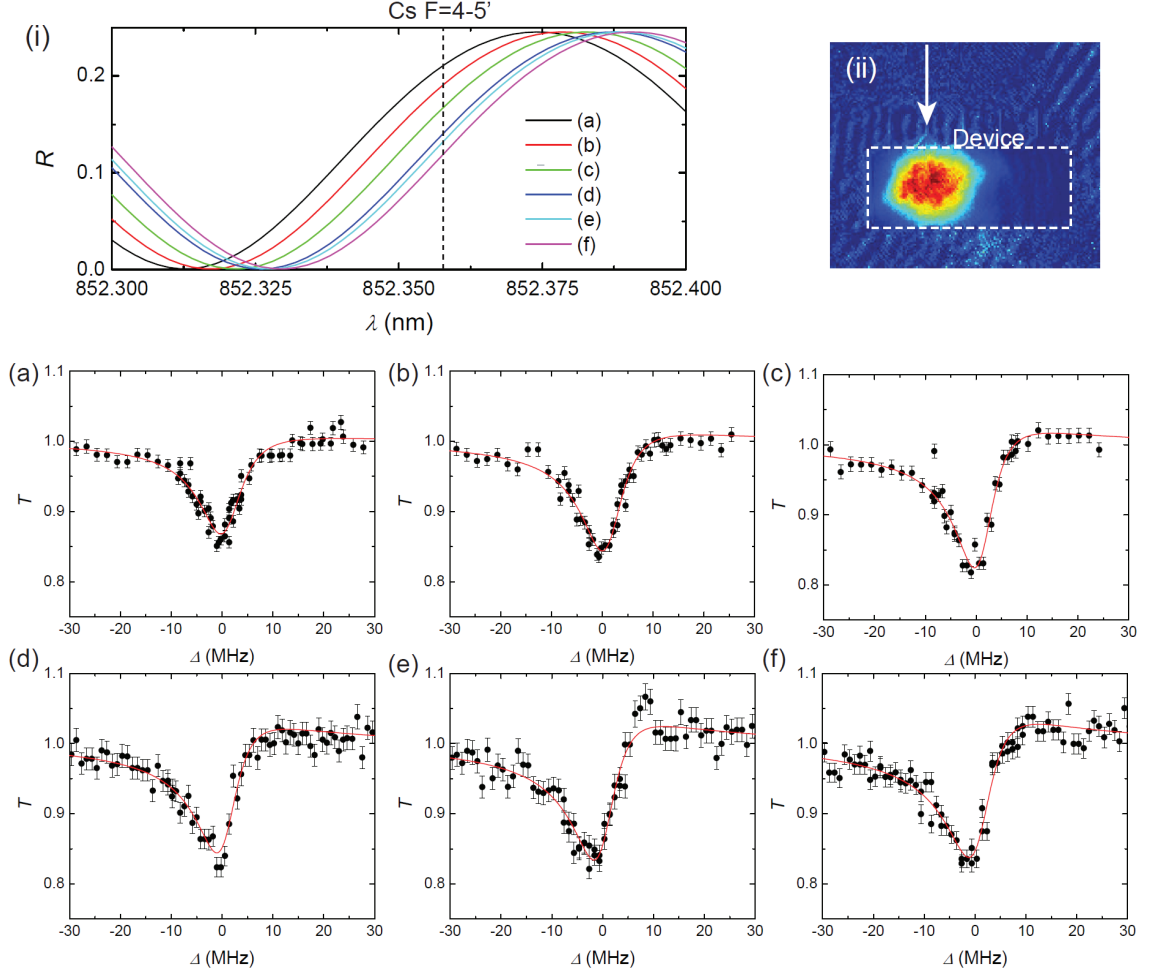


Figure 3.16: **Transmission Spectra for Thermal Atoms Detuned from $F = 4 \rightarrow F' = 5$ Cs Transition.** (i): Shows the fitted reflection spectra at different positions of fringes (a)-(f) where the dashed vertical line shows the $F = 4 \rightarrow F' = 5$ Cs transition. (ii): Shows an absorption image of cold atoms (at $\tau = 1$ ms) with a free space optical depth of typically ≈ 3 , spatially overlapped with the waveguide. Figures (a)-(f) show the transmission spectra at the different positions of the fringes shown in (i). The red lines are fitted transmission spectra with (a) $d_0 = 0.09 \pm 0.005$, $\Gamma = 8.0 \pm 0.8$ MHz, $\Delta_0 = 2.3 \pm 0.3$ MHz (b): $d_0 = 0.1 \pm 0.005$, $\Gamma = 8.7 \pm 0.7$ MHz, $\Delta_0 = 2.1 \pm 0.2$ MHz (c): $d_0 = 0.07 \pm 0.003$, $\Gamma = 10.7 \pm 0.8$ MHz, $\Delta_0 = 2.0 \pm 0.2$ MHz (d): $d_0 = 0.08 \pm 0.004$, $\Gamma = 9.1 \pm 0.7$ MHz, $\Delta_0 = 1.8 \pm 0.2$ MHz (e): $d_0 = 0.07 \pm 0.003$, $\Gamma = 9.6 \pm 0.6$ MHz, $\Delta_0 = 2.4 \pm 0.2$ MHz.

determined from the simple cavity model. The measured resonant optical depths, linewidths and frequency shift from Figure 3.16(a)-(f) average to $d_0 = 0.15$, $\Gamma = 9.0$ MHz, and $\Delta_0 = 0.84$.

Compiling measured linewidths from 13 different data set average to $\Gamma = 8.9$ MHz, as compared to the free-space radiative linewidth $\Gamma_0 = 5.2$ MHz. Since the resonant frequencies of atoms at different distances from the waveguide surface are unequally shifted by the van der Waal potential, the absorption line shape is inhomogeneously broadened [60]. Furthermore, we expect the center of the profile to be red-shifted due to the van der Waal shift and measured frequency shifts from the 13 data sets average to 1.2 MHz red-detuned. This was on the same order as the drifts of our probe laser frequency and too small to be experimentally quantified using these devices. From the measured optical depth of $d_0 = N_{\text{eff}}\sigma_0/A_{\text{eff}} \approx 0.15$, we estimate an effective density of atoms interacting with the probe mode $n_{\text{eff}} = N_{\text{eff}}/A_{\text{eff}}L_0 \approx 2.7 \times 10^9$ atoms/cm³. N_{eff} is the effective number of atom interaction with a probe mode, $\sigma_0 = \lambda^2/(2\pi)$ is the resonant absorption cross section, A_{eff} is an effective optical mode of the probe's evanescent field, and L_0 is a cloud diameter of ≈ 400 μm . The effective density n_{eff} is about 100 times smaller than the density of free space, typically $\approx 1 \times 10^{11}$ atoms/cm³. Since a probe mode is strongly localized near the nanostring characterized by an evanescent field decay length (1/e length) of $\Lambda \approx 150$ nm, the local density near the device could be modified by the presence of the dielectric due to the van der Waal force and light-induced dipole forces. In the next section we will discuss the evolution of the photonic crystal mirror and atom-coupling regions in order to enhance the coupling.

3.2.5 Photonic Crystal Overview

3.2.5.1 Nanobeam Waveguide Photonic Crystal Design

Here we will discuss the general design of photonic crystal mirrors fabricated into waveguides in order to maximize their reflectivities [61]. Let us first consider a single-mode waveguide with a photonic crystal mirror consisting of periodic series of holes in the waveguide as shown in Figure 3.17(i). The total electromagnetic field in the waveguide, Ψ , can be decomposed into a series of normal modes at $x < x_0$ (Figure 3.17) where

$$\Psi = W^{(1)} + rW^{(-1)} + \sum r^{(p)}W^{(-p)} \quad (3.8)$$

and $W^{(1)}$ is the incident fundamental mode of the waveguide and $W^{(-1)}$ is the associated backward propagating mode, both defined for $x < x_0$. $W^{(-p)}$ are backward propagating radiation modes and the $r^{(p)}$ are the reflection coefficients of these modes. Modes in the mirror characterized by forward-propagating Bloch modes, $B^{(p)}$, can be used to decompose the total field Ψ in a similar way for $x > x_0$ such that

$$\Psi = tB^{(1)} + \sum t^{(p)}B^{(-p)} \quad (3.9)$$

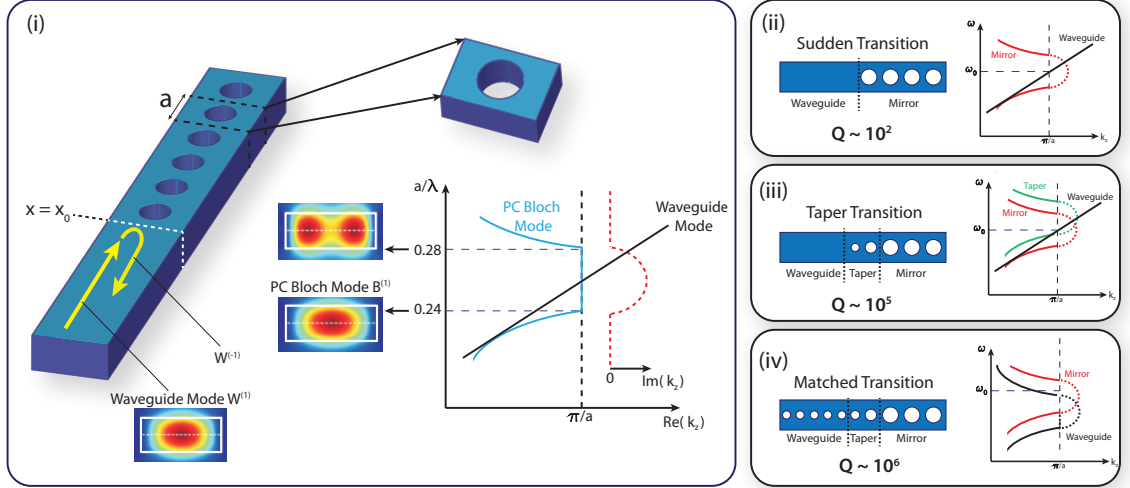


Figure 3.17: **Photonic Crystal Matching Conditions.** (i): Shows waveguide with sudden transition into a photonic crystal mirror at $x = x_0$ and the associated modal profiles of the Bloch modes in the mirror and the waveguide. On the left we have the associated band structure of the mirror unit cell (light blue) and the waveguide (black). On the right we show a geometric example and band-structure of (ii): sudden transition which produces $Q \approx 100$'s. (iii): Tapered transition from waveguide to PC mirror and (iv): matched waveguide with holes which transitions to PC mirrors.

where $t^{(p)}$ are the transmission coefficients of the $B^{(p)}$ modes. We specifically separate the $B^{(1)}$ from the summation in order to discuss matching conditions. Let us consider a photonic crystal consisting of holes with infinitesimal small radii such that there's little difference between the waveguide modes and Bloch modes. In this case each waveguide mode $W^{(p)}$ (guided or radiative) can be associated with a corresponding mode of the photonic crystal mirror, $B^{(p)}$. We then see that $B^{(1)}$ is the mode associated with $W^{(1)}$. But even with very small holes there is a bandgap in the band structure of the photonic crystal. Figure 3.17(i) shows the associated band structure of the photonic crystal mirror $B^{(1)}$ (light blue) and the waveguide $W^{(1)}$ (black curve) where the dashed red line inside the bandgap shows the imaginary component Bloch mode's propagation constant k_z . The Bloch mode $B^{(1)}$ is mainly responsible for the reflection of the fundamental guided mode $W^{(1)}$ but because of the slight mismatch between them, the Bloch mode $B^{(1)}$ exists in the hole, which consists of low-index material. This mismatch excites other Bloch modes $B^{(p)}$ (many of them radiative) which contribute to losses from light that leaks out of the structure. Figure 3.17 shows the importance of adiabatically tapering the hole size/lattice constant in order to smoothly transition from waveguide modes to Bloch modes without inducing severe optical losses. This can be seen in Figure 3.17(ii) where we show a sudden transition from waveguide to PC mirror. This sudden mismatch causes large losses such that cavities formed with these type of mirrors are limited to optical quality factors on the order of few hundred. In Figure 3.17(iii) we show a waveguide which adiabatically transitions to the PC mirror region with a taper region as used in our first generation devices for detecting atomic absorptions

(3.8). In our first designs we kept the lattice constant, a , unchanged throughout the taper region and slowly increased the hole radii. An optical cavity formed using these type of tapered mirrors can produce optical cavities with $Q \approx 100,000$ as shown in Figure 3.7. One of the limits of this design is that one cannot realistically fabricate infinitesimal holes which smoothly transition into the hole-less waveguide with no holes. This is discussed in the next section. Figure 3.17(iv) shows a waveguide consisting of a series of periodically placed holes which are then adiabatically transitioned into the PC mirrors holes. An optical cavity made in such a configuration is not limited by making holes which are extremely small and can produce structures with $Q \approx 10^6$, as shown in [6]. Because our devices are fiber coupled with waveguide coupler 130 nm wide, we could not realistically fabricate a waveguide with holes throughout, so our design is limited to transitioning from a waveguide (with no holes) to a PC mirrors using a tapered region as shown in Figure 3.17(iii).

3.2.5.2 Design Evolution of Photonic Crystal Mirrors

In this section we will review the design optimization of our photonic crystal mirrors, which was primarily motivated by the stringent fabrication and testing requirements. Because these devices required several components to work well with high accuracy, a majority of the design changes were made with the goal of making the probability of success higher. Figure 3.18 (left) shows different designs for atom-coupling/PC mirror regions of the nanostring. Our initial design (Figure 3.18(a)) consisted of a single tapered beam with a 300×200 nm atom-coupling waveguide which uses an evanescent field of the guided mode to couple with atoms as shown in Figure 3.18(ii). The PC mirror consists of a PC taper region with small holes which adiabatically transition into the PC mirror designed to have a bandgap centered around the Cs 852 nm transition. One of the first problems with this generation of devices was that the nanostrings would overheat and thermally fracture when they were fiber-coupled with relatively low trapping powers (< 150 nW) in ultra-high vacuum environments required for atomic experiments (Figure 3.18(i)). Because this design relied on trapping atoms using the evanescent field (low intensity tail) of the guided mode, a significant amount of power was required to make sufficiently deep optical traps. By introducing an adiabatically transitioned y-split which created a “double-beam” waveguide, we utilized an optical guided mode through two dielectric beams which created a high intensity guided maximum between the beams as shown in Figure 3.18(iii). We could achieve traps an order of magnitude better using the same trap powers which improved our ability to trap atoms without overheating and destroying the devices. In order to avoid losses which inevitably come from a second y-split, our design turned to parallel photonic crystals on each beam which would reflect the incoming guided mode (Figure 3.18(c)). One of the most significant problems with using holes to transition adiabatically from a waveguide to a photonic crystal is that we were limited by our ability to fabricate a well-defined small hole through the 200 nm Si_3N_4 layer. As seen in Figure 3.18(iv), we see that smaller holes (diameter ≈ 50 nm) begin to look

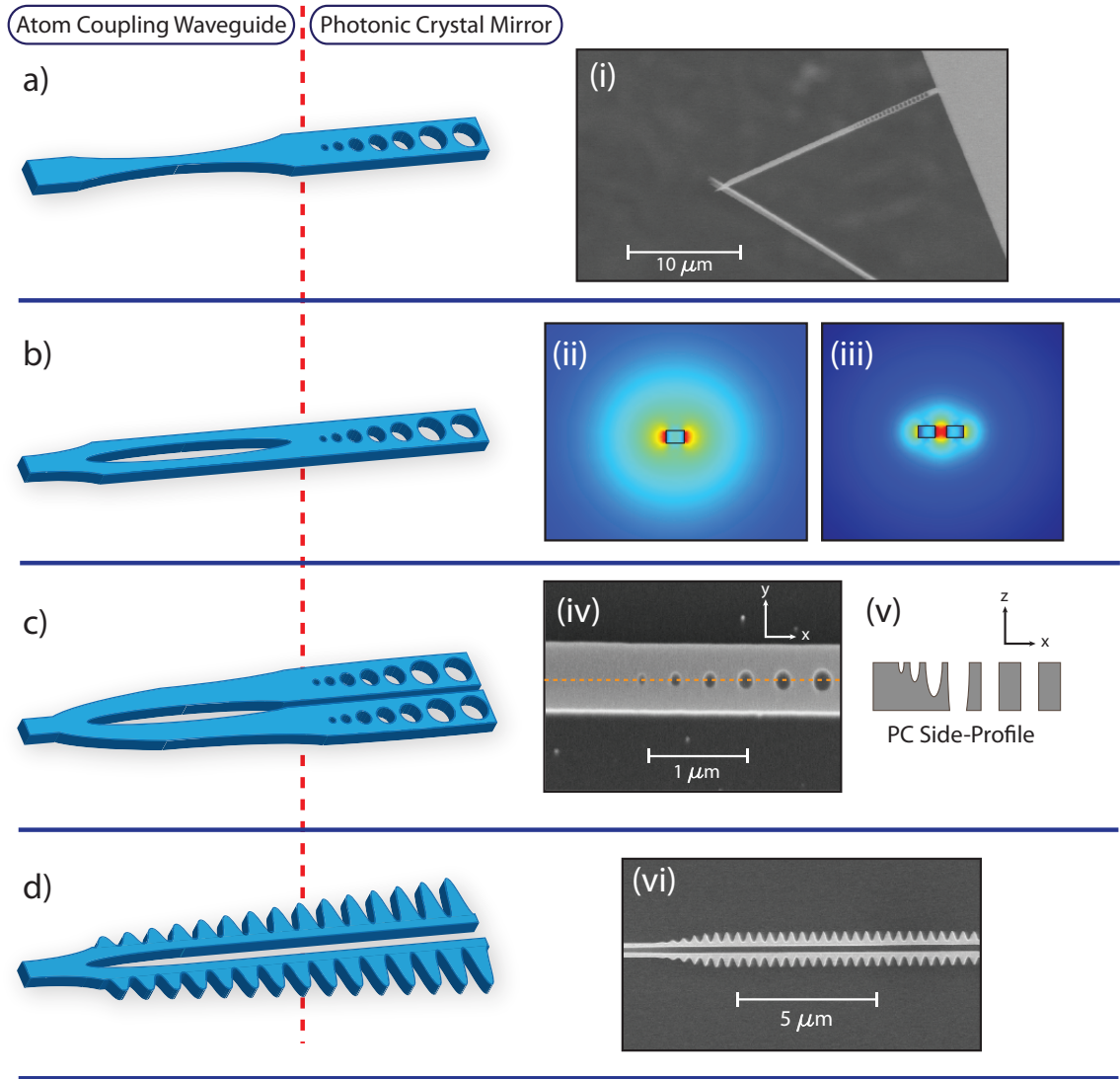


Figure 3.18: PC Mirror Design Evolution. (a): Illustration of single beam atomic-coupling waveguide connected to a hole-defined tapered PC mirrors. (i): SEM of the single-beam PC waveguide which has been thermally fractured due to high trapping powers needed to trap in the evanescent field of the mode in (ii). (b): Shows similar structure with single PC hole mirror connected to a waveguide which has been adiabatically y-split into two parallel beams. (iii): Shows the even parity supermode profile of the two beams in (b) where trapping maximum between the two beams is used to couple stronger with less trapping powers (compared to (ii)). (c): In order to minimize losses from y-splits, separate PC hole mirrors are fabricated on each beam. (iv): SEM showing how unevenly plasma etched and defined the PC taper holes become as they fabricated smaller. (v): Shows an illustrated side-profile of (iv) and how aperture effects result in much slower vertical etches within the small holes and vice versa. (d): Shows an illustration of the Alligator Photonic Crystal Waveguide (APCW). This is chosen in order to make very good adiabatic PC tapers as small bumps are easier to fabricate than small holes. (vi): SEM of an APCW.

shallow compared to larger holes. This is caused by “aperture effects” during the plasma etching in which the small size of the holes physically restricts the hole from being etched at the same rate as the larger holes. This produces photonic crystal hole z-profile as seen in Figure 3.18(v) where the smallest taper holes are etched significantly slower than the larger PC mirror holes, resulting in a photonic crystal which varies in the z-direction in an uncontrolled manner. This type of z-variance can produce large losses (low reflectivities) and more importantly variance in the photonic crystal, making it more difficult to accurately tune our photonic crystals to the Cesium transition. In order to avoid these aperture effects we designed a periodic structure using a corrugated pattern derived from a sinusoidal function. By slowly increasing the amplitude of the corrugations we could adiabatically transition from a waveguide to photonic crystal without etching different sized corrugations at different etch rates. Because the corrugations are located on the outside of the beam, the design does not depend on small enclosed hole features. Defining increasingly small corrugation “bumps” are much easier to fabricate than small holes. Typically corrugated structures which form Bragg mirrors are composed of rectangular corrugations [51], however, the sharp corners (e.g., rectangular holes or corrugations) are difficult to achieve as electron beam lithography tends to expose in a way that rounds these corners, making them slightly and unpredictably different from simulations (which do simulate sharp corner). In our case we used a corrugated structure which is defined with a modulated sinusoid with smooth transitions from one unit cell to the next and is by its nature free of sharp corners. This type of photonic crystal structure allows one to possibly calibrate these structures with high precision and minimal stochastic defects. The exact mechanisms for trapping and band-structure are discussed in Section 3.4.1.

3.3 Fabrication of Nanowire Photonic Crystal Waveguides

In this section we give an overview of the fabrication process required for the delicate high-aspect ratio structures required for coupling of light and Cs atoms. The 200 nm-thick Si_3N_4 devices held up by small tethers are ≈ 2 mm long with an average width of ≈ 300 nm, making the structures extremely fragile. The fragility of these structures is further exacerbated by the large hole which is fabricated through the silicon substrate for optical access. The hole required for this process must be very large (1.5×3 mm) in order to accommodate a number of MOT beams which require near 4π Steradian access. This large hole through the Si substrate made the wet-release of these nanostrings extremely difficult since it allowed large viscous flow through the chip and suspended nanostrings. Fracturing was repeatedly observed with the inclusion of an optical access window through the chip. We could confirm this phenomena when trying to fabricate a 2 mm long nanostring device held up only by a single 100 nm wide support tether (absent the tether array); given the exact same device design with the same clamping, without a substrate hole, our device yield would be $\approx 100\%$, which

would dramatically decrease to $\approx 0\%$ with the inclusion of a hole through the substrate. In order to maximize the yield and repeatability, all of the nanostring devices were processed using turbulence-shielding techniques outlined in Chapter 2. In addition to the extreme physical dimensions of our waveguide structures, the optical requirements were also a fundamental challenge. The photonic crystal mirrors on the nanostring needed to be tuned very closely to the Cs transitions (e.g., D2 transition at 852 nm), which required high levels of accuracy and precision in the fabrication process. In conventional nano-scaled optical devices, one can fabricate thousands of devices onto a chip with fine sweeps of several dimensional parameters such that one can drastically improve the chances of fabricating a device with the correct optical properties. Our delicate nanostrings were limited to $\approx 6 - 10$ nanostrings per chip due the limit on the number of optical fibers we could physically fit onto the 1×1 cm chip. Because of the small number of devices we would fabricate per chip, we required extreme fabrication control over the dimensions of our nanostring optical elements. Photonic crystal fabricated for 852 nm tend to be approximately scaled down to about half the size of a photonic crystals designed for telecom wavelengths (e.g., ≈ 1550 nm) with the waveguide and PC holes being approximately half the size. This resulted in optical elements that were extremely sensitive to imperfections in the fabrication process. Using 852 nm laser light also required using much thinner optical fiber with a much smaller fiber mode diameter of $5 \mu\text{m}$ which required very good alignment of the fiber center and waveguide coupling tip. This alignment was dependent on the precision wet-etching of the V-grooves, which would induce large coupling losses if the V-groove was wet-etched even a micron too large. The devices also had stringent cleanliness requirements in order to be suitable as an optical element in an ultra-high-vacuum environment common in atomic experiments. Because of the small wavelength light used at relatively high powers to induce an optical trap, these devices were extremely sensitive to contamination (i.e., dust and residues) during and *after* fabrication. In this section we outline the fabrication process developed in order to robustly produce these delicate structures with high accuracy and precision required of several parameters in this system.

3.3.1 General Fabrication Process for Nanostrings

LPCVD stoichiometric Si_3N_4 grown on a [1-0-0] silicon substrate was used to fabricate our nanostrings for atom-light coupling. Si_3N_4 is grown at high temperatures and low pressures, which give a high intrinsic stress and very low optical absorption at sub-infrared and infrared wavelengths ([22] [9] [62]) with imaginary refractive index $n_i \approx 10^{-6}$. [1-0-0] orientation silicon substrate is used in order to etch directionally through the substrate using potassium hydroxide wet etch (KOH), but more importantly because it has the correct orientation in order to wet-etch V-grooves into the substrate for guiding and aligning the optical fiber to the waveguide tip of our device. The substrate used was $200 \mu\text{m}$ thick in order to drastically shorten the amount of time we needed to etch through it using KOH.

Figure 3.19 is an overview of our fabrication process. We start with a 1×1 cm silicon substrate with 200 nm of high stress Si_3N_4 on 200 μm silicon substrate (Figure 3.19(a)). The first step is making a large window in the back of the chip which will eventually connect with a large front window (with suspending nanostrings) resulting in a large hole through the chip for MOT beam access. We spin positive photoresist AZ-5214 onto both sides of the chip in order to protect the front layer of silicon nitride (where the nanostrings will be fabricated) while we perform photolithography on the back of the chip, where we define the large window. The front side of the chip is spun at 4000 rpm with AZ-5214 and baked at 100°C on a hotplate. The same is done for the back of the chip which usually becomes dirty from the vacuum chuck while spinning the first layer of resist (which does not matter for exposing such large patterns with no small critical features). Using a Karl Suss MA6/BA6 mask aligner we exposed a 1.5×3 mm window in the back side of the chip using 365 nm UV light for 20 seconds (Figure 3.19(c)). Photolithography is a good method for exposing several chips at once since the windows are large and lack small features. The chip is developed using developer CD-26 and rinsed in deionized water for 45 seconds and dried (Figure 3.19(d)). We then use a ICP-RIE plasma etch using a combination of C_4F_8 and SF_6 in an Oxford Instruments PlasmaLab System 100 ICP-RIE 180 to etch into the back layer of silicon nitride (Figure 3.19(e)). We require that the substrate be extremely clean of contamination (dust, films of AZ-5214, water-spots, etc.) since the electron-beam lithography has small features (i.e., long nanostring with small photonic crystal features) that can easily be written badly because of the interference between contamination and the electron-beam. To ensure a contamination-free surface we perform a hot piranha solution clean consisting of a sulfuric acid (H_2SO_4) solution heated to $\approx 90^\circ\text{C}$ and then mixed with hydrogen peroxide (H_2O_2), resulting in an exothermic 3:1 $\text{H}_2\text{SO}_4:\text{H}_2\text{O}_2$ solution whose temperature raises to $\approx 140^\circ\text{C}$. The solution bubbles violently and thoroughly cleans the surface of organic contaminants. The chip is cleaned in the solution for 10 minutes and rinsed in deionized water (Figure 3.19(f)). The chip is then flipped over in order to start fabrication of the nanostrings, V-groove, and front window into the front layer of Si_3N_4 . From this point on in the fabrication process, the front side of the chip is *always* pointing up, which reduces the chances of small scratches that could easily destroy the nanostring along its 2 mm length (Figure 3.19(g)).

In order to use electron-beam (e-beam) lithography to define the nanostring devices, we first spin a layer of e-beam resist (ZEP-520A) onto the front of the chip at 4000 rpm and bake on a hotplate at 180°C for 2 minutes (Figure 3.19(h)). Using the scanning electron microscope integrated with our electron-beam pattern generator's (EBPG) precision stage, we find the coordinates corresponding to the physical corners of the chip in order to write our device pattern such that it aligns with the window etched into the back layer of Si_3N_4 . Using a 300 pA beam with a 2.5 nm step resolution, we write a large front window connected to a series of rectangular channels which run off the edge of the chip (these eventually define our V-grooves). Inside the window we define a series of photonic

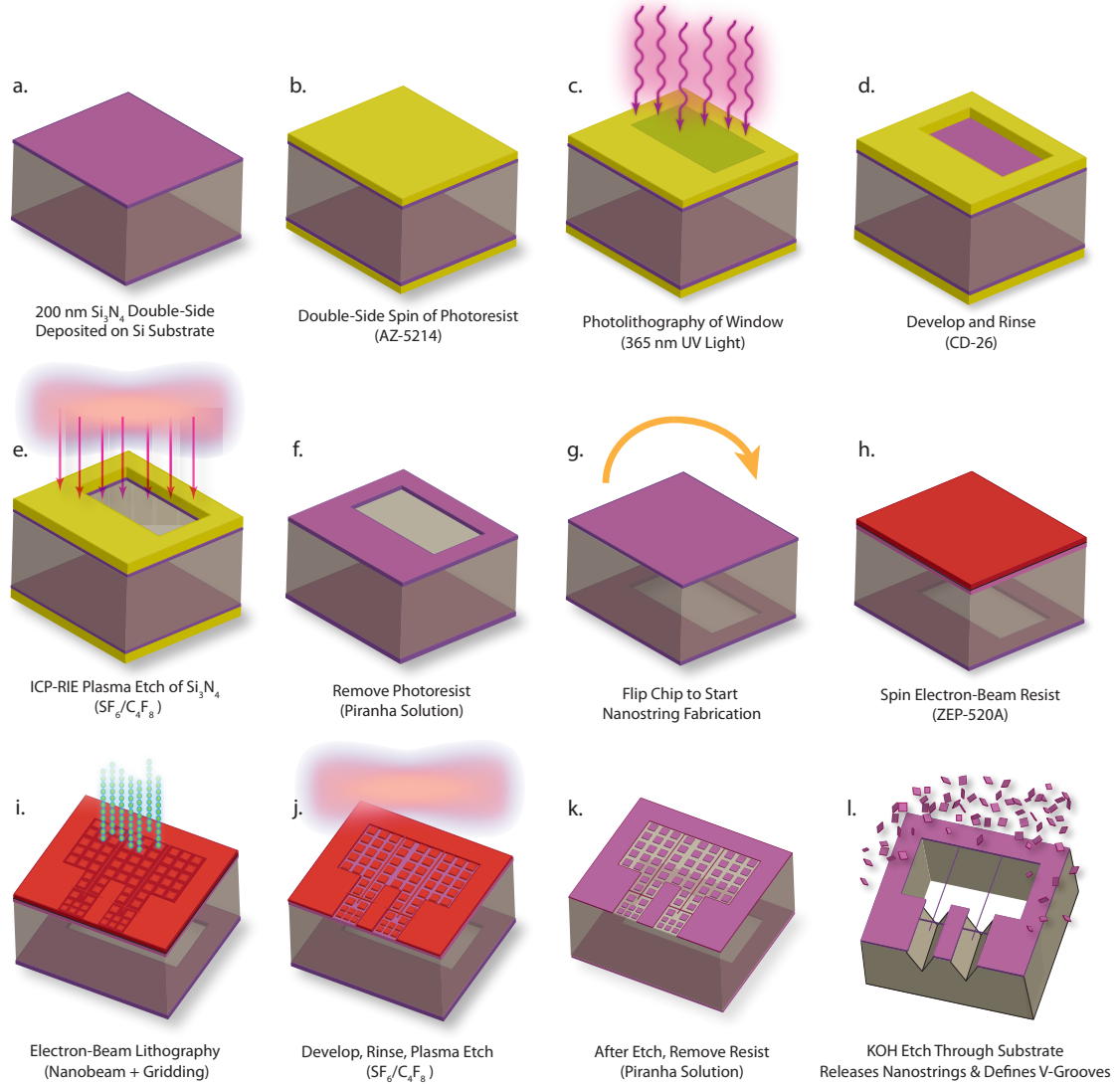


Figure 3.19: Nanostring Chip Fabrication for Atom-Light Coupling.

crystal nanostring structures clamped to the inside of the V-grooves by small tethers. In order to dramatically reduce the stochastic exposure from back-scattering electrons resulting from writing large areas (front window + V-grooves) surrounding small and sensitive photonic features along the nanostring, we also fill the large areas with a grid of small unexposed squares which are lifted off during the KOH undercut (Figure 3.19(l)). Once the patterns are written we develop for 2.5 minutes in ZND-N50 developer and 30 seconds in MIBK rinse, and another $\text{C}_4\text{F}_8/\text{SF}_6$ plasma etch is carefully performed in our ICP-RIE plasma etching system (Figure 3.19(j)). Because of our stringent precision and accuracy requirements on our photonic elements this plasma etch must be done with extreme care to repeatably transfer the pattern onto the silicon nitride layer. We utilize a piranha solution (same as the first) to clear the device of ZEP520A and other contamination before the structure is

released. We then use a ≈ 4 hour KOH etch at 75°C to release the sample (Figure 3.19(1)) using turbulence-free fabrication techniques described in Chapter 2. This is a crucial step that must also be done with extreme care as we have two requirements: (i) that we etch completely through the chip to make optical access for the MOT beam and (ii) that (i) happens in a repeatable amount of time such that the KOH etches V-grooves the same way each time, otherwise they could be a micron too large and induce large optical losses when the optical fiber center is misaligned with the waveguide coupler tip (Figure 3.22). Once we etched completely through the chip we rinsed the sample in deionized water and cleaned the sample using hot Nanostrip (similar to piranha solution but without the violent exothermic reaction which can destroy the sensitive devices). The sample is then rinsed again in deionized water, rinsed with IPA, and critical point dried in a Leica Critical Point Dryer CPD300. Because these devices are 2 mm long, thin and very fragile and clamped to the substrate by only a few small tethers ≈ 100 nm wide, we must critical point dry these samples to avoid droplets evaporating on the chip since the droplet's surface tension can pull on the delicate devices, resulting in structural failure at one of the nanostrings joints. Once the samples are critical point dried, the samples are additionally cleaned using a high power oxygen plasma to clean any remaining organic contaminants on the surface before the device goes into the vacuum test chamber.

We then mount the fibers onto the chip under optical microscope. Our CCD camera is sensitive to near-infrared (NIR) wavelengths. We inject laser power into the fiber while it is being mounted into the V-grooves, giving us alignment information which can be seen in the camera since we can measure the reflected signal real-time as the fiber is mounted. The chip is glued onto a UHV compatible aluminum mount using UV epoxy. The aluminum mount (and chip) is screwed into a x-y stage while the optical fiber is lowered and raised using a vertically oriented stage. The fiber is lowered into the V-grooves and positioned at close vicinity with the waveguide coupler tip. Once we have optimized the coupling from the fiber, it is glued into place using Dymax optical glue. The sample can be placed into a positive-pressure nitrogen container for testing optical signal or a UHV chamber for characterization with Cs atoms.

In the next few subsections we will go over in detail some of the challenging aspects of this fabrication process that are extremely sensitive, crucial, and must all repeatably work in unison to make a fully working device. We developed techniques that allowed us to fabricate successful devices with significantly increased probability. First we will go over our “gridding” techniques which allowed us to significantly increase the precision of lithographically-patterned high-aspect-ratio devices (containing several small crucial features). Without such a technique it would not be possible to reliably define small photonic elements for 852 nm light in the middle of a large window required for atomic experiments. Second, we will review methods for undercutting with a KOH wet etch that allow us to fabricate these delicate high-aspect-ratio nanostring devices without structural failure. This includes turbulence-shielding fabrication (discussed in Chapter 2) which

does two things: (i) makes sure that the devices can be fabricated without structural failure and (ii) makes sure we can precisely KOH wet-etch which is important for producing repeatable V-groove dimensions. Without this repeatability one could make several devices that survive structurally but cannot be coupled efficiently because the V-groove sets the optical fiber alignment to the nanostring coupler. Third, we will discuss additional structural elements like “safety-rails” which are essential in preventing tearing in the high-stress silicon nitride layer which can also tear apart our devices. And finally we discuss the cleaning methods used to ensure the nanostring devices are clean and suitable for UHV environments, and high input powers for trapping atoms. The specifics of the KOH undercut are discussed in Chapter 2.

3.3.1.1 Electron-Beam Lithography Techniques for Nanostrings

One of the most significant challenges in fabricating these devices was reproducing the very small nano-photonic elements for 852 nm light on the nanostring structures. Because the physical dimensions of the photonic elements scale almost linearly with wavelength, devices designed for 852 nm are half the size of conventional C-band telecom wavelengths ($\approx 1530 - 1565$ nm) which make them extremely sensitive to small nm-sized defects. The big challenge is then using electron-beam lithography to define these photonic elements in the middle of very large exposed areas that define our windows for MOT access, since the electron back-scattering from exposing these areas creates significant variation in the e-beam exposure of our photonic devices. With only 6-10 devices per chip, it is extremely important that these elements can be written reliably from write to write. Two elements in the nanostring in which reduction of these small variations can make a large difference between testable and untestable devices are the waveguide tip width for coupling to the optical fiber and the photonic crystal. The waveguide coupler tip has an optimal width at 130 nm which maximizes the transmission of light from the fiber into the device, but we see in Figure 3.2(b) that even the small 20 nm difference in the width of the waveguide coupling tip (at the limits of resolvability in an SEM) can produce huge reductions of ≈ -2 dB in the transmission into the fiber. This coupler sits in the center of a large exposed area which defines the V-grooves. The large amount of backscattering exposure from these areas can easily vary the coupler from 10-40 nm and make it incredibly hard to reliably produce a device which can couple in light, even if all other elements of the device are successful. Using the “gridding” technique (also shown in Figure 1.7) we can fill the the large areas that define the window and V-grooves with a grid of unexposed squares which are eventually undercut and released from the device, as shown in Figure 3.19(l). Figure 3.20(a) shows an example of the “gridding” written around the waveguide coupler tip. The area between the dashed red lines indicates the V-groove area that would conventionally need to be exposed. Figure 3.20(bc) shows SEM images of photonic crystal waveguides with and without the implementation of the gridding technique. In both cases a proximity effect correction (optimized for 200 nm silicon nitride films on

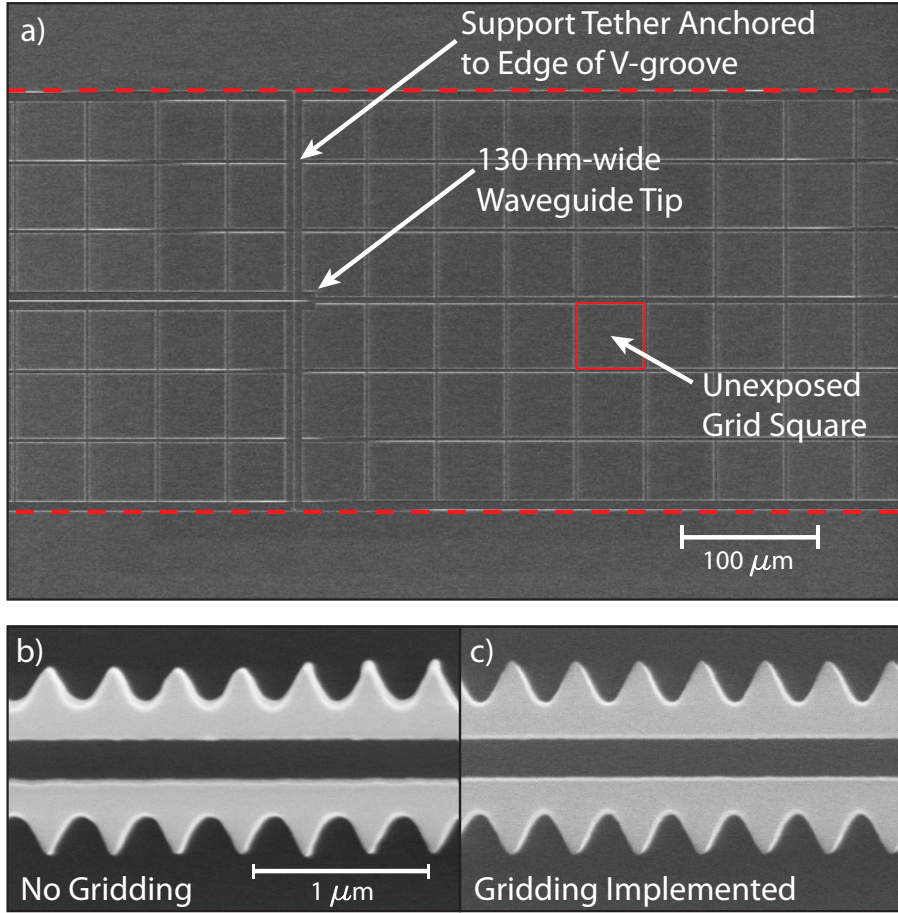


Figure 3.20: **Gridding Technique for Nanostring Lithography.** (a): SEM image demonstrating the gridding patterns around the waveguide coupler tip of the nanostring to achieve robust e-beam lithography which consistently achieves the optimal coupler width of 130 nm by reducing back-scattering exposures. (b): SEM image of corrugated photonic crystal without gridding shows misshapen and inconsistent heights of corrugation caused by stochastic electron back-scattering during e-beam lithography. (c): SEM image of corrugated photonic crystal with gridding implemented resulting in consistently sized corrugations of equal sizes.

silicon substrate) was utilized in the e-beam lithography to account for back-scattering electrons by reducing or increasing the dose in areas which are calculated to have more or less back-scattering, respectively. In Figure 3.20(b) we can see that the photonic crystal suffers from irregularities in the shape and size of the corrugated structure caused by back-scattering electron exposure, which can vary greatly between different e-beam lithographies. Figure 3.20(c) shows that reduced electron back-scattering resulting from the surrounding unexposed gridding can produce robust and well dosed photonic crystals. Without gridding these open areas, it would not be possible to fabricate the nanostrings with any reasonable precision when attempting to fabricate the devices very close to Cesium's 852 nm D2 transition. When the EBPG writes patterns larger than several hundred microns, it splits the pattern up into smaller subsection (main-fields) which it stitches together.

With large patterns that take a long times to write, there can be small drifts in the EBPG positioning stage which result in stitching errors between main-fields. This is especially relevant to our 2 mm long waveguides which cross numerous main-field boundaries. A single stitching error between main-fields can render the waveguide lossy and untestable. The longer the writing time, the longer the time between writing different main-fields and the more susceptible an e-beam written pattern becomes to stitching errors like those shown in Figure 3.21. In Figure 3.21(a) we can see how two main-fields have drifted apart slightly, leaving a clear unexposed line where the boundary between the two main-field. In this case the stitching errors run straight through our waveguide. In Figure 3.21(b) we can see the clear shift between main-fields by observing stitching errors running through the photonic crystal. Using gridding techniques can reduce the e-beam writing time by up to 95%, significantly reducing the probability of stitching errors in our waveguides by immensely reducing the time between the exposure of different main-fields and lowering the chances of stage-drift during the lithography step. This shortened time is especially useful because our waveguides are extremely long with small features which require a low-current beam (300 nA) to attain high resolution. This higher resolution results in smaller main-fields, which increases the number of main-field boundaries where stitching errors can occur.

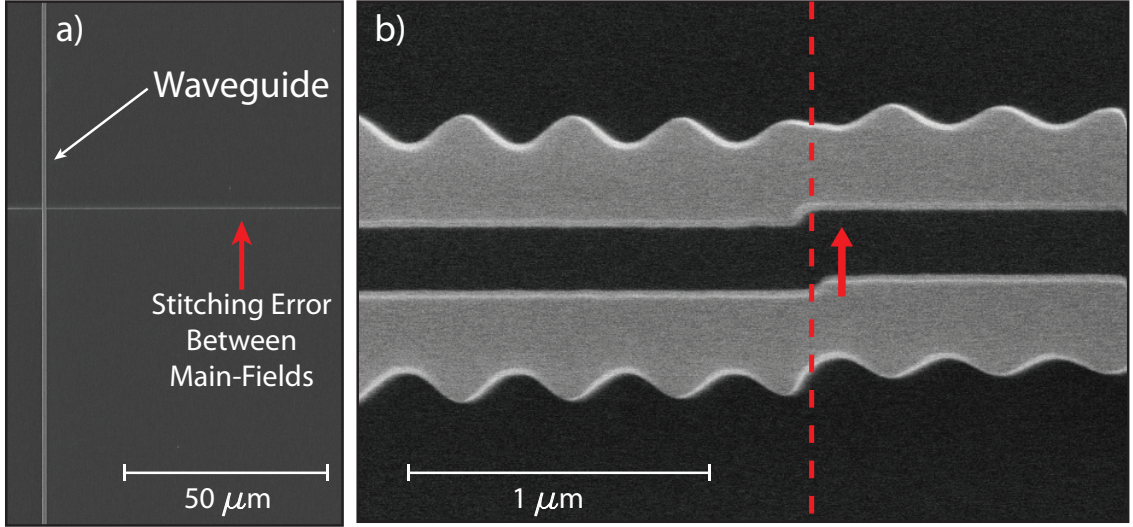


Figure 3.21: **Stitching Errors Between Main-Fields.** (a): SEM of waveguide where a stitching error occurs between main-field boundaries, leaving a line of unexposed area running through the waveguide. (b): SEM of stitching error caused by a lateral shift along a boundary between main-fields. These types of errors become more frequent with longer writes due to small drifts in the EBPG positioning stage. (SEM image courtesy of Su-Peng Yu)

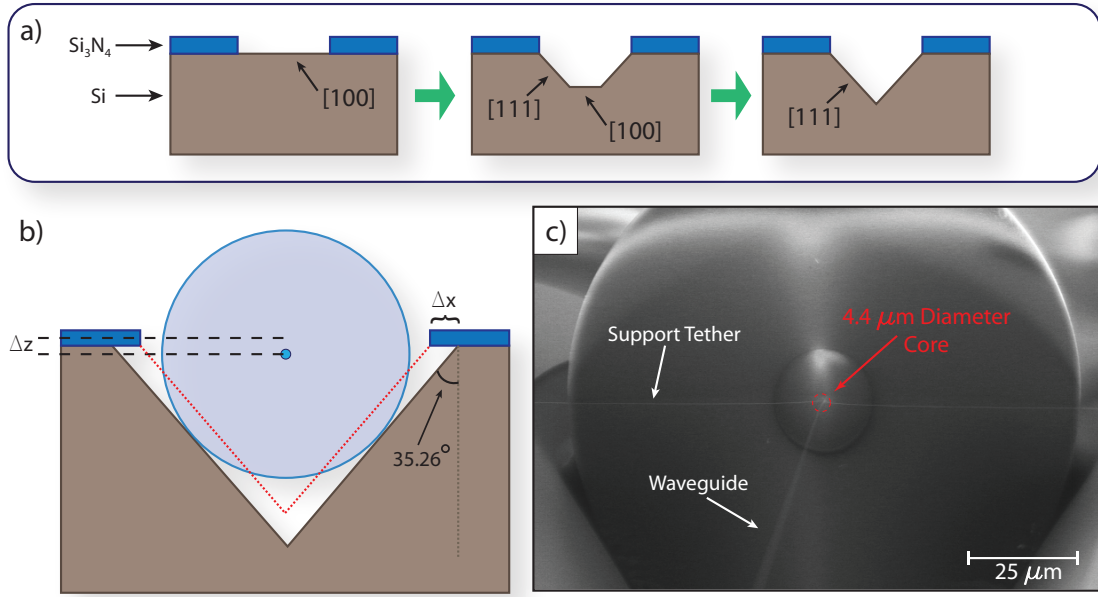


Figure 3.22: **V-groove Alignment.** (a): Illustration showing how V-grooves are formed by etching $[1-0-0]$ plane faster than the $[1-1-1]$ planes of silicon. (b): Schematic of the V-groove Fiber Coupling. Show how small undercut Δx can change the V-groove shape from the ideal shape (red dashed) by a displacement of Δz . (c): SEM image showing optical fiber glued into a V-groove and aligned with a nanostring device.

3.3.1.2 V-grooves Coupled with MOT Beam Window

Optical fiber coupling to devices on a silicon substrate rely on etching V-grooves into a silicon substrate. This technology relies on anisotropic KOH etch which etches the $[1-0-0]$ plane of silicon more rapidly than the $[1-1-1]$ plane, as shown in Figure 3.22(a). Idealistically once the $[1-1-1]$ planes meet, resulting in a V-shape etch into the silicon, there is no longer any $[1-0-0]$ planes exposed for etching. This effectively works as an etch stop. Practically, if one were to continue wet etching, the $[1-1-1]$ planes would still continue to etch slowly and open the width of the V-groove, making a small undercut Δx as shown in Figure 3.22(b). This small undercut can have drastic effects on the alignment of the optical fiber core ($\approx 4.4 \mu\text{m}$ diameter) to the waveguide coupler tip. We can express the misalignment in z produced by these undercuts with $\Delta z = -\frac{\Delta x}{.707}$. With such a small core, and $5 \mu\text{m}$ diameter mode diameter from the fiber, even a small undercut of $\Delta x = 1 \mu\text{m}$, will produce a significant z -misalignment of $\Delta z = 1.41 \mu\text{m}$. It seems that by KOH etching the same amount of time every time, we could simply calibrate how much the V-groove sides are undercut after a certain amount of time and simply define V-groove widths that are smaller by $2\Delta x$. However, long KOH etches are challenging to calibrate well as the etch rate are exponentially reliant on temperature. One can attempt to keep the minimize temperature gradients within the KOH solution by having a Teflon spinner to constantly mix the solution during the etch and keep the temperature homogeneous.

This in itself creates a problem as our nanostrings are very fragile and could collapse from the flow resulting from spinner speeds which are too high. The KOH etch rate is also very dependent on the flow of fresh KOH over the silicon and depending on the flow of KOH inside our setup, we can have drastically varying rates of etching. The biggest problem is that KOH etch time is not a set time, but variable depending on how fast it takes for the KOH to etch through the entire chip to create a window for optical access. If KOH takes too long to etch a window through the substrate, then the V-grooves widths will be much larger, leading to large coupling losses of the optical fiber to the device due to misalignment. This requires developing a KOH wet etch setup which is calibrated to high precision. In order to avoid large amounts of water evaporation from 30% KOH solution during the ≈ 4 hour KOH etch, we used an enclosed condensation setup, shown in Figure 3.23(a). As the water evaporates the condensation collects at the top of the enclosed glass piece (which is cooler because of its distance away from the hotplate surface) and falls back into the solution. This kept the solution at the same concentration, which is essential, achieving consistent local silicon etching rates. If too much water were to evaporate and escape, the solution concentration would rise and continuously decrease the etch rate throughout the 4 hour etch. A small hole was made in the condenser set-up to allow a temperature probe connected to the hotplate through a proportional-integral-derivative (PID) controller operated as a control loop feedback system which kept the solution approximately at the same temperature throughout KOH etch. The spinner was spun at low speeds to alleviate temperature gradients in the solution. The turbulence-shielding described in Chapter 2 was also essential in keeping the flow through the sample as constant as possible and shielding the delicate nanostrings from viscous forces induced by the spinner. Using these numerous methods, we were able to etch through the silicon substrate with consistent etch times (4.25 hours ± 10 minutes). These etching considerations were crucial in operable devices with efficient light coupling to 780-HP fibers.

3.3.1.3 Finite Element Simulations: Structural Failure Due to Stress

For delicate nanostrings with extreme aspect ratios, even if a fabrication process is developed that minimally exposes the structures to outside forces, if the structure is designed with very high stress at critical joints, the structure will fracture. With 2mm long nanostring, even the collapse of one structure on the chip can mean that it touches or drapes across several adjacent devices, rendering other devices untestable. We use FEM solver, COMSOL, to simulate the stresses within the structure. As discussed in Chapter 1, because we use LPCVD silicon nitride (for its excellent optical properties) this also means that our structures are under high levels of stress that can have several effects. The biggest concern is that the internal stress can be too high at certain points, leading to complete structural failures from tearing. We find that any structure designed with stress $\approx 3 - 4$ GPa anywhere on the nanostring would break at those simulated points upon being released with

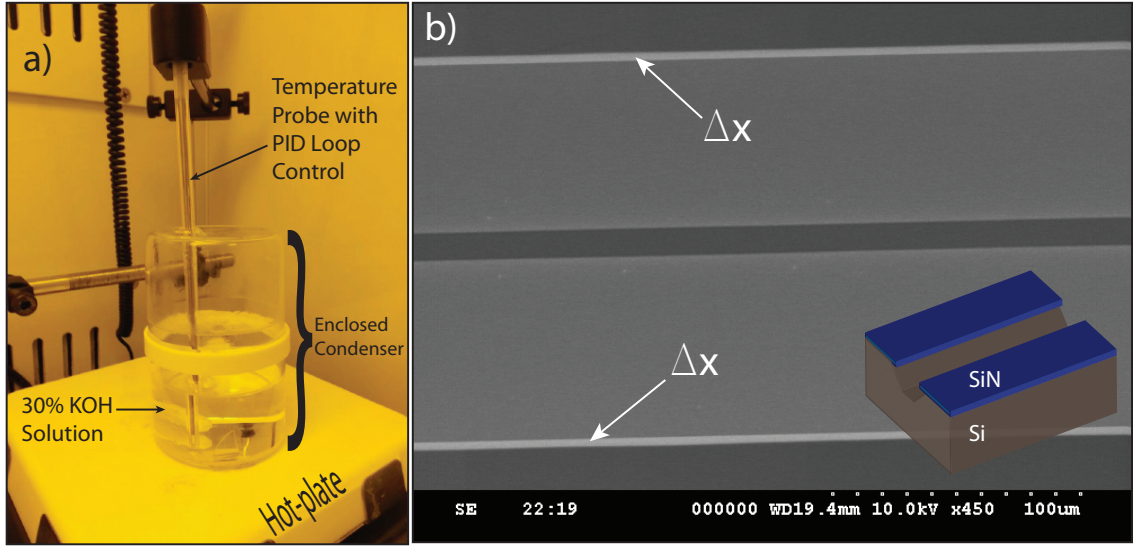


Figure 3.23: **KOH Etching Techniques.** (a): Photograph of enclosed condenser set-up for KOH etching. A temperature probe is inserted into KOH solution and connected to the hotplate with a PID loop to allow real time measurement and control of the solution's temperature. (b): SEM image showing a top-view of a V-groove. We could measure the KOH undercut, Δx , by measuring the width of lighter silicon nitride which outline the V-groove.

KOH, making the simulations an extremely useful tool for predicting structural failures before the structure is fabricated. At the top of Figure 3.24 we see an image showing the entire 2 mm long simulated nanostring structure with a 100 nm wide support tether. For initial simulations of structural stability we simplify the model by simulating a linearly increasing width of our nanostring from 130 nm at the waveguide coupler tip to ≈ 600 nm at the end and define fixed boundary conditions where the nanostring is attached to the substrate (for simplicity we did not include the tether array). It is important to simulate the displacements (due to tensile stress) in these long structures because the longer the structure, the more material which contracts from the tensile stress, resulting in very large displacements on the order of microns. We can see from the inset at the top of Figure 3.24, that the contraction along the length of the nanostring causes a displacement away from the support tethers. A closer look at the simulated support tethers (Figure 3.24(a)) reveals that the support tethers are pulled back $\approx 5 \mu\text{m}$ from the contraction of the nanostring under tensile stress. Because of this large displacement there is a tremendous stress (≈ 2.59 GPa) placed on the joint where the support tether and waveguide meet (Figure 3.24(b)). The COMSOL simulation has very good predictive capabilities. Fabricated structures harboring joints with tensile stress $< 3 - 4$ GPa always certainly break at simulated spots of high stress. From Figure 3.24, it is clear that one side of the support tether would be more susceptible to tears since the right edge of the tether is being pulled open by the contraction of the nanostring. High-aspect ratio structures with long and small dimensions all at once are computer-memory intensive simulations which can be simulated using thin-film approxi-

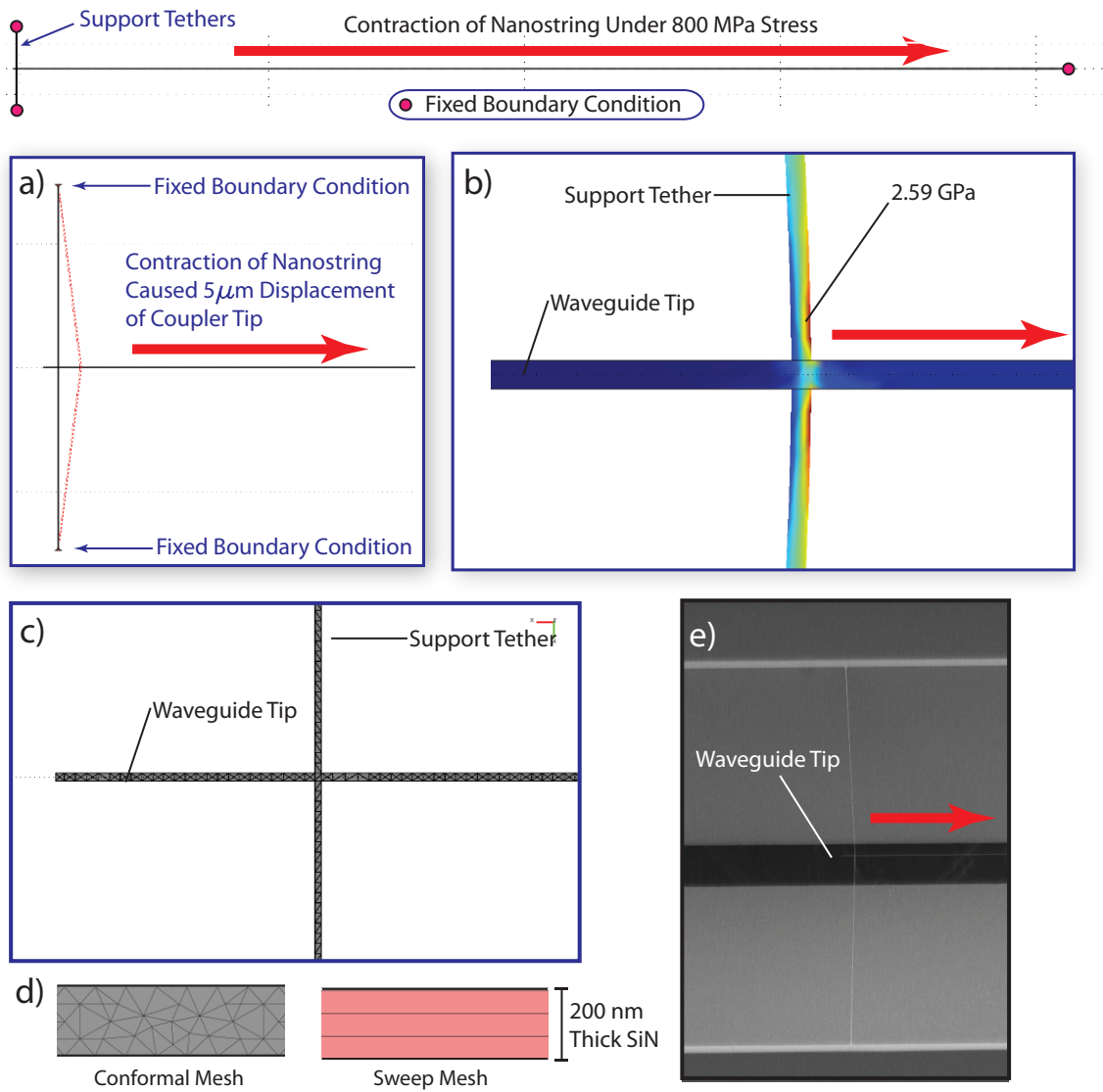


Figure 3.24: **FEM Simulations of Internal Stress.** (Top Inset): Illustration showing wide-angle view of the entire simulated 2 mm nanostring structure. One can see where the nanostring is clamped to the substrate and how the structure contracts under tensile stress after being released. (a): Zoom-in view of the fiber coupling region shows the displacement of the support tethers due to the nanostring contraction. (b): Simulation of the stress at the support-tether/waveguide joint. (c): 2D swept mesh which used thin-film approximation to efficiently simulate the nanostring structure and produce reliable results. (d): Shows the difference between conformal and swept meshes through the z-direction of the film. The swept meshes considerably simplify the simulation and reduce the number of finite elements needed. (e): SEM micrograph showing the coupler region on a fabricated device which displaces as simulated by $\approx 5 \mu\text{m}$.

mation and swept meshes. Figure 3.24(d) shows the thin-wise slices which are made to considerably reduce the number of finite elements in the simulation (as opposed to the conformal mesh which treats the thin-direction on equal footing as the other dimensions). The FEM simulation’s predictive abilities are demonstrated in Figure 3.24(e), where we can measure the $5\text{ }\mu\text{m}$ displacements of the support tethers on fabricated devices using an SEM and find that they match well with predicted COMSOL simulated displacements.

These types of simulations allowed us to predict the stress effects of including the 15-tether-array in the nanostring. Simulations found that including a tether array as an extra anchor also reduced the stress at the joint where the support tether and waveguide meet and found that including it reduced the stress to $\approx 1.67\text{ GPa}$. We concentrate on the stress at this joint, as this is where we discovered most of our structural fractures during the fabrication process. One would think that we could reduce the stress and increase the stability of this join by replacing the sharp corners with small fillets. This did reduce stress, but it also significantly increased simulated optical losses. Because the optical properties were extremely sensitive to features that could increase stability it was important to have the ability to simulate the our real structures before the fabrication process with these simplified models. These simplified simulations were also important in designing mirrors

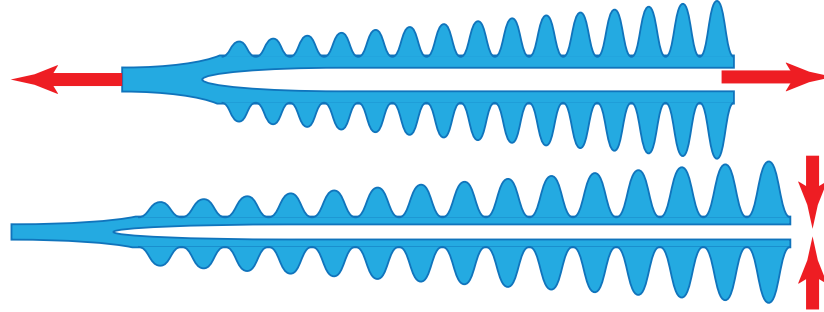


Figure 3.25: Effects of Stress on “Double-Beam” Mirrors.

with the proper dimensions. Our corrugated double-beam structure (APCW) is reliant on producing beams with the proper spacing between the beam. The large contractions of the nanobeam can pull on the mirror/atom-coupling structure and produce smaller gaps between the beams as a result (Figure 3.25). In order to correctly fabricate the mirror with the correct spacing between the beams that achieve optimal mirrors and atomic coupling, we simulate the stress and displacements of these structures (without the corrugation as it has a negligible effect on the displacement).

3.3.1.4 Safety Rails Required for High Nanostring Fabrication Yield

Fabricating surviving nanostrings not only required consideration of the stresses within the nanostring, but it also required considering different parts on the chip that were indirectly connected to

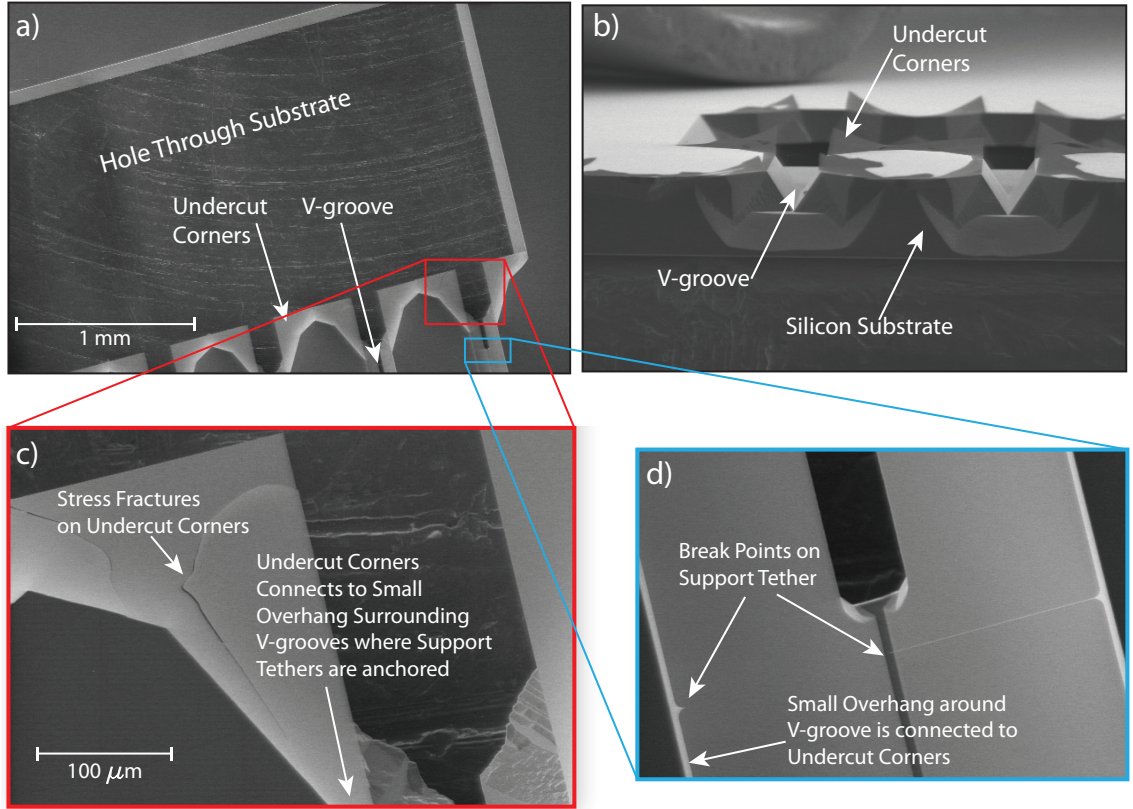


Figure 3.26: **Undercut Corners.** (a): SEM image showing layout of the 1×1 cm with a 1.5×3 mm hole through the substrate connected to V-groove channels for fiber coupling. The wet-etch of the chip also produces undercut corner-flaps. (b): SEM image shows the side profile of the chip which flaps which deflect upward due to linear stress gradients within the film as discussed in Section 1.3.2.3. (c): SEM of propagating fractures on the corner flaps which are connected to the anchoring points for the support tethers shown in (d). (d): SEM image showing a typical break at the support tether where it meets the waveguide (where simulations show the largest stress gradients).

the nanostrings. Figure 3.26(a) shows a wide-view SEM of the 1×1 cm chip with a 1.5×3 mm hole through the silicon substrate which has been etched with KOH. The corners where the large window and V-groove channels intersect are aggressively undercut by wet etching, leaving large undercut flaps of silicon nitride as shown in Figure 3.26(c). Because of linear stress gradients in the film these corner flaps also deflect out of plane, as shown in Figure 3.26(b). Because these large pieces of Si_3N_4 are left to freely move during the fabrication process they develop tears which were found to be correlated with the survival of associated nanostrings. It was noticed that these large undercut flaps were connected to the small overhangs surrounding the V-grooves (shown in Figure 3.22(b)) where the support tethers are anchored. We believe the strain resulting from the movement of these corner flaps produced stresses on the joint where the support tether and waveguide met. In order to keep these undercut flaps constrained we designed $1 \mu\text{m}$ wide “safety rails” which connected to the corner of the flaps and traversed across the large window through the chip and attached to

the other side of the substrate shown as dashed red lines in Figure 3.27(a). These safety rails were patterned into the design in the same lithographic step as the rest of the nanostring pattern. In

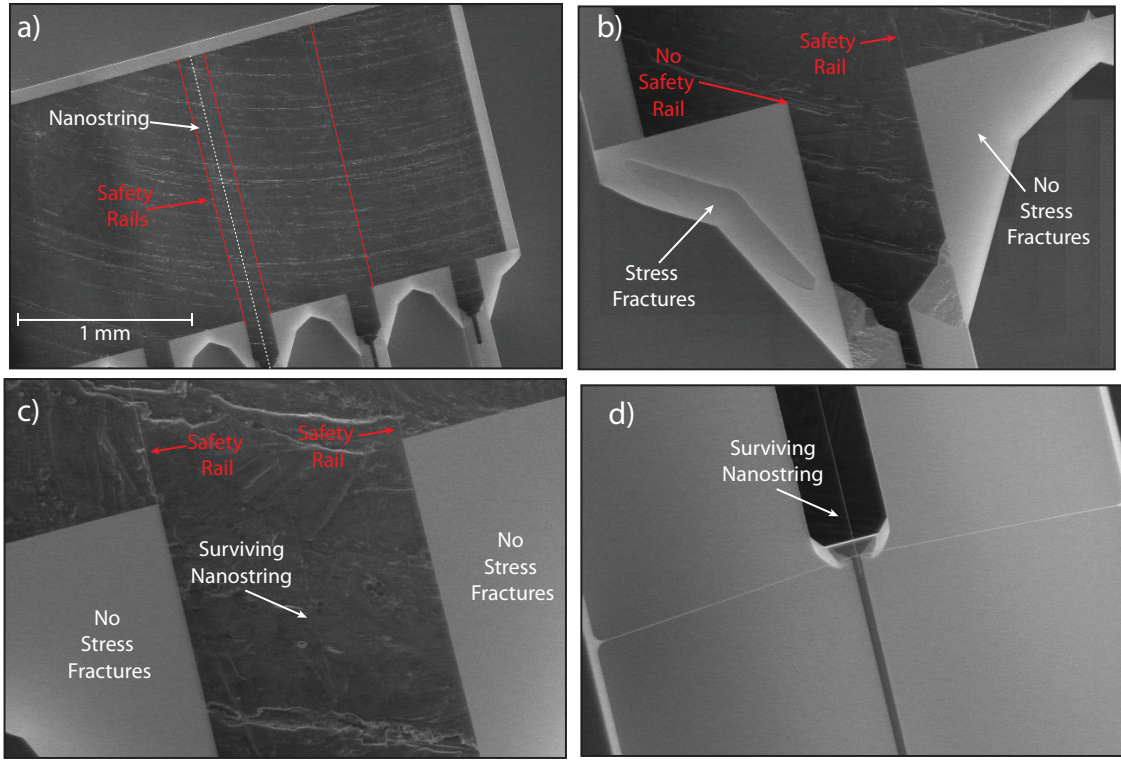


Figure 3.27: Safety Rails. The safety rails are used to restrain the corner-flaps which, if left to move freely, are associated with fractures in the nanostrings at their points of highest stress near the support tether junction with the waveguide. (a): SEM image of the chip showing how the safety-rails are attached to the undercut corners (red dashed lines). (b): SEM image shows V-groove end in which only one side was written with a safety rail. The nanostring associated with this V-groove broke at the support tether junction. (c): SEM image shows V-groove with both corner-flaps restrained using safety-rails and a suspended nanostring which has survived. (d): SEM image showing the waveguide coupler of the nanostring in (c).

order to see the effects of the safety rails we fabricated a chip in which some V-groove channels had (i) no safety-rails, (ii) only one side clamped with safety rails (Figure 3.27(b)), and (iii) both sides clamped down with safety rails (Figure 3.27(c) and (d)). We see that with safety rails there were no tears in the corner-flaps. When both corner-flaps were attached to safety rails the nanostring would survive the fabrication process. We found that the safety rails made the biggest difference in yield; without the inclusion of safety-rails the yield was very low regardless of where we clamped the support tether within the V-groove. The safety rails were also designed to be thin enough to cause negligible interference with the incoming MOT beams. The safety rails were a subtle addition that allowed us to fabricate the nanostrings with reasonable yield by restraining previously loose corner flaps of silicon nitride which would momentarily increase the stress at crucial joints in the structure.

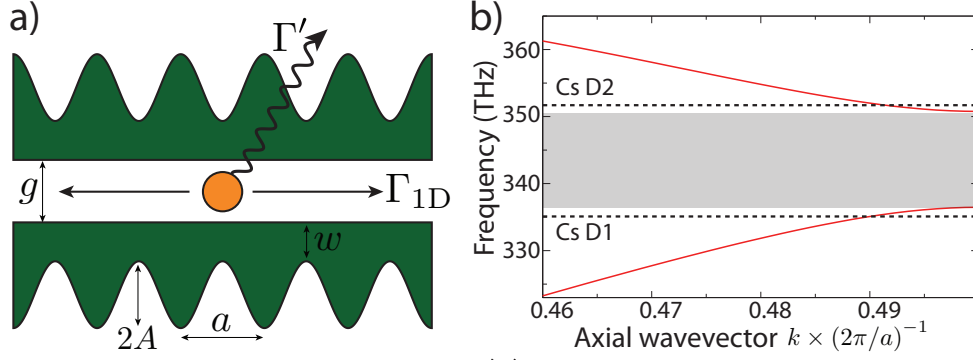


Figure 3.28: **Band Structure and Atomic Transitions.** (a): Schematic of the APCW with dimensional parameters thickness $t = 200$ nm, inner waveguide width $w = 187$ nm, gap $g = 260$ nm, and lattice constant (one unit of the periodic structure) $a = 371$ nm and the sinusoidally-modulated outer waveguide edge with a “tooth” amplitude $A = 129$ nm. (b): Photonic bandstructure of the fundamental TE-like modes of a nominal alligator waveguide device calculated with the dimensions derived from a typical fabricated device. Small adjustments are made to the waveguide parameters within the absolute uncertainty of the SEM ($< 5\%$) to obtain better agreement between measured band structures and those computed using SEM image measurements.

3.4 Measurement and Characterization

3.4.1 APCW Design for Trapping Cs Atoms

In this section we describe our final designs and measurements [63] utilizing the “alligator” photonic crystal waveguide (APCW) region shown in Figure 3.28(a). It consists of two parallel Si_3N_4 waveguides with refractive index $n = 2$. This configuration is fabricated such that the trapping of atoms in the gap between the dielectrics, where the atomic spontaneous emission rate into the single guided mode, Γ_{1D} , can be greatly enhanced with respect to spontaneous emission into all other free-space and guided modes, Γ' , which here is approximately equal to the free-space spontaneous emission rate Γ_0 . Figure 3.28(b) shows the optical bandstructure of the TE-like modes for the APCW, which are simulated using the MIT Photonic-Bands (MPB) package. This program computes definite-frequency eigenstates of Maxwell’s equations in periodic dielectric structure for arbitrary wave-vectors. The waveguides are designed such that the Cesium D1 ($\nu = 335.1$ THz) transition is aligned near lower/“dielectric” (ν_D) band-edge while the D2 ($\nu = 351.7$ THz) transition is aligned near upper/“air” (ν_A) band-edge, as seen in Figure 3.28(b). An enhanced density of states near the X-point band-edge, along with the strong field confinement of the even parity supermodes in the gap can be used to create large atom-photon interactions. Intensity images of the dielectric and air band mode are plotted in Figure 3.29(a) and Figure 3.29(b) respectively. The corresponding enhancement of Γ_{1D} is shown in Figure 3.29(f). One scheme for trapping Cs atoms within the gap of the APCW is to use the dielectric-band mode blue-detuned from the Cs D1 line as a trapping beam and the air-band modes as a probe on the D2 line of the trapped atoms. When using

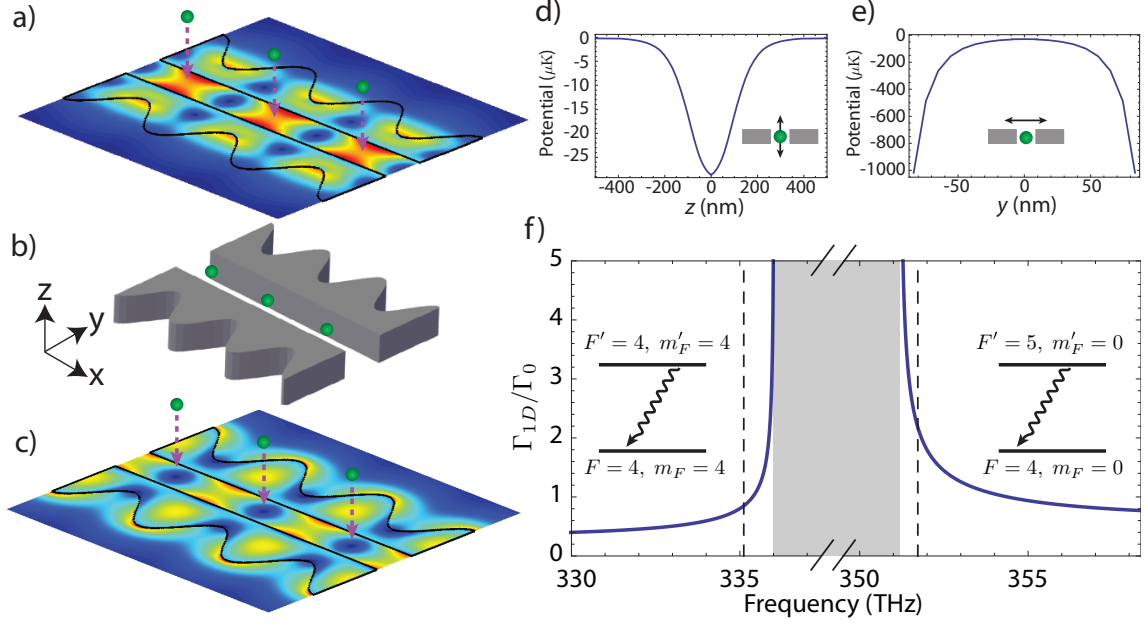


Figure 3.29: **Design of APCW.** (a): Finite-element-method (FEM) simulation of the near-X-point guided mode electric field magnitudes $|\mathbf{E}(\mathbf{r})|$ in the x-y plane for the (a) air band and the (c) dielectric band of the even parity TE-like supermodes for the periodic structure shown in (b). The optical frequencies correspond to the Cs D1 and D2 lines, and the corresponding band structure is shown in Figure 3.28(b). (d): Numerically computed Casimir-Polder potential along direction (x_m, y_m, z) for dielectric-band trapping mode around the minima of the optical trapping potential at (x_m, y_m, z_m) . (e): Numerically computed Casimir-Polder potential along the (x_m, y, z_m) direction for dielectric-band trapping mode around the minima of the optical trapping potential at (x_m, y_m, z_m) which is the position at which the illustrated Cs atoms in (c) are positioned. (f): Calculated rate of radiative decay Γ_{1D} into the guided mode in the (a) for the cases of an initially excited atom trapped at (x_m, y_m, z_m) in an infinite photonic crystal for transitions between atomic levels. The shaded area indicates the photonic bandgap region and the dashed lines the Cs D1 and D2 transition frequencies. Γ_0 is the free-space decay rate.

the air and dielectric modes in this way, the Cs atoms are trapped between the parallel dielectrics where the dielectric-band mode has an intensity null in the x-y plane as seen in Figure 3.29(c) and the Casimir-Polder force provides additional confinement in the vertical z-direction shown in Figure 3.29(de). In order to achieve stronger vertical confinement a guided mode red-detuned from the Cs D2 transition can be utilized. For the band structure shown in Figure 3.29(b) and with the counter-propagating $30 \mu\text{W}$ TE-mode fields blue-detuned by 30 GHz from the Cs D1 $F = 4 \rightarrow F' = 4$ transition combined with $15 \mu\text{W}$ of counterpropagating TE-mode fields red-detuned 300 GHz from the D2 $F = 4 \rightarrow f' = 5$ transition, we expect a trap depth of $\approx 5 \text{ mK}$ and trap frequencies of $[\nu_x = 3.5, \nu_y = 1.4, \nu_z = 0.7] \text{ MHz}$. Here the total power within the device is $90 \mu\text{W}$.

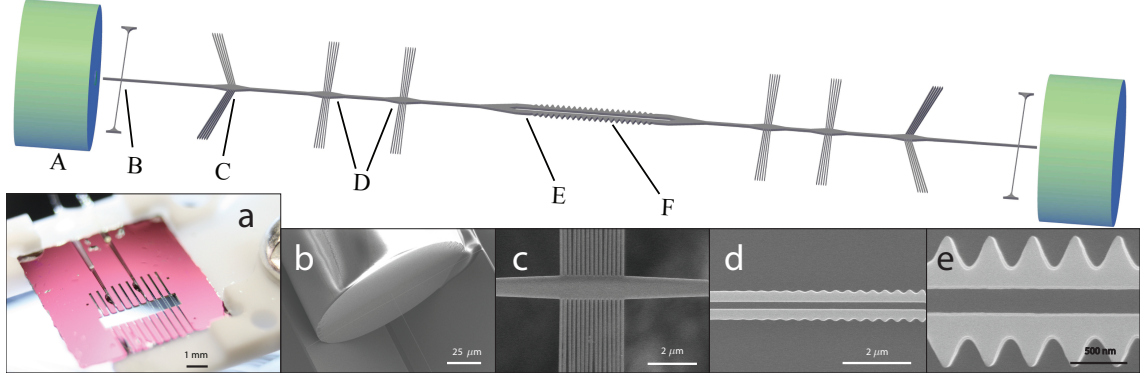


Figure 3.30: **Schematic of Final APCW Structure.** TOP: Schematic of the waveguide chip illustrating the various regions of the waveguide. (a): Optical image of the fiber coupled waveguide chip showing the through-hole for optical access. Zoom-in SEM image of (b) the adiabatic fiber-coupling (A), (c) the alignment, mechanical support, and thermal heat-sink tether (B,C,D), (d) the tapered region of the APCW (E), and (e) the central APCW region (F). The sinusoidal modulation facilitates high-precision fabrication. Other elements (not shown) are side thermal contacts which consist of a pair of $7.5\ \mu\text{m}$ wide Si_3N_4 rails extending across the entire length of the waveguide and connecting to the substrate.

3.4.2 Nanostring Photonic Crystal Waveguide Components

We have previously described in detail many of the components which make up the final design. Here we will briefly describe the structure of our final APCW nanostrings. We incorporate several elements into the waveguide structure to in-couple and collect light, provide mechanical support, and to improve heat dissipation. SEM images taken along the length of the Si_3N_4 waveguide show the various sections of the device including a waveguide-to-fiber coupling region described in Section 3.2.1. This coupling region can be seen Figure 3.30(b), which consists of a waveguide coupler tip with a optimal width of 130nm for coupling with the $5\ \mu\text{m}$ diameter mode profile from the optical fiber (780-HP). This waveguide tip is clamped to the substrate with a single small support tether shown in Figure 3.30(b). The waveguide then adiabatically increases in width to $\approx 1\ \mu\text{m}$ where the first tether array lies indicted in Figure 3.30(C) which consists of 15 tethers spaced at a 220 nm pitch. FDTD simulations (Lumerical) show that the input coupling efficiency of the taper and single support tether is $\approx 75\%$ for light near the D2 transition of Cs. The tether arrays play two roles: (i) provide mechanical stability against fractures induced by the high tensile stress which resides in the Si_3N_4 nanostring and (ii) provide increased thermal contact to the substrate when high trapping powers are applied to the device. The mode is well confined inside the dielectric in this $1\ \mu\text{m}$ wide region of the waveguide with the 15 tether array acting as a photonic crystal, which increases the transmission of the evanescent field of the guided modes. According to FDTD simulations, the scattering loss in this tether array is $< 0.5\%$. Additional tether arrays as seen in Figure 3.30(D) are added throughout the structure to increase thermal dissipation into the substrate

since the device can structurally survive with only a couple of tether arrays, but devices with only a few suffer from thermal fracturing when high power guided modes propagate through the device in UHV environments. The guided modes are then guided to the middle region of waveguide consisting of the APCW structure. After the APCW, the structure's out-coupling half geometrically mirrors the in-coupling half of the waveguide in order collect light from a second V-groove aligned optical fiber.

3.4.3 Measurements and Characterization of APCW Devices

Once fabricated, anti-reflection coated optical fibers are mounted into the input and output v-grooves in the Si substrate. The fiber-waveguide separation is set for optimal coupling (typically $\leq 10 \mu\text{m}$) before the fibers are affixed in place with UV cured epoxy. The chip and fibers are then attached to the vacuum-compatible mount (Figure 3.30(a)) and loaded into a vacuum enclosure (reaching $\approx 10^{-9}$ Torr) with optical fiber feedthroughs. In order to measure the broadband reflectivity and transmission of the APCW, a broadband super-luminescent diode optical source and optical spectrum analyzer was used. Figure 3.31(a) shows the measured normalized reflection R and transmission T spectra over a frequency range of 320-360 THz for a typical APCW waveguide. The measured spectra demonstrate that the fabricated APCW has the desired photonic bandgap, with the dielectric and air band-edges closely aligned with D1 and D2 lines of Cs, respectively, and in reasonable agreement with the theoretical spectra in Figure 3.31(c) and (d). From the average reflection level within the photonic bandgap, we estimate the total single-pass coupling from the optical fiber to APCW to be $\approx (60 \pm 5)\%$. The high frequency oscillatory behavior of the reflected and transmitted intensities is due to parasitic reflections from the AR-coated input fiber facet ($\approx 0.1\%$ reflection) and the input tether ($\approx 0.2\%$). Based upon previous measurements for similar waveguides, we estimate that the power loss coefficient of the unpatterned nanobeam section is $\approx 4 \text{ dB/cm}$. Because of the finite length of the APCW in these final devices, the spectral regions near the bandgap exhibit slowly oscillating fringes in transmission and reflection which can be interpreted as low-finesse cavity resonance of the APCW section. FDTD simulations reproduce this oscillatory behavior as shown in Figure 3.31(c) and (d). The enhancement of the Γ_{1D} will be similarly oscillatory, in analogy with the Purcell effect in cavity QED [46]. We image the scattered light directly above the waveguide as the frequency of a laser source is scanned across the slow fringes at the band-edge. As demonstrated in Figure 3.31(d) (red and blue traces), the scattered radiation from the APCW region of the waveguide is modulated as the input frequency is scanned from resonance to anti-resonance. Based upon the measured enhancement of intensity within the APCW (normalized with respect to illumination several THz from the bandgap) of ≈ 30 (i.e., a cavity finesse of ≈ 10), we estimate that at the reflection minimum nearest the bandgap, $\Gamma_{1D}/\Gamma_0 \approx 20$ for a Cs atom in the $6^2P_{3/2} |F=5, m_f=0\rangle$ excited state. The optical power handling capabilities of our devices ultimately limit the trapping

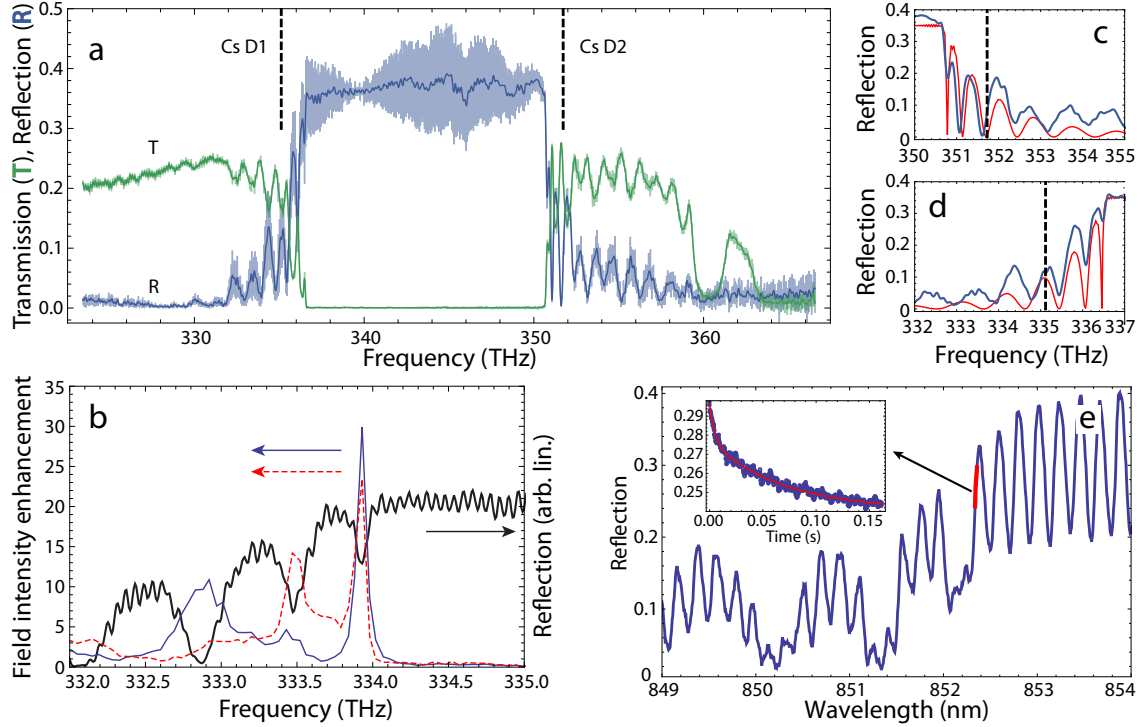


Figure 3.31: **Reflection and Transmission Spectra.** (a): Plot of the measured reflection and transmission spectra of the complete device. A smoothing filter is applied to the raw (transparent curves) reflection measurement, yielding the solid lines. Within the bandgap, the transmitted optical power is 30 dB below the reflected power, consistent with optical spectrum analyzer noise floor. (b): Intensity of the scattered light imaged from a region near the center (blue) and 1/3 from the end (red) of the photonic crystal section and (black) reflected optical power as functions of the wavelength of an incident probe laser. (c,d): FDTD simulation (red) and measurements (blue) of the reflection spectra near the air (c) and dielectric (d) band of the device. (e): Thermal tuning of a waveguide reflection spectrum (red line) with respect to the device reflection spectrum (blue) and time domain response of the device reflectivity (inset) to a step function input for which the intra-device power is $\approx 60 \mu\text{W}$. The time-domain response is fit with a double-exponential function with time constants of 70 ms and 5 ms.

schemes we can consider. Figure 3.31(e) shows the time and frequency dependent reflection signal of the single-mode laser, with frequency tuned to the band edge of the APCW. In this measurement, a heating laser, with a frequency of 335 THz is abruptly switched on at the input fiber port using an acousto-optic modulator at time $t = 0$, and then switched off at $t = 200$ ms. The increases in the temperature for a device in ultrahigh vacuum can be estimated by measuring the shift of the fast fringe shown in Figure 3.31(a). For an input power of $95 \mu\text{W}$, which corresponds to an intra-device power of approximately $60 \mu\text{W}$, we measure a wavelength shift of the reflection spectrum of $\Delta\lambda = 40$ pm. For a thermo-optic coefficient of Si_3N_4 , this corresponds to an average temperature rise of $\Delta T \approx 2^\circ\text{C}$. This rise is roughly an order of magnitude smaller than the temperature rise of our waveguide devices without extra tether arrays used to dissipate heat. The waveguide technology presented here resemble an important step towards experiments with ultracold atoms and nanophotonic chip-based optical circuits. The chip-based technology allows nearly full optical access for cooling manipulation of atoms in the near-field of nanowire waveguides. Integrated optical fibers also allow for highly efficient optical input and output channels for light coupled to arrays of atoms trapped along the slot of the APCW. Through lithographically patterned nanowire waveguides, we have shown that photonic bandgaps and band-edges may be reliably produced in the vicinity of electronic transitions of atoms, a key requirement for strong coupling atoms to the guided modes of the structure. Indeed, current experiments [53] with the same waveguide design have yielded a spontaneous emission coupling factor of $\Gamma_{1D}/\Gamma' = 0.32 \pm 0.08$ for one Cs atom localized near the peak of the probe mode of the APCW (Figure 3.31(a)). Further improvements in waveguide performance resulting from lower optical absorption and scattering loss in the nanowire waveguides should enable the trapping of atoms via the fields of far off-resonant guided modes [57]. In addition, the mechanical compliance of the suspended nanowire waveguide enables novel electro-mechanical tuning methods to those recently demonstrated in tunable Si nanophotonic structures [64]. Such fine-tuning would not only allow for precise alignment of photonic band-edges with atomic resonance, enabling strong light-matter interactions, but also dynamic atom-photon circuits in which optical dispersion of the APCW could be changed rapidly in comparison to the time scales for atomic radiative processes (e.g., photon mediated atom-atom interactions).

Chapter 4

Integrated Phononic Cavity with Superconducting Circuits on Si_3N_4 Membranes

This chapter is an overview of our electromechanical system consisting of phononic cavity coupled with a superconducting LC resonator. One of the main motivations behind such a system is to implement an optical-to-microwave conversion for quantum networks. We will review the theory behind the optical-to-microwave conversion and realistic parameters for such a system. This chapter also covers the design of the mechanics and microwave circuits and reviews our extensive investigation of substrate material properties to achieve high-quality parameters in both these regimes. We then illustrate in detail the fabrication process used to produce superconducting wires coupled with mechanics on a silicon nitride membrane. Using a dilution refrigerator to cool our samples down to temperatures ≈ 10 mK, we show the measurement procedures which allow us to characterize our system.

4.1 Optical to Microwave Conversion

4.1.1 Motivations for Optical to Microwave Wavelength Conversion

One of the overarching goals of research in quantum information and processing is the ability to build networks of quantum nodes which can efficiently communicate with one another [59]. There are a variety of systems that have been investigated in order to build such a network, each having benefits that make them ideal for this endeavor. Optics has been envisioned as a fundamental building block of communication in these arrangements in part because of their high detection efficiencies, noise resilience and low losses in optical fibers over long distances. Superconducting microwave circuits have been a focus of research because of their ability to utilize strong quantum non-linearities and large coupling strengths for quantum processing. Optomechanical systems have been proposed as

a coherent interface between noise resilient telecom optics and superconducting circuits consisting of fast, high fidelity quantum gates in order to build hybrid quantum networks. It was recently experimentally demonstrated that one could operate electromechanical systems in their mechanical ground state by engineering large electromechanical couplings as shown with piezoelectric systems [8] and capacitive drum-head resonators [7]. Coherent state transfer between electromagnetic fields and mechanical modes has been demonstrated in both optical [65, 66] and microwave regimes [67]. It is currently an open challenge to integrate high-quality optics, mechanics, and microwave devices in order to perform efficient quantum limited wavelength conversion at single microwave photon powers as mechanical transduction between microwave and optics has only been demonstrated on classical states [68]. Coupling GHz mechanics to the optics and microwave systems provides a way to bridge these two systems into an integrated electro-optomechanical quantum circuit. Such a system could provide an interface for circuits and atoms, quantum state synthesis and distribution, and microwave photon counting. One could use GHz phonons to perform experiments with photon to phonon translators, phonon waveguides, and non-classical phonon states.

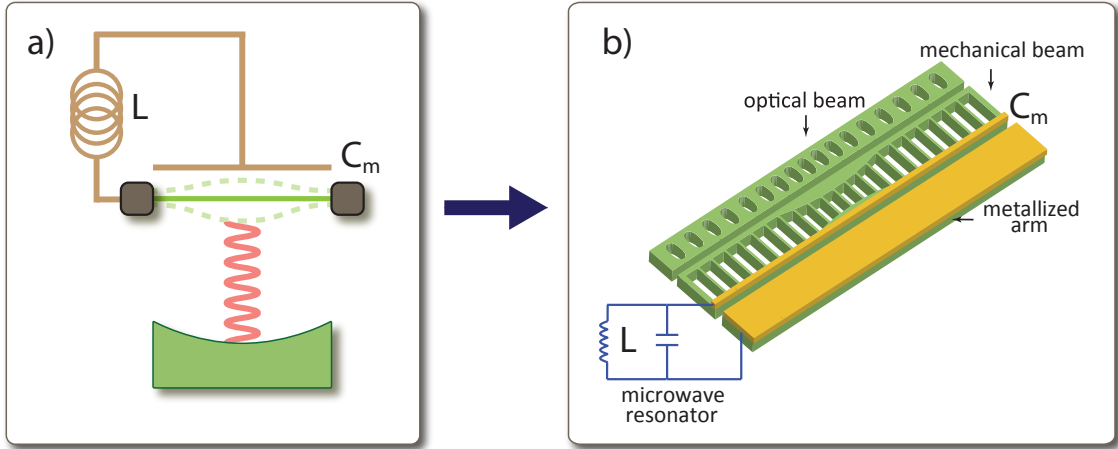


Figure 4.1: **Envisioned Wavelength Conversion Scheme.** (a) Here we show a general analogue of a shared mechanical mode (a movable membrane) as a transducer between an optical mode (optical cavity) and a microwave resonator. Here the membrane modulates the frequency of the LC resonator capacitively and modulates the optical resonator dispersively. (b) General schematic of the wavelength conversion setup which utilizes nanobeams. An optical cavity nanobeam can be designed to couple to the center phononic cavity, which is also capacitively coupled to a superconducting LC resonator

4.1.2 Theoretical Background for Wavelength Conversion

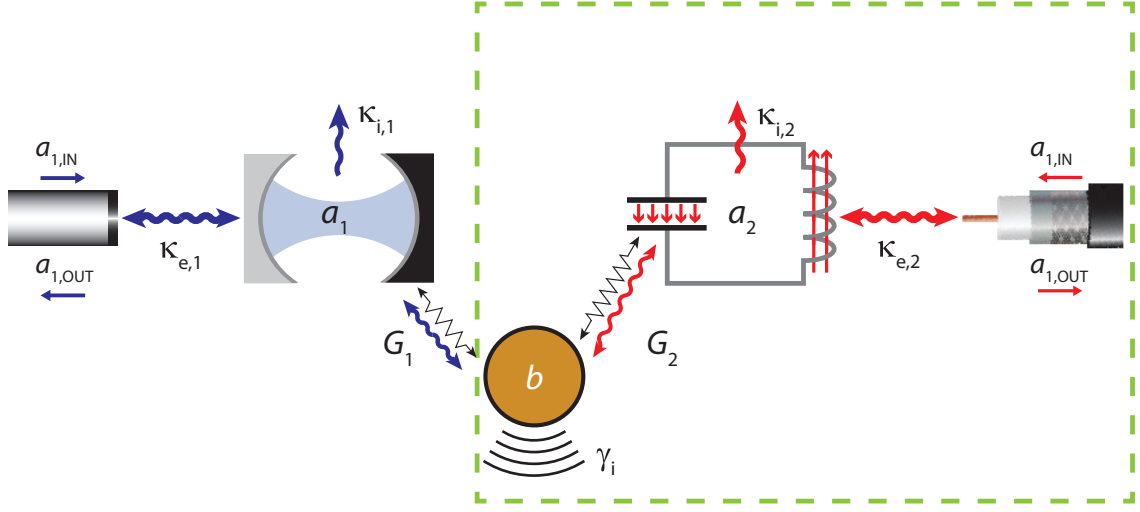


Figure 4.2: **General Model for Optical to Microwave Conversion.** A telecom optical mode, \hat{a}_1 , and microwave mode, \hat{a}_2 , are coupled to the same mechanical mode, \hat{b} , each with a coupling strength to the mechanics of G_1 and G_2 . The coupling of the optical input and output signals, $\hat{a}_{in,1}$ and $\hat{a}_{out,1}$ to the optical resonator are characterized by the extrinsic coupling, $\kappa_{e,1}$, just as the microwave input and output, $\hat{a}_{in,2}$ and $\hat{a}_{out,2}$ are characterized by $\kappa_{e,2}$. The intrinsic loss rates for the optical, microwave, and mechanical modes are $\kappa_{i,1}$, $\kappa_{i,2}$, and γ_i , respectively. Black colored components of the resonators are mechanically compliant components that couple to the mechanical mode. (Based on Figure from [65])

We begin by considering an optical mode, \hat{a}_1 , and a microwave mode, \hat{a}_2 , coupled to the same mechanical mode, \hat{b} , as shown in Figure 4.2. This coupling can be through capacitive or dispersive coupling. The Hamiltonian can be written as,

$$\hat{H} = \hbar\Delta\hat{a}_1^\dagger\hat{a}_1 + \hbar\Delta\hat{a}_2^\dagger\hat{a}_2 + \hbar\omega_m\hat{b}^\dagger\hat{b} + \hbar g_1\hat{x}\hat{a}_1^\dagger\hat{a}_1 + \hbar g_2\hat{x}\hat{a}_2^\dagger\hat{a}_2 \quad (4.1)$$

The optical and microwave mode have frequencies, $\omega_{o,1}$, and, $\omega_{o,2}$, and each driven by a laser at $\omega_{\ell,1}$ and $\omega_{\ell,2}$, respectively. The Hamiltonian above is described in an interaction picture where $\Delta = \omega_{o,1} - \omega_{\ell,1} = \omega_{o,2} - \omega_{\ell,2}$. We drive the system with a strong coherent field red-detuned by a mechanical frequency, $\Delta_1 = \Delta_2 = \omega_m$, which brings a beam splitter interaction between the mechanical modes and optical modes at an enhanced coupling rate $G_1 = g_1 |\alpha_1|$ and $G_2 = g_2 |\alpha_2|$ where α_1 and α_2 are the square root of the photon occupation in the optical mode such that $\alpha_1 = \sqrt{n_{c,1}}$ and $\alpha_2 = \sqrt{n_{c,2}}$. When the coupling between optical and mechanical modes, G_1 and G_2 are weak compared to the linewidths of the optics and microwave, κ_1 and κ_2 we have a system where the cavities are adiabatically eliminated giving us a effective mechanical loss rates, γ_{OM} into each of the optical modes. This allows for a transfer of excitations from one mode to another. Here we derive

the efficiencies of these conversions using scattering matrices to demonstrate how this system works in the weak-coupled, sideband-resolved case where $\omega_m \gg \kappa \gg \gamma_{OM}$.

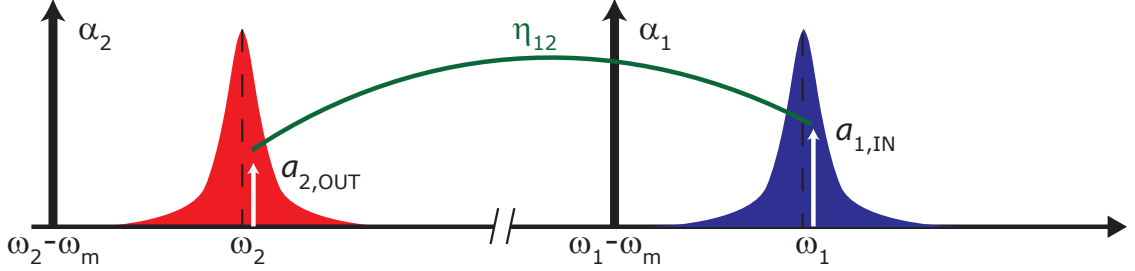


Figure 4.3: **Coherent pump tones for wavelength conversion.** This schematic shows an optical mode (in blue) at ω_1 with a strong coherent drive, α_1 , at frequency red-detuned by a mechanical frequency $\omega_1 - \omega_m$ and a microwave mode (in red) at ω_2 also pumped by a coherent drive with strength α_2 at a frequency $\omega_2 - \omega_m$. This allows linearization of the Hamiltonian such that one can write the interaction Hamiltonian in the form of a beam splitter Hamiltonian. η_{12} is the conversion efficiency from higher frequency mode at ω_1 to the lower frequency mode at ω_2

We begin by looking at the Hamiltonian of this system with strong coherent driving tones set at mechanical frequency red-detuned from each of the resonator's frequencies as shown in Figure 4.3. After linearization of the Hamiltonian and implementing a rotating wave approximation for red-detuned pumping we arrive at the Hamiltonian with a beam-splitter like interaction term,

$$\hat{H}' = \hbar\Delta\hat{a}_1^\dagger\hat{a}_1 + \hbar\Delta\hat{a}_2^\dagger\hat{a}_2 + \hbar\omega_m\hat{b}^\dagger\hat{b} + \hbar G_1(\hat{a}_1^\dagger\hat{b} + \hat{a}_1\hat{b}^\dagger) + \hbar G_2(\hat{a}_2^\dagger\hat{b} + \hat{a}_2\hat{b}^\dagger) \quad (4.2)$$

The last two terms of equation 4.4 are the interaction Hamiltonian of the system,

$$\hat{H}'_{int} = \hbar G_1(\hat{a}_1^\dagger\hat{b} + \hat{a}_1\hat{b}^\dagger) + \hbar G_2(\hat{a}_2^\dagger\hat{b} + \hat{a}_2\hat{b}^\dagger) \quad (4.3)$$

which give a clear representation of the physics involved in the wavelength conversion scheme. We see with the first term in \hat{H}'_{int} that optical photons in cavity mode 1 are annihilated to coherently create a phonon in the mechanical mode at a rate G_1 and vice versa. Accordingly the second term shows how a phonon in the mechanical mode can be annihilated to coherently create microwave photons in cavity 2 at a rate G_2 and vice versa. This is a symmetric process so that this type of wavelength conversion can happen in either direction (microwave-to-optical or optical-to-microwave). We can understand the wavelength conversion process and conversion efficiencies by using the Heisenberg-

Langevin equations to describe the time-evolution of operators, which can be expressed as

$$\dot{\hat{a}} = -\frac{i}{\hbar} [\hat{a}, H] - \frac{\kappa}{2} \hat{a} - \sqrt{\kappa_e} \hat{a}_{\text{in}} - \sqrt{\kappa'} \hat{\eta}_{\text{opt}} \quad (4.4)$$

The first term is the nominal time-evolution of an operator in the interaction picture, $\dot{\hat{a}} = -\frac{i}{\hbar} [\hat{a}, H]$. The terms that follow are empirically added with internal dissipation of the resonator modes (κ), the couplings with the input fields ($\sqrt{\kappa_e} \hat{a}_{\text{in}}$) and other noise terms represented as $\sqrt{\kappa'} \hat{\eta}_{\text{opt}}$ where $\hat{\eta}_{\text{opt}}$ is a non-correlated noise operator such that $\langle \hat{\eta}_{\text{opt}}^\dagger(t) \hat{\eta}_{\text{opt}}(t') \rangle = n_{\text{opt}} \delta(t - t')$ where n_{opt} is the optical noise occupation. Applying this time evolution to the optical mode, (\hat{a}_1), microwave mode, (\hat{a}_2), and the mechanical mode (\hat{b}) we get

$$\dot{\hat{a}}_1 = -i\Delta_1 \hat{a}_1 - \frac{\kappa}{2} \hat{a}_1 - \sqrt{\kappa_{e,1}} \hat{a}_{\text{in},1} - \sqrt{\kappa'} \hat{\eta}_{\text{opt},1} - iG_1 \hat{b} \quad (4.5)$$

$$\dot{\hat{a}}_2 = -i\Delta_2 \hat{a}_2 - \frac{\kappa}{2} \hat{a}_2 - \sqrt{\kappa_{e,2}} \hat{a}_{\text{in},2} - \sqrt{\kappa'} \hat{\eta}_{\text{opt},2} - iG_2 \hat{b} \quad (4.6)$$

$$\dot{\hat{b}} = -i\omega_m \hat{b} - \frac{\gamma}{2} \hat{b} - \sqrt{\gamma} \hat{\eta}_m - iG_1 \hat{a}_1 - iG_2 \hat{a}_2 \quad (4.7)$$

We have evaluated the commutator, $-\frac{i}{\hbar} [\hat{a}, H]$, in Equation 4.4. $\hat{\eta}_m$ in the time-evolution equation for the mechanical mode is the mechanical thermal fluctuation field. The equations for the time evolution of the mode operators are linear which makes them easier to convert into the frequency domain using Fourier transforms $F(\dot{\hat{a}}(t)) = i\omega \hat{a}(\omega)$ which gives the expressions

$$\hat{a}_1(\omega) = \frac{-iG_1 \hat{b} - \sqrt{\kappa_{e,1}} \hat{a}_{\text{in},1} - \sqrt{\kappa'} \hat{\eta}_{\text{opt},1}}{i(\Delta_1 - \omega) + \frac{\kappa}{2} \hat{a}_1} \quad (4.8)$$

$$\hat{a}_2(\omega) = \frac{-iG_2 \hat{b} - \sqrt{\kappa_{e,2}} \hat{a}_{\text{in},2} - \sqrt{\kappa'} \hat{\eta}_{\text{opt},2}}{i(\Delta_2 - \omega) + \frac{\kappa}{2} \hat{a}_2} \quad (4.9)$$

$$\hat{b}(\omega) = \frac{-iG_1 \hat{a}_1 - iG_2 \hat{a}_2 - \sqrt{\gamma} \hat{\eta}_m}{i(\omega_m - \omega) + \frac{\gamma}{2}} \quad (4.10)$$

Using these equations, we can solve for the optical mode operator in terms of input signals such that,

$$\hat{a}_1(\omega) = \alpha \hat{a}_{\text{in},1} + \beta \hat{a}_{\text{in},2} + \delta \quad (4.11)$$

where α , β , and δ are coefficients used to simplify the expression. One can then impose the boundary condition such that

$$\hat{a}_{\text{out},1} = \sqrt{\kappa_{e,1}} \hat{a}_1 + \hat{a}_{\text{in},1} \quad (4.12)$$

in which we can use the equation 4.11 to arrive at

$$\begin{aligned} \hat{a}_{\text{out},1} &= \alpha \sqrt{\kappa_{e,1}} \hat{a}_{\text{in},1} + \beta \sqrt{\kappa_{e,1}} \hat{a}_{\text{in},2} + \delta \sqrt{\kappa_{e,1}} + \hat{a}_{\text{in},1} \\ &= (1 + \alpha \sqrt{\kappa_{e,1}}) \hat{a}_{\text{in},1} + \beta' \hat{a}_{\text{in},2} + \delta' \end{aligned} \quad (4.13)$$

where β' and δ' are newly assigned coefficients that include $\sqrt{\kappa_{e,1}}$. One can then interpret the coefficient β' as the conversion matrix element between the input to optical mode to the output of microwave mode which in its full form is

$$\beta' = \frac{\sqrt{\kappa_{e,1}}\sqrt{\kappa_{e,2}}G_1G_2}{\chi_1\chi_2\left(-\chi_m - \frac{G_1^2}{\chi_1} - \frac{G_2^2}{\chi_2}\right)} \quad (4.14)$$

where χ_1 , χ_2 , χ_m are the susceptibilities of the optical mode, microwave mode, and mechanical mode, respectively, and can be shown to be

$$\chi_1 = \frac{\kappa_1}{2} + i\Delta_1 - i\omega \quad (4.15)$$

$$\chi_2 = \frac{\kappa_2}{2} + i\Delta_2 - i\omega \quad (4.16)$$

$$\chi_m = \frac{\gamma}{2} + i\omega_m - i\omega \quad (4.17)$$

We assume we are in the sideband-resolved limit where $\omega_m \gg \kappa$ and we consider the case when we pump around a mechanical frequency red-detuned from the cavity. Now we look at the optomechanical damping terms $\gamma_{OM,1}$ and $\gamma_{OM,2}$, which represent the coupling of the mechanics to the optical and microwave mode and are given by

$$\begin{aligned} \gamma_{OM,k} &= 2|G_k|^2 \text{Re} \left[\frac{1}{i(\Delta_k - \omega_m) + \kappa_k/2} - \frac{1}{-i(\Delta_k + \omega_m) + \kappa_k/2} \right] \\ &= \frac{4|G_k|^2}{\kappa_k} \quad \text{for } \Delta \approx \omega_m \quad k = (1, 2) \end{aligned} \quad (4.18)$$

The last simplification is made for detuning of a mechanical frequency where this becomes the same as looking at spectral characteristics at detunings from ω_m that are very small compared to κ . We can make sense of this approximation as the mechanical mode spectrally filtering the wavelength conversion scheme with bandwidth $\gamma \ll \kappa$. Using the our approximations for the optomechanical damping rates at $\Delta \approx \omega_m$, we can write the conversion coefficient as

$$\begin{aligned} \beta' &= \sqrt{\kappa_{e,1}}\sqrt{\kappa_{e,2}} \left(\frac{G_1}{\kappa_1} \right) \left(\frac{G_2}{\kappa_2} \right) \frac{1}{\left(\chi_m + \frac{\gamma_{OM,1}}{2} \frac{\gamma_{OM,2}}{2} \right)} \quad \text{for } \Delta \approx \omega_m \\ &= \sqrt{\frac{\kappa_{e,1}}{\kappa_1}} \sqrt{\frac{\kappa_{e,2}}{\kappa_2}} \frac{\sqrt{\gamma_{OM,1}\gamma_{OM,2}}}{2} \frac{1}{i(\omega_m - \omega) + \frac{\gamma_{TOT}}{2}} \\ &= \sqrt{\eta_{ex,1}\eta_{ex,2}} \frac{\sqrt{\gamma_{OM,1}\gamma_{OM,2}}}{i(\omega_m - \omega) + \frac{\gamma_{TOT}}{2}} \end{aligned} \quad (4.19)$$

where the total damping rate $\gamma_{TOT} = \gamma + \gamma_{OM,1} + \gamma_{OM,2}$ and $\sqrt{\eta_{ex,i}} = \sqrt{\kappa_{ex,i}/2\kappa_i}$ and $k = (1, 2)$ [65]. It is worth noting that susceptibilities $\chi_k = \kappa_k/2 + i\Delta_k - i\omega \approx \kappa_k/2 + i\Delta_k - i\omega_m$ for $\omega \approx \omega_m$ which simplifies even further to $\chi_k \approx \kappa_k/2$ for $\Delta_k \approx \omega_m$. Equation 4.19 has been the conversion coefficient for the case of symmetric coupling where G_1 and G_2 have the same sign. For the asymmetric case

we obtain

$$\beta' = -\sqrt{\eta_{ex,1}\eta_{ex,2}} \frac{\sqrt{\gamma_{OM,1}\gamma_{OM,2}}}{i(\omega_m - \omega) + \frac{\gamma_{TOT}}{2}} \quad \text{for } \Delta \approx \omega_m \quad (4.20)$$

The physical quantity we want to measure is the spectral density of the output signal, which is expressed as

$$S_{out}(\omega) = \int_{-\infty}^{+\infty} d\omega' \left\langle \hat{a}_{out}^\dagger(\omega) \hat{a}_{out}(\omega') \right\rangle \quad (4.21)$$

In order to properly evaluate the spectral density, we will work through the expectation value in the integrand using a general operator \hat{c} for the moment. We begin with the definition of the expectation value where

$$\begin{aligned} \langle \hat{c}^\dagger(\omega_2) \hat{c}(\omega_1) \rangle &= \int_{-\infty}^{\infty} \int_{-\infty}^{\infty} e^{i\omega_2 t_2} e^{i\omega_1 t_1} \langle \hat{c}^\dagger(t_2) \hat{c}(t_1) \rangle dt_1 dt_2 \\ &= \int_{-\infty}^{\infty} \int_{-\infty}^{\infty} e^{i\omega_2 t_2} e^{i\omega_1(t_2+\tau)} \langle \hat{c}^\dagger(t_2) \hat{c}(t_2+\tau) \rangle dt_2 d\tau \quad \text{for } t_1 = t_2 + \tau \end{aligned} \quad (4.22)$$

We consider the fact that auto-correlations are invariant for time-translations such that

$$= \int_{-\infty}^{\infty} \int_{-\infty}^{\infty} e^{i\omega_2 t_2} e^{i\omega_1(t_2+\tau)} \langle \hat{c}^\dagger(0) \hat{c}(\tau) \rangle dt_2 d\tau \quad (4.23)$$

$$= \underbrace{\int_{-\infty}^{\infty} dt_2 e^{i(\omega_1+\omega_2)t_2}}_{2\pi\delta(\omega_1+\omega_2)} \underbrace{\int_{-\infty}^{\infty} e^{i\omega_1\tau} \langle \hat{c}^\dagger(0) \hat{c}(\tau) \rangle d\tau}_{S_{cc}(\omega_1)} \quad (4.24)$$

We recognize that the second integral is by definition the spectral density S_{cc} of the operator \hat{c} . We can use these to evaluate the original expectation value, Equation 4.22, so that

$$\langle \hat{c}^\dagger(\omega_2) \hat{c}(\omega_1) \rangle = 2\pi\delta(\omega_1 + \omega_2) \cdot S_{cc}(\omega_1) \quad (4.25)$$

and from here we can solve for

$$S_{cc}(\omega_1) = \frac{1}{2\pi\delta(\omega_1 + \omega_2)} \langle \hat{c}^\dagger(\omega_2) \hat{c}(\omega_1) \rangle \quad (4.26)$$

and if we consider that $\omega_1 = \omega$ and $\omega_2 = -\omega$, then

$$S_{cc}(\omega) = \frac{1}{2\pi\delta(0)} \langle \hat{c}^\dagger(\omega) \hat{c}(\omega_1) \rangle \quad (4.27)$$

Now we can go back to considering our original system where we would like to evaluate the free spectral range of our output signal $\hat{a}_{out,1}$

$$S_{out,1}(\omega) = \frac{1}{2\pi\delta(\omega + \omega')} \left\langle \hat{a}_{out,1}^\dagger(\omega') \hat{a}_{out,1}(\omega) \right\rangle \quad (4.28)$$

In order to calculate the wavelength conversion efficiency from the input signal at microwave mode, $\hat{a}_{in,2}$, into the output in the optical cavity, $\hat{a}_{out,1}$ we want to look at the term of interest in equation 4.13, $\beta' \hat{a}_{in,2}$ whose spectral density is expressed as

$$\begin{aligned} & \frac{1}{2\pi\delta(\omega + \omega')} \langle (\beta'(\omega') \hat{a}_{in,2}(\omega'))^\dagger (\beta'(\omega) \hat{a}_{in,2}(\omega)) \rangle \\ &= \beta'^*(\omega') \beta'(\omega) \delta(\omega' + \omega) \frac{1}{2\pi\delta(\omega' + \omega)} \langle \hat{a}_{in,2}^\dagger(\omega') \hat{a}_{in,2}(\omega) \rangle \\ &= \beta'^*(-\omega) \beta'(-\omega) \frac{1}{2\pi\delta(\omega + \omega')} \langle \hat{a}_{in,2}^\dagger(\omega') \hat{a}_{in,2}(\omega) \rangle \end{aligned} \quad (4.29)$$

which allows us to express the spectral density of the optical output signal in terms of the microwave input spectral density.

$$S_{out,1}(\omega) = \beta'^*(-\omega) \beta'(-\omega) S_{in,2}(\omega) \quad (4.30)$$

And using our expression for β' in equation 4.20 we can express our wavelength conversion efficiency as

$$\eta = \eta_{ex,1} \eta_{ex,2} \frac{\gamma_{OM,1} \gamma_{OM,2}}{(\omega + \omega_m)^2 + \left(\frac{\gamma_{TOT}}{2}\right)^2} \quad (4.31)$$

We see that we can get the maximum wavelength conversion efficiency when $\omega = -\omega_m$. And for both the symmetric and asymmetric cases we find our maximum efficiency can be expressed as

$$\eta_{max} = 4\eta_{ex,1} \eta_{ex,2} \frac{\gamma_{OM,1} \gamma_{OM,2}}{(\gamma + \gamma_{OM,1} + \gamma_{OM,2})^2} \quad (4.32)$$

4.2 Microwave Resonator Coupling to Phononic Cavity

We have reviewed the mathematical formalism behind the wavelength conversion scheme from the microwave to optical regime. As seen in Figure 4.2 (boxed in green), the topic of the following sections will specifically concentrate on our work towards an electromechanical system with a high coupling rate that could be integrated with an electro-optical system towards a full wavelength conversion platform. We look at formalism for calculating the electromechanical coupling which affects our ability to achieve high η_{max} . Our system envisions a system in which a superconducting LC resonator has a capacitance, C_m , which is modulated by a mechanical oscillator. A system possessing a high $\omega_m \times Q_m$ product makes it easier to sideband cool the system down to its motional ground state from relatively high temperatures ($T \approx 3K$) using passive dilution refrigeration. With an oscillator near its motional ground state one can arbitrarily control its quantum states and detect these states near the Heisenberg limit. This is possible when the oscillator's temperature T is reduced so that $k_B T < \hbar(\omega_m Q_m)$, where ω_m is the resonance frequency of the oscillator, k_B is Boltzmann's constant and $\hbar = h/2\pi$. In order to get a system with high $\omega_m \times Q_m$ one can achieve this by using

high frequency mechanics ($\omega_m = 450\text{MHz}$) with high mechanical quality factors ($Q_m \approx 10,000$) like those experimentally achieved with breathing modes in optomechanical beams [6]. The mechanical element consists of a localized breathing mode in the center of the nanobeam using phononic mirrors. The motion of the breathing mode would then be coupled capacitively to an LC resonator in order to form an electromechanical quantum system. A nanobeam is structure that can be easily integrated with another optical nanobeam to have an on-chip wavelength conversion system using optical and mechanical nanobeam resonators as seen in Figure 4.2.

4.2.1 Overview of Electromechanical Coupling

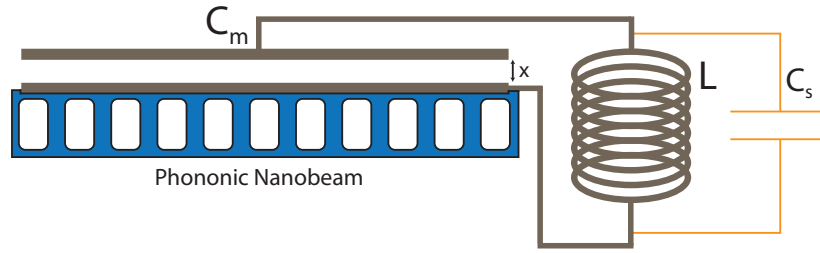


Figure 4.4: **One-sided Circuit Coupling to Nanobeam.** Schematic shows how the nanobeam is coupled capacitively to the LC resonator. The mechanically modulated capacitance C_m is the capacitance of the capacitor formed by the nanobeam. The size of the gap, x , is modulated at the frequency of the vibrations in the nanobeam, ω_m which opens and closes the gap. C_m forms an LC resonator with inductor, L . Parasitic capacitance is an additional capacitance resulting from potential difference between inductor wires and capacitance between the inductor and the substrate.

In this section, we will review electromechanical coupling strength, g_{EM} , of an LC microwave resonator to the mechanical mode of a nanobeam which is directly related to the achievable wavelength conversion efficiencies, η_{max} from microwave to optical, as seen in Equation 4.32 where $\gamma_{OM,1} \propto g_{EM}$. We have already been over the mathematical formalism behind the wavelength conversion and we will concentrate on the formalism for calculating the electromechanical coupling, g_{EM} . We consider a nanobeam which forms one side of a movable capacitor which together with an inductor forms an LC microwave resonator with resonance frequency $\omega_{LC}/2\pi = 1/\sqrt{LC_{tot}}$ where L is the inductance and $C_{tot} = (C_m + C_s)$ is the sum of the modulated capacitance and the stray capacitance of the inductor. We can calculate the electromechanical coupling as the rate of change in the frequency of the LC resonator with respect to a change in the size of the capacitive gap which we can show is,

$$g_{EM} = \frac{g_0}{x_{zpf}} = \frac{\partial \omega_{LC}}{\partial \Delta x} = -\eta \frac{\omega_{LC}}{2C_m} \frac{\partial C_m}{\partial \Delta x} \approx -\eta \frac{\omega_{LC}}{2x} \quad (4.33)$$

where x_{zpf} is the zero-point fluctuation displacement, Δx the mechanical mode displacement (change in size of the capacitive gap), and the participation factor $\eta = C_m/C_{tot} = C_m/(C_m + C_s)$. Com-

pared to other similar systems with drum-head resonators capacitively coupled to superconducting circuit [7] where the modulated capacitance is large compared to stray capacitance, $C_m \gg C_s$, our nanobeam system has a small modulated capacitor as one would expect from the capacitance between two small low-mass aluminum wires only $\approx 100\text{nm}$ tall (as opposed to the large C_m achieved with drum-head resonators with larger capacitive surface area). Because of the small-mass (i.e., high frequency) geometry of our system where we modulate the capacitance between two wires, we find that our modulated capacitance can be on the order of our stray capacitance ($C_m \approx C_s$). Looking at the phononic nanobeam's electromechanical coupling to the superconducting circuit where $g_{\text{EM}} \propto \eta$ we find that our electromechanical coupling is maximized when $C_s \ll C_m$ and $\eta \approx 1$. The maximization of the participation factor, η , then relies on how large we can make C_m and how small we can make the stray capacitance C_s . The stray capacitance of the inductor will be determined by the geometry of the inductor and by the material substrate, we fabricate the superconducting circuit on.

4.3 Substrate Materials for Microwave and Mechanics

We reviewed how the maximal electromechanical coupling can be achieved by increasing the modulated capacitance, C_m , and decreasing the stray capacitance, C_s , as much as possible. Modulated capacitance will be a function of the geometric design of the mechanical element, mainly the capacitive gap size (discussed in Section 4.4.4). Parasitic capacitance is an intrinsic capacitance that exists between parts of an electrical circuit just from their proximity to one another. We also know that a non-zero capacitance always exists between any two conductors and only becomes more dominant at high frequencies with closely spaced conductors. This is especially true with nanofabricated MEMS inductor coil operating in the GHz range with wires that can have tight spacings only limited by electron-beam lithography resolution (on the order of 100nm spacing). When two conductors at different potentials are in close proximity, they are affected by one another's electric field and store opposite electric charges like one would observe in a capacitor. Changing the potential, V , between two conductors requires a current i in/out of the conductors to charge/discharge them. We can express that current as $i = C(dV/dt)$ where C is the capacitance between the conductors. This is simple to imagine with an inductor coil which often behaves as though it has a parallel capacitance, as seen in Figure 4.4 because of the closely spaced windings. When a potential difference exists across the coil, wires lying next to each other are at different potentials. They act like plates of a capacitor and store charge. A change in voltage across the coil requires extra current to charge and discharge these small capacitors that are formed between wires. In a low-frequency circuits where the voltage changes slowly this extra current, i , is negligible. But in high frequency circuits used in quantum optics applications, the voltage change, dv/dt , is significant because of the quickly chang-

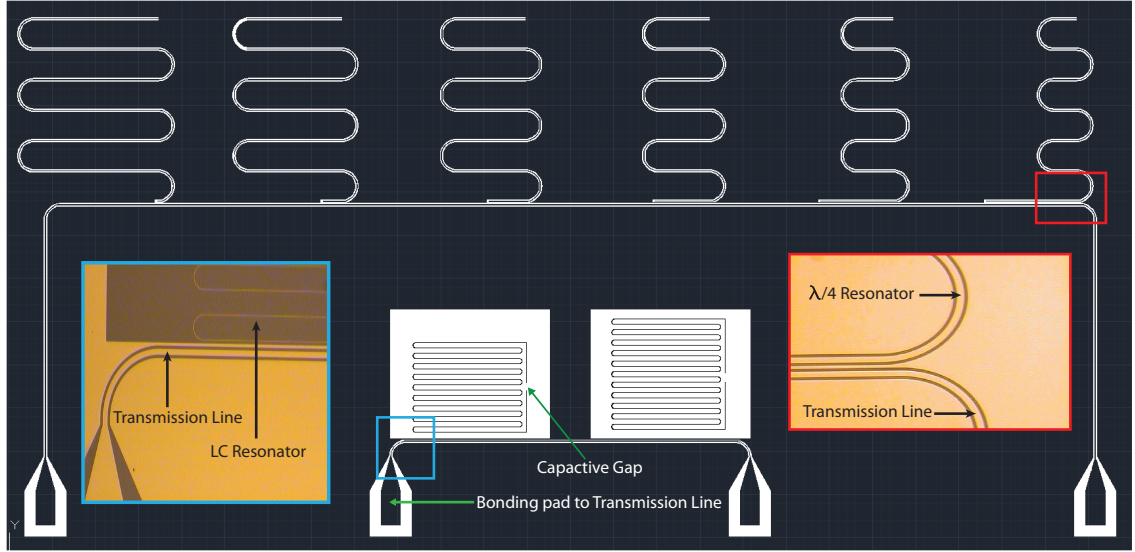


Figure 4.5: **Resonator and Transmission Line Layout.** Here we show a schematic of the circuit layout we evaporated onto different high resistivity substrates in order to test the quality of our aluminum films. We show 6 CPW quarter-wave resonators (light blue) capacitively coupled to a transmission line (surrounded by insulator in pink). The transmission line and the surrounding areas (in black) consists of a 100nm layer of electron-beam-evaporated aluminum. The insulation around the transmission line is just area where no aluminum has been evaporated. The quarter-wave resonators are also lithographically defined in the same way. We vary the coupling between each resonator to the transmission by varying the capacitor overlap (weakly coupled on the left to strongly coupled on the right).

ing voltage and induces a large extra current which effects the performance of our circuit resonator. The stray capacitance we just described is reliant on the wiring geometry of our inductor, which is discussed in Section 4.5.

However, another dominant source of stray capacitance is that which occurs between the wires and the substrate on which we fabricate our circuits. Because parasitic capacitance occurs between two conductors, we can try to eliminate it by using substrates which are insulators (high resistivity, ρ) and absent of doping or defects which can act as a charge carrier (conductors) and induce this parasitic capacitance. As seen in Section 4.2.1, large parasitic capacitances can dominate and significantly decrease the electromechanical coupling, g_{EM} . It is important to choose the appropriate chip substrate platform to fabricate the LC microwave resonators in order to reduce parasitic capacitance between them and the substrate. The optimal substrate required several properties that would allow us to fabricate high-quality superconducting circuits as well as high-quality mechanical nanobeam we can etch from the substrate using conventional fabrication methods. Substrates with high resistivities have decreased carrier concentrations whose presence can increase losses of the LC resonator circuit and adversely affect the microwave quality factor. We consider the dielectric losses

characterized by an effective loss tangent of a wire on a substrate,

$$(\tan \delta)_{\text{eff}} = F \tan \delta = \frac{F}{(\rho \omega \epsilon_0 \epsilon_1)} = \frac{1}{Q_D} \quad (4.34)$$

where $(\tan \delta)_{\text{eff}}$ is the effective loss tangent of the wire and substrate, F is the filling factor (of wire and substrate), $\tan \delta$ is the loss tangent of the dielectric substrate, ω is the angular frequency of the wave, ϵ_1 is the relative dielectric constant of the substrate, $\epsilon_0 = 8.85 \times 10^{-14}$ F/cm is the free space permittivity, and ρ is the resistivity of the substrate.

In order to characterize the suitability of the substrates for fabricating microwave resonators we fabricated a series of 6 aluminum CPW quarter-wave resonators coupled capacitively to a CPW transmission line as seen in Figure 4.5 in red. We also use a smaller second transmission line which coupled inductively to 2 LC resonators with meandering inductors and a static capacitor formed from a gap in the wire (in blue). The microwave resonators and the ground plane were evaporated onto different substrates in order to study the substrate's effects on the microwave circuit's quality factors. In our design we varied the external coupling to the quarter-wave resonators by changing the amount of capacitive overlap between them and the transmission line. These samples were then cooled to 10mK in a dilution refrigerator where the aluminum is superconducting, allowing us to significantly reduce losses due to resistance in the aluminum resonator wires and achieve high quality factors and provide significant suppression of the thermal noise around GHz microwave frequencies. We used high frequency microwave signals at room temperatures which have been shielded and filtered to mitigate the thermal noise that enters the dilution refrigerator setup. This allows us to send an RF transmission signal and probe the all the coupled resonators' properties by fitting to their Lorentzian dips in our output VNA spectrum corresponding to microwave cavity resonances where we could fit the resonators' internal, external, and loading quality factors.

4.3.1 Experiments: Substrate Effects on Microwave Resonator Quality Factors

Previous work in the nano-optomechanics community [44] [6] [21] [69] has shown the viability of semiconductor substrates (specifically silicon and silicon nitride) for fabricating high quality optical and mechanical materials, but in order to build an integrated wavelength conversion system, the substrate must also be suitable for fabricating high quality *microwave* cavities circuits. We fabricated the same pattern of aluminum LC and quarter-wave resonators on different types of substrates in order to test the losses incurred on the resonator through charge carriers in the substrate, resulting in lowered intrinsic quality factors.

Using a vector network analyzer measurement to measure the resonator's amplitude and phase response with a Lorentzian lineshape, as seen in Figure 4.6. We can retrieve microwave cavity param-

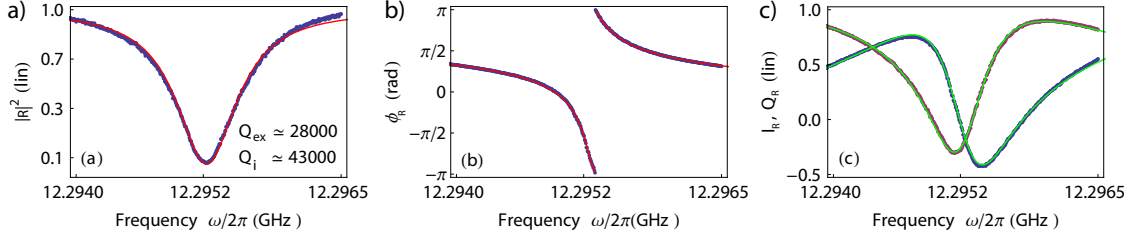


Figure 4.6: **Microwave Resonator Plots.** Normalized LC resonator reflection. (a): Amplitude response. (b): Phase response of the cavity. (c) Theoretical model of I and Q quadratures. Courtesy of Lukas Heinzle.

eters by fitting our I and Q quadratures from the VNA and fitting to the transmission and reflection coefficients. We fit the Lorentzian lineshapes from the microwave cavities in order to retrieve loaded, external and intrinsic quality factors (Q_L , Q_E , Q_i) which are related by the expression,









$$Q = \left(\frac{1}{Q_i} + \frac{1}{Q_E} \right)^{-1} \quad (4.35)$$

where we know the external coupling κ_{ex} can be in the complex form $\kappa_{ex}e^{iq}$ where q is the Fano-parameter and $Q_E = 1/\kappa_{ex}$. The substrates we tested in Figure 4.7 were done using the transmission circuit layout as seen in Figure 4.5, however, the data seen in Figure 4.6 is an example of the VNA measurements of LC cavities on silicon nitride membranes using a reflective geometry (the reasons for this are discussed in the Fabrication Section 4.4.2). The chips were wirebonded to a printed circuit board and connected to coaxial cables in the dilution refrigerator where they were cooled to ≈ 10 mK. In order to assess the suitability of different materials as substrates for superconducting circuits we first studied *standard candle* high resistivity (HR) substrates which are known for their low carrier densities that minimizes the loss tangent of a superconducting microwave resonators and minimize parasitic capacitance between the resonator and the substrate underneath. Starting with these ideal substrates allowed us to investigate the quality of the electron-beam evaporated aluminum that we would use to test the other substrates as seen in Figure 4.7. The standard candle materials used to test the inherent quality of the evaporated aluminum were high resistivity silicon ($\rho > 10,000 \Omega \cdot \text{cm}$) and sapphire substrates ($\rho > 10^{16} \Omega \cdot \text{cm}$), both well known for being ideal substrates for achieving low-loss microwave circuits.

High resistivity 1-0-0 silicon wafer (200 μm thick) has low doping concentrations, minimizing the free charge carriers that increase loss tangents of microwave resonators. We cleaved the wafer into 1cm \times 1cm pieces. Using a ZEP520A as a mask for a liftoff process we expose everything but the gaps in the coplanar waveguides using electron beam lithography. After developing and rinsing the exposed electron beam resist, we use a CHA Mark-40 electron beam evaporator to deposit 100nm of aluminum at rates of 5 Angstroms/sec at a pressure of $\approx 10^{-6}$ Torr. The lift-off step is performed

using acetone to remove the ZEP520A layer and unwanted aluminum film that's been deposited on top of the ZEP520A. It is then rinsed in IPA as a final step. We test two treatments of the HR Si substrate: HR Si and HR Si dipped in HF as a last step. It is known in the microwave community that the interface between silicon and grown silicon dioxide can harbor charge carriers that can deteriorate the quality of microwave cavities. We saw small improvements in the intrinsic quality factors when the silicon surface oxidation was removed with 48% HF, as seen Figure 4.7. We use IPA as the only and final rinse after the HF dip. It is important to note that HF reacts with the surface of aluminum converting the aluminum oxide to aluminum fluoride. However a dilute 10:1 $\text{H}_2\text{O}:\text{HF}$ solution would etch aluminum aggressively as the additional water provides extra means for aluminum oxidation, which is etched by the HF. Rinsing a HF-dipped sample with water would be similar to putting the sample in very dilute HF and would aggressively etch our thin aluminum wires.

Sapphire (Al_2O_3) is the single crystal form of alumina and often used microwave substrate. Sapphire has a dielectric constant, loss tangent, and high resistivity which are $\epsilon \approx 9.39$ (at 25°C from 10^3 - 10^9 Hz), $\tan \delta \approx .0001$, and $\rho > 10^{16} \Omega \cdot \text{cm}$, respectively. In order to fabricate the same aluminum resonator circuit, an inverse version of the liftoff process is used to fabricate microwave cavities on sapphire substrates. Because of weak adhesion of the ZEP520A to the sapphire substrate we evaporate the aluminum over the bare sapphire chips first. ZEP520A is spun onto the metalized chip and microwave resonators are defined using electron beam lithography such that an aluminum wet etch (Transene) can remove the aluminum anywhere the lithography has exposed and removed ZEP520A. This process requires us to write resonator wires that are wider ($+2 \cdot \text{Thickness}_{\text{Al}}$) to compensate for the aluminum etch's isotropic etch (40 angstroms/sec). ZEP520A, which functions as a mask for our aluminum wet etch, is removed with 1165 Remover at 60°C for 2 hours and rinsed in solvents (acetone, IPA). High resistivity substrates gave us upper limits on the quality factors attainable with our evaporated aluminum so we could compare to other multilayer substrates (i.e., SOI, SiN on Si), giving us intrinsic LC resonator cavity quality factors of $Q_i \approx 30,000 - 152,000$. We investigate the viability of these multilayer substrates, as both nanophotonics and nanomechanics rely on having a free-standing nanobeam which is conventionally fabricated with multilayer substrates. In nanophotonic structures, one can guide and confine light with a nanobeam using photonic crystals which rely on having a refractive index contrast between a nanobeam and the surrounding air. For nanomechanics, one must have a physically isolated mechanical structure in order to allow it to physically oscillate. Conventionally to fabricate such isolated free-standing mechanical structures, a multilayer substrate is used which is composed of a device layer at the top and a sacrificial layer underneath. A selective etch is then used to remove the sacrificial layer under mechanical structure etched into the top layer, resulting in a free-standing mechanical structure. For example, SOI substrates consist of a device layers of silicon (top), a sacrificial layer of glass,

		Frequency (ν_{RF})	Intrinsic Quality Factor (Q_i)	Loaded Quality Factor (Q_L)	External Quality Factor (Q_E)
	High Resistivity(HR) Si Substrate	4.72 GHz (LC)	~30,000	~20,000	~70,000
	High Resistivity Si Substrate (HF dipped)	6.11 GHz (LC)	~78,000	~66,000	~410,000
	Sapphire Substrate	5.51 GHz (LC)	~152,000	~99,000	~670,000
	Si ₃ N ₄ on Si ($\rho = 1 \Omega \cdot \text{cm}$)	No Modes	—	—	—
	Si ₃ N ₄ on HR Si ($\rho = 10 \text{k}\Omega \cdot \text{cm}$)	No Modes	—	—	—
	SOI w/ Si Handle($\rho = 15 \Omega \cdot \text{cm}$)	11.5 GHz (LC)	~1,600	~700	~6,000
	SOI w/ Si Handle($\rho = 5 \text{k}\Omega \cdot \text{cm}$)	No Modes	—	—	—
	HR SOI on Si ($\rho = 5 \text{k}\Omega \cdot \text{cm}$)	No Modes	—	—	—






 LR Si
  HR Si
  SiO₂
  Si₃N₄
  Sapphire

Figure 4.7: **Intrinsic Quality Factors for Different Substrates.** Using a simple aluminum circuit consisting of LC and $\lambda/4$ resonators (as seen in Figure 4.5), we cooled down the samples to 4mK in a dilution refrigerator and measured their quality factors. The table outlines resonators with the best intrinsic quality factors, Q_i , on different substrates, along with corresponding Q_L and Q_E .

SiO₂ (middle) and a handling substrate generally made of silicon hundreds of microns thick. One could fabricate mechanical silicon structures from the top layer, remove the glass underneath using HF and produce a suspended mechanical structure that could be coupled to superconducting circuit fabricated on the same chip. This conventional process is also possible in LPCVD silicon nitride thin films deposited on silicon substrates where one can plasma etch a nanobeam into the silicon nitride layer and undercut the sample by wet etching away the silicon underneath with KOH (which does not etch silicon nitride) leaving a free-standing oscillating Si₃N₄ nanobeam. This type of standard process for producing free-standing mechanical elements is not possible with single material substrates which do not have a sacrificial layer. Our characterization experiments did not include mechanical elements since we only tested the substrate effects on microwave circuit properties, but it was important to select substrates that we could feasibly use to fabricate a free-standing nanobeam.

Using the circuit layout seen in Figure 4.5 to test the influence of different substrates on microwave cavity quality factors, we fabricated quarter-wave and LC resonators on high resistivity bulk substrates (HR Si and Sapphire), Si₃N₄ on Low Resistivity (LR) Si, Si₃N₄ on High Resistivity (HR) Si, SOI with LR Si Handle Wafer, SOI with HR Si Handle wafer, and SOI with HR device layer and handling wafer as seen in Figure 4.7.

Superconducting resonators fabricated on LPCVD Si₃N₄ on Si (LR and HR) seem to suffer from

large losses resulting in an inability to resolve microwave cavity resonances in our output signal. The silicon nitride is an insulator with a resistivity $\rho > 10^{16} \Omega \cdot cm$ which should have few charge carriers. The losses could possibly be attributed to free-carriers forming at the Si_3N_4/Si interface or the fact that LPCVD silicon nitride is deposited at very high temperatures ($\approx 600 - 800^\circ C$) and possibly leads to a reduction in the resistivity of the silicon substrate below. We tested 300 nm of LPCVD silicon nitride on low resistivity silicon ($\rho = 1 \Omega \cdot cm$) and high resistivity silicon ($\rho > 10,000 \Omega \cdot cm$) deposited at $800^\circ C$. As seen in Figure 4.7, we did not detect modes on either of the silicon nitride substrates. One possibility would be to deposit the silicon nitride at lower temperature, but this has been known to produce silicon nitride films with inferior optical properties and mechanical properties (mechanics deteriorated by the decreased intrinsic stress in the SiN film and optics deteriorated by increased optical absorbers inherent to low temperature Si_3N_4 depositions [62] [9]).

Silicon-on-insulator is a standard material used in a wide variety of opto-mechanical and electro-optical systems. SOI was purchased from Soitec and consists of a thin silicon device layer (≈ 200 nm), on $3\mu m$ thick SiO_2 layer, on a $500 \mu m$ thick handle substrate. In order to test the influence of the free carriers present in the silicon and the free carriers at the Si/SiO_2 , we tested several permutations of the device and handle resistivities, as seen in Figure 4.7. LC and quarter-wave resonators on SOI substrates produced either no detectable modes or modes with very small internal $Q_i \approx 1,600$. One known issue with superconducting circuits on SOI is the high density of free-carriers at the Si/SiO_2 interface which creates a large loss channel for the microwave cavities, resulting in low internal Q s. Measuring the same large losses with different combinations of resistivities in both the device and handle substrate would indicate that the interface carriers would be the biggest reason for large microwave cavity losses on SOI substrates (this is discussed next when we still find no modes or low Q modes despite aggressive removal of the SiO_2 layer).

To investigate the role of free carriers at the Si/SiO_2 interface, we patterned slits into the silicon device layer and used an HF dip to aggressively remove the SiO_2 under the wire, as seen in Figure 4.8. We used both SOI substrates with high resistivity handle wafers and device layers. We spun ZEP520A onto our SOI chips, and defined an array of slits using electron beam lithography and a C_4F_8/SF_6 plasma etch to define the slit holes in the silicon. Using 48% HF, we aggressively undercut a majority of the glass under the silicon device layer, leaving small pillars to hold up the silicon membrane. These pillars are needed because we require another spinning of ZEP520A resist, aligned e-beam lithography of the meandering inductors, aluminum evaporation, and liftoff, which would not work well if the membrane were completely undercut. Completely removing all of the glass layer leaves a membrane that is floppy (because the silicon device layer has an intrinsic compressive stress) making it difficult to spin homogeneous resist layers and align circuit patterns onto a wrinkled silicon layer. Using several types of SOI substrates, we still saw no modes in these aggressively undercut structures even after most of the SiO_2 was removed. Because we saw no im-

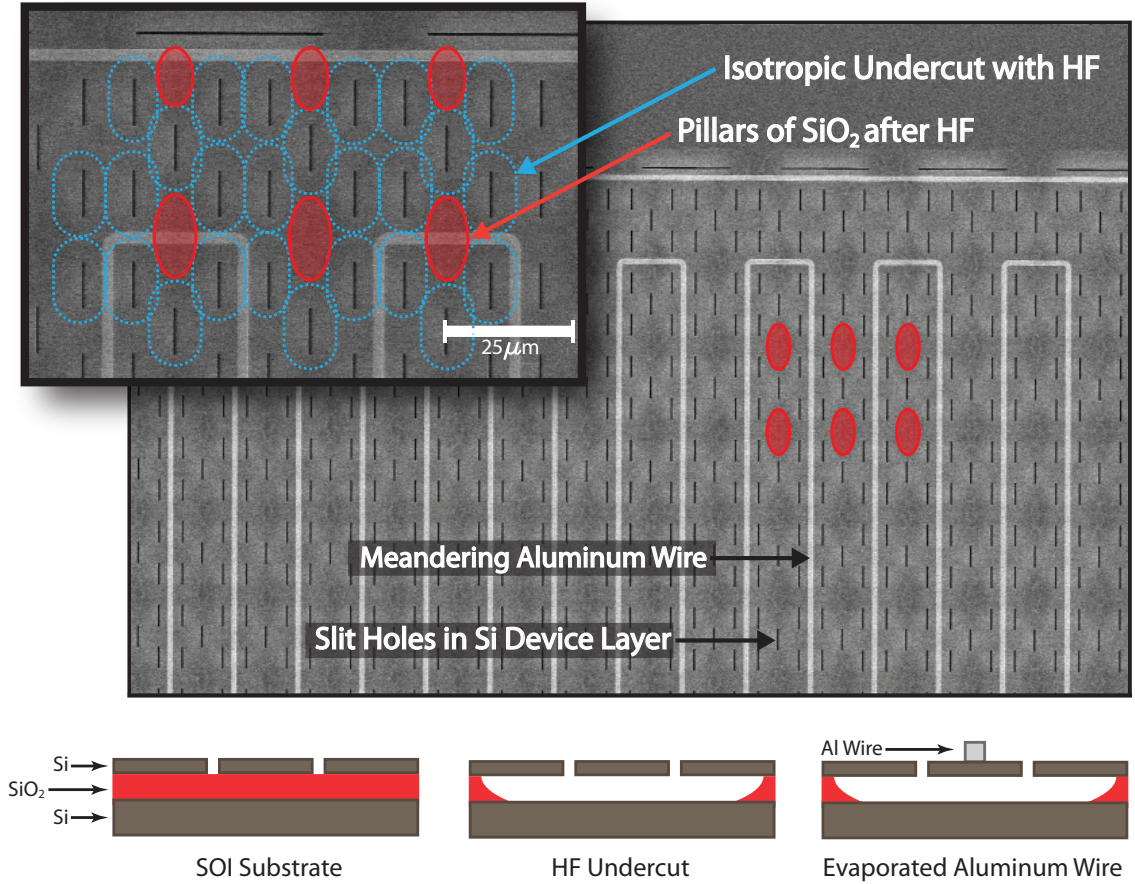


Figure 4.8: **Aggressively Undercut Silicon-on-Insulator.** TOP: SEM image of our undercut SOI devices. Using slit holes that have been etched in the top silicon device layer allows us to undercut the SiO_2 beneath leaving a silicon membrane with small pillars of SiO_2 in order to decrease the losses from free carriers that exist at the Si/SiO_2 interface on our microwave circuits. Our inductor meanders between the slits. We show how the isotropic wet etch from HF (in blue) etches away the glass underneath leaving glass pillars (in red) to hold up the membrane. BOTTOM: Cross-sectional view of fabrication process. The SOI substrate is HF undercut first, and the aluminum wire is evaporated on and defined using ZEP520A liftoff procedure and ebeam evaporated aluminum

provement in the performance of our microwave resonators, the device and handle layers became the possible source of losses. An important note is that when SOI is produced from high resistivity silicon using the Smart-Cut[®] process [70], it involves high temperature oxidation of at least one silicon layer to form the SiO_2 sacrificial layer and high temperature bonding of device layer to the handle substrate, both of which can significantly reduce the resistivity of the silicon. At high furnace temperatures the free-carriers in the silicon (from doping) will migrate within the substrate to the surfaces of the substrate, where our devices are located, locally increasing the resistivity of the surrounding substrate. SOI substrates sold with high resistivity specifications ($\rho > 5,000 \, \Omega \cdot \text{cm}$) on the handle and device layers are referring to the measured substrate resistivities (Four-terminal

sensing) before they are manufactured into SOI substrates, which could have final resistivities as low as $950 \Omega \cdot \text{cm}$. In general we can conclude that SOI substrates are not suitable substrates for high quality microwave resonators.

4.3.2 Single Material Substrate Mechanical Structures

We know that single-material high resistivity substrates are ideal for fabricating superconducting circuits but we also need to couple those circuits to nanomechanical elements. We focused on Si_3N_4 on Si and SOI because there are established fabrication methods for producing nanobeam oscillators from these substrates. We looked at the viability of fabricating free-standing mechanical oscillators from single material bulk substrates such as high resistivity silicon substrate. Without a sacrificial layer, producing high quality nanobeams is difficult with conventional etching methods since the material that one needs to remove to undercut the nanobeam is the same as the nanobeam itself. One option would be to physically mill the structures at an angle to release a nanobeam using a focused ion beam (FIB), but this process sputters unwanted contaminants onto the structures and negatively impacts the optical and mechanical quality of the structures. One approach in realizing suspended nanobeams in bulk substrates is a plasma etching technique utilized in the diamond MEMS community for fabricating free-standing mechanical and photonic nanostructures in bulk single-crystal diamond substrates [71]. Generally ICP-RIE plasma etches use a DC-bias on the order of 50-80V that directs charged particles vertically into the substrate. The method involves plasma etching the substrate at an angle in order to undercut the sample, as shown in Figure 4.9. The angled etching is achieved by inserting the sample inside an aluminum Faraday cage made of a fine mesh which attenuates the external DC-bias from the plasma a small distance from the mesh. The potential gradient in the plasma process builds up over the face of the Faraday cage and accelerates ions along a path perpendicular to the cage surface. Once the ions are inside the Faraday cage there are they are no longer accelerated by the external DC-bias and travel ballistically toward the substrate at an angle determined by the shape of the Faraday cage. One of the simplest ways to undercut a sample is using a triangular shaped Faraday cage, as seen in Figure 4.9(c), which allows one to accelerate ions towards the substrate in two different directions. The angle of the Faraday cage, θ , determines the cross-sectional profile of the nanobeam we produce, as seen in Figure 4.9(d). We tried this method on a single-crystal high resistivity silicon substrate. The fabrication process is outlined in Figure 4.9(d). We evaporated the silicon substrate with a 50nm layer of aluminum. We spun the sample with ZEP-520A and patterned simple nanobeams using electron beam lithography. We then used aluminum etchant from Transene which etched any aluminum not protected by the ZEP-520A. Now that we have an aluminum nanobeam mask on high resistivity silicon (the first step in Figure 4.9(d)), we perform a conventional ICP-RIE plasma etch using a $\text{C}_4\text{F}_8/\text{SF}_6$ to vertically mill into the silicon substrate. Now using our Faraday cage we are able to use the same plasma

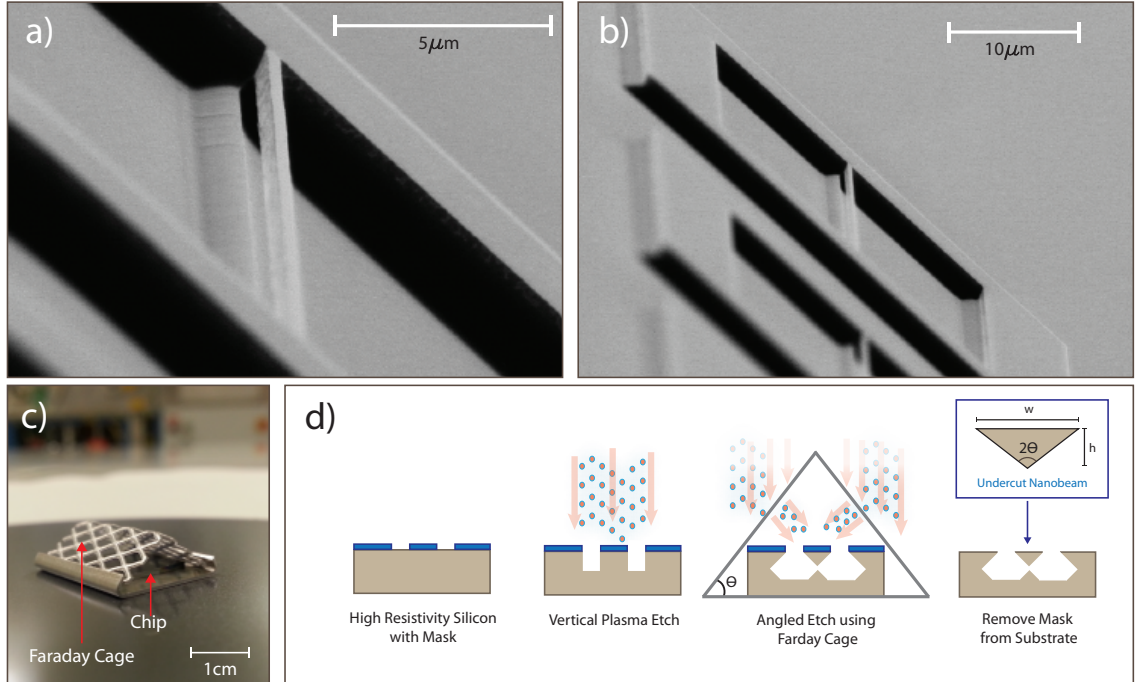


Figure 4.9: **General Device Geometry.** (a): Shows a close-up SEM image of a nanobeam which has been etched from a high resistivity ($\sigma > 10,000\Omega \cdot cm$) silicon substrate using millimeter sized Faraday cage. (b): This SEM image shows an array of the single-crystal suspended silicon nanobeams. (c): Shows millimeter sized Faraday cage which surrounds the $1cm \times 1cm$ chip substrate. (d): Schematic shows the general process for angle etching. An aluminum mask is used to define the nanobeam on a silicon substrate. We use a conventional C_4F_8/SF_6 plasma etch to vertical etch into the substrate. Then the sample is placed into a Faraday cage which plasma etches at an angle in order to produce a suspended nanobeam. (d): The mask is removed using aluminum wet etch.

etching recipe to etch at an angle in order to undercut the sample. Devices near the center of the Faraday had an even amount of etching from both directions, unlike nanobeams near the edges of the chip where one direction of etching dominated over the other. Once the nanobeams were undercut with the plasma etch, we removed the aluminum mask using aluminum etchant. This method, while promising, had several problems that made it difficult to use for making electromechanical devices. The first was that the nanobeam undercut seemed to be very reliant on the position of the device on the chip which determined its position inside the Faraday cage. This type of undercutting would only produce reliable nanobeam in a very limited part of the chip. One could use a larger Faraday cage which would make the etch more homogeneous throughout the chip, but the Faraday had to be just tall enough to safely clear the slit-valve between the Oxford's load lock and ICP-RIE etching chamber during the automatic transfer with a robotic arm. Because we are using a plasma etch to not only define a nanobeam in a device layer, but also to undercut the beam, we must etch for a much longer time. This longer plasma etch time also means that making small capacitive gaps (\approx

50nm) around the nanobeam becomes very challenging since longer etch times also produce more blowout of the gap size. The smaller one makes the gap, the longer the etch (due to aperture effects) and a bigger blow out on the gaps. While this method allows us to make simple nanobeam oscillators on a substrate with excellent microwave properties, the method makes it prohibitively difficult to make small gaps which are essential in achieving high electromechanical coupling.

4.4 High Stress LPCVD Silicon Nitride Membranes

4.4.1 Material Properties of Silicon Nitride Membranes

Stoichiometric high-stress LPCVD silicon nitride membranes (Si_3N_4) have several properties that make them ideal as a substrate for superconducting circuits. One of the dominant sources of loss for a superconducting circuit is through substrate losses. Si_3N_4 membranes eliminate a significant amount of these losses by eliminating the substrate beneath the circuit. By eliminating the substrate beneath the circuit we were able to also effectively eliminate contributions to the loss tangent due to free charge conduction in the substrate. While these circuits were characterized in $\approx 10\text{mK}$ environment where carriers in Si are well-known to freeze out, the membrane geometry assured that any potential free carriers formed at the interface between LPCVD grown Si_3N_4 and the Si substrate would not contribute to losses of the microwave resonator. LPCVD silicon nitride is known to have a low defect concentration compared to other silicon nitrides, which reduces free carriers and two-level systems in a material already known for its high resistivities, $\sigma_{\text{SiN}} > 10^{16} \Omega \cdot \text{cm}$. Parasitic capacitance of the circuit from surrounding dielectric material is significantly reduced due to the removal of the Si substrate, leaving only the thin Si_3N_4 membrane as a negligible source of parasitic capacitance. This ability to produce circuits with stray capacitance on the order of $C_s \approx 2.5\text{fF}$ allows us to significantly enhance the electromechanical coupling, g_{em} . This feature allows us to design electromechanical system with small mechanically modulated capacitances whose electromechanical coupling is large, high frequency and not dominated by parasitic loss. While our initial experiments did not integrate optical elements into our devices, silicon nitride is a material that is easily adaptable for optical applications where low defect concentrations produce low optical absorption with an imaginary refractive index of $n_i \approx 10^{-6}$ at IR and NIR wavelengths. A useful attribute of Si_3N_4 on Si is the ability to use the 1-0-0 planes to wet V-grooves into the silicon substrate that could allow for integrated fiber coupling of optics [2].

High Stress Si_3N_4 is well known for its excellent mechanical properties. 300 nm thick film of LPCVD Si_3N_4 is deposited on a HR Si substrate at high temperatures around 600-800°C and then cooled to room temperature. Because of the large difference in thermal expansion coefficients of Si_3N_4 and Si, there is a large residual in-plane tensile stress on the order of 800 MPa to 1GPa (Figure 1.12). The ability of thin dielectric films under high stress to produce devices with high

mechanical quality factors on the order of $Q_m = 10^6 - 10^7$ has been extensively studied. Si_3N_4 films on Si substrate have the additional advantage of being a very flat surface under tensile stress which allows for robust and repeatable fabrication of circuits on the membrane. Many materials such as the device layer in Si in SOI have thermal expansion coefficients that produce films with compressive stress and produce membranes with wrinkles that would make fabrication of circuits very difficult. Because the membranes are completely undercut, one can fabricate mechanical elements from the membrane film itself and isolate both the mechanics and the superconducting circuit from the bulk Si substrate.

4.4.2 Electromechanical Device on Membranes

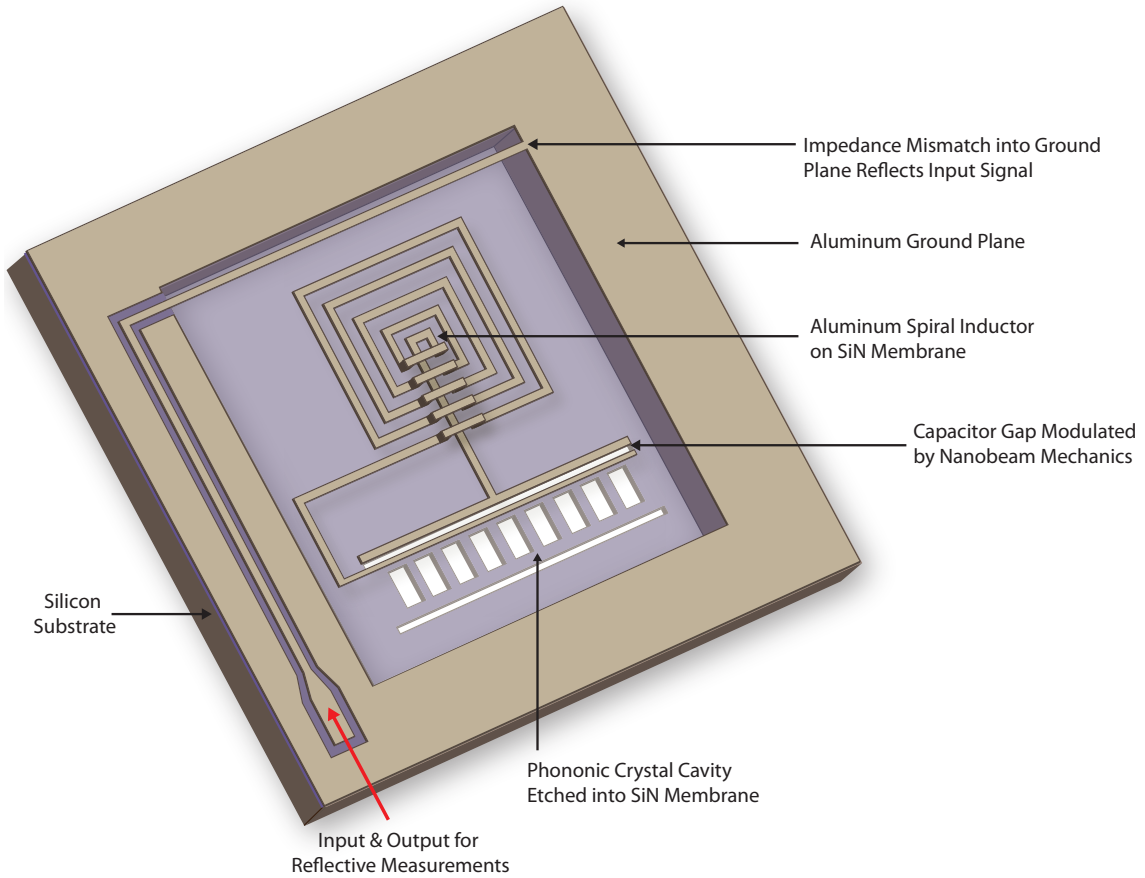


Figure 4.10: **General Device Geometry.** Here we show a basic illustration of our device. A hole through the silicon substrate leaves a suspended Si_3N_4 membrane. A phononic cavity is etched into the silicon nitride membrane and capacitively coupled to a spiral inductor. In this one-sided configuration, we only couple capacitively to one side of the nanobeam. The input signal is sent in and inductively couples with the spiral. The signal reflects off the impedance mismatch created by connecting our input line directly into the ground plane.

In Figure 4.10 we show a simplified illustration of our nominal electromechanical system. In order to capacitively couple high frequency mechanics ($\approx 400 - 500$ MHz) with a ≈ 12 GHz LC circuit resonator, we would utilize the 450 MHz high- Q_m breathing mode of a $75\text{ }\mu\text{m}$ long phononic cavity nanobeam. The breathing mode of the nanobeam modulates the capacitance of the superconducting LC resonator and changes the resonator's frequency, ω_{LC} . A major component of our geometry consists of fabricating the entirety of the electromechanical system on an undercut 300nm thick Si_3N_4 membrane in order to achieve parasitic capacitances as low as $C_s \approx 2.5\text{fF}$. The motion of our nanobeam beam is connected to an LC resonator which consists of a capacitor formed by two aluminum wires (one which resides on the oscillating nanobeam) and a spiral inductor with an inductance of $L \approx 75\text{ nH}$. The spiral geometry also contributes to the low stray capacitance as discussed in Section 4.5. We couple our input signal through a wire-bonding pad connected to a $50\text{ }\Omega$ impedance input line. The input is shorted directly to the ground plane where the impedance mismatch between the signal and ground causes the input signal to perform reflection measurements. Figure 4.10 shows a one-sided coupling of the superconducting circuit to the nanobeam meant to couple to the fundamental violin mode of the entire beam. For detection of the breathing mode, we would use a double-sided coupling (as seen in Figure 4.12) in which each side of the nanobeam modulates the capacitance. This thesis focuses on experiments which use the one-sided coupling to detect low frequency fundamental modes ($\approx 4\text{MHz}$) but in the next section we review the design of our high frequency mechanics.

4.4.3 Phononic Cavity Design

It is known in the nanomechanics community that achieving high quality factors can become increasingly difficult with increasing frequency as the size of the mechanical element becomes smaller [24]. In order to achieve the high frequency and high quality mechanics, we utilize phononic crystal mirrors which localizes the 450 MHz breathing mode of a perforated nanobeam. Using COMSOL, a finite element solver, we can simulate the mechanical band structure of a phononic crystal unit cell, as shown in Figure 4.11(a) with periodic boundary conditions in x and keeping free boundary conditions in y (side with aluminum wire). We produce a mechanical band structure and engineer a bandgap at the desired frequency of the mode we are trying to localize (Figure 4.11(b)). We engineer these bandgaps by optimizing parameters of the simulated unit cell such as the lattice constant (a), the width of the nanobeam (W), the width of the hole (W_x), and the height of the hole, (W_y), and the width of the aluminum wire on the nanobeam (W_{Al}) and the approximate thickness of the side-wall of aluminum which is deposited during an electron beam evaporation ($W_{sidewall}$). These phononic mirrors surround a defect region which harbors a breathing mode (Figure 4.11(c)) oscillating at ≈ 450 MHz. The phononic mirrors at the edges of the nanobeam have a bandgap which spans around this breathing mode frequency, shielding phonons from dissipating from the

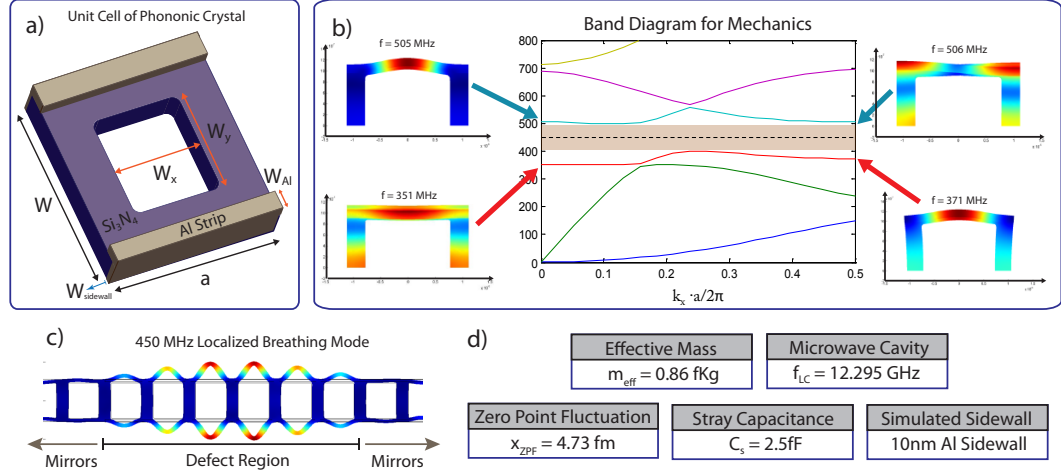


Figure 4.11: **Phononic Crystal Design.** (a): Schematic of a simulated unit cell of a phononic crystal. The aluminum wire is included in the simulation. (b): Simulated mechanical band diagram simulated with finite element method solver, COMSOL. Here we show the different bands across k -space, along with their corresponding images of their mode shapes. In the middle we can see the mechanical bandgap between modes. (c): Shows a COMSOL simulation of the 450 MHz breathing which we coupled capacitively to the superconducting LC resonator. (d): Shows different parameters of our system.

nanobeam. This can allow the breathing mode to achieve high mechanical quality factors on the order of 10^4 at room temperature. Once the mirror regions are designed, we simulate the entire phononic nanobeam to get a frequency for the breathing mode of the entire defect region. We find that frequencies of higher order bulk modes like the breathing mode are not affected by the stress in the LPCVD Si_3N_4 and we do not include tensile stress into the simulations of the breathing mode.

Our goal is to see the localized breathing mode of the beam, but we can also use other lower frequency modes which are easier to detect in our measurement setup (i.e., due to larger coupling). In this thesis, we also looked at coupling of a 4 MHz in-plane fundamental mode which would be present in the nanobeam even when patterned with holes. Figure 4.12 shows the different configurations of the nanobeam-circuit coupling. We see that for an asymmetric mode like the in-plane fundamental mode we maximize our coupling by connecting to the superconducting circuit with one capacitive gap on one side of the phononic nanobeam as seen in Figure 4.12(a). Notice that in this configuration the single wire runs completely along the entire side of the nanobeam in order to maximize the coupling since the whole nanobeam oscillates in fundamental modes.

If we want to sense the breathing mode with maximal coupling, we would fabricate two wires on the nanobeam and two wires on the other side of the gap which form two capacitive gaps around the nanobeam. As the 450 MHz breathing mode oscillates the external walls bulge out, making both surrounding capacitive gaps smaller, and modulating the frequency of the LC resonator by increasing the capacitance, C_m . Notice in Figure 4.12(b) that the capacitive coupling only happens

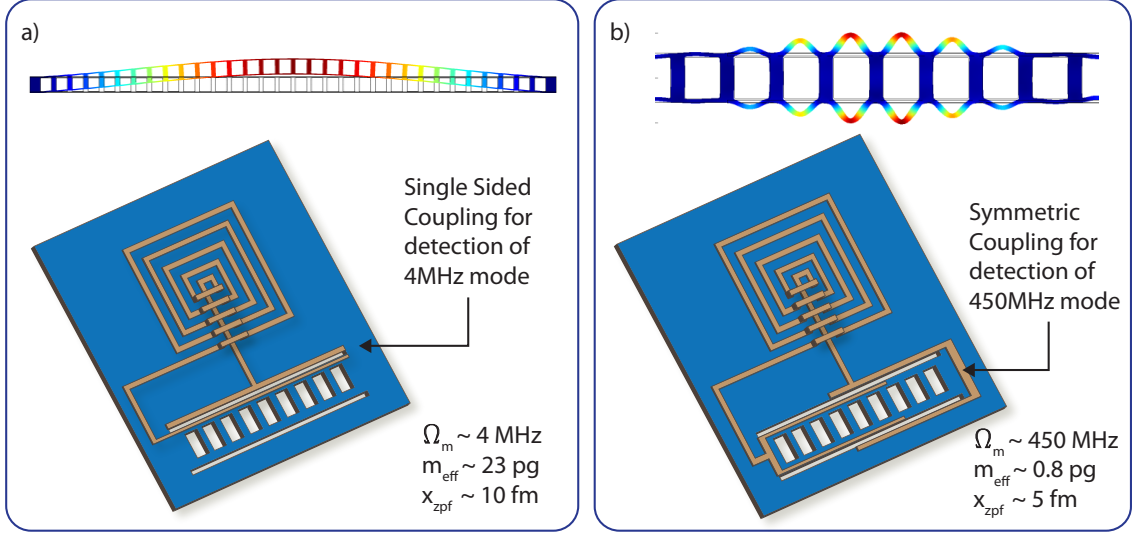


Figure 4.12: **Different Circuit Geometries for Different Couplings.** (a): One-sided circuit coupling to the nanobeam for detecting the in-plane fundamental mode of the entire beam (b): Two-sided coupling in order to maximize coupling to symmetric breathing mode.

in the defect region, near the center of the nanobeam. Having both sides coupled doubles the size of the modulation by effectively doubling the length of your modulating capacitor. If we were to use this symmetric double sided coupling to detect the in-plane fundamental mode in Figure 4.12(a), we would get very weak coupling since the nanobeam would oscillate to one side, making one of the capacitive gaps smaller while simultaneously making the gap on the other side larger, effectively canceling the effects of the in-plane modulation on the superconducting circuit.

4.4.4 Gap Engineering Using Internal Membrane Stress

One of the most significant challenges when wanting to increase the coupling as seen Section 4.2.1 is increasing the variable η in our electromechanical coupling $g_{\text{EM}} \approx -\eta\omega_{LC}/2x$. We could increase η by making our modulated capacitance $C_m \gg C_s$. This can be done by either decreasing stray capacitance of the inductor in the LC resonator, which has its limits dependent on substrate and geometry of the circuit. While reducing C_s is important, it is also important to increase the modulated capacitance C_m by making the gaps as small as possible. We have developed several methods for reliably achieving capacitive gaps as small as 20-50nm by manipulating the high stress of the entire Si_3N_4 membrane.

Let us consider what happens when we fabricate a membrane with a nanobeam defined by two small slot gaps. We etch the nanobeam pattern into the top layer of the Si_3N_4 , etch a corresponding rectangular window on the bottom layer of Si_3N_4 (on the other side of the chip), then wet etch through the $200\mu\text{m}$ Si substrate to produce an undercut Si_3N_4 membrane with a freestanding

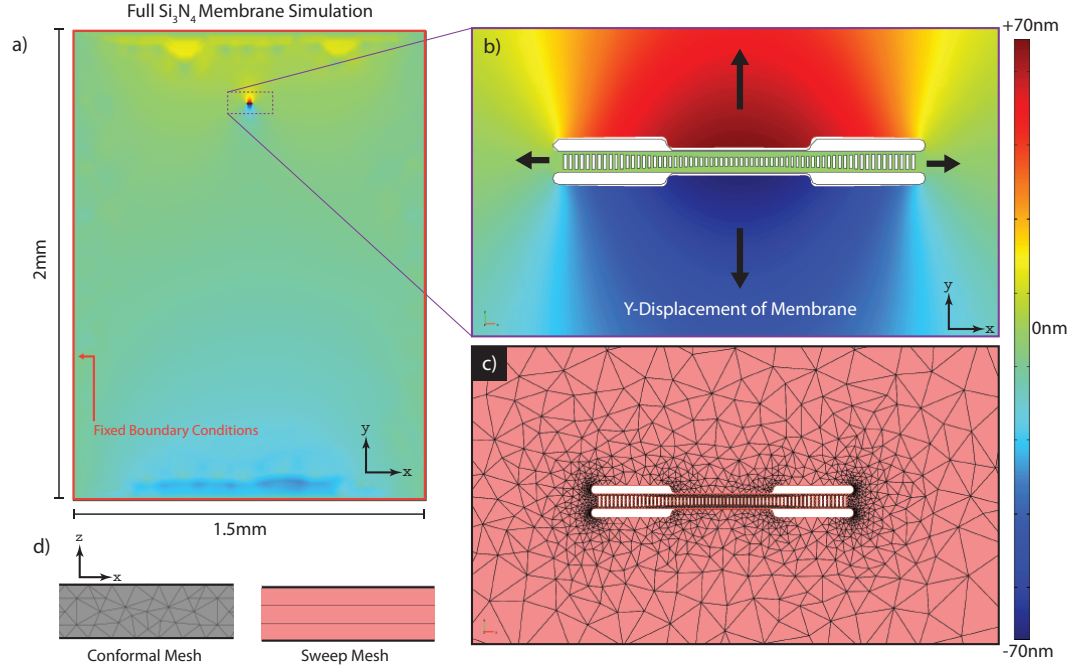


Figure 4.13: FDTD Simulations of Membrane and Nanobeam. (a): Shows 1.5mm \times 2mm Si₃N₄ membrane with a color map of total y-displacement after the membrane is undercut. (b): Close up of simulation of y displacement around the nanobeam. One can see that membrane is pulled outward away from the nanobeam by the tensile stress. The nanobeam only see contracts in the x direction and does not displacement it in y. (Left): Color Scale where y-displacements can be as large as +70nm (or -70nm) in the y direction. (c): Close up image showing the 2D surface mesh of the nanobeam. Finer mesh elements near the nanobeam which has the smallest features and adiabatically increase in size moving away from it in order to simulate quickly and accurately. (d): Shows a 300nm thick cross section of membranes with different mesh algorithms. The conformal free mesh (left) splits up the FEM in the z-direction using prisms as it does in the x-y directions. The swept mesh (left) treats the membrane as thin-film and slices membrane into layers.

nanobeam etched into it. Once this membrane is undercut it relaxes and displaces due to the residual stress in the film. The 800 MPa of intrinsic tensile stress in the film make the membrane contract once it is undercut. In order to see how the membrane relaxes and displaces after the wet-etch undercut we utilize the FEM analysis tool, COMSOL, to run a full simulation of the membrane as seen in Figure 4.13(a). We directly input the same CAD files used in the electrobeam lithography system to do an accurate simulation of the devices we fabricate. When we simulate the membrane we assume that fixed boundaries for the perimeter of the membrane as seen in red in Figure 4.13(a). The membrane is very large compared to the mechanical device but it is important to simulate the entire membrane for several reasons. The entirety of the membrane film contracts and thus the membrane's dimensions have a significant effect on the amount of relaxation in the membrane and significantly affecting the displacements. There can also be asymmetries in the way the membrane pulls on the nanobeam depending on whether the nanobeam is positioned near the center or edges of

the membrane. Figure 4.13(a) shows a color graph of the entire membrane which shows the amount of displacement in the y-direction. We are interested in the y-direction because these displacements have the largest effect on the final gap sizes in our configuration. If the slit gaps of the nanobeam were turned 90 degrees, we would then simulate and look at the displacements in the x-directions. We simulate a 300 nm thick silicon nitride membrane taking into account its material properties such as Young's modulus ($E_{\text{SiN}} = 270 \text{ GPa}$), Poisson ratio ($\nu_{\text{SiN}} = 0.27$), silicon nitride density ($\rho_{\text{SiN}} = 2700 \text{ kg/m}^3$), and temperature of deposition ($T_{\text{dep}} = 820^\circ\text{C}$). Using these we can calculate the thermal mechanical strain of silicon nitride, $\epsilon = \sigma(1 - \nu)/E$. We know that the temperature difference from deposition at 820°C to room temperature, 25°C , causes a thermal mismatch which creates the stress in the membrane, so we also simulate the system after initially being at a temperature $T_0 = 820^\circ\text{C}$ and finally being at a temperature $T_1 = 25^\circ\text{C}$. Figure 4.13(c) shows how the nanobeam is split into smaller pieces using a mesh generation which the finite element solver uses to solve the partial differential equation for a larger complex system. As we can see the mesh becomes finer around the nanobeam since it has the smallest features, and becomes more coarse as the mesh moves outward from the nanobeam, increasing the efficiency of the simulation. Even with this efficient splitting of the finite element model in 2D, such a large simulation with small features (high-aspect-ratio) would be prohibitively difficult to simulate without simplifying the mesh generation in the z direction. Because the thickness in the z-direction is much smaller than other dimensions in x or y, we can make thin film approximations which make the simulation manageable. Because the z dimension of our device is thin, any stress gradients in z have no effect on the displacements of well-clamped systems like a membrane, and the stresses and displacements induced in the membrane are dominantly in the x and y directions. Because of this we can use a swept mesh which is implemented by creating a 2D surface mesh as seen in Figure 4.13(c) and extrude the elements in z so that one slices the membrane in the z-direction, as shown in Figure 4.13(d) (right). Figure 4.13(d) also shows the conventional mesh (on the left) which illustrates how COMSOL would freely mesh the FEM in a manner that assumes that all dimensions are equally important to the simulation. The swept mesh makes it possible to perform economical simulations which have less total mesh elements than a free conformal mesh, making it possible to simulate a membrane with extreme aspect ratios between the x-y dimensions and z.

Figure 4.13(b) gives a close up look at the y-displacement of the membrane around the nanobeam. Here we see the initial position of the beam before release (as written by the electron-beam lithography) overlayed with the deformed nanobeam after the release (in rainbow color). As the membrane relaxes we see that large areas of membrane surrounding the nanobeam contract, pulling the portions of membrane around the nanobeam outward. The nanobeam itself does not feel a displacement in the y-direction and only gets pulled in the x-direction, but this does not cause a displacement since it is pulled symmetrically from both sides (-x and +x directions). The important thing to notice is

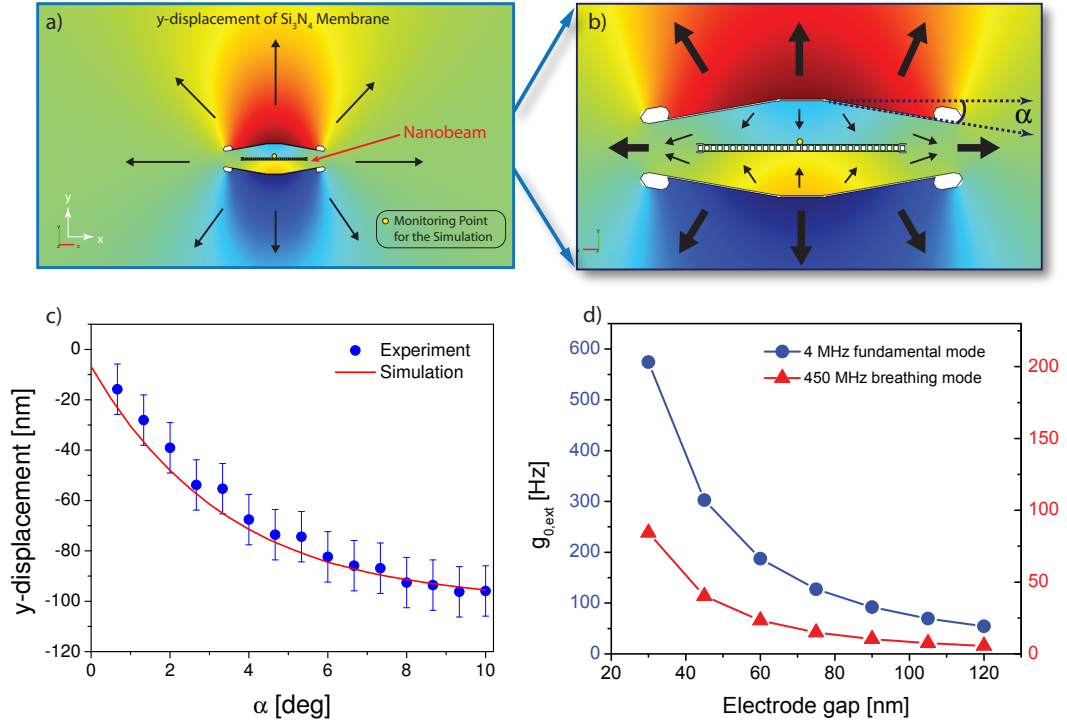


Figure 4.14: **FDTD Simulations of Membrane and Nanobeam.** (a): We show a phononic nanobeam surrounded above and below by pull-in slits. The tensile pull from the contraction of the membrane pulls in all directions. The pull-in slits shield the nanobeam from stress in the y -direction. (b): Closer look at (a) illustrates how the tensile forces of the membrane are shielded from pulling the capacitive open. We illustrate how the pull-in slits redirect the tensile stress in order to produce pull-in of the membrane towards the nanobeam, creating smaller gaps. We simulate the amount of pull-in of the gaps we achieve by monitoring the displacement of the yellow monitoring point above the nanobeam as a function of the angle α . (c): Shows y -displacement of the yellow monitoring point as a function of the angle of the slits, α from our simulation and measured pull-ins from real fabricated devices. The negative values correspond to membrane above the nanobeam moving downward towards the nanobeam. (d): Simulation results for electromechanical coupling as a function of capacitive gap for both the 4MHz and 450MHz modes.

that the portions of the membrane above and below the nanobeam which define the capacitive gaps are pulled outward by the contractive displacement of the membrane, making the gaps larger by 50-70 nm. We observed these simulated effects when fabricated the membrane devices. This was a large problem as 50-70 nm increase in the gap size would dramatically reduce the electromechanical coupling, g_{EM} , from 250 Hz (at 30nm gap in 450 MHz mode) to ≈ 30 Hz (at 80nm gap). We instead use the stress in the silicon nitride membrane to our advantage in order to engineer smaller gaps. We etch additional slits above and below the nanobeam as seen in Figure 4.14. These stress relief slits ensure that the large membrane contractions in the y direction do not pull on the parts of the membrane above and below the nanobeam which forms our capacitive gaps. In addition to keeping our gaps from getting larger, the slits shield the nanobeam from stress in the y direction. Now when

the membrane contracts, it pulls on these additional slits instead of the capacitive gaps around the nanobeam. The slits have an additional purpose which is redirecting the stress in the x-direction to produce displacements in the y-direction. This is illustrated in Figure 4.14(b) where we see that the pull in the x-direction also pulls the capacitive gaps closer together. We design the shape of the additional pull-in slits by simulating the entire membrane as before in Figure 4.13, with the addition of the pull-in slits. In order to know how the gap around the nanobeam displaces with the inclusion of the pull-in slits we monitor a point next to the gap and see how it displaces. In Figure 4.14(ab) we represent that monitoring point as a yellow point above the nanobeam. If the y-displacement is positive we can say that the membrane above the nanobeam will move upward and increase the size of the gap while a negative y-displacement indicates a membrane above the nanobeam that moves downward toward the nanobeam, making the gap smaller. Because the nanobeam and slits are far from the edges of the membrane, the contraction will about the same around the nanobeam so we can reliably simulate one point above the nanobeam (or below). Because the membrane is pulling symmetrically in x on the portion of membrane above the nanobeam, the x-displacements are negligible. There are several parameters of the pull-in slits one can use to fine-tune the pull in of the gaps (distance from the nanobeam, length, angle of the slits, etc.) and we chose the angle of the slits, α , as seen in Figure 4.14(b). We simulated the final y-displacement of the membrane above the nanobeam as we adjust the angle α and then compared with real fabricated devices as seen in Figure 4.14(c). This allowed us excellent control of the final gap sizes. In Figure 4.14(d), we also simulated the expected electromechanical coupling, g_{EM} , as a function of the gap size for both the 4 MHz fundamental mode (in blue) and the 450 MHz (in red). This illustrates the importance of achieving the smallest gap possible since, to first order, the coupling increases inversely to the distance and becomes significantly larger at gap sizes approaching 30 nm.

Being able to engineer the pull-in of the capacitive gaps is an important tool in achieving large electromechanical couplings with small gaps. The conventional method of fabricating a small gap would be to use electron beam lithography to produce a small gap ($\approx 20 - 50$ nm) in the resist mask which is then used to plasma etch directionally through the 300 nm thick silicon nitride using gasses C_4F_8/SF_6 . The ability to get straight etch profiles in silicon nitride becomes more difficult the thicker the silicon nitride is and the smaller the gap is. While the plasma etch can be very directional, the ability of plasma to infiltrate the deep small gaps becomes significantly impeded, resulting in reduced plasma etch rates of the silicon nitride. This is referred to as an aperture effect. This results in a “booting” of the side-wall which becomes more pronounced the deeper one etches into the silicon nitride, as seen in Figure 4.15(b). We can see that the “booting” results in a difference between the gap sizes at the top and bottom of the silicon nitride layer which we write as 2β . It’s important to note that the aluminum wire sits on top of the silicon nitride layer, and thus having having a “booted” etch profile will put physical limits on how close one can make the

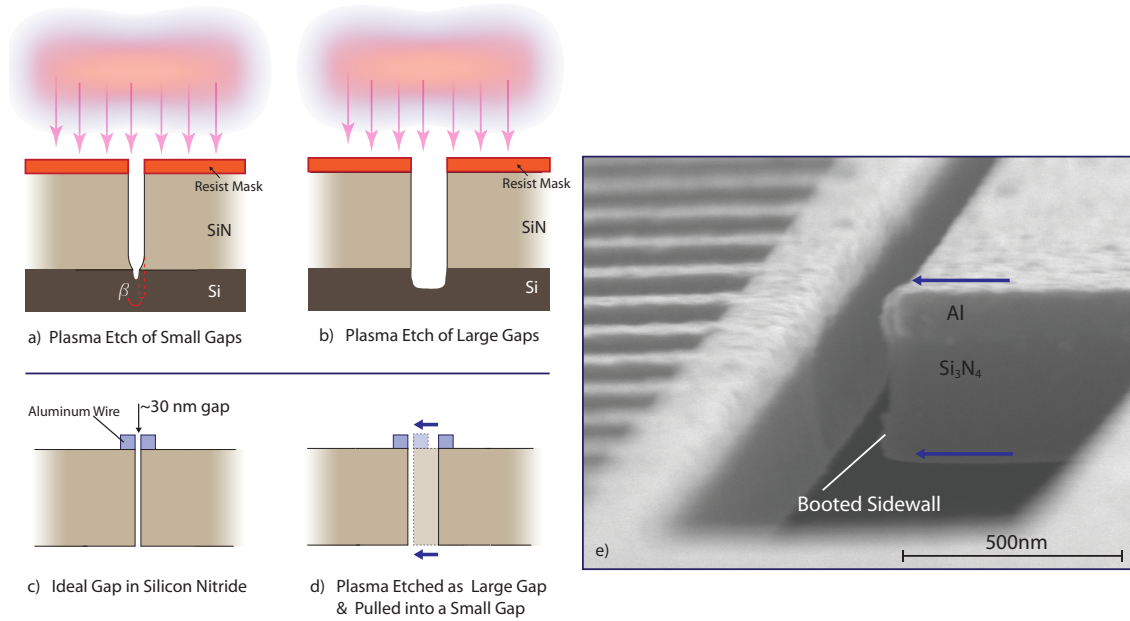


Figure 4.15: Achieving Small Gaps. (a): Shows the ideal small gap in silicon nitride with straight side-wall profiles. (b): Shows aperture effects that come into effect when one tries to plasma etch small and deep gaps. The etch rate will significantly decrease the deeper one etches into the gap resulting in a “boot” side-wall profile. (c): Shows how it can be easier to produce smooth side-walls in large gap using a plasma etch. As the gap gets larger the aperture effects lessen as more gas is able to infiltrate the gap, allowing the etch rate to remain constant throughout the etch. (d): Shows how we utilize a large gap (≈ 100 nm) with smooth side-walls and use the pull-in slits techniques to make small gaps with vertical sidewalls. (e): SEM image of nanobeam capacitive gap.

capacitive gap between metal wires at the top of the silicon nitride layer. For example, in order to achieve a 30 nm gaps between our aluminum wires (such that no parts of the gap are touching), each slab’s 300 nm tall side-wall must have a difference between top and bottom of $\beta < 15$ nm. This type of profile with small gaps would be prohibitively difficult to plasma etch reliably and repeatably.

ICP-RIE Plasma etching for a longer amount of time to straighten out the side-walls or increasing the DC bias to make the etch more directional to also produce straighter side-walls in the Si_3N_4 layer but would also slowly etch out the sidewalls, increasing the size of the gap. Both of these approaches would significantly increase the amount the gaps blow out. Using these techniques, one must make a choice between smooth side walls and small gaps. Plasma etching for longer times also means that thicker e-beam resist masks would be required, which itself would start to limit how small one can write gaps. Thicker resist requires more aggressive dosings with electron beam lithography to expose the thick resist completely. It is generally known that exposing small features with large dosing becomes a challenge as effects like electron backscattering from the substrate begins to expose more resist, resulting in gaps that are much larger than intended. If we try to etch wider gaps on the order of ≈ 100 nm, the plasma etch is able to diffuse into the gaps more easily, producing little

difference between the etch at the top and bottom of the silicon nitride. This absence of an aperture effect in large gaps produces straighter side-walls as seen in Figure 4.15(c). It's important to note in Figure 4.15(c) that even when plasma etching larger gaps there is always a “booting” features at the end of the etch. Because the gap is wider, the plasma is able to etch at a faster rate in the vertical direction. This allows us to completely etch through the silicon nitride layer quickly such that the end of the etch is mostly etching through the silicon substrate underneath. The “booting” feature is thus left in the silicon (which will be wet-etched anyway). In thinner gaps, the etch rate is greatly slowed, making it hard to completely etch through 300 nm of silicon nitride without either increasing the time or DC-bias of the plasma (both which blow out the gaps) and thus our “boot” features are generally in our silicon nitride layer. As shown in Figure 4.14(cd), the ability to simulate and accurately predict the amount of pull-in displacement of the surrounding membrane, using the pull-in slits, allows us to begin with large gaps with straight side-walls (before the undercut of the membrane) and then pull in the vertically smooth sidewalls to produce a small gap. This allowed us to benefit from the ease of etching smooth sidewalls in larger gaps ($\approx 110\text{nm}$) and engineering the pull-in slits so that the gaps pulled in by about $\approx 80 - 90\text{ nm}$ in order to reliably produce 30-50 nm wide gaps.

Manipulating the high tensile stress in silicon nitride must be done carefully in order to fabricate devices that can realistically be undercut without tearing from excessive stress. Each design for the pull-in slits results in different stress profiles across the membrane which we must also simulate. While the intrinsic tensile stress in the Si_3N_4 films on Si is 800 MPa, the membrane fabricated from this film will nominally relax to a lower tensile stress as the silicon underneath is no longer providing rigid support. However, when small patterns are etched into the membrane (i.e., the nanobeam and slits) local stress hotspots at corners or sharp edges of the pattern will arise. If these stress hotspots are large enough, the stress differentials in the membrane will create tears at those points which propagate throughout the membrane and destroy the device (Figure 4.16(c)). We initially minimize these stress hotspots by rounding corners of our pattern as can be seen at the end of our pull-in slits and capacitive gaps (circled in red) in Figure 4.16b. We do not observe hotspots at the ends of the smaller capacitive gap slits because the surrounding pull-in slits shields these gaps from the relaxation of the membrane, resulting in a low stress differential there. Without the pull-in slits, the stress hotspots would be at the end of the capacitive gap slits.

Even with the rounding of all the corners in the design, by changing the distance of the pull-in slits from the nanobeam, y , and the angle of the pull-in slits, α , (Figure 4.16c) it is possible to create a design with stress hotspots above a fracturing limit (in this case, $\approx 9.2\text{ GPa}$). In Figure 4.16c, we can see an example of a design which resulted in simulated stress hotspots of 10.2 GPa. It is clear from the SEM that tearing begins at the simulated hotspot and propagates across the membrane. The nanobeam itself is a very small perturbation compared to the millimeter-sized

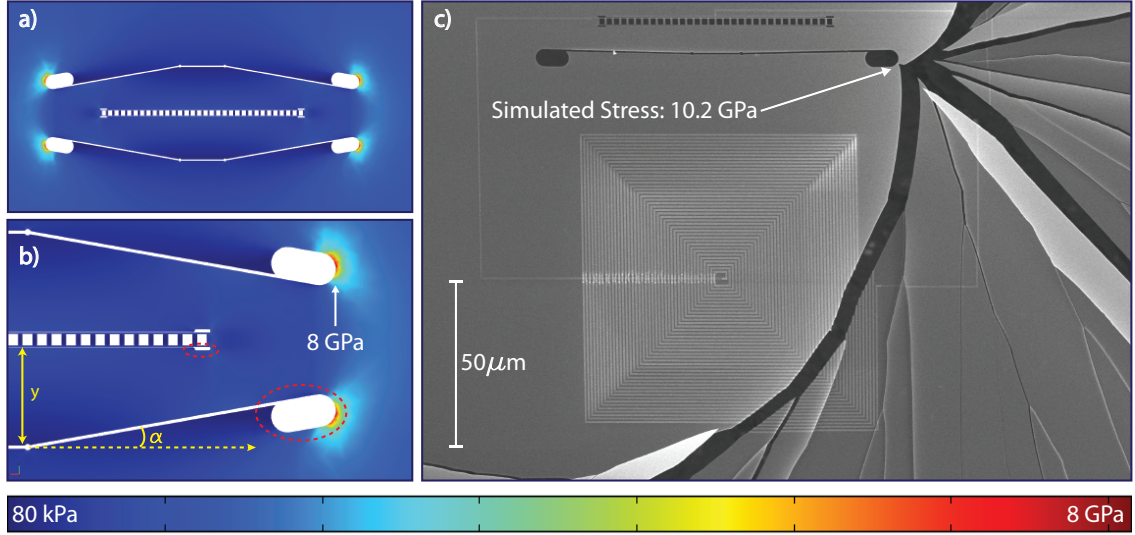


Figure 4.16: **Tensile Stress Simulations.** (a): Simulation of tensile stress near the nanobeam. 8 GPa hotspots simulated near the end of the slits. (b): Closer look at stress near the nanobeam. We round all as seen circled in red. (c): SEM image demonstrating a pull-in slit design that result in stress hotspots of 10.2 GPa (well over the fracturing limit of 9 GPa). Because of the high stress in the membrane, the membrane breaks at the stress hotspot and propagates throughout the membrane.

membrane and in simulations the design of the nanobeam will have little effect on the stress of this large membrane, but because of the high tensile stress in the membrane, one overly stressed hotspot on the nanobeam will destroy the membrane. Through fabrication trial and error we were able to figure out the stress limit at which our devices would break and design all patterns such that we were under this fracture limit.

4.5 Microwave Resonator Designs

Now that we have shown how the mechanical elements are engineered, we will review the design of the superconducting LC resonator that is coupled to the mechanics. While we have discussed in detail how the capacitor of the LC resonator is coupled to our phononic cavity, we have not discussed the design of the inductor. In order to simulate aluminum circuits we use Sonnet[®], which analyzes high frequency planar circuits based on electromagnetics. It utilizes Method of Moments applied to Maxwell's Equations in order to solve planar systems whose mathematical formulism is derived in Reference [72]. Assuming some modulated capacitance, C_m , we design the inductor such that the superconducting LC resonator operates at frequencies between 8-12 GHz (the operational range of our RF equipment). Sonnet inputs the entire metal circuit layout, including reflection lines starting at input ports in the simulation. This is all included in one layer of the simulation. Layers are

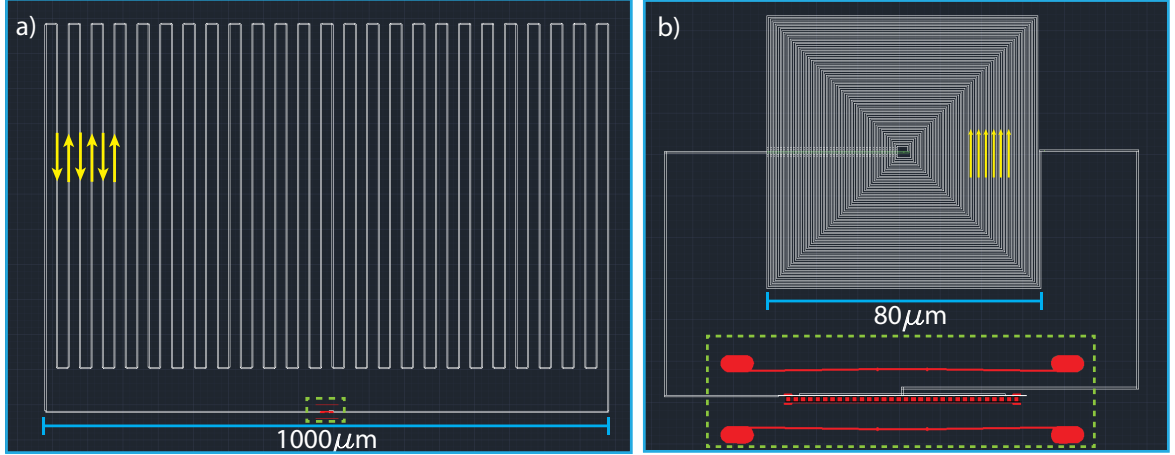


Figure 4.17: **Different Circuit Designs for Superconducting LC Resonator.** Here we compare two different circuit designs with similar inductances such the frequencies of both LC resonators are similar. (a): Shows initial designs for a rastering inductor. The phononic cavity we couple this rastering inductor to (outlined in red) is shown inside a green box. This type of circuit geometry requires circuits with dimensions on the order of millimeters and have simulated stray capacitance $C_s \approx 12$ fF on a silicon nitride membrane. (b): Shows layout of spiral inductor which is capacitively coupled to a phononic cavity (outlined in red). With the use of cross-over wires we can design spiral inductors and compactify them to much smaller dimensions on the order $80\mu m \times 80\mu m$ micron square spiral. This geometry results in improved stray capacitance $C_s \approx 2.5$ fF on a silicon nitride membrane.

then added above and below the circuit in order to simulate surrounding air, dielectrics, and other materials. We can then design and simulate different inductor geometries on different substrate geometries such as Si_3N_4 membranes or SOI substrates. We will focus on simulations of circuits on 300 nm thick silicon nitride circuits.

In Figure 4.17, we have included nanobeams in order to demonstrate difference in scales between the spiral inductor and the meandering inductor. However, when we simulate the circuit using Sonnet, we only simulate the metal circuit from which Sonnet can output modulated capacitance, C_m , stray capacitance C_s , and effective permittivity ϵ_{eff} of the circuit and surrounding substrate. Because we have included the entirety of the metallic layer in the simulation including the input and output lines, Sonnet simulates the RF signal one would detect in the outgoing ports (same as the input port for reflective measurements). In order to get the intrinsic quality factor, Q_i , loading quality factor, Q_L , and extrinsic quality factor, Q_E , we fit to the simulated Sonnet peaks from the outgoing port. A meandering inductor in Figure 4.17(a) was initially chosen for its fabrication simplicity because it does not require crossover wires and can be done with one lithography and aluminum evaporation. However, the meandering inductor has a lower inductance per unit chip area compared to the spiral design in Figure 4.17(b). For a meandering and a spiral inductor with equal inductance, the peak Q for the meandering design will be lower due to increased conductor length. One of the

major drawbacks to meandering inductors is that due to the negative turn-to-turn of the mutual inductance, they suffers from very low inductance value which then requires very large inductors to achieve frequencies in the 8-12 GHz range. These inductors can consist of meanders that span areas which are $1\text{mm} \times 1\text{mm}$ which drastically limits of the number of devices we can fit on a chip. When the spacing between adjacent wires in an inductor decreases, the inductance of a meandering inductor will decrease, whereas the inductance of a spiral coil increases with decreasing wire spacing. This is because the spiral coil has a positive mutual inductance and the meander coil has a negative inductance which is determined by the direction of the current in adjacent wires, as shown with yellow arrows in Figure 4.17.

Spiral inductors involve a tightly-wound spiraling wire which crosses over an incoming wire. Fabricating such crossovers involves two additional lithography steps that makes the spiral inductor significantly more difficult to fabricate. Despite this, spiral inductors have many properties that make them superior to meanders. From Figure 4.17, we can see that because spiral inductors can be tightly wound and compactified to sizes that are a factor of $150\times$ smaller in area than meandering inductors with spiral dimensions that are $\approx 80\mu\text{m} \times 80\mu\text{m}$, this allows us to fit several of these devices on a membrane. We can then use one input line to inductively couple to several of these devices at the same time. Sonnet allows us to simulate several LC resonators in proximity to one another on a membrane, allowing us to simulate not only the properties of the individual resonators but also their effect on each other through inductive coupling. Spiral inductors allow us to take advantage of tight coiling and geometrically-small inductors, which have smaller stray capacitance compared to a meander inductor. Sonnet simulated a stray capacitance, $C_s \approx 2.5\text{ fF}$ for 12 GHz spiral inductor compared to $C_s \approx 12\text{ fF}$ for a 12 GHz meandering inductor.

4.6 Fabrication of Electromechanical Device

Here we give a detailed review of the fabrication process for the envisioned electromechanical devices. The fabrication process has several steps, so we split up our review into three parts: (A) fabrication and etching of mechanics elements, (B) aligned fabrication of an aluminum circuit to those mechanical elements, and (C) undercutting of the membrane as shown in Figure 4.18. Our fabrication process starts with 300 nm of LPCVD high stress silicon nitride deposited with 800 MPa of tensile stress originating from a difference in thermal expansion coefficients of deposited silicon nitride and $200\mu\text{m}$ thick silicon substrate. The silicon substrate used for these experiments were high resistivity ($\rho > 10,000\ \Omega \cdot \text{cm}$) 1-0-0 silicon wafers. After the deposition the double-side polished Si wafers are double-side spin coated with photoresist, baked, and cleaved into $1\text{cm} \times 1\text{cm}$ pieces. This keeps the chips from getting debris on them during the cleaving process. Our process etches a nanobeam (phononic cavity) into the Si_3N_4 on one side of the chip and rectangular win-

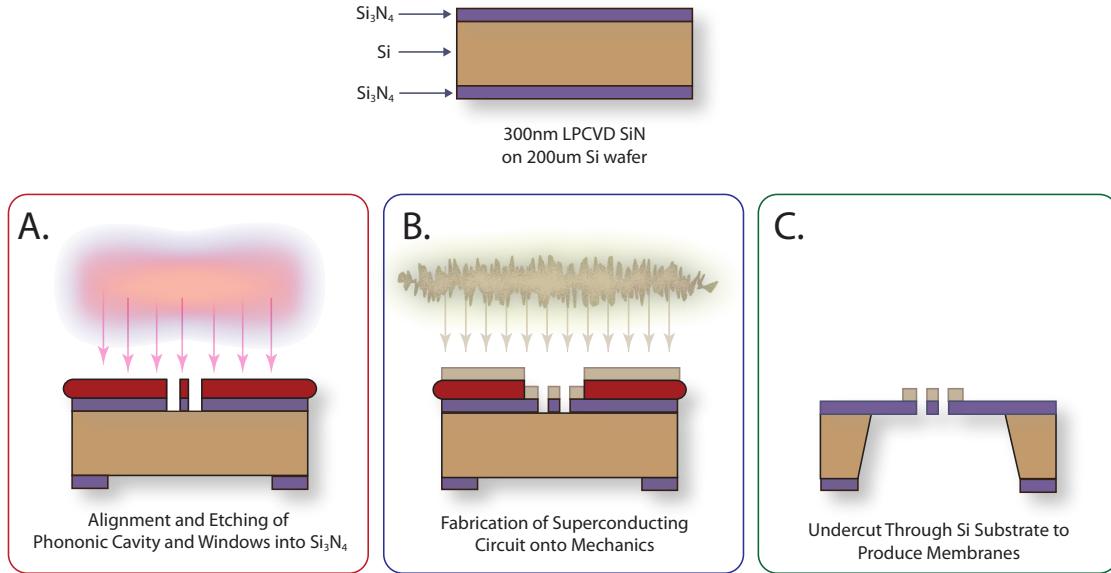


Figure 4.18: **General Overview of Fabrication Process.**

dows on the other side such that they align. Using alignment markers that we have etched into the silicon nitride, we perform a series of three aligned electron beam lithographies and two aluminum evaporations. We wet etch through the substrate using a saturated TMAH solution to undercut a silicon nitride membrane with an imbedded phononic crystal cavity and superconducting LC resonator.

4.6.1 (A): Fabrication of Mechanics

4.6.1.1 Window Alignment Methods and Dry Etch

We begin the process by removing the initial photomask protection layer on the chip using acetone and isopropyl alcohol. We spin a thin layer of ZEP520A (electron beam resist) at 4000 rpm for 1 minute over the front of the chip where the phononic cavity and superconducting circuit will eventually be fabricated in order to protect it while we undergo the etching of the back-windows that define the membranes. We bake the sample at 180°C for 2 minutes on a hotplate. We then spin a thicker layer of ZEP520A spun at 2000 rpm for 1 minute over the back side in order to later define our rectangular windows using electron beam lithography. We spin the first layer at a faster rate so that the surface of the e-beam resist is flat. A slower spinning speed produces beads at the edges of the chip where the resist has built up during the initial spin, whereas a faster spin speed would immediately kick off any superfluous resist on the chip. These beads on the edge of the chip can make a substrate sit unevenly on the EBPG holder, making it more difficult to accurately align both sides. After the second layer of ZEP520A is spun, it is baked on a hotplate at 180°C for 2 minutes.

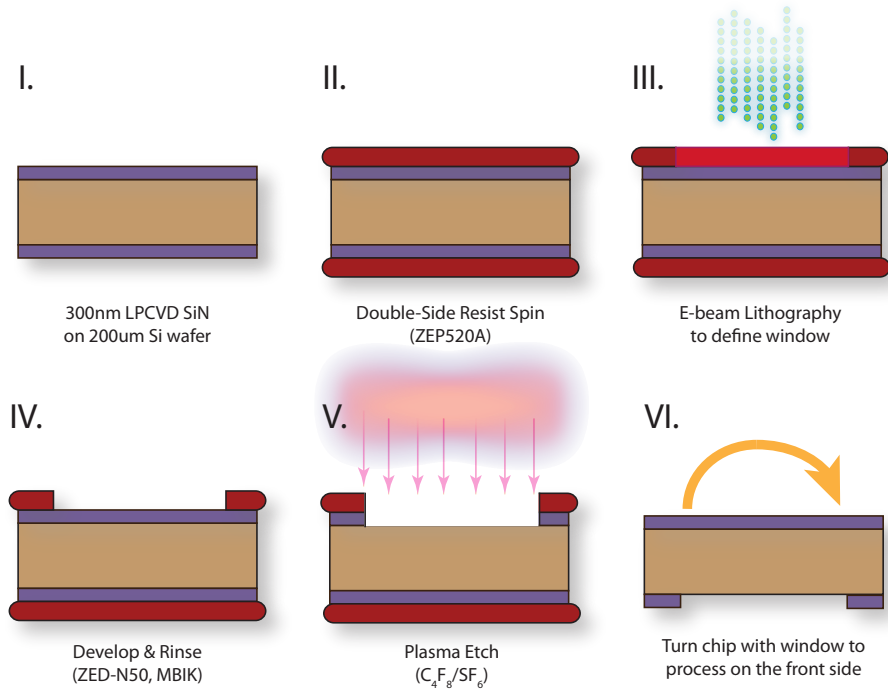


Figure 4.19: **Fabrication of Back Windows.**

Figure 4.19(ii) shows the chip at this stage. The first thin layer of the resist is meant as a protection layer for the front of the chip, as this side would scratch against surfaces when the chip was placed upside down to fabricate windows on the back side. Without this layer, we would easily scratch that side of the chip when we place the chip on the holder for the electron-beam lithography system (EBPG). Because the chip is cleaved along a crystal plane of the silicon wafer, we use the edge of the chip to align to the axes of the EBPG using an optical microscope. Once inside the EBPG, we use its internal scanning electron microscope to find the coordinates of the chip edge and write the window pattern relative to these corners. One could use the external microscope with calibrated position stage to get the position on the edges of the chip, but this can often be tens of microns different from the adjusted table coordinates used by the EBPG, leading to severe misalignment between patterns written on the front and back of the chip. This method ensures proper alignment of the patterns on the front and back of the chip by writing both patterns relative to the same physical edges of the chip. As shown in Figure 4.19(iii) the windows encompass large areas on the order of millimeters, and we use a 201 nA beam with a large $50\mu\text{m}$ resolution and $200\mu\text{C}/\text{cm}^2$ dosing. Once the patterns are written we develop for 2.5 minutes in ZND-N50 developer and 30 seconds in MIBK rinse.

The chips are thermally contacted to a carrier silicon wafer using thermal paste. This thermal paste keeps the chip thermally equilibrated to the silicon carrier wafer and the chamber of the ICP-RIE system. Using a SF_6/C_4F_8 Bosch etching process and a ZEP520A film as a mask, we etch

through a 300 nm layer of silicon nitride. Because the next step in the process involves phononic crystals with small features, we remove the ZEP520A masks on both sides of the chip with piranha solution to ensure the substrate is especially clear of surface contaminants for this electron beam lithography.

4.6.1.2 Nanobeam Alignment and Short Undercut for Shadowing

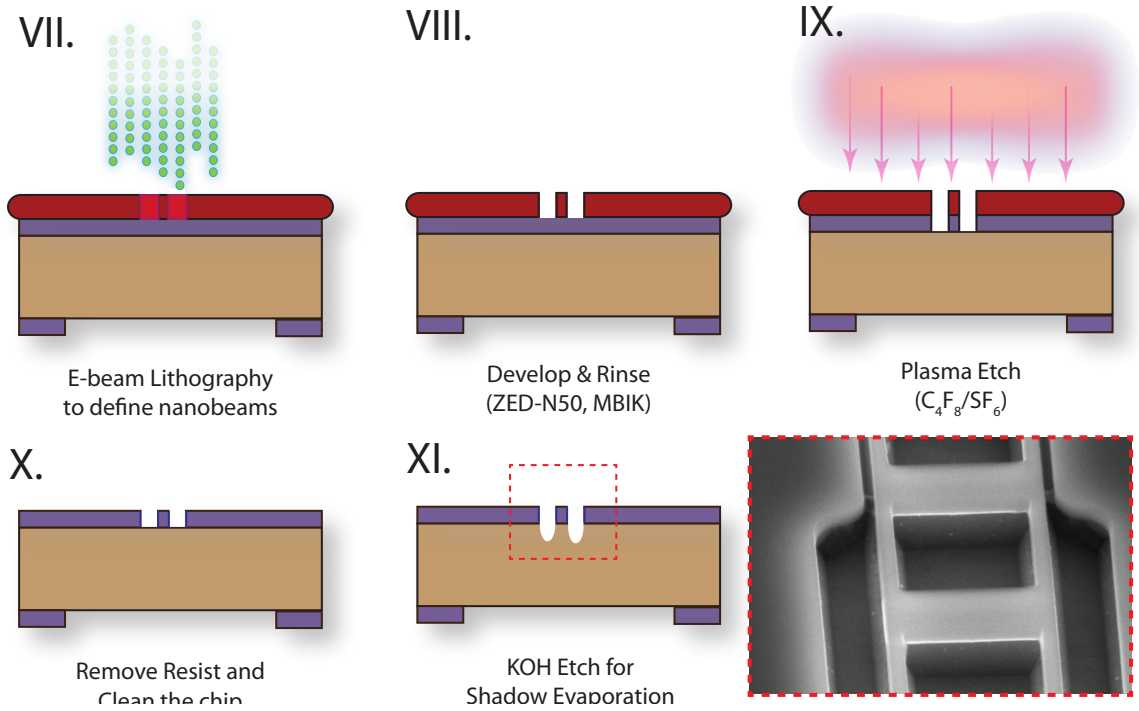


Figure 4.20: **Etching of Nanobeams.**

We spin the ZEP520A on the front of the chip at 2000 rpm for 1 minute and bake at 180°C on a hotplate for 2 minutes. In contrast to the first preparation for the electron beam lithography, we only spin on the front side of the chip. Protecting the backside of the chip would require putting the front of the chip on a vacuum chuck of a spinner where we can damage the surface or contaminate it. With such small features required for the nanobeam lithography, we try to keep the surface as clean as possible. The windows are also large millimeter sized rectangles which are not very sensitive to minor defects. We use electron beam lithography to define the nanobeams and markers on the front side of the chip. Because of the small features involved in the writing the phononic cavities, the lithography is done with small current 300 pA beam in order to expose with a 2.5 nm resolution at $275 \mu\text{C}/\text{cm}^2$ as seen in Figure 4.20(vii). Again we use the edges of the chip to align with the axes of the EBPG and use EBPG's internal scanning electron microscope to get the position of the

chip's edges and get good alignment between the front and back of the chip. Because we choosing to write the center of the patterns a set distance away from the chip's physical edges, we do not have to worry about differences in the calibration of the EBPG's adjusted table coordinates from one write to the next. When we examine the edges of the chip to get their adjusted table coordinate positions, we switch to a 5nA beam, as this gives us good resolution. One could use higher current beams for better resolution, but one begins exposing the resist so severely that the resist can begin to expand and move as it is being imaged, making it difficult to pinpoint a corner of the chip. After the lithography, we develop the resist with a 2.5 minute dip in ZND-N50 and 30 seconds in MIBK rinse.

Using ZEP520A as a mask, we dry etched the nanobeam and marker patterns into the silicon nitride with a directional $\text{SF}_6/\text{C}_4\text{F}_8$ ICP-RIE plasma etch. Although we implement the same ICP-RIE process used to etch the windows into the back side of the chip, it is crucial that this plasma etch is done very precisely since small features become increasingly sensitive to small changes in the plasma etch parameters. One the smallest and most crucial features is the capacitive gaps that define the edges of the nanobeams. As shown in Figure 4.15(a), even when the gaps are written 100 nm wide to begin with, aperture effects as can be a problem when the etch is not properly calibrated to etch through the entire Si_3N_4 layer (i.e., leaving both some of the mask after and smooth sidewalls). While the large windows would require about 4 minutes of plasma etching to completely etch through the 300 nm layer of silicon nitride, a small feature such as a 100 nm wide capacitor gap would require 7 minutes of the same etch to completely etch through because of aperture effects. The plasma etch of the nanobeams must be done with high precision because the longer etch times means competing with etching of the ZEP520A mask by the plasma. We began with about ≈ 400 nm of ZEP520A and were left with about a ≈ 60 nm thick layer after the 7 minute plasma etch.

In Figure 4.21 is an example of the type of plasma etch calibrations needed to improve the profile of vertical sidewalls. We see with the top etch (Fig. 4.21a) that there is a significant amount of booting in the profile. We show how "booting" features can occur when the gaps are small and aperture effects restrict the plasma's ability to etch deeper into the gap. For thick layers of silicon nitride ($\approx 300 - 400$ nm), where there is a larger difference between the plasma etch at the top and bottom of the Si_3N_4 layer. Our plasma involves two gases: sulfur hexafluoride (SF_6) and octafluorocyclobutane (C_4F_8). SF_6 works as an etchant when it is disassociated in the plasma into SF_x AND F_y which combined with a DC bias in the chamber accelerates these etchants towards the the substrate in order to etch directionally downward. Even with a DC bias, the SF_6 still etches isotropically such that during the 7 minute etch the top of the gap will be etched longer (isotropically) than the bottom of the gap, leaving a gap that is smaller at the bottom and more blown out at the top, also resulting in a booting features. We can counteract this uneven isotropic etching by including C_4F_8 , which ionizes in the plasma and dissociates into CF_2 , which adsorbs on

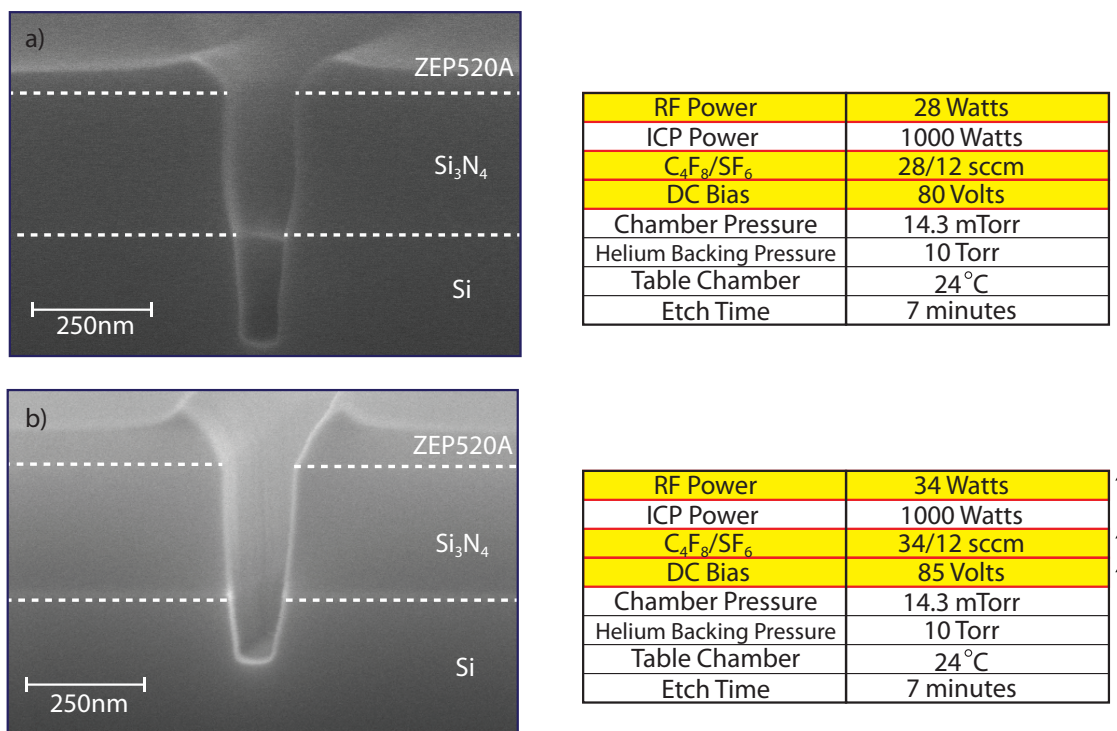


Figure 4.21: **Etching Straight Capacitive Gap Sidewalls.**

the surface and produces cross-linked polymer. This polymer acts as a thin passivation layer. It also acts as a passivation layer for the ZEP520A resist layer allowing one to etch for longer without etching away the mask. Because of the DC bias, this passivation layer will be the most effective on the sidewalls as the passivation deposited at the bottom of the gap will be directly in the path of the accelerated etchants. With the right etch recipe, the passivation layer builds on the sidewalls allowing for smooth sidewalls through the entire etch. We also cannot simply continue adding C_4F_8 to make the mask last longer and make the sidewalls straight, as eventually the rate at which the passivation layer is deposited becomes faster than the rate that it can be etched away by the plasma etch in the vertical direction which can slow the etch or even make it stop completely. Adding C_4F_8 to the etch results in longer etch times (to etch through the Si_3N_4) which slowly heat up the sample and can make the mask susceptible to etching away completely. The correct proportion of gases, dc bias, and powers are required in order to produce an etch that is vertically straight and can be done in a reasonable time such that the mask is reliable from one etch to another. Figure 4.21 shows the profiles of two etches and the ICP-RIE parameters used in the etch recipes where we have highlighted in yellow the etch parameters we change in order to optimize the etch. In Figure 4.21(a), one can see the booted sidewall profile of 90 nm wide gaps with an etch that has not been optimized. In Figure 4.21(b) we increase the $\text{C}_4\text{F}_8:\text{SF}_6$ ratio which increases the amount of passivation layer we

deposit on the sidewalls, making the width of the gap more homogeneous between top and bottom of the silicon nitride layer. However, increasing the C_4F_8 (and the passivation layer deposition rate) we also slow the etch in the vertical direction. In order to keep the etch time the same, we increase RF power from 28 W to 34 W, which increases our DC bias from 80 V to 85 V, which in turn increases the acceleration of the etchants into the substrate. This increases the etch rate to counteract the extra passivation layer produced from additional C_4F_8 in the gas mixture. We see that with this small optimization we are also left with a much thicker layer of ZEP520A which has been protected by passivation layer making the recipe more robust to small changes in the etch.

In order to perform a “shadow” evaporation one needs to perform a short undercut on the nanobeam using 30% potassium hydroxide (KOH) to allow sufficient space under the nanobeam. Instead of using the electron-beam lithography to precisely write two wires onto the nanobeam, which will inevitably suffer from small misalignments, we write large areas that encompass places where there are wires and their gaps are located (Figure 4.22). The space under the silicon nitride gaps should be deeper than the thickness of the evaporated aluminum so that different parts of the aluminum do not attach to one another. This requires partially undercutting the nanobeam without completely releasing the nanobeam. It is important that the nanobeam is not completely undercut because there are a large number of processing steps that follow, each of which could damage the nanobeam when it is free to move and attach itself to surrounding silicon nitride across the small gap. In order to make the etch slow and well controlled, we partially undercut the nanobeams with a 60°C KOH etch for 45 seconds (depending on design dimensions of the nanobeam) which partially undercuts the perimeter of the nanobeam where the capacitor gaps are located. Before this short undercut we remove the ZEP520A from the surface using ZDMAC (N,N-Dimethylacetamide), acetone, and IPA. We specifically avoid a piranha clean which oxidizes the silicon surface under the silicon nitride gaps. The KOH etch rate of the surface SiO_2 is slow (81 nm/hour) compared to the etch rate of silicon ($25\mu\text{m}/\text{hour}$), so even a thin layer of SiO_2 can delay the start of the short KOH etch by several seconds of this short wet etch. By avoiding a piranha clean before this KOH undercut, one can minimize this delay and increase the repeatability of this step. Consistency is an important aspect of this step since one can easily undercut the structure too aggressively with the short KOH undercut and release the nanobeam, thus ruining the sample. One can also undercut too little and allow the aluminum in the shadowing process to connect, which is something that cannot be completely verified until the structure is released (this is exceedingly risky as the steps that follow are numerous and time-consuming). The undercut is done in a beaker with a Teflon spinner spinning at 100rpm which allows a small continuous flow in the KOH in order to keep the temperature homogeneous. When the sample is inserted into the KOH using tweezers, we keep the sample as still as possible, as any shaking or moving of the sample can increase the flow of KOH to the silicon and imprecisely increase the etch rates. After the KOH etch the sample is immediately

rinsed with water and dried with an N_2 dry. After the undercut, we piranha clean the sample to thoroughly clean it as this is the last acid clean we can perform on the chip before we begin the evaporation steps for the aluminum circuit which is quickly etched by these cleans. The piranha solution is made from a 3:1 solution of sulphuric acid to hydrogen peroxide heated to $150^\circ C$ where the sample is cleaned for 10 minutes and then rinse with deionized water and IPA.

4.6.2 (B): Fabrication of Superconducting LC Resonator

4.6.2.1 Electron Beam Lithography and Shadow Evaporation

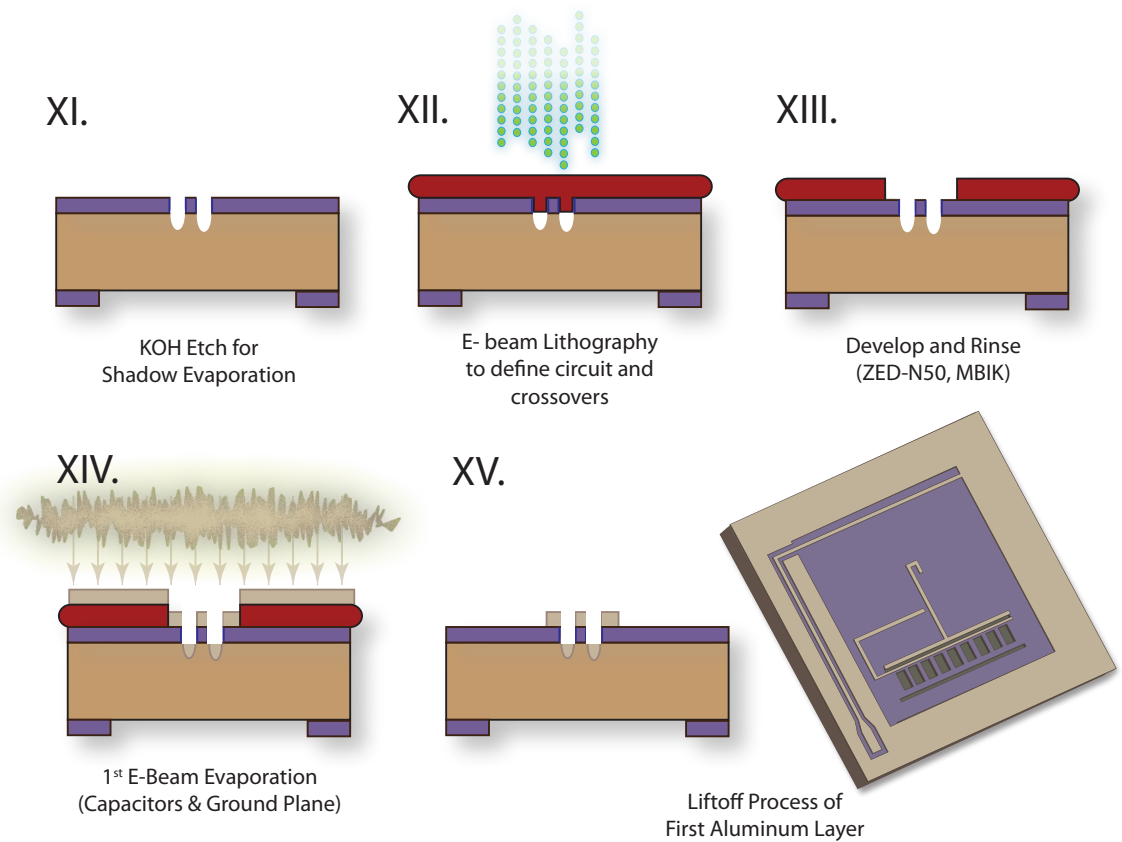


Figure 4.22: **Evaporation of First Aluminum Layer.**

Now that the chip is clean we can prepare the sample for the first layer of the aluminum circuit (Figure 4.22). We spin ZEP520A at 4000 rpm for 1 minute and bake the sample at $180^\circ C$ for 2 minutes. The nanobeam gaps and the small undercut are small enough that the ZEP520A remains homogeneous when it is spun over them. This allows one to repeatably have the same thickness of resist each time and consistently dose the resist layer the same amount. The electron beam

lithography then defines the first layer of the circuit which consists of the wire coupling the spiral inductor to the metallization on the nanobeam using a 10 nA beam with 10 nm resolution at $300\mu\text{m}/\text{cm}^2$. In the same lithographic step we write the coplanar waveguides, bonding pads, and ground plane surrounding the membranes and coplanar waveguides using a 200 nA beam at 50 nm resolution at $275\mu\text{m}/\text{cm}^2$. Because these features are large we can use large beam currents and resolution so that a large portion of the chip can be exposed for the ground plane in a short time. We use the negative square markers etched into the silicon nitride to align our first circuit layer to the nanobeam (negative markers which made easier to detect by the EBPG because of the short undercut which increases its contrast). After the lithography, we develop the resist using 2.5 minutes in ZND-N50 and 30 seconds in MIBK rinse. Before the aluminum evaporation we perform a low power O_2 plasma clean using a Branson P3100 asher/stripper system for 2 minutes with 100 W of forward power and 300 sccm of oxygen. This O_2 plasma is used to clear off the surfaces of the silicon nitride before the first layer of aluminum is evaporated onto it. Using a CHA Mark-40 Evaporation System, we evaporated 50 nm of aluminum at a rate of 2.5 angstroms/sec and a pressure of 5×10^{-7} Torr. Because the aluminum material source gets contaminated and oxidized over time, we run an initial electron beam sweep over our aluminum source with the shutter closed to avoid evaporation of these contaminants onto our sample. This initial beam sweep also allows one to stabilize the deposition rate before the shutter is opened and evaporation onto the sample begins. We used hot NMP (N-Methyl-2-pyrrolidone) to perform a liftoff procedure which removes the ZEP520A on the sample. The NMP is set on a hotplate at 100°C for 1 hour before the rest is removed more forcefully using a pipette to increase the flow of NMP over the sample. Using a shallow bath of IPA, we check the circuit under an optical microscope to make sure the liftoff was successful. We need inspect the sample while it is still immersed in liquid since drying the sample could allow pieces of loose aluminum to permanently attach (through Van der Waal Forces) to unwanted areas or even short different regions on the chip. Once the liftoff has been done successfully we rinse the chip in acetone and IPA. One must be careful not to include water anywhere in this step since NMP on its own does not etch aluminum, but when combined with water can begin to etch aluminum. In this step it is important not to rinse glassware with water as even trace amounts combined with NMP could have significant effects on our thin 50 nm layers of aluminum.

4.6.2.2 Sacrificial LOR Layer and Reflow

Now that we have the aluminum wire connecting the center of the spiral inductor to the nanobeam, we need to create the sacrificial infrastructure that allows us to evaporate a spiraling inductor that crosses over (and does not touch) the first wire we evaporated. In this portion of the fabrication a double layer of resist consisting of LOR5B as the sacrificial layer and e-beam resist PMMA950A on top of the LOR5B is used to define the desired pattern (Figure 4.23XVI). We use LOR5B lift-

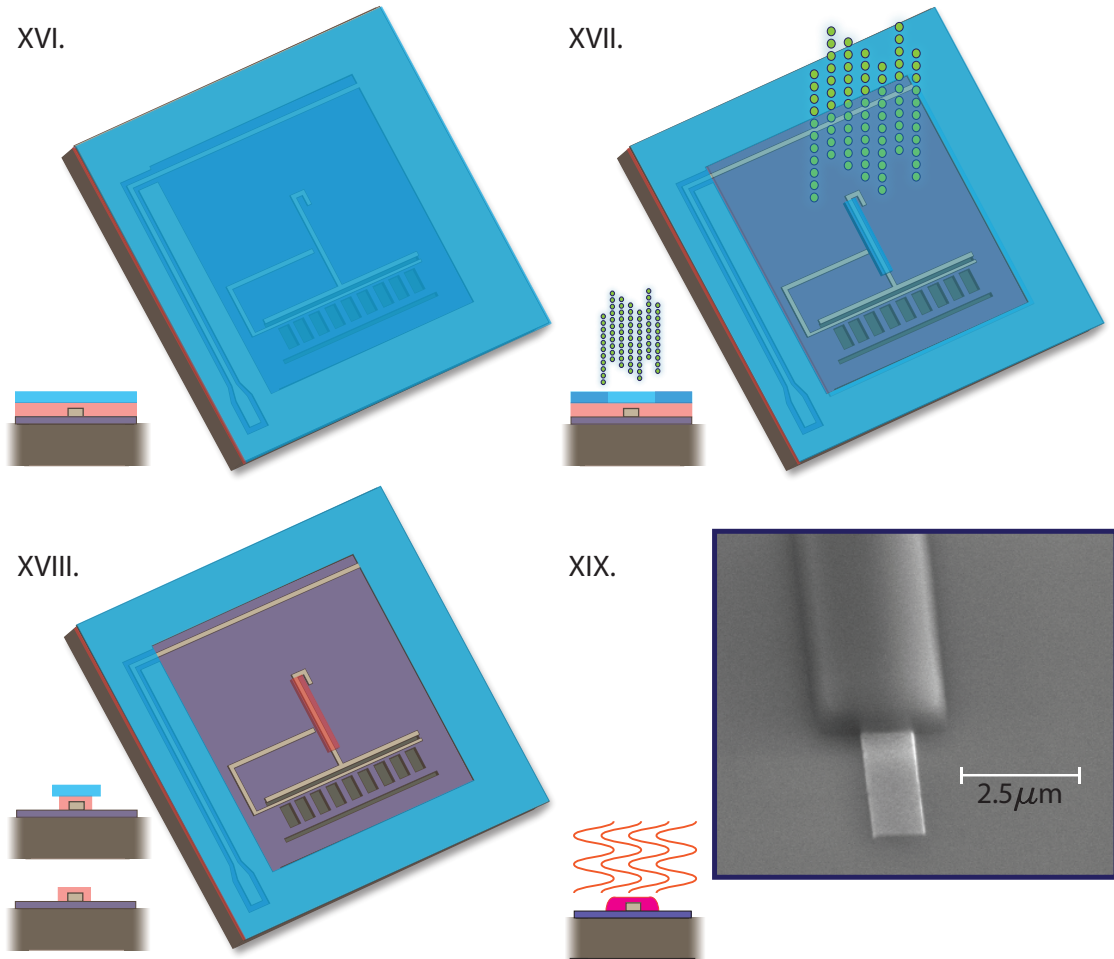


Figure 4.23: **LOR Bridge Fabrication for Circuit Cross-Overs.**

off resist because of its relatively high dissolution rates which makes it ideal for creating a thick sacrificial layer and tall crossovers on the order of 500 nm and its The LOR5B is spun at a rate of 3000rpm for 1 minute. Normally to deposit an even layer of resist one would place every droplet of resist on the same spot on the chip, allowing the growing droplet of resist to spread homogeneously across the chip. When spinning LOR5B, we use the pipette to evenly distribute the resist across the chip before the spin, allowing this thick resist to spread across the chip. The chip is then baked on a hotplate for 5 minutes at 180°C. After allowing the chip to cool, we spin on electron beam lithography resist PMMA950A on top of the LOR5B layer. This layer is spun at a 4000 rpm for 1 minute and baked on a hotplate for 5 minutes at 180°C.

The next electron beam lithography step is dedicated to writing the inverse of the sacrificial layer (Figure 4.23XVII). This requires exposing large areas so we use 200 nA beam with a 10 nm resolution and a dose of $800\mu C/cm^2$. Using the same negative markers, we align the written pattern to the previous layers. After the electron beam exposure, we use a 1:3 solution of MIBK to IPA as

a PMMA developer for 1 minute and rinse in IPA for 30 seconds. Now the e-beam exposed areas of the PMMA950A have been cleared after the development step, leaving a wide strip of double layer resist (LOR5B/PMMA950A) over the initial aluminum wire. Using the PMMA950A as a mask, and TMAH-based etchant MF-319 is used etch away the layer of LOR5B except under the strip of PMMA950A. We initially make this strip much wider than the initial aluminum wire because the PMMA950 can only protect the LOR5B from vertical etching, but does not protect the sides of the LOR5B strip underneath. We etch the LOR5B layer with MF-319 for 7 seconds, which is just enough time to etch through the 500 nm thick LOR5B layer, and not so long that it etches away the entire strip of LOR underneath the PMMA from the sides (Figure 4.23XVIII). While the pre-bake of the LOR5B is the most important aspect in determining the amount of etch rate of the MF-319, we are also careful not to shake the sample during this short 7 second etch, as any inconsistencies in movement of the sample during the etch can result inconsistencies in the etch rate due to differing flow rates across the sample. Once the PMMA has been used as a mask for this wet etch, we remove the PMMA950A mask layer by rinsing the sample for 2 minutes in acetone and a second rinse in IPA. There are a number of LOR-series lift-off resists, but LOR5B is specifically used for this process because of its ability to withstand acetone.

We are now left with a sacrificial bridge of LOR5B that covers the first layer of aluminum wire with a rectangular profile (Figure 4.23XVIII). Since we use a bridge of LOR5B as a spacer layer in order to evaporate the spiral inductor and have it jump over the initial aluminum wire, it is important that the layer defining the crossovers does not have a rectangular cross section with vertical walls. The electron beam evaporations of aluminum are performed at high vacuum ($\approx 10^{-6} - 10^{-7}$ Torr), making the evaporation of aluminum onto the sample a ballistic evaporation. Such a cross-section would not allow smooth crossover of the spiral inductor and would produce jumps with a rectangular profile which might not connect well. In order to smoothen out the profile of the LOR5B bridge we use a reflow heating process where the sample is heated to high temperature with a hotplate at 200°C for 10 minutes. The high temperatures slightly melt the LOR5B layer results in a profile with rounded edges which define the shape of the crossovers (Figure 4.23XIX). Such a bridge profile produces smooth and robust inductor crossovers after the aluminum evaporation.

4.6.2.3 Spiral Inductors Fabrication

Now that the bridge is the appropriate profile we begin preparations for the electron beam lithography of the spiral inductor. We spin a double layer of PMMA resists which are used to define the spiral inductor. We spin PMMA495A at 4000rpm for 1 minute and bake at 180°C for 2 minutes. We allow the chip to cool before we spin the second layer consisting of PMMA950A which is spun and baked with the same parameters as the first layer. We use electron beam lithography to expose the spiral inductor pattern onto the sample using a 10nA beam with 2.5 nm resolution with a dose of

$1500\mu C/cm^2$ in order properly dose the double layer (Figure 4.24XX). The top layer of PMMA950A is developed using a 1:3 solution of MIBK to IPA for 1 minute followed by a rinse in IPA for 30 seconds (Figure 4.24XXI).

After the spiral inductor has been defined in our double layer of resist, we perform a second aluminum evaporation using a CHA evaporation system. As opposed to the first evaporation of aluminum where a low power O_2 plasma was used to clean the substrate before the evaporation, this is not done before the second evaporation since it increases the oxidation on the first layer of aluminum. On top of introducing two-level systems in the layer of aluminum oxide, there are regions where first and second layers overlap and connect, and in these regions having a layer of aluminum oxide between two aluminum wires creates an unwanted capacitance (although a layer of aluminum oxide forms within seconds of exposure to atmosphere). At pressures of 10^{-7} Torr, we evaporate 120 nm thick layer of aluminum at a rate of 5 angstroms/sec (Figure 4.24XXII). In order to perform a liftoff of the evaporated aluminum we put our sample in a closed container of acetone for 30 minutes on a hotplate at $80^\circ C$ to properly remove the PMMA layers. Often it is required to use a pipette to implement an aggressive flow of acetone across the chip to completely liftoff the spiral (Figure 4.24XXIII).

Once the liftoff of the inductor spiral has been completed, we want to remove the sacrificial bridge of LOR5B from under the crossover wires of the spiral (Figure 4.24XXIV). For this removal we immerse the sample in an enclosed breaker of NMP on a $100^\circ C$ hotplate for 30 minutes. Once the LOR5B bridge is removed we can rinse the sample in acetone and IPA, being extremely careful not to introduce water anywhere in the process (as the combination of NMP and H_2O etches aluminum).

4.6.3 (C): Membrane Undercut using TMAH

A significant challenge in the construction of our electromechanical devices was planning a process that allowed us to create complex, fabrication-intensive circuits on a membrane with a freely moving nanobeam. Because most weak bases used to etch through the silicon substrate (i.e. TMAH, KOH, etc.) aggressively etch aluminum, the initial strategy was to completely undercut the membrane (and nanobeam) first, and subsequently fabricate the circuit on the suspended membrane. This would allow one to produce the membrane with nanobeam and circuit without exposing the aluminum circuit to these wet etchants. An insurmountable problem with this order was that a free moving nanobeam separated from the surrounding membrane by gaps on the order of 50 nm could not survive the large number of spins ($\approx 2000 - 4000$ rpm), evaporations, rinses, and processing involved in the fabrication of the superconducting circuits. Several attempts at such a processing order (undercut first, circuit second) produced very low yield as most of the nanobeam had stuck (through Van der Waals forces) to the adjacent membrane.

In order to overcome this challenge, we etch the mechanics into the silicon nitride, fabricate the

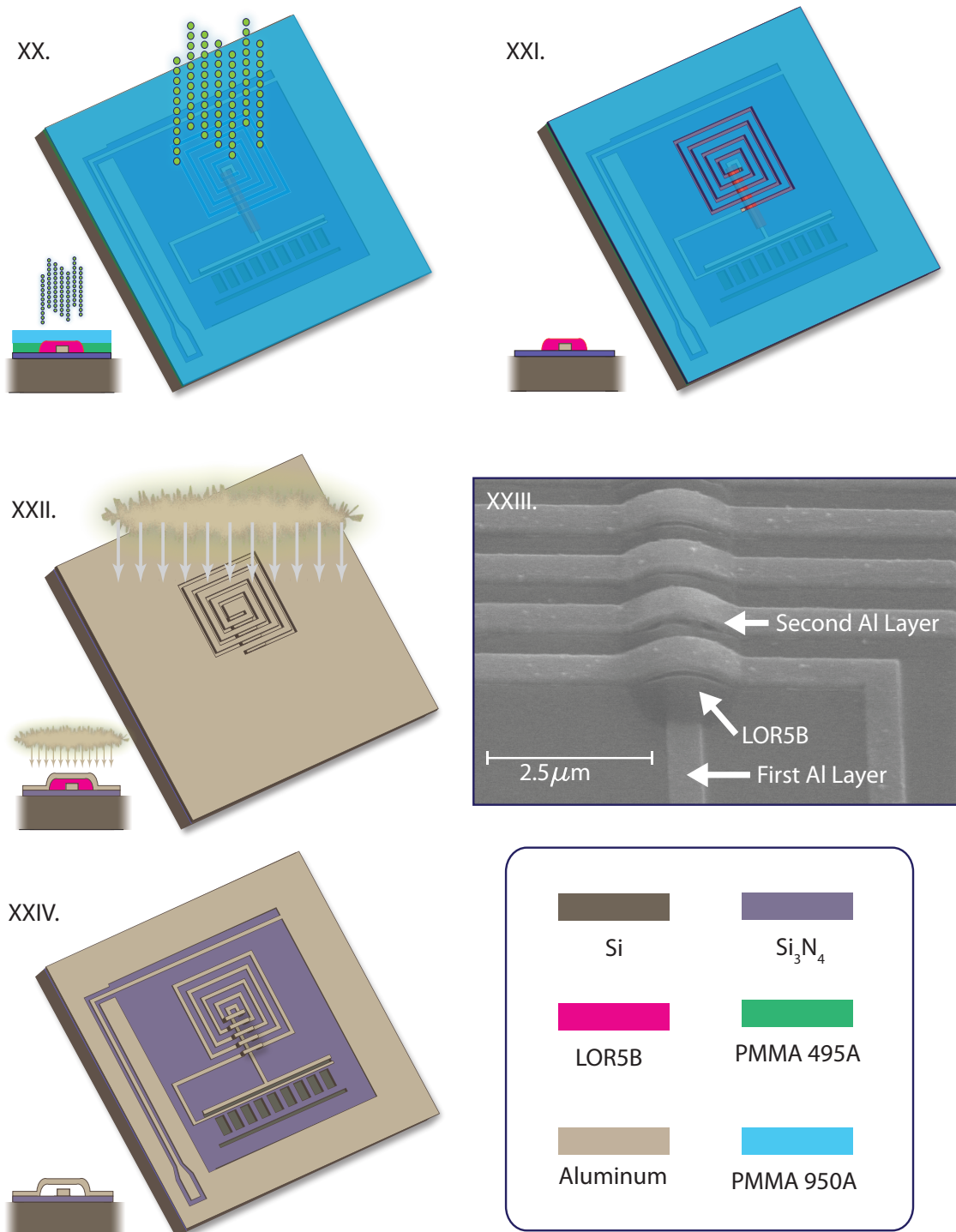
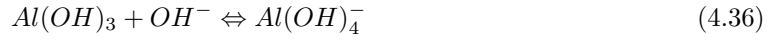
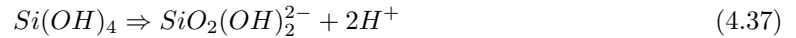


Figure 4.24: Fabrication of Spiral Inductor (Second Aluminum Layer).

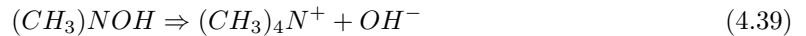
superconducting circuit onto it, and undercut the entire membrane as the last step using a saturated form of TMAH (Tetramethylammonium Hydroxide) that etches through the silicon substrate but does not etch the aluminum circuit. TMAH in its conventional form etches aluminum very quickly. When aluminum is exposed to air, a thin layer of aluminum oxide immediately grows on the surface. The oxide layer that is formed contains $\text{Al}(\text{OH})_3$, which reacts with alkaline solutions (i.e. TMAH) to form alumina by the reaction:



We notice that if the pH is lowered then the chemical equilibrium shifts toward the left side of the reaction, and there one can calibrate the solution such that aluminum is surface passivated and protected while still etching silicon along its 1-0-0 plane. In order to get the same effect in TMAH, we lower its pH by saturating the solution with high purity silicon. By dissolving silicon into the TMAH, the solution forms aluminosilicates (thin Si rich oxide layer) on the aluminum surface. When we dissolve silicon to introduce silicates into the solution we gradually lower pH and also the TMAH's ability to etch silicon, but the silicates also work to create a passivation layer on the aluminum surface. We know that the silicates release H^+ ions which react with hydroxyl ions to form H_2O and decrease the TMAH solution's pH, as seen with reactions:



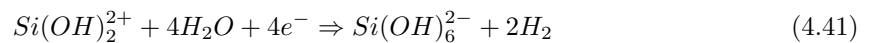
Generally, we can look at the nominal mechanisms that simply allow TMAH to dissolve silicon. This etching involves a series of reactions starting with



wherein TMAH is reduced to form hydroxyl ions. Then the silicon atoms react with the hydroxyl ions to form oxidized silicates $\text{Si}(\text{OH})_2^{2+}$ and 4 electrons into the conduction band as seen in the following reaction:



which happens simultaneously with the reduction of water to form more hydroxyl ions which bond to the silicates formed in Equation 4.40 as seen in the reaction,



We can see in Equation 4.41, that silicic acid is produced and outgasses hydrogen as a byproduct. The less concentrated the TMAH solution (higher concentration of water) the faster silicon is etched. However, if the TMAH+Si solution is a low concentration TMAH with a reduced pH from the dissolving silicon, it will produce more hydrogen when H_2O is added to a reaction like Equation 4.41. In order to counter the rough silicon etch that can be produced from using a TMAH with a lowered pH, we introduce a strong oxidizer like ammonium persulfate, $(\text{NH}_4)_2\text{S}_2\text{O}_8$, which replaces H_2O in Equation 4.41 and consumes hydrogen, producing smoother silicon surfaces. We found the solution's success in providing good selectivity with the aluminum to be dependent on preparation and time since solution was made. The solution was carefully prepared fresh before each undercut. Other groups that have investigated this aluminum-selective silicon etchant ([73] [73] [74]) have found the solution's effectiveness to be dependent on preparation (i.e., small organic contaminations are known to affect the solution's ability to remain selective to aluminum). Because the fabrication process for our electromechanical system is lengthy and tedious (requiring 5 electron beam lithography steps and 2 evaporations) it is important to prepare the final wet-etch solution very systematically.

We start with standard TMAH solution (25% concentration) which we dilute with water to produce $\approx 10\%$ TMAH which we then use to dissolve the silicon. We used high purity 1-1-1 silicon wafers (99.999999% Si) which are crushed into a dust and dissolved in TMAH. In preparing the modified TMAH (mTMAH), it is important that the dissolution of silicon into the TMAH is done as quickly as possible. Dissolving for long periods of time increases the chances of contamination with the potential to lose a significant amount of water to evaporation since the dissolution is performed at high temperatures ($\approx 80^\circ\text{C}$) in order to increase the etch rate. Crushing the silicon wafer pieces into dust increases the etch rate since each silicon particle can be etched from several directions (TMAH preferentially etches Si in the 1-0-0 direction). We create a final mTMAH solution that is 3.2 wt.% Si, 1.3 wt.% ammonium persulfate, and 10 wt.% TMAH. For a mTMAH solution of 250g, we dissolve 8g of silicon. The TMAH must be diluted from 25% to 10% since a less concentrated TMAH etches silicon faster and more crucially, and adding this amount of silicon to 25% TMAH oversaturates the solution with silicates, leaving behind large deposits of solidified salt byproduct. Depending on the particle size of the silicon dust, the dissolution of the silicon lasted $\approx 3 - 4$ hours at 80°C in 10% TMAH. In order to dissolve such a large amount of silicon in TMAH we use a tall glass cylinder which is sealed with a glass condenser that continuously runs water through it to keep it cool. When the solution evaporates it condenses on the cold surface of the glass condenser and drips back into the cylinder. The setup needs to be well sealed in order to do etches that last several hours since a small opening in the setup will allow a significant amount of water vapor to escape. This would raise the concentration of the mTMAH and slow the silicon etch rate and compromise the aluminum selectivity. We use a large and tall glass setup (tall compared to the level of mTMAH we are producing) since adding a large amount of fine silicon dust to TMAH will produce a very fast

etch rate that produces large amounts of hydrogen as a byproduct. This sudden release of hydrogen gas makes the solution bubble violently, and a tall container is required to make sure the addition of silicon dust to the TMAH does not cause overflow out of the condenser setup. Once the silicon was completely dissolved in the TMAH, we measured a pH change from 13 to 12.5. Ammonium persulfate is added to the solution and allowed to dissolve for about 30 minutes before we add our samples. It was found that dissolving the silicon before the ammonium persulfate was important in preventing aluminum etching [74].

As seen in Figure 4.25, the devices were then etched in the mTMAH at 85°C for ≈ 4 hours in order to completely etch through the 200 μm silicon substrate. We could easily determine when we finish etching through the silicon substrate when clear membranes appear on the front side of the chip. In order to fabricate high quality optics and mechanics, one must be able to thoroughly clean the sample after the wet release. Several of the acids one would normally use to clean silicon nitride and silicon of contaminants and the salts left over from the mTMAH would etch aluminum quickly. Because of the high stress in membranes, the clean cannot etch the silicon nitride in any way, or this will lead to explosion of the membrane. The salts produced from a typical TMAH etch can be seen covering the sample even if it is well rinsed in deionized water and other solvents (acetone, IPA, TCE, etc.). These are typically produced when one transfers a sample from hot TMAH to a cold water rinse where the sudden change in temperature allows the salts to crystallize on the surface and are difficult to remove without acids. We avoid this by following the mTMAH etch with a hot water rinse at 85°C so that the sample is rinsed completely of the TMAH without allowing salts to solidify on the surface. We rinse the sample two times more in room temperature water before transferring to IPA rinses without drying the sample. Once the sample is completely rinsed of mTMAH and submerged in IPA, we transfer the sample to the critical point dryer (CPD). Because of the combination of small gaps on the order of 20-50 nm, a floppy nanobeam and millimeter-sized membrane which moves freely, we cannot allow droplets of solvent to evaporate on the device since the surface tension of an evaporating droplet would pull the gaps together, causing shorting in the capacitive gaps. This method of fabricating electromechanical devices on silicon nitride membranes allows one to produce complex superconducting circuits coupled with small-gap mechanics which must be released as a last step due to their fragility. This method produces very clean samples with small gaps. One-sided holders that seal the chip on one side (side with circuit) and allow wet etching through the other could work for producing circuits on unpatterned membranes, but if mechanics are etched into the membrane, this inevitably leaves an opening in the membrane that would make the one-sided holder ineffective once the membrane was completely undercut by allowing the TMAH to flow through. The need to critical point dry the device in order to preserve the small gaps in the mechanics illustrates why undercutting the membrane (and nanobeam) first followed by the fabrication of the circuit would not be possible, as the nanobeams would require critical-point-drying

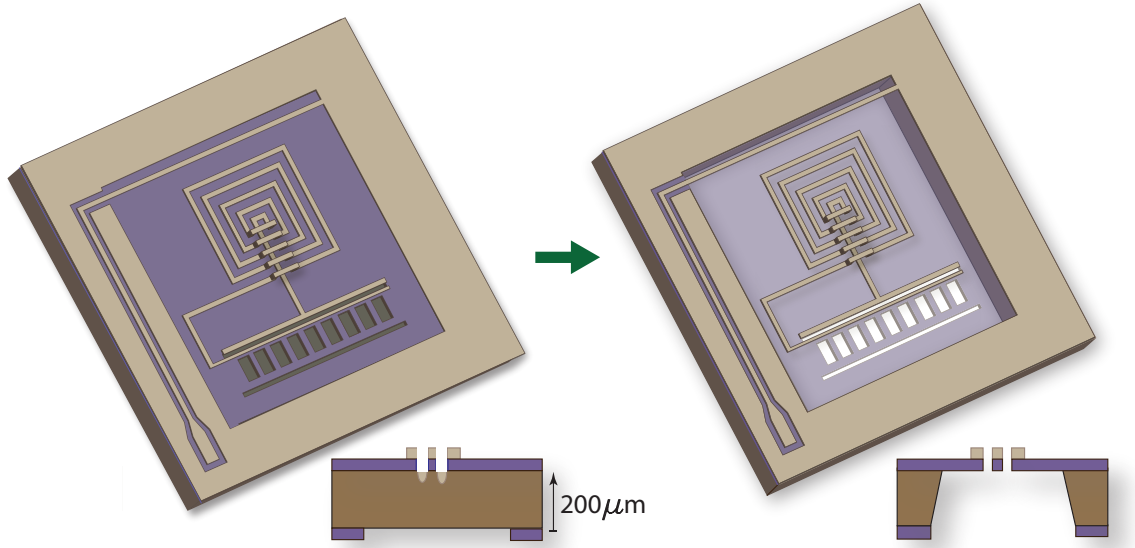


Figure 4.25: **Undercut of the Membrane Electromechanics** . Illustration showing the sample (top and cross-sectional view) before etching through the silicon substrate and after the undercut of the membrane.

every time the sample is involved in a wet-process during the fabrication of the circuit (i.e., liftoffs, resist spins, etc). Our fabrication allows us to fabricate complex circuits on patterned membranes and avoid the handling issues that commonly arise when implementing several fabrication steps on a delicate membrane.

4.6.4 Final Devices

Here we review the final parameters of the electromechanical devices we are able to fabricate. A $10\text{cm} \times 10\text{cm}$ which has 4×4 array of $1\text{mm} \times 1\text{mm}$ Si_3N_4 300 nm thick membranes, each which fit 4 electromechanical devices (LC resonators coupled to phononic crystals). There are four microwave launchers each which lead to an input lines that inductively couple to devices on four membranes. Using our rinsing techniques we are able to produce a very clean sample that is absent of salt by-products left from the mTMAH wet etch. This is important in trying to achieve small 30-50 nm gaps as even a miniscule salt residue could short a small gap and restrict the physical oscillations of the nanobeam. The 64 devices on the chip are each coupled with different strengths to the input line by varying their distance from it. In order to fabricate a variety of small gaps and ensure the smallest gaps, we vary the angle of the pull-in slits from very small pull-ins to large pull-ins. Our crossovers wires lie 400 nm nanometers above the in-coming line. The smallest capacitive gap we were able to achieve was ≈ 30 nm. The width of the wire in our inductors was $1\mu\text{m}$ with a thickness of 120 nm, while the thickness of the ground plane and capacitor wires on the nanobeam was ≈ 60 nm. We fabricated both symmetrically and asymmetrically coupled devices for measuring

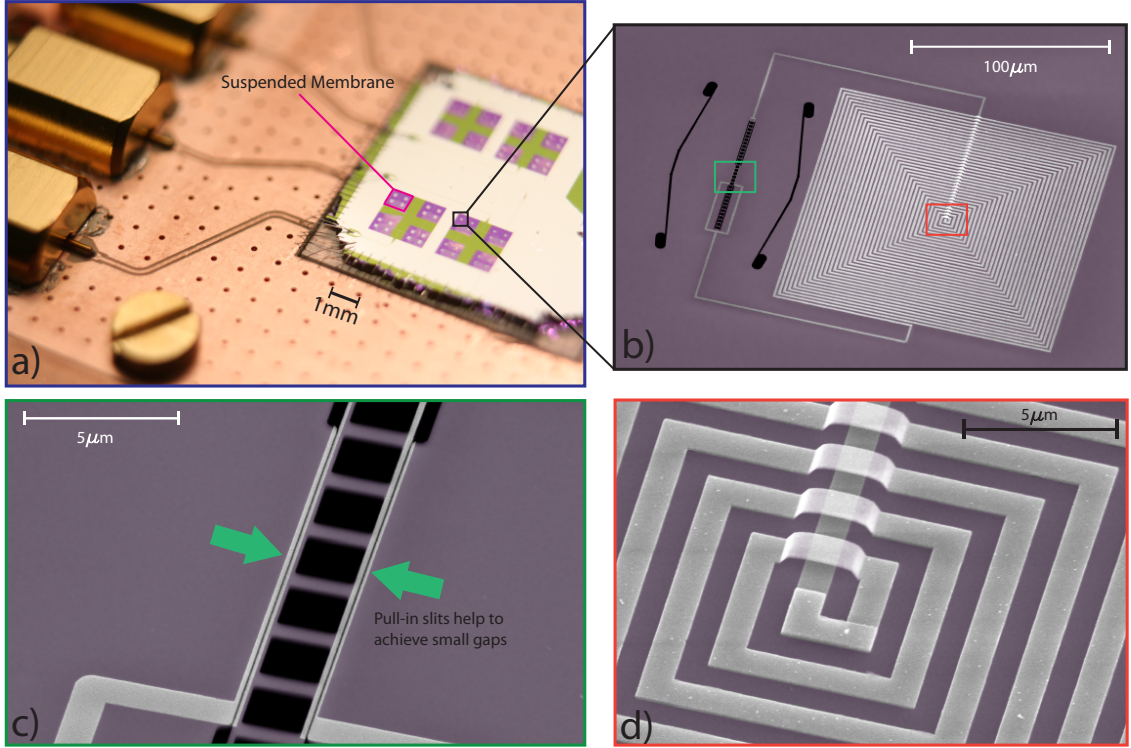


Figure 4.26: **Final Device Images.** (a): Image shows the final chip wire-bonded onto a printed circuit board. The purple squares are 300 nm thick silicon nitride membranes produced by etching through the silicon chip from the backside (b): Colorized SEM image of a nanobeam coupled to a superconducting LC resonator. (c): SEM image of nanobeam with 50 nm gap capacitive gap achieved with pull-in techniques. (d): Colorized SEM image of crossovers required to form a spiral inductor.

the 450 MHz breathing mode and the 4MHz fundamental mode. Figure 4.26 shows an example of a symmetrically coupled device. Our chips are examined with an SEM and wirebonded to a printed circuit board (Figure 4.26(a)) where one can see the 16 undercut silicon nitride membranes (purple square). Looking closer we see that each has an spiral inductor connected symmetrically to a nanobeam, and that the aluminum wires are unetched by the ≈ 4 hour modified-TMAH etch.

4.6.5 Post-Fabrication Examination of Gaps

Because of the small imperfections in the vertical profile of the plasma etch that defines the nanobeams and gaps there is difference in the size of the gap at the top and bottom of the gap, as seen in Figure 4.15. This type of geometry means that the gaps can look well separated from a top view but be smaller or closed at the bottom face of the membrane. We take advantage of the large hole through the chip needed to undercut the membrane which allows us to turn the chip upside-down and image from above into the bottom of the membrane. In order to look at the sample from the top, we machined a custom sample holder for the scanning electron microscope which allowed

us to place the sample upside down without damaging the devices on the front of the chip.

Because the gaps are generally smaller at the bottom of the silicon nitride layer (≈ 20 nm smaller),

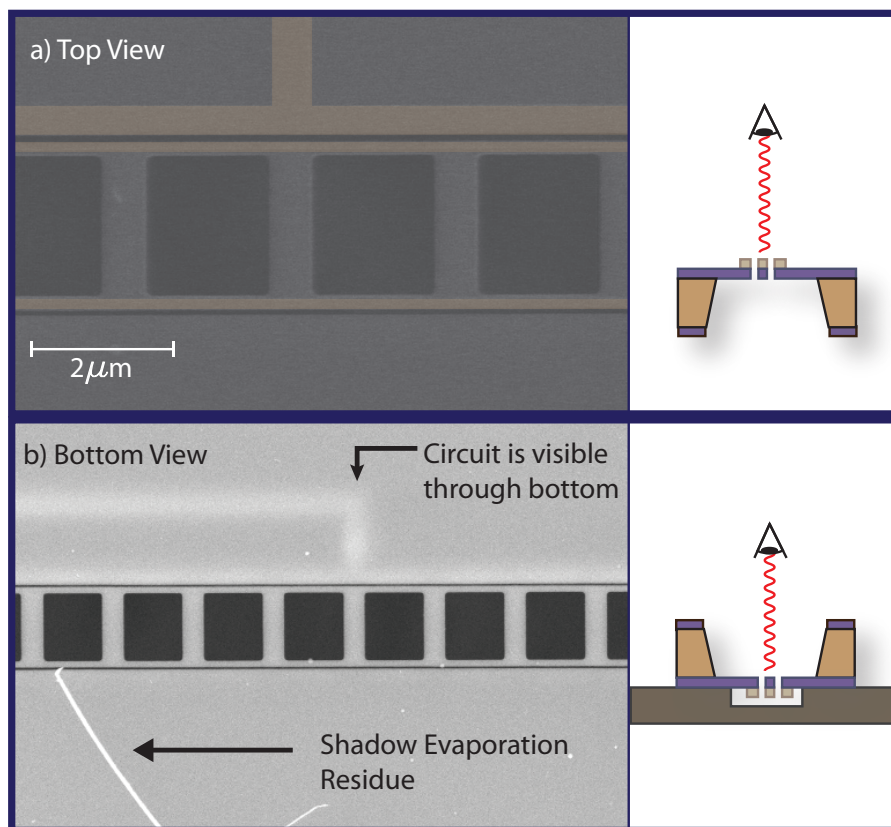


Figure 4.27: **Imaging of Gaps.** (a): SEM micrograph showing top view of nanobeam and capacitive gap. (b): SEM micrograph of membrane device gaps imaged from the back. We fabricated a custom SEM holder which allows us to safely clamp the sample upside down. Because the capacitive gaps can look open in the front but be closed in the back (due to slight changes in the gap width along the membrane thickness due to non-ideal sidewall profiles), the membrane geometry gives us the ability to check that the gaps are fully separated to avoid shorts in our circuit. We can also check for aluminum “residues” from the shadow evaporation which can also create shorts and inhibit our mechanics.

it becomes important to check the bottom side of nanobeams in order to make sure there are no shorts in the capacitor. The most common reason for shorts is the nanobeam’s movements during the undercut which allow it to stick to the adjacent membrane (i.e., closing and shorting the capacitive gap). Another reason for shorts can be seen by imaging the bottom of the electromechanical device. Figure 4.27(b) shows how one can observe residue (strips of aluminum) left from the shadow evaporation of the gaps which would not be seen by imaging from the top of the chip, but could short the capacitive gap from bottom. Cooling the sample with a dilution refrigerator in order to take measurements and detect shorts (no signal) takes a significant amount of time and having the ability to image the devices from the bottom allowed us to verify that small gaps were completely

open and absent of shorts without having to cool down and measure the sample.

4.7 Nanobeam Fundamental Mode Measurements

We have reviewed the motivations, design, and fabrication of our electromechanical system such that we can discuss our measurements. Detecting signals attributed to mechanical oscillations of our electromechanical system requires cooling down the system to ≈ 10 mK where it will be well below the superconducting critical temperature of aluminum. Our initial experiments involve using electromagnetically induced transparency to measure properties of the mechanical nanobeam's 4 MHz fundamental mode because of its high coupling strength compared to the high frequency breathing mode. Our measurements allow us to measure properties about the microwave circuit, mechanics, and the electromechanical coupling, g_{EM} .

4.7.1 Dilution Refrigerator Overview

We will describe the measurements conducted on our devices at cryogenic temperatures using a BlueFors dry dilution refrigerator to cool to temperatures ≈ 10 mK. These low temperatures allow us to prepare the aluminum wiring into a superconducting state and to fabricate LC resonators with low loss and high quality factors. The low temperatures also allow us to probe the devices with a reduced thermal noise in the GHz microwave regimes.

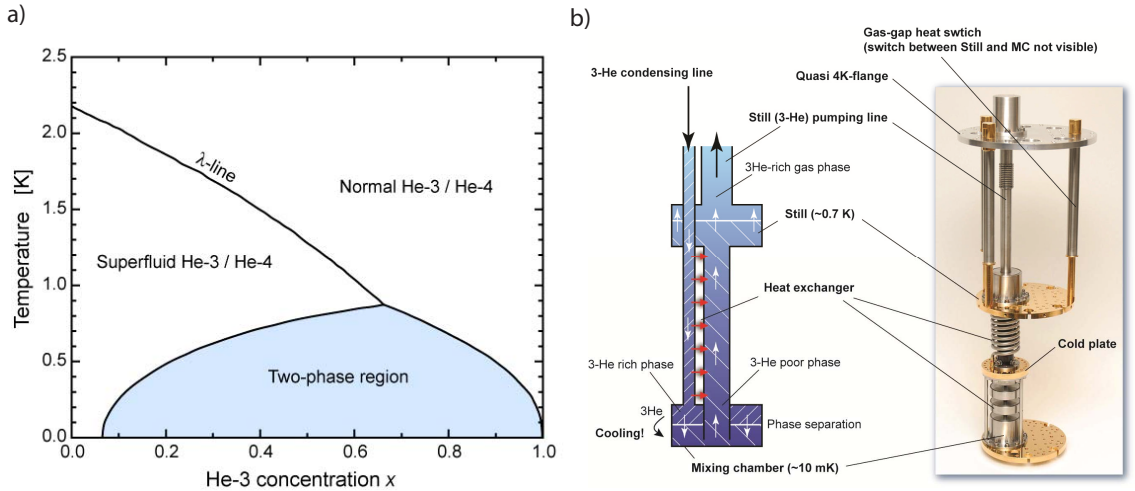


Figure 4.28: **Dilution Refrigerator Operation.** (a): Phase diagram of liquid ^3He - ^4He (b): Schematic showing the general operation of dilution refrigeration alongside corresponding photograph of the real components. (Taken from BlueFors Manual)

The BlueFors cryogen-free dilution refrigerator is based on the heat of mixing of ^3He and ^4He to continuously cool to ≈ 10 mK. A pulse tube cooler delivers cooling to the cryostat which achieves pre-

cooling to temperatures of 4.2 K using helium. After pre-cooling, a compressor raising the pressure of the $^4\text{He}/^3\text{He}$ mixture to ≈ 2 bar. The incoming ^3He condensing line is cooled through the heat exchangers which achieve low enough temperatures for the mixture to condense after the mixture is forced through the main flow impedance of the system. The mixing chamber, heat exchangers, and the still are filled with $^4\text{He}/^3\text{He}$ condensate. Once in this state, the dilution refrigeration cycle begins when we pump on the still, which lowers the vapor pressure in the still, allowing evaporation of ^3He which is pumped away and recycled back into the system through the condensing line as seen in Figure 4.28. The evaporation of ^3He from the still evaporatively cools it to a temperature of ≈ 870 mK. The dilution refrigerator operates on the principle that ≈ 870 mK the mixture spontaneously undergoes a phase separation to form a ^3He -rich phase (concentrated phase) and a ^4He -rich phase (dilute phase). We can see in phase diagram in Figure 4.28 where at extremely low temperatures the concentrated phase becomes entirely ^3He while the dilute phase contains about 93.4% ^4He and 6.6% ^3He . We know the enthalpy of ^3He in the dilute phase is larger than the concentrated phase so energy is needed to move ^3He from concentrated to dilute phase. The dilute phase is heavier due to gravity and settles at the bottom of the chamber. Because of the difference in vapor pressure between ^3He and ^4He , the helium pumped away from the dilute phase condensate in the still is almost entirely ^3He . Once again the ^3He is pumped into the incoming condensing line and cooled with counter flow heat exchangers. Once the cooled ^3He enters the mixture chamber it is forced through the phase boundary which separates the dilute and concentrated phases and achieves cooling. Through osmosis, the ^3He is forced through this phase boundary as it moves into the still to equalize the increase the concentration of ^3He in the still which is being pumped and deprived of ^3He . We can increase this flow of ^3He through the phase boundary by applying heat to the still to raise its temperature and also its vapor pressure resulting in larger flow rate of the dilution refrigeration process.

4.7.2 Experimental Setup

The RF components used in our measurement setup operate in the 8-12.5 GHz range which sets the frequencies we choose for our microwave LC resonators. Our setup outside the dilution fridge at room temperature includes two Rohde & Schwarz SMB100-A microwave sources, Rohde & Schwarz ZVL-13 vector network analyzer (VNA) and a Rohde & Schwarz FSV30 spectrum analyzer (SA). As seen in Figure 4.29, the two microwave sources and VNA are added together using two MiniCircuit ZX10-2-126+ combiners outside of the dilution refrigerator. We use RF coaxial cables which are connected to high vacuum feedthrough in order to send our microwave signals to the 10mK stage. We reduce the thermal noise that enters the cryogenic system with XMA attenuator before arriving at the circulator 1. The circulator consists of a RADITEK cryogenic circulator which operates in the 8-12 GHz regime. The signal continue on through a coaxial cable into the MMPX connectors of

our printed circuit board (PCB) as seen in Figure 4.29(d).

The custom designed PCB allows us to connect our nano-scale devices to coaxial lines in our dilution refrigerator. We glue our chips to a PCB with RF waveguides and connect our chip's lithographically defined CPW launchers to the PCB RF waveguides using aluminum wire-bonding which uses heat, pressure, and ultrasonic energy to weld 30 μm diameter aluminum bonding wire to metal surfaces. In Figure 4.29(d), we can see one aluminum bonding wire connecting to the launcher on the chip. The numerous adjacent bonding wires that surround the chip are there to short the ground planes of the chip and PCB. The CPW launchers are adiabatically transitioned (lithographically) into the feed-line which inductively couples to our microwave cavities. The feed-line is shorted into the ground plane of the chip, causing the signals to be reflected back to circulator

1 and onto circulator 2, which is used for isolation from noise coming into dilution refrigerator at the 10 mK stage through the output lines. After the low-power microwave signals have passed through a second circulator (isolator), they are amplified using a Caltech CIICRYO01-12A HEMT amplifier which works at the 4 K stage of the dilution refrigerator with a gain of 31 dB. This 4 K HEMT amplifier adds the majority of the noise to our detection signal and is followed by a second amplifier at room-temperature which gives us more gain on our signal with negligible noise added to our signal. The detection signal gets a total amplification of 55-60 dB and is split using MiniCircuits ZX10-2-126+ and detected using the vector network analyzer and spectrum analyzer.

4.7.3 Microwave Cavity Characterization

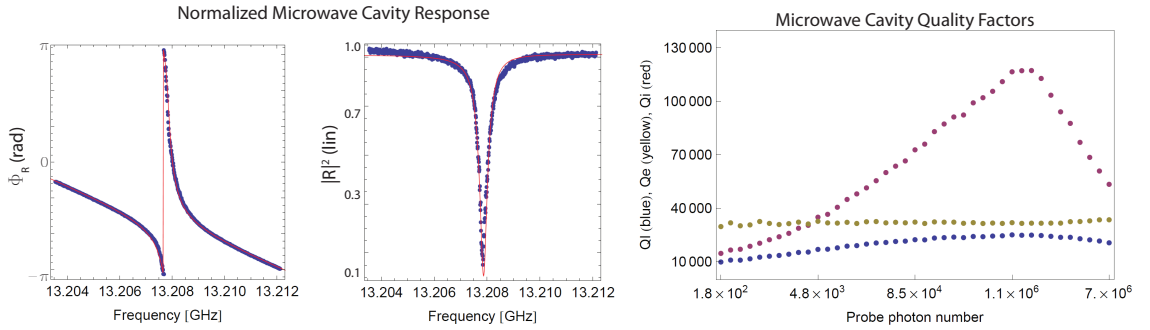


Figure 4.30: **Microwave Cavity Characterization.** (a): Resonator phase response (left) and the normalized reflection amplitude response. (b): Quality factors as a function of intra-cavity photon number.

Superconducting LC resonators are characterized by their resonance frequency, ω_{LC} , internal quality factor, Q_i , and external quality factor, Q_E . Using VNA measurement as a source and detector we can retrieve the resonator's amplitude and phase response seen in Figure 4.30(a). We can use these responses to fit to theory and determine Q_i and Q_E using the I and Q quadratures from the VNA. We found that our microwave cavities could attain internal quality factors of $Q_i \approx 10,000$ at low probe powers and $\approx 120,000$ at higher powers with external quality factors, $\approx 30,000$ for all probe powers (Figure 4.30(c)). It is well-known in the microwave community that variation in the internal quality factor, Q_i can be attributed to two-level systems (TLS) formed from O-H bonds in the aluminum oxide residing on our aluminum wires. The low Q_i at low powers come from the saturation of TLS loss tangent whereas the high Q_i at high powers comes about from power saturation of the two level fluctuators[75]. The sudden drop in Q_i at 10^6 intra-cavity photons can be attributed to non-linearity of superconductors at high power and is not TLS related. This is discussed in detail in [75]. We are able to achieve relatively high quality factors with circuits on membranes despite concerns that the protective oxide layer, a byproduct of the mTMAH etch, would introduce an

excessive amount of two level systems to the LC resonator.

4.7.4 Nanobeam Mechanical Frequency Characterization

Nanofabrication inherently has small variabilities from device to device produced by small variations in every step of the process (i.e., variations in e-beam lithography, etches, evaporations, etc). This can produce $\approx 10\%$ deviations in the frequency of the mechanical beam's fundamental mode which must be measured for every individual device. When an electromechanical system has a cooperativities larger than 1, we can use self-induced mechanical oscillations to easily find the frequency of individual nanobeams. With a sufficiently strong blue-detuned coherent drive, the mechanical oscillations can display anti-damping ($\Gamma_{\text{eff}} < 0$) which leads to exponential growth of any initial fluctuations which finally saturate due to nonlinear effects resulting in self-sustained mechanical oscillations. We can look at the effective electromechanical linewidth,

$$\Gamma_{\text{eff}} = \Gamma_m - \frac{4g_0^2 \bar{n}_d \kappa}{\kappa^2 + 4(\Delta - \Omega_m)^2} \quad (4.42)$$

and see when a drive tone is strong (large \bar{n}_d) and blue-detuned a mechanical frequency away ($\Delta \approx \Omega_m$) that Γ_{eff} becomes negative. Using COMSOL we simulate the nanobeam (without the membrane) with aluminum wires and get an approximate value for fundamental mode frequency, as seen in Figure 4.12(a). Using our simulated frequency of ≈ 4 MHz, we find our microwave cavity center and sweep our drive tone ≈ 4 MHz blue-detuned from it until we observe a mechanical lasing peak in the power spectral density (PSD) in our spectrum analyzer as seen in Figure 4.31. We can see that the difference between our strong blue-sideband detuned microwave drive at ≈ 11.434 GHz and the fundamental lasing peak of the nanobeam's fundamental mode at ≈ 11.430 GHz is the mechanical frequency Ω_m of the nanobeam ($\Omega_m \approx 4.05$ MHz). The extra peaks seen in the PSD are signatures of higher harmonics of mechanical non-linearities and the microwave cavity envelope produced by two-level systems [76]. As long as the strong coherent drive introduces enough intra-cavity photons, we can still detect this blue-detuned lasing when we are slightly off the ideal mechanical frequency detuning, making it easy to quickly determine the actual fabricated frequency of our nanobeams which we can use to perform red-sideband detuned measurements.

4.7.5 Introduction to Electromagnetically Induced Transparency: Atomic Ensembles

Interference between alternative pathways in quantum-mechanical processes is a well known effect in physics. This interference is similar to constructive and destructive interference between classical

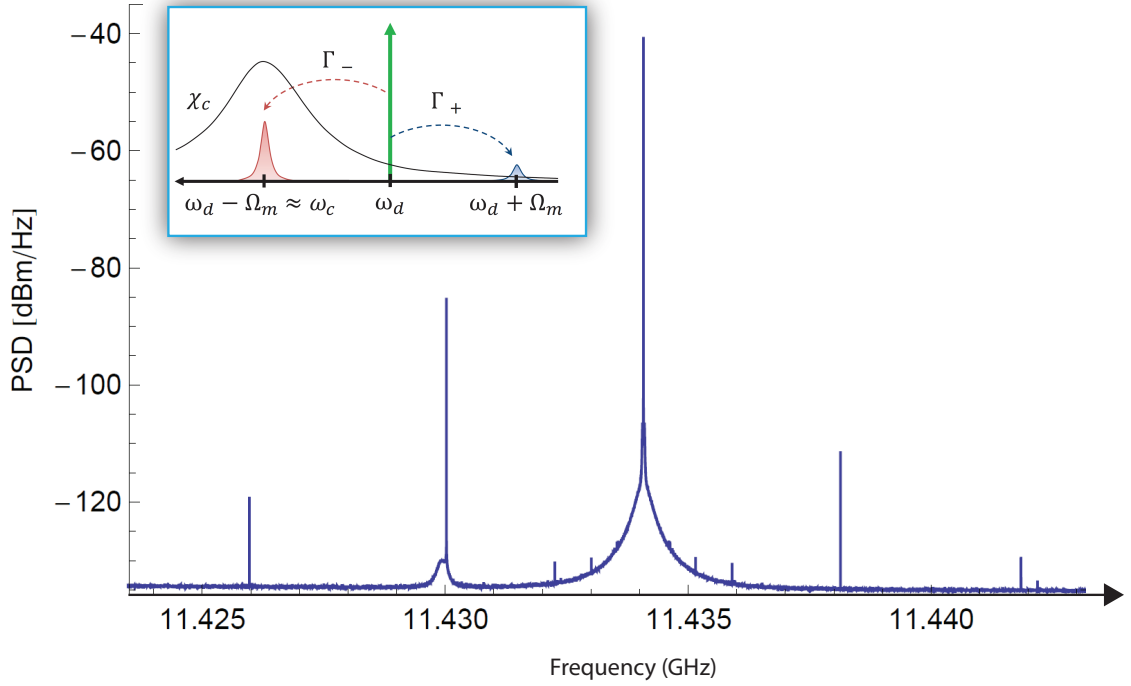


Figure 4.31: **Self Sustained Mechanical Oscillations.** Here we we the measured power spectral density of self-sustained mechanical oscillations with a strong blue-detuned tone at 12.3 GHz and the lasing peak of a flexural mechanical mode at 12.296. The difference in frequency between these two signals gives us the mechanical frequency of the nanobeams flexural mode. (Plots taken from [77])

waves where classical wave interference is the field amplitudes that are interfering, but in the quantum regime we can use quantities such as probability amplitudes to explain quantum interference effects. Electromagnetically induced transparency (EIT) is an interference phenomena between transition pathways within the internal quantum states of the atoms coupled to one or more laser fields. In particular, three-level atomic and molecular systems coupled to 2 laser fields exhibit interference effects that can result in cancellation of the absorption at a resonance transition frequency. This similar effect has been observed in optomechanical systems [78]. A strong coherent drive at ω_d red-detuned from the microwave cavity resonance can open a small transparency window for a second weak probe beam at ω_p . First we will look at the three-level atomic version of EIT to get a general idea of physical mechanisms involved and then move onto to EIT observed in our electromechanical system.

We look at the simplest configuration of atomic three-level system in which one could observe EIT as seen in Figure 4.32. If one were to look specifically at the cascade configuration in Figure 4.32(a) one would see that a weak probe beam is tuned to the $|1\rangle \rightarrow |2\rangle$ transition and the strong drive beam is tuned to the $|2\rangle \rightarrow |3\rangle$ transition. We know that $|1\rangle \rightarrow |2\rangle$ and $|2\rangle \rightarrow |3\rangle$ are allowed electric dipole transitions but $|1\rangle \rightarrow |3\rangle$ is not an allowed dipole transition in line with selection rules.

We can then think about the way that EIT arises from such configurations by focusing on the

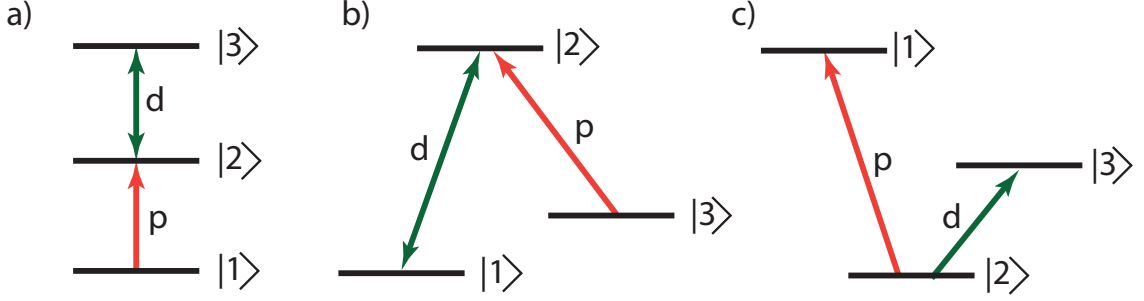


Figure 4.32: **Basic Configurations for EIT.** (a): Cascade configuration (b): Λ configuration (c): V configuration. The strong drive beam is labeled as d and weak probe as p.

simplest cascade configuration as seen in Figure 4.32(a). In this instance we look at the excitation of state $|2\rangle$ through two pathways (although more exist). The simplest is the $|1\rangle \rightarrow |2\rangle$, but the strong drive beam allows for an alternative route for the excitation of state $|2\rangle$: $|1\rangle \rightarrow |2\rangle \rightarrow |3\rangle \rightarrow |2\rangle$. The destructive interference of the probability amplitudes for these pathways gives us a transparency window for the probe beam. Figure 4.33(bc) shows the imaginary and real components of the electromagnetic susceptibility, $\chi(\omega_p)$ of the three-level atomic gas medium with and without the drive beam (solid and dashed plots, respectively) plotted as a function of the weak probe beam at ω_p relative to the atomic resonance at ω_p^0 . For the cascade configuration we will specify ω_p^0 with $\omega_{21}^0 = (E_2 - E_1)/\hbar$ where E_1 and E_2 are the energy levels of $|1\rangle$ and $|2\rangle$. Figure 4.33(b) shows the imaginary part of the electromagnetic susceptibility $\text{Im}[\chi(\omega_p)]$ which is related to the absorption coefficient of the atomic gas medium by $\alpha(\omega_p) = k \text{Im}[\chi(\omega_p)]$ where $k = 2\pi/\lambda$. The absorption coefficient is simply related to the transmission t by $T(\omega_p) = \exp(-\alpha(\omega_p) \cdot x)$ where x is the distance traveled in the absorbing atomic medium. In both Figure 4.33(bc), it has been assumed that the strong drive beam at ω_d is tuned to the atomic resonance frequency, ω_d^0 for the $|2\rangle \rightarrow |3\rangle \rightarrow$ transition. It is easy to see that the dip in $\text{Im}\chi(\omega_p)$ then creates a narrow peak of increased transmission which is centered at the frequency of the probe beam at ω_p^0 which is the main attribute of EIT.

Figure 4.33(c) shows the real part of the electromagnetic susceptibility $\text{Re}[\chi(\omega_p)]$ which is related to the refractive index of the atomic gas medium by $n(\omega_p) = 1 + (1/2)\text{Re}[\chi(\omega_p)]$. Again we see that with a strong drive tuned to the atomic transition ω_d , we find there is a narrow dip in refractive index. This corresponds to an interesting atomic medium with a dispersion relation such that $dn/d\omega_p > 0$ which depends on ω_p (solid line). This is interesting for application in slowing the group velocity of light which is given by

$$v_g = \frac{c}{n(\omega_p) + \omega_p \frac{dn}{d\omega_p}} \quad (4.43)$$

In order to understand how the three-state configuration with drive and probe beams manifests

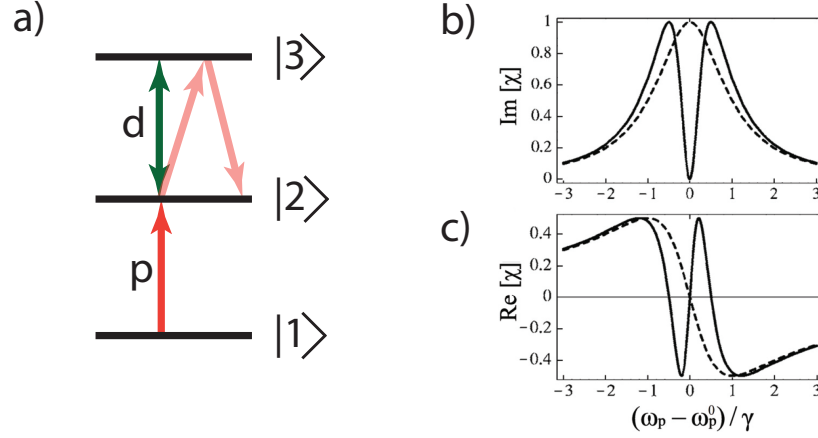


Figure 4.33: **EIT Transparency Windows.** (a): Shows 2 pathways for a excitation of state $|2\rangle$. One transition is $|1\rangle \rightarrow |2\rangle$. With the strong drive beam, d , we open up another pathway, $|1\rangle \rightarrow |2\rangle \rightarrow |3\rangle \rightarrow |2\rangle$. Changes in susceptibility seen in (b) are a result of destructive interference of transition probabilities of these two pathways. (b): Shows imaginary component of susceptibility $\chi(\omega_p)$ which is related to absorption and transmission coefficients of the probe beam. (c) Shows real component of susceptibility related to the refractive index related to slow-light effects of the probe beams group velocity. In both (b) and (c) one sees the nominal profiles of each without a drive beam (dashed) and with a drive beam to induce EIT effects (solid). Figures (b) and (c) were taken from [79].

itself in the electromagnetic susceptibility $\chi(\omega_p)$ we still concentrate on the cascade configuration (Figure 4.32(a)). Let's consider a weak probe beam with frequency, ω_p , nominal atomic transition $|1\rangle \rightarrow |2\rangle$ with resonance frequency $\omega_{21} = \omega_p^0$, and detuning of probe beam from resonance $\Delta_1 = \omega_p - \omega_{21}$. Let's also consider the strong drive beam with frequency, ω_d , nominal atomic transition $|2\rangle \rightarrow |3\rangle$ with resonance frequency ω_{32} , and detuning of the drive beam from this resonance frequency, $\Delta_2 = \omega_d - \omega_{32}$. As shown in [80], in the weak probe limit, the matrix element ρ_{21} associated with absorption and dispersion can be written as

$$\rho_{21} = -E_p \frac{i\mu_{21}/2\hbar}{\gamma_{21} - i\Delta_1 + \frac{\Omega_d^2}{\gamma_{31} - i(\Delta_1 + \Delta_2)}} \quad (4.44)$$

where $\Omega_d = \mu_{32}E_d/\hbar$, μ_{21} and μ_{32} are elements of the dipole moment operator for transition $1 \rightarrow 2$ and $2 \rightarrow 3$, respectively, E_d is the amplitude of the drive beam, and E_p is the amplitude of the probe beam. Neglecting other relaxation processes such as dephasing collisions (we assume a collisionless atomic ensemble), the decay rates γ_{ij} for atomic coherence ρ_{ij} can be written as

$$\gamma_{ij} = \frac{\Gamma_i + \Gamma_j}{2} \quad (4.45)$$

and since we associate state $|1\rangle$ with the ground state then $\Gamma_1 = 0$ and so $\gamma_{21} = \Gamma_2/2$ and $\gamma_{31} = \Gamma_3/2$.

We can relate the electromagnetic susceptibility $\chi(\omega_p)$ with ρ_{21} by the polarization P of the atomic ensemble written as

$$P = \frac{1}{2}\epsilon_0 E_d [\chi(\omega_p)e^{-i\omega_p t} + c.c.] = -\mu_{21}N\rho_{21}e^{-i\omega_p t} + c.c. \quad (4.46)$$

where N is the density of the atomic ensemble. Using the expressions for ρ_{21} and P we get a susceptibility of

$$\chi = \frac{i\mu_{21}^2 N / \hbar \epsilon_0}{\gamma_{21} - i\Delta_1 + \frac{\Omega_d^2}{\gamma_{31} - i(\Delta_1 + \Delta_2)}} \quad (4.47)$$

whose imaginary and real components are plotted in Figure 4.33. The absorption minimum manifests itself provided that the detuning Δ_1 and Δ_2 satisfy the conditions for a two photon resonance such that $\Delta_1 + \Delta_2 = 0$.

4.7.6 EIT Analog in Electromechanical System

An analog of EIT has been found in cavity electromechanical systems ([81], [82], [82], [78]), where one utilizes electromechanical coupling to manipulate the system's response to a weak microwave probe tone by using a strong coherent microwave tone that drives the lower motional sideband. We consider a weak probe tone $\bar{\alpha}_p$ and strong coherent drive tone, $\bar{\alpha}_d$, which results in the displacement of cavity microwave modes $\hat{a} \rightarrow \hat{a} + \bar{\alpha}_d + \bar{\alpha}_p$. In this EIT configuration we can assume (as was done in the case of an atomic ensemble) that fluctuations in the tones will average out and that we can, to first order, replace $\hat{a} \approx \bar{\alpha}_p$. We can then write the Heisenberg-Langevin equations for the intra-cavity probe $\bar{\alpha}_p$ as

$$\dot{\bar{\alpha}}_p = \left(-i\omega_c - \frac{\kappa}{2}\right)\bar{\alpha}_p + ig_0\sqrt{\langle\bar{n}_d\rangle}\hat{b} + \sqrt{\kappa_{ex}}\hat{a}_{p,in} \quad (4.48)$$

$$\dot{\hat{b}} = \left(-i\omega_m - \frac{\Gamma_m}{2}\right)\hat{b} + ig_0\sqrt{\langle\bar{n}_d\rangle}\bar{\alpha}_p \quad (4.49)$$

in which thermal noise operators of the cavity and mechanics are negligible. Because we work in the limit where drive tone is much larger than our probe tone we can linearize the Hamiltonian resulting in reflection coefficient for the probe written as

$$R_{\text{EIT}} = 1 - \frac{\kappa_{ex}}{i(\omega_p - \omega_c) + \kappa/2 + \frac{G^2}{i(\omega_p - \Omega_m - \omega_d) + \Gamma_m/2}} \quad (4.50)$$

where G is the parametric coupling strength $G = g_0\sqrt{\langle\bar{n}_d\rangle}$. We can then look at the theoretical magnitude reflected probe, $|R_{\text{EIT}}|^2$ in the ideal case when $\Delta = -\Omega_m$ as seen in Figure 4.34. We can clearly see that with low drive powers (and low cooperativities) we see the unperturbed microwave cavity. As we increase the drive power we see a narrow mechanical feature with a linewidth propor-

tional to $\Gamma_m(1 + C)$ at a frequency $\omega_d + \Omega_m$ as seen in Figure 4.34. A more detailed derivation can be found in [77].

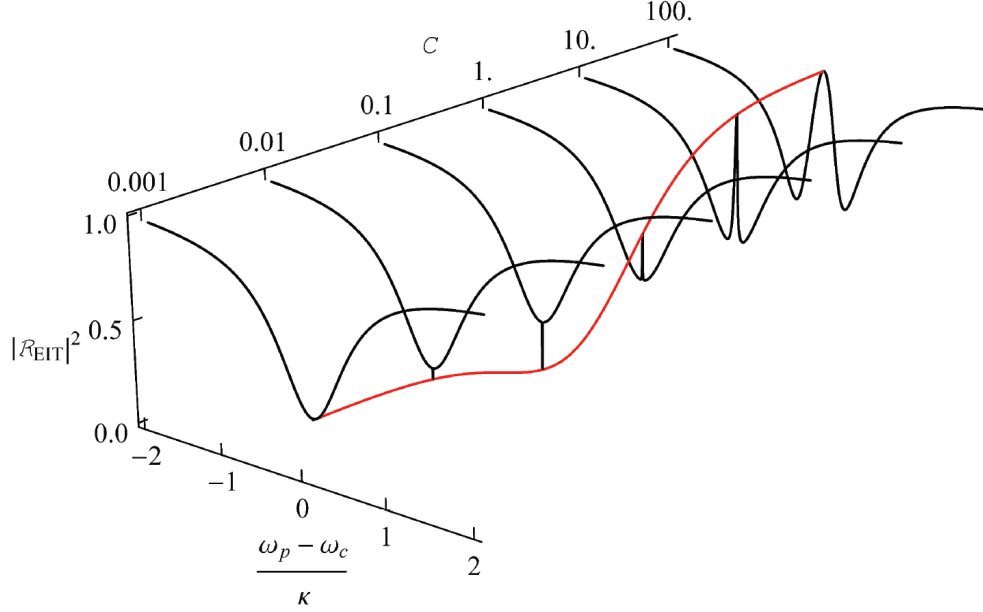


Figure 4.34: **Theoretical EIT Probe Reflection.** Here we see analytical plots of $|R_{\text{EIT}}|^2$ as a function of cooperativity C for a set ideal detuning of $\omega_d - \omega_p = -\Omega_m$ and a coupling efficiency of $\kappa_{\text{ex}}/\kappa = 0.75$. The red line is a plot of mechanical peak reflection versus cooperativity, C .

4.7.7 EIT measurements

Now we discuss the observation of an EIT transparency window for a probe tone exactly one mechanical frequency Ω_m detuned from a strong drive tone, ω_d in our fabricated structures. We emphasize the utility in finding the exact mechanical frequency of each nanobeam using self sustained oscillations with a strong pump blue-detuned of the cavity resonance. While the self sustained oscillations allow us to see large peaks arise as we sweep our blue-tune our strong drive across the region a mechanical frequency away, the same cannot be done easily with a strong drive red-detuned from the microwave cavity center because the mechanical peaks that arise have linewidths on the order of Hz which are difficult to observe if one does not already know the exact mechanical frequency of the nanobeam device being measured. We first measure the EIT peak as a function of detunings of the strong microwave drive, $\Delta + \Omega_m$. We then fit our observed peaks on the VNA to our theoretical reflected signal Equation 4.50 as seen in Figure 4.35. The plots we see the VNA signal in blue and the fits in red. Because of the very narrow linewidths of the EIT peaks, we plot the entire microwave cavity resonance as the EIT peaks moves across the cavity center as the microwave drive tone is detuned from $\Delta + \Omega_m \approx -334.6$ kHz to $\Delta + \Omega_m \approx 522.9$ kHz (Figure 4.35(a)) as well as the zoom-in

view of each EIT peak (Figure 4.35(b)). Because our model can also fit to small Hz linewidths we can estimate that our electromechanical system has $C \approx 3 - 5$. We find the maximum cooperativity by tuning our drive tone to the red-sideband $\Delta = -\Omega_m$.

One important feature to notice in Figure 4.35(b) is the inversion of electromagnetic induced

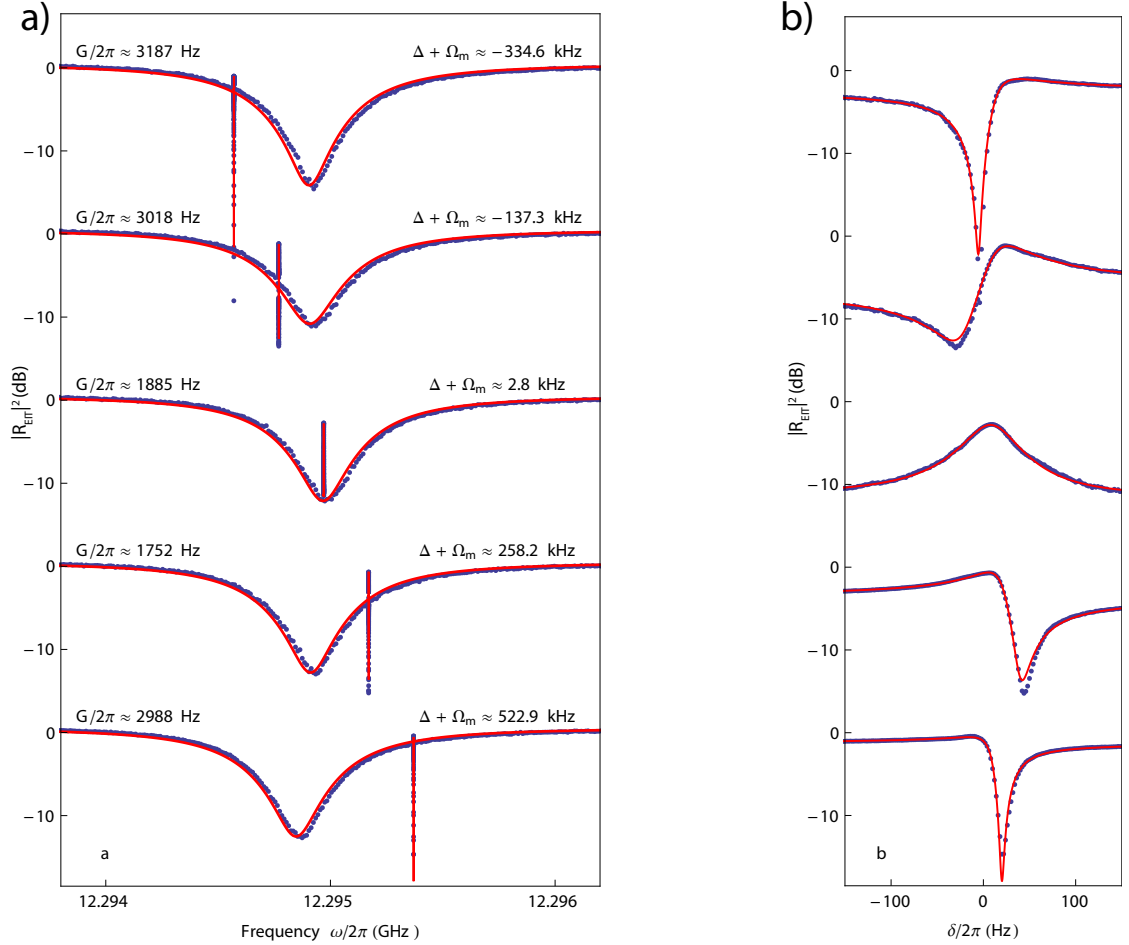


Figure 4.35: EIT for Different Drive Detuning. (a): Broad spectrum look at microwave cavity resonance with electromagnetically induced transparency as it moves across the cavity center as a function of strong drive detuning $\Delta + \Omega_m$. (b): Zoomed in view of EIT with corresponding peaks in (a).

transparency from peaks to dips. This is also observed in Figure 4.36 where we have kept an ideal detuning of the strong drive tone at $\Delta = -\Omega_m$ while observing the microwave cavity center. We also observe the same behavior as we increase the number of intra-cavity photons from the drive tone. We see that the reflection coefficient begins with a dip at low photon number and evolves into a peak as the photon number is increased, which is possible because the reflective cavity geometry

with coupling efficiencies $\eta = \kappa_{\text{ex}}/\kappa > 0.5$. Our electromechanical devices achieve coupling efficiencies of $\eta \approx 0.7$. From fits to the EIT model in Figure 4.36, we can estimate g_0 and Γ_m . We find from

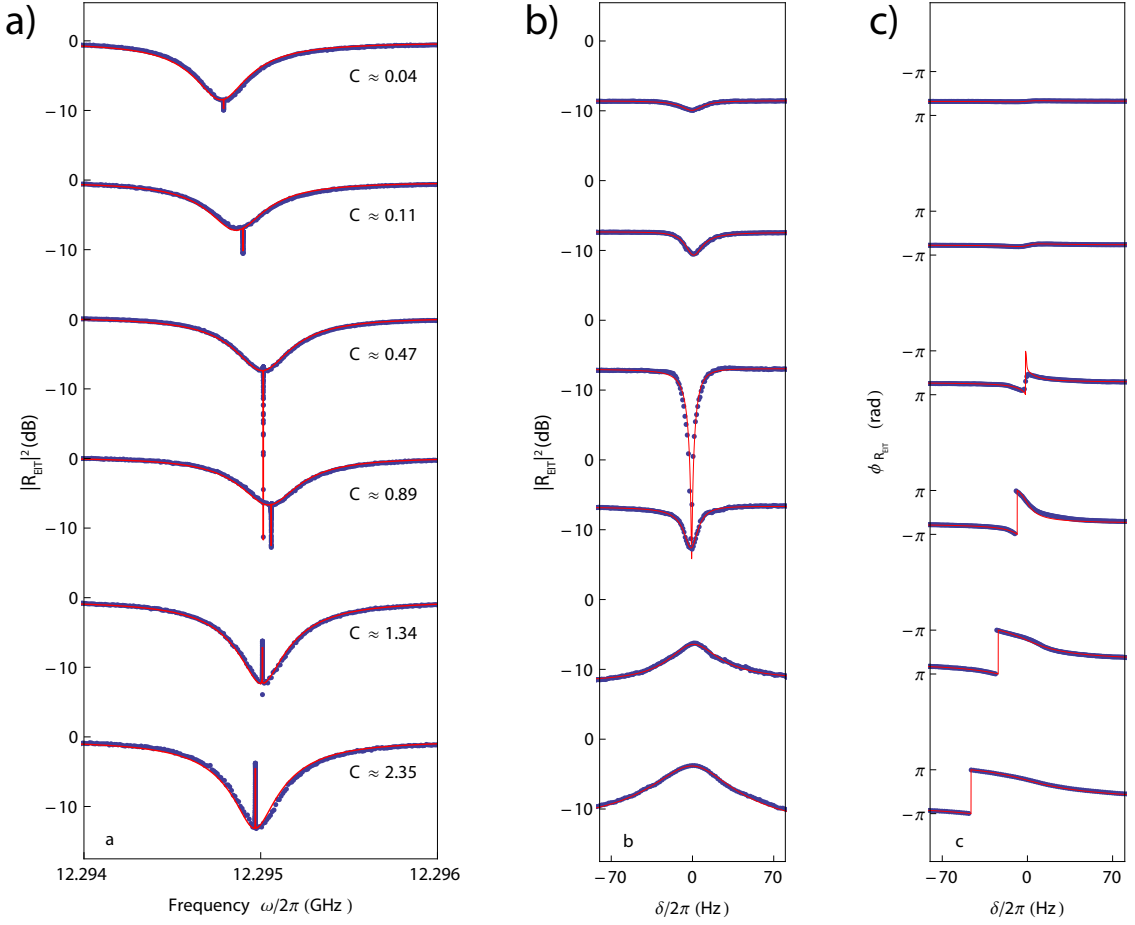


Figure 4.36: **EIT for Different Photon Number.** (a): Broad spectrum look at microwave cavity resonance with electromagnetically induced transparency as a function of strong drive photon number at ideal detuning $\Delta = -\Omega_m$. (b): Zoomed in view of EIT with corresponding peaks (c): Zoomed in view of EIT with corresponding phase responses. Red lines are fits to the reflectivity coefficient.

measurements seen Figure 4.36(b) that mechanical linewidths vary between $\Gamma_m/2\pi \approx 10 - 25$ Hz as shown in Figure 4.37. The fitted values for the parametric coupling rate G as a function of intra-cavity photon number \bar{n}_d . We find by doing a linear fit of this parameters gives us an estimate on the vacuum coupling rate of $g_0 \approx 11.4$ Hz. We estimate the intra-cavity drive photons by taking into account our microwave source and all the attenuations and losses before the signal enters the electromechanical circuit, properties of the LC resonators, and the drive detuning. We find that the maximum cooperativities in our system are $C \approx 7$ which is limited by the non-linearities of the microwave circuit at high drive powers (not attributed to TLS).

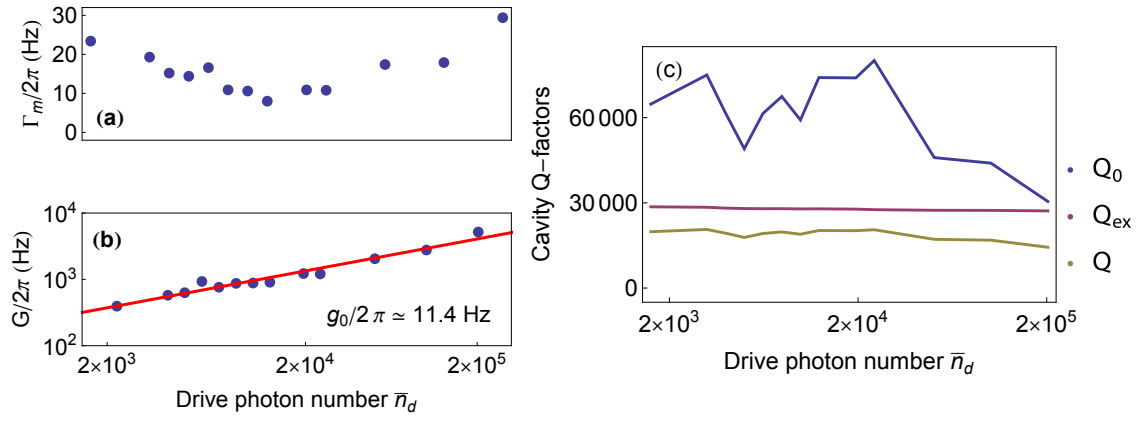


Figure 4.37: **EIT Parameter Fits.** (a): Intrinsic linewidth Γ_m vs. intra-cavity drive photon number (b): parametric coupling rate $G = g_0\sqrt{\bar{n}_d}$ (c): LC resonator quality factors. All of these were done at ideal detuning $\Delta = -\Omega_m$

Chapter 5

Publications

1. Paolo Pani, Emanuele Berti, Vitor Cardoso, Yanbei Chen, Richard Norte, “Gravitational-wave signatures of the absence of an event horizon. I. Nonradial oscillations of a thin-shell gravastar,” *Phy. Rev. Lett D* (2009).
2. Paolo Pani, Emanuele Berti, Vitor Cardoso, Yanbei Chen, Richard Norte, “Gravitational-wave signatures of the absence of an event horizon. II. Extreme mass ratio inspirals in the spacetime of a thin-shell gravastar,” *Phy. Rev. Lett D* (2010).
3. Kang-Kuen Ni, Richard Norte, Dalziel Wilson, Jon Hood, Darrick Chang, Oskar Painter, H. J. Kimble “Enhancement of Mechanical Q Factors by Optical Trapping,” *Phy. Rev Lett* **15**, 035007– (2012).
4. S.-P. Yu, J. D. Hood, J. A. Muniz, M. J Martin, Richard Norte, C.-L. Hung, Sean M. Meenehan, Justin Cohen, Oskar Painter, H. J. Kimble, “Nanowire photonic crystal waveguides for single-atom trapping and strong light-matter interactions,” *Appl. Phys. Lett.* **104**, 1111-3– (2014).

Bibliography

- [1] A. Goban, K. Choi, D. Alton, D. Ding, C. Lacroûte, M. Pototschnig, T. Thiele, N. Stern, and H. Kimble, “Demonstration of a state-insensitive, compensated nanofiber trap,” *Physical review letters* **109**, 033603 (2012).
- [2] J. D. Cohen, S. M. Meenehan, and O. Painter, “Optical coupling to nanoscale optomechanical cavities for near quantum-limited motion transduction,” *Optics express* **21**, 11227–11236 (2013).
- [3] A. Cleland, “Optomechanics: Photons refrigerating phonons,” *Nature Physics* **5**, 458–460 (2009).
- [4] O. Usenko, A. Vinante, G. Wijts, and T. Oosterkamp, “A superconducting quantum interference device based read-out of a subattonewton force sensor operating at millikelvin temperatures,” *Applied Physics Letters* **98**, 133105 (2011).
- [5] A. N. Cleland and M. R. Geller, “Superconducting qubit storage and entanglement with nanomechanical resonators,” *Physical review letters* **93**, 070501 (2004).
- [6] J. Chan, T. M. Alegre, A. H. Safavi-Naeini, J. T. Hill, A. Krause, S. Gröblacher, M. Aspelmeyer, and O. Painter, “Laser cooling of a nanomechanical oscillator into its quantum ground state,” *Nature* **478**, 89–92 (2011).
- [7] J. Teufel, T. Donner, D. Li, J. Harlow, M. Allman, K. Cicak, A. Sirois, J. Whittaker, K. Lehnert, and R. Simmonds, “Sideband cooling of micromechanical motion to the quantum ground state,” *Nature* **475**, 359–363 (2011).
- [8] A. D. OConnell, M. Hofheinz, M. Ansmann, R. C. Bialczak, M. Lenander, E. Lucero, M. Neeley, D. Sank, H. Wang, M. Weides, et al., “Quantum ground state and single-phonon control of a mechanical resonator,” *Nature* **464**, 697–703 (2010).
- [9] D. Wilson, C. Regal, S. Papp, and H. Kimble, “Cavity optomechanics with stoichiometric SiN films,” *Physical review letters* **103**, 207204 (2009).

- [10] Z. Hao, A. Erbil, and F. Ayazi, “An analytical model for support loss in micromachined beam resonators with in-plane flexural vibrations,” *Sensors and Actuators A: Physical* **109**, 156–164 (2003).
- [11] A. Ashkin, “Optical trapping and manipulation of neutral particles using lasers,” *Proceedings of the National Academy of Sciences* **94**, 4853–4860 (1997).
- [12] A. Ashkin and J. Dziedzic, “Optical levitation in high vacuum,” *Applied Physics Letters* **28**, 333–335 (2008).
- [13] K. G. Libbrecht and E. D. Black, “Toward quantum-limited position measurements using optically levitated microspheres,” *Physics Letters A* **321**, 99–102 (2004).
- [14] D. E. Chang, C. Regal, S. Papp, D. Wilson, J. Ye, O. Painter, H. J. Kimble, and P. Zoller, “Cavity opto-mechanics using an optically levitated nanosphere,” *Proceedings of the National Academy of Sciences* **107**, 1005–1010 (2010).
- [15] I. Wilson-Rae, N. Nooshi, W. Zwerger, and T. Kippenberg, “Theory of ground state cooling of a mechanical oscillator using dynamical back-action,” *arXiv preprint cond-mat/0702113* (2007).
- [16] F. Marquardt, J. P. Chen, A. Clerk, and S. Girvin, “Quantum theory of cavity-assisted sideband cooling of mechanical motion,” *Physical Review Letters* **99**, 093902 (2007).
- [17] D. Chang, K. Ni, O. Painter, and H. Kimble, “Ultrahigh-Q mechanical oscillators through optical trapping,” *New Journal of Physics* **14**, 045002 (2012).
- [18] L. D. Landau and E. Lifshitz, “Theory of Elasticity, vol. 7,” *Course of Theoretical Physics* **3** (1986).
- [19] T. Li, S. Kheifets, D. Medellin, and M. G. Raizen, “Measurement of the instantaneous velocity of a Brownian particle,” *Science* **328**, 1673–1675 (2010).
- [20] N. Kiesel, F. Blaser, U. Delić, D. Grass, R. Kaltenbaek, and M. Aspelmeyer, “Cavity cooling of an optically levitated submicron particle,” *Proceedings of the National Academy of Sciences* **110**, 14180–14185 (2013).
- [21] J. Thompson, B. Zwickl, A. Jayich, F. Marquardt, S. Girvin, and J. Harris, “Strong dispersive coupling of a high-finesse cavity to a micromechanical membrane,” *Nature* **452**, 72–75 (2008).
- [22] D. J. Wilson, *Cavity optomechanics with high-stress silicon nitride films* (2012).
- [23] S. Schmid, K. Jensen, K. Nielsen, and A. Boisen, “Damping mechanisms in high-Q micro and nanomechanical string resonators,” *Physical Review B* **84**, 165307 (2011).

- [24] S. S. Verbridge, J. M. Parpia, R. B. Reichenbach, L. M. Bellan, and H. Craighead, “High quality factor resonance at room temperature with nanostrings under high tensile stress,” *Journal of Applied Physics* **99**, 124304 (2006).
- [25] P. E. Barclay, K. Srinivasan, O. Painter, B. Lev, and H. Mabuchi, “Integration of fiber-coupled high-QSiNx microdisks with atom chips,” *Applied physics letters* **89**, 131108 (2006).
- [26] H. Lee, T. Chen, J. Li, O. Painter, and K. J. Vahala, “Ultra-low-loss optical delay line on a silicon chip,” *Nature communications* **3**, 867 (2012).
- [27] J. Laconte, D. Flandre, J.-P. Raskin, et al., *Micromachined thin-film sensors for SOI-CMOS co-integration* (Springer, 2006).
- [28] G. Cagnoli, J. Hough, D. DeBra, M. Fejer, E. Gustafson, S. Rowan, and V. Mitrofanov, “Damping dilution factor for a pendulum in an interferometric gravitational waves detector,” *Physics Letters A* **272**, 39–45 (2000).
- [29] K. Y. Yasumura, T. D. Stowe, E. M. Chow, T. Pfafman, T. W. Kenny, B. C. Stipe, and D. Rugar, “Quality factors in micron-and submicron-thick cantilevers,” *Microelectromechanical Systems, Journal of* **9**, 117–125 (2000).
- [30] S. D. Penn, A. Ageev, D. Busby, G. M. Harry, A. M. Gretarsson, K. Numata, and P. Willems, “Frequency and surface dependence of the mechanical loss in fused silica,” *Physics Letters A* **352**, 3–6 (2006).
- [31] D. Armani, T. Kippenberg, S. Spillane, and K. Vahala, “Ultra-high-Q toroid microcavity on a chip,” *Nature* **421**, 925–928 (2003).
- [32] E. Hecht, “Hecht optics,” *Addison Wesley* **997**, 213–214 (1998).
- [33] B. Stipe, H. Mamin, T. Stowe, T. Kenny, and D. Rugar, “Noncontact friction and force fluctuations between closely spaced bodies,” *Physical review letters* **87**, 096801 (2001).
- [34] S. S. Verbridge, D. F. Shapiro, H. G. Craighead, and J. M. Parpia, “Macroscopic tuning of nanomechanics: substrate bending for reversible control of frequency and quality factor of nanos-tring resonators,” *Nano Letters* **7**, 1728–1735 (2007).
- [35] J. Yang, T. Ono, and M. Esashi, “Surface effects and high quality factors in ultrathin single-crystal silicon cantilevers,” *Applied Physics Letters* **77**, 3860–3862 (2000).
- [36] K. Usami, A. Naesby, T. Bagci, B. M. Nielsen, J. Liu, S. Stobbe, P. Lodahl, and E. S. Polzik, “Optical cavity cooling of mechanical modes of a semiconductor nanomembrane,” *Nature Physics* **8**, 168–172 (2012).

- [37] D. Kleckner, B. Pepper, E. Jeffrey, P. Sonin, S. M. Thon, and D. Bouwmeester, “Optomechanical trampoline resonators,” *Optics express* **19**, 19708–19716 (2011).
- [38] A. Ashkin and J. Dziedzic, “Optical levitation in high vacuum,” *Applied Physics Letters* **28**, 333–335 (1976).
- [39] O. Romero-Isart, A. C. Pflanzner, M. L. Juan, R. Quidant, N. Kiesel, M. Aspelmeyer, and J. I. Cirac, “Optically levitating dielectrics in the quantum regime: Theory and protocols,” *Physical Review A* **83**, 013803 (2011).
- [40] T. Li, S. Kheifets, and M. G. Raizen, “Millikelvin cooling of an optically trapped microsphere in vacuum,” *Nature Physics* **7**, 527–530 (2011).
- [41] M. Aspelmeyer, S. Gröblacher, K. Hammerer, and N. Kiesel, “Quantum optomechanics throwing a glance [Invited],” *JOSA B* **27**, A189–A197 (2010).
- [42] C. Genes, D. Vitali, and P. Tombesi, “Simultaneous cooling and entanglement of mechanical modes of a micromirror in an optical cavity,” *New Journal of Physics* **10**, 095009 (2008).
- [43] H. Müller-Ebhardt, H. Rehbein, R. Schnabel, K. Danzmann, and Y. Chen, “Entanglement of macroscopic test masses and the standard quantum limit in laser interferometry,” *Physical review letters* **100**, 013601 (2008).
- [44] A. G. Krause, M. Winger, T. D. Blasius, Q. Lin, and O. Painter, “A high-resolution microchip optomechanical accelerometer,” *Nature Photonics* **6**, 768–772 (2012).
- [45] J. Thompson, T. Tiecke, N. de Leon, J. Feist, A. Akimov, M. Gullans, A. Zibrov, V. Vuletić, and M. Lukin, “Coupling a single trapped atom to a nanoscale optical cavity,” *Science* **340**, 1202–1205 (2013).
- [46] K. J. Vahala, “Optical microcavities,” *Nature* **424**, 839–846 (2003).
- [47] B. Lev, K. Srinivasan, P. Barclay, O. Painter, and H. Mabuchi, “Feasibility of detecting single atoms using photonic bandgap cavities,” *Nanotechnology* **15**, S556 (2004).
- [48] F. Le Kien and K. Hakuta, “Cavity-enhanced channeling of emission from an atom into a nanofiber,” *Physical Review A* **80**, 053826 (2009).
- [49] E. Vetsch, D. Reitz, G. Sagué, R. Schmidt, S. Dawkins, and A. Rauschenbeutel, “Optical interface created by laser-cooled atoms trapped in the evanescent field surrounding an optical nanofiber,” *Physical review letters* **104**, 203603 (2010).

- [50] C. Wuttke, M. Becker, S. Brückner, M. Rothhardt, and A. Rauschenbeutel, “Nanofiber Fabry–Perot microresonator for nonlinear optics and cavity quantum electrodynamics,” *Optics letters* **37**, 1949–1951 (2012).
- [51] K. Nayak, F. Le Kien, Y. Kawai, K. Hakuta, K. Nakajima, H. Miyazaki, and Y. Sugimoto, “Cavity formation on an optical nanofiber using focused ion beam milling technique,” *Optics express* **19**, 14040–14050 (2011).
- [52] S. Dawkins, R. Mitsch, D. Reitz, E. Vetsch, and A. Rauschenbeutel, “Dispersive optical interface based on nanofiber-trapped atoms,” *Physical review letters* **107**, 243601 (2011).
- [53] A. Goban, C.-L. Hung, S.-P. Yu, J. Hood, J. Muniz, J. Lee, M. Martin, A. McClung, K. Choi, D. Chang, et al., “Atom–light interactions in photonic crystals,” *Nature communications* **5** (2014).
- [54] S. John and J. Wang, “Quantum electrodynamics near a photonic band gap: Photon bound states and dressed atoms,” *Physical review letters* **64**, 2418 (1990).
- [55] N. A. Bhat and J. Sipe, “Hamiltonian treatment of the electromagnetic field in dispersive and absorptive structured media,” *Physical Review A* **73**, 063808 (2006).
- [56] E. Shahmoon and G. Kurizki, “Nonradiative interaction and entanglement between distant atoms,” *Physical Review A* **87**, 033831 (2013).
- [57] C. Hung, S. Meenehan, D. Chang, O. Painter, and H. Kimble, “Trapped atoms in one-dimensional photonic crystals,” *New Journal of Physics* **15**, 083026 (2013).
- [58] P. Lodahl, S. Mahmoodian, and S. Stobbe, “Interfacing single photons and single quantum dots with photonic nanostructures,” *arXiv preprint arXiv:1312.1079* (2013).
- [59] H. Kimble, “The quantum internet,” *Nature* **453**, 1023–1030 (2008).
- [60] G. Sagué, E. Vetsch, W. Alt, D. Meschede, and A. Rauschenbeutel, “Cold-atom physics using ultrathin optical fibers: light-induced dipole forces and surface interactions,” *Physical review letters* **99**, 163602 (2007).
- [61] P. Lalanne, C. Sauvan, and J. P. Hugonin, “Photon confinement in photonic crystal nanocavities,” *Laser & Photonics Reviews* **2**, 514–526 (2008).
- [62] M. Borselli, *High-Q microresonators as lasing elements for silicon photonics*, Ph.D. thesis, California Institute of Technology (2006).

- [63] S.-P. Yu, J. Hood, J. Muniz, M. Martin, R. Norte, C.-L. Hung, S. M. Meenehan, J. D. Cohen, O. Painter, and H. Kimble, “Nanowire photonic crystal waveguides for single-atom trapping and strong light-matter interactions,” *Applied Physics Letters* **104**, 111103 (2014).
- [64] M. Winger, T. Blasius, T. Mayer Alegre, A. H. Safavi-Naeini, S. Meenehan, J. Cohen, S. Stobbe, and O. Painter, “A chip-scale integrated cavity-electro-optomechanics platform,” *Optics express* **19**, 24905–24921 (2011).
- [65] J. T. Hill, A. H. Safavi-Naeini, J. Chan, and O. Painter, “Coherent optical wavelength conversion via cavity optomechanics,” *Nature communications* **3**, 1196 (2012).
- [66] L. Tian and H. Wang, “Optical wavelength conversion of quantum states with optomechanics,” *Physical Review A* **82**, 053806 (2010).
- [67] T. Palomaki, J. Harlow, J. Teufel, R. Simmonds, and K. Lehnert, “Coherent state transfer between itinerant microwave fields and a mechanical oscillator,” *Nature* **495**, 210–214 (2013).
- [68] C. Regal, J. Teufel, and K. Lehnert, “Measuring nanomechanical motion with a microwave cavity interferometer,” *Nature Physics* **4**, 555–560 (2008).
- [69] M. Eichenfield, R. Camacho, J. Chan, K. J. Vahala, and O. Painter, “A picogram-and nanometre-scale photonic-crystal optomechanical cavity,” *Nature* **459**, 550–555 (2009).
- [70] M. Bruel, B. Aspar, and A.-J. Auberton-Herve, “Smart-Cut: a new silicon on insulator material technology based on hydrogen implantation and wafer bonding,” *Japanese journal of applied physics* **36**, 1636–1641 (1997).
- [71] M. J. Burek, N. P. de Leon, B. J. Shields, B. J. Hausmann, Y. Chu, Q. Quan, A. S. Zibrov, H. Park, M. D. Lukin, and M. Loncar, “Free-standing mechanical and photonic nanostructures in single-crystal diamond,” *Nano letters* **12**, 6084–6089 (2012).
- [72] R. F. Harrington and J. L. Harrington, *Field computation by moment methods* (Oxford University Press, 1996).
- [73] G. Yan, P. C. Chan, I. Hsing, R. K. Sharma, J. K. Sin, Y. Wang, et al., “An improved TMAH Si-etching solution without attacking exposed aluminum,” *Sensors and Actuators A: physical* **89**, 135–141 (2001).
- [74] N. Fujitsuka, K. Hamaguchi, H. Funabashi, E. Kawasaki, and T. Fukada, “Aluminum Protected Silicon Anisotropic Etching Technique Using TMAH with an Oxidizing Agent and Dissolved Si,” *RD Review of Toyota CRDL* **39**, 34–40 (2004).

- [75] J. Gao, *The physics of superconducting microwave resonators*, Ph.D. thesis, California Institute of Technology (2008).
- [76] F. Marquardt, J. Harris, and S. Girvin, “Dynamical multistability induced by radiation pressure in high-finesse micromechanical optical cavities,” *Physical review letters* **96**, 103901 (2006).
- [77] L. Heinzle, *Microwave Cavity Optomechanics on Silicon Nitride Membranes* (2014).
- [78] A. H. Safavi-Naeini, T. M. Alegre, J. Chan, M. Eichenfield, M. Winger, Q. Lin, J. T. Hill, D. E. Chang, and O. Painter, “Electromagnetically induced transparency and slow light with optomechanics,” *Nature* **472**, 69–73 (2011).
- [79] K. Kowalski, V. Cao Long, K. Dinh Xuan, M. Głódź, B. Nguyen Huy, and J. Szonert, “Electromagnetically induced transparency,” *Comput. Meth. Sci. Technol. Special* p. 145 (2010).
- [80] J. Gea-Banacloche, Y.-q. Li, S.-z. Jin, and M. Xiao, “Electromagnetically induced transparency in ladder-type inhomogeneously broadened media: Theory and experiment,” *Physical Review A* **51**, 576 (1995).
- [81] G. Agarwal and S. Huang, “Electromagnetically induced transparency in mechanical effects of light,” *Physical Review A* **81**, 041803 (2010).
- [82] F. Hocke, X. Zhou, A. Schliesser, T. J. Kippenberg, H. Huebl, and R. Gross, “Electromechanically induced absorption in a circuit nano-electromechanical system,” *New Journal of Physics* **14**, 123037 (2012).